

Sverre Magnus Selbach

**Structure, stability
and phase transitions
of multiferroic BiFeO_3**

Thesis for the degree of Philosophiae Doctor

Trondheim, November 2009

Norwegian University of Science and Technology
Faculty of Natural Sciences and Technology
Department of Materials Science and Engineering



NTNU

Norwegian University of Science and Technology

Thesis for the degree of Philosophiae Doctor

Faculty of Natural Sciences and Technology
Department of Materials Science and Engineering

© Sverre Magnus Selbach

ISBN 82-471-1841-2 (printed ver.)
ISBN 82-471-1842-9 (electronic ver.)
ISSN 1503-8181

IMT-Report 2009:118

Doctoral theses at NTNU, 2009:219

Printed by NTNU-trykk

This thesis has been submitted to

Department of Materials Science and Engineering
Norwegian University of Science and Technology

in partial fulfilment of the requirements for
the academic degree

Philosophiae Doctor

September 2009

Acknowledgements

First of all I would like to thank my main advisor Professor Tor Grande for giving me the opportunity and freedom to work with this project. His enthusiasm, his confidence in my work and his broad knowledge of materials science (especially thermodynamics!) has been an invaluable source of encouragement and motivation. I am also grateful to my co-advisor Professor Mari-Ann Einarsrud for her support and valuable comments to my work. Particularly during the writing of this dissertation her quick and thorough response to my numerous drafts has been greatly appreciated. I would also like to thank my co-advisor Professor Thomas Tybell for his support and interest in my work. His insight and complementary perspectives as a physicist have been very important to me.

I am indebted to the technical staff supporting the “Ceramics group” for always being helpful. Especially Elin Nilsen, Eli Beate Jakobsen and Jools (Dr. Julian Tolchard) have gone out of their way to assist me in the labs.

I would like to thank everyone in the “Ceramics group” for making it such a wonderfully diverse, inspiring and fun environment to work in. A big thank you goes to my former and present office mates Dr. Guozhong Wang, Dr. Per Martin Rørvik and Sidsel Meli Hanetho for all our numerous non-scientific discussions and brakes.

I am grateful to Professor Ram Seshadri at the University of California, Santa Barbara, for hosting me as a visitor in his group during 3.5 months in the autumn of 2008. I greatly appreciated the open and pleasant atmosphere in his group, and I thank all its members for the time I spent with them. Dr. Serena Corr is especially acknowledged for looking after me in SB. I must also thank Jim Rondinelli for courageously letting me rent his room during my stay in SB, and my house mates Dan, Mike and Zeric for helping me with all sorts of everyday practical issues.

I thank Dr. James O’Brien at Quantum Design Inc. in San Diego, CA for the three very enjoyable days of intense learning I spent with him in QD’s laboratories. I would also like to thank Professor Gavin Lawes at Wayne State University, Detroit for our ongoing collaboration.

Professor Valeri Petkov at the Central Michigan University invited me to spend two days with him at Argonne National Laboratory, Chicago, IL and I would like to thank him for our ongoing work on finite size effects.

Throughout the course of this work I’ve also had the joy of co-supervising some outstanding students carrying out their project works or master theses in our group. Thank you, Kati Tschöpe, Waldemar Fegler, Kristin Bergum, Torbjørn Cederløv and Amund Nordli Løvik, your efforts have been greatly appreciated.

I have spent nine wonderful years in Trondheim, and I owe that to all my friends here, thank you, all of you! Finally, I would like to thank my parents for their encouragement and support, and for inspiring curiosity from early childhood.

Preface

The present dissertation is based on work carried out at the Inorganic Materials and Ceramics Research Group, the Department of Materials Science and Engineering (DMSE), the Norwegian University of Science and Technology, NTNU, under the supervision of Prof. Tor Grande (main advisor), Prof. Mari-Ann Einarsrud (co-advisor) and Prof. Thomas Tybell (co-advisor, Department of Electronics and Telecommunications, NTNU). The work was done during the period August 29th 2005 to September 2009, including one year of teaching duties and four months leave to teach TMT4245 Functional Materials in the spring semester of 2008. Literature published after September 1st 2009 is not referenced in the present dissertation.

All experiments have been conducted by the author, except the following characterisation work. Transmission electron microscopy (TEM) of nanoparticles was done by Dr. Yingda Yu at DMSE, NTNU. Vibrating sample magnetometry (VSM) was carried out at Quantum Design Inc. in San Diego, CA, USA by Dr. James O'Brien. Atomic pair distribution functions (PDF) for nanoparticles were obtained at Argonne National Lab, IL, USA by Prof. Valeri Petkov at the Dept. of Physics at Central Michigan University, MI, USA.

Parts of this dissertation have been published in the following papers:

Sverre M. Selbach, Mari-Ann Einarsrud, Thomas Tybell and Tor Grande
"Synthesis of BiFeO₃ by wet chemical methods"
J. Am. Ceram. Soc. **90** (2007) 3430-3434.

Sverre M. Selbach, Thomas Tybell, Mari-Ann Einarsrud and Tor Grande
"Size-dependent properties of multiferroic BiFeO₃ nanoparticles."
Chem. Mater. **19** (2007) 6478-6484.

Sverre M. Selbach, Thomas Tybell, Mari-Ann Einarsrud and Tor Grande
"The ferroic phase transitions of BiFeO₃"
Adv. Mater. **20** (2008) 3692-3696.

Sverre M. Selbach, Mari-Ann Einarsrud and Tor Grande
"On the thermodynamic stability of BiFeO₃"
Chem. Mater. **21** (2009) 169-173.

Sverre M. Selbach, Thomas Tybell, Mari-Ann Einarsrud and Tor Grande
"High-temperature semiconducting cubic phase of BiFe_{0.7}Mn_{0.3}O_{3+δ}"
Phys. Rev. B **79** (2009) 214113.

Sverre M. Selbach, Thomas Tybell, Mari-Ann Einarsrud and Tor Grande
"Structure and properties of multiferroic oxygen hyperstoichiometric BiFe_{1-x}Mn_xO_{3+δ}"
Chem. Mater. DOI:10.1021/cm9021084, 2009.

Sverre M. Selbach, Thomas Tybell, Mari-Ann Einarsrud and Tor Grande
“Phase transitions, electrical conductivity and chemical stability of BiFeO₃ at high temperatures.”
Submitted September 2009.

Throughout the course of this work, I have also contributed to the following publications not directly related to the present dissertation:

Sverre M. Selbach, Guozhong Wang, Mari-Ann Einarsrud and Tor Grande
“Decomposition and crystallization of a sol-gel-derived PbTiO₃ precursor”
J. Am. Ceram. Soc. **90** (2007) 2649-2652.

Fride Vullum, Fabian Nitsche, Sverre M. Selbach and Tor Grande
“Solid solubility and phase transitions in the system LaNb_{1-x}Ta_xO₄”
J. Solid State Chem. **181** (2008) 2580-2585.

Guozhong Wang, Sverre M. Selbach, Yingda Yu, Xitian Zhang, Tor Grande and Mari-Ann Einarsrud
“Synthesis and characterization of KNbO₃ nanorods”
Cryst. Eng. Comm. **11** (2009) 1958-1963.

Trondheim, September 6th 2009

Sverre Magnus Selbach

Summary

Multiferroic materials combine two or more of the ferroic properties ferromagnetism, ferroelectricity and ferroelasticity. These materials are prime candidates for future computer memory concepts, as well as for sensors and spintronic devices. The perovskite bismuth ferrite (BiFeO_3) is the most studied multiferroic material. BiFeO_3 is ferroelectric below $830\text{ }^\circ\text{C}$ and antiferromagnetic below $370\text{ }^\circ\text{C}$. Epitaxial thin films of BiFeO_3 have attracted tremendous interest from the scientific community, but a thorough understanding of bulk materials with respect to synthesis, stability and properties at high temperatures has received comparatively less attention.

The aim of this work has been to prepare phase pure bulk and nanocrystalline BiFeO_3 and to investigate the thermodynamics governing the stability of BiFeO_3 . Moreover, the structural phase transitions at high temperatures have been investigated, as well as the effect of isovalent substitution of both Bi and Fe. Finally, the thesis includes a study of the effect of reduced size of nanoparticles.

Simple aqueous synthesis routes to obtain phase pure nanocrystalline BiFeO_3 were developed using nitrate solutions as metal precursors. The carboxylic acids tartaric, malic and maleic acid were found to complex both Bi and Fe cations. Ethylene glycol could be used as a polymerising agent, but was not a necessary requirement for formation of phase pure BiFeO_3 by aqueous chemical methods.

Preparation of phase pure bulk BiFeO_3 by solid state reaction synthesis from Bi_2O_3 and Fe_2O_3 has been known to be difficult with poor reproducibility since the early 1960's. The secondary phases $\text{Bi}_{25}\text{FeO}_{39}$ and $\text{Bi}_2\text{Fe}_4\text{O}_9$ are commonly found as bi-products. Using high temperature X-ray diffraction (HTXRD) and calculations from thermodynamic data of the system, it has been shown that BiFeO_3 is thermodynamically metastable with respect to $\text{Bi}_{25}\text{FeO}_{39}$ and $\text{Bi}_2\text{Fe}_4\text{O}_9$ at temperatures between 450 and $800\text{ }^\circ\text{C}$, but is the energetically stable compound above $800\text{ }^\circ\text{C}$. This is the thermodynamic origin of the difficulties in preparing phase pure BiFeO_3 by solid state reaction. Contrary to decades of belief that BiFeO_3 is metastable at high temperatures, it is proposed that decomposition of BiFeO_3 in the paraelectric phase below the peritectic temperature of $935 \pm 5\text{ }^\circ\text{C}$ is due to chemical incompatibility towards adjacent materials in contact with the sample rather than intrinsic thermodynamic instability. BiFeO_3 is stabilised with respect to peritectic decomposition in O_2 atmosphere relative to N_2 and air.

The polymorphic transitions of BiFeO_3 have been studied by HTXRD, calorimetry, dilatometry and electrical conductivity measurements. At the ferroelectric Curie temperature, T_C , of 820 - $830\text{ }^\circ\text{C}$, BiFeO_3 undergoes a strongly first order phase transition from the ferroelectric polymorph with the rhombohedral, polar space group $R3c$ to the paraelectric polymorph with the orthorhombic, centrosymmetric space group $Pbnm$. This transition is accompanied by a $\sim 1.5\%$ reduction of the unit cell volume and a discontinuous increase of the electrical conductivity. A reversible, first order phase transition at $925 \pm 5\text{ }^\circ\text{C}$ was inferred from thermal analysis and electrical conductivity measurements. The volume of the transition was shown to be positive by dilatometry and the electrical conductivity decreases discontinuously across this phase transition. The sign and

magnitude of the discontinuous change in electrical conductivity reflect the sign and magnitude of the discontinuous change of the molar volumes of the transitions. BiFeO₃ remained semiconducting in all three polymorphs.

Substitution with Mn on the Fe site of BiFeO₃ lowers the polymorphic phase transition temperatures, and the phase transitions sequence was inferred to be $R3c \leftrightarrow Pbnm \leftrightarrow Pm\bar{3}m$ by HTXRD of BiFe_{0.7}Mn_{0.3}O₃. The latter space group corresponds to the ideal, cubic perovskite structure.

BiFeO₃ substituted with Mn can exhibit oxygen hyperstoichiometry, BiFe_{1-x}Mn_xO_{3+δ} due to partial oxidation of Mn from +3 to +4, evidenced by thermogravimetical analysis. Excess oxygen is accompanied by cation vacancies; Bi_{1-δ/3}(Fe_{1-x}Mn_x)_{1-δ/3}O₃. Electrical conductivity measurements in N₂ and O₂ atmospheres supported this defect chemistry model, and *p*-type semiconductivity was inferred. The ambient temperature crystal structure becomes less distorted, but more disordered, with increasing *x* and *δ*. The Néel temperature *T_N*, the Curie temperature *T_C* and the temperature of the transition to cubic structure *T_{cub}* all decreased with increasing *x* and *δ*. For *x* = 0.3 *T_{cub}* was observed in the temperature range 855-895 °C, decreasing with increasing *δ*. The influence of defect chemistry has previously not been described for Mn-substituted BiFeO₃. A phase diagram was reported for the system BiFe_{1-x}Mn_xO_{3+δ} for 0 ≤ *x* ≤ 0.3, 0 ≤ *δ* ≤ 0.06 and 20 ≤ *T* ≤ 950 °C.

Bi_{1-x}La_xFeO₃ remained single phase up to *x* = 0.1 and the unit cell became less distorted with La-substitution. *T_N* increased subtly, *T_C* decreased strongly and *T_{cub}* increased with increasing *x*. The effect of La substitution on *T_C* and *T_{cub}* resembled the anticipated effect of hydrostatic pressure given their opposite Clapeyron slopes, La can thus be regarded to inflict chemical pressure. For 0.1 < *x* ≤ 0.25 phase separation occurred and the new phase was structurally similar to the orthorhombic paraelectric structure. The new phase can be regarded as Bi substituted LaFeO₃ from mass balance considerations. Limited solid solubility in Bi_{1-x}La_xFeO₃ can be rationalised from regular solution thermodynamics, which implies that a morphotropic phase boundary for single phase material with *x* ≥ 0.1 would correspond to a metastable state. A phase diagram for 0 ≤ *x* ≤ 1 was proposed for the system Bi_{1-x}La_xFeO₃.

Finally, the lattice parameters of BiFeO₃ nanoparticles deviate from bulk values towards a metrically cubic structure below 30 nm crystallite size, with concomitant increasing unit cell volume. However, the polar cation displacements increase with decreasing size below 50 nm. Prevailing dipoles on a local scale in an average more cubic lattice indicate that ferroelectric ordering is lost through a disordering process rather than a uniform, displacive distortion of the crystal structure in ferroelectric nanoparticles. The polar displacement of Fe is the most sensitive to reduced crystallite size, and the associated changes in Fe-O bond lengths and Fe-O-Fe bond angles provide a microscopic explanation for the observed decrease in *T_N* below 50 nm.

Table of contents

Acknowledgements	v
Preface	vi
Summary	ix
Table of contents	xi
List of acronyms	xiv
1 Background	1
2 Aim of work	3
3 Introduction	5
3.1 Ferroic ordering phenomena and multiferroism	5
3.1.1 Ferroelectricity	5
3.1.2 Ferro- and antiferromagnetism	8
3.1.3 Ferroelasticity	10
3.1.4 Multiferroism	10
3.2 Properties of BiFeO ₃	14
3.2.1 Crystal structure	14
3.2.2 Ferroelectricity and Piezoelectricity	19
3.2.3 Piezoelectricity and epitaxial strain in thin films	20
3.2.4 Electronic structure	20
3.2.5 Magnetic structure	22
3.2.6 Ferroelastic, ferroelectric and antiferromagnetic domains	22
3.2.7 Magnetoelectric coupling	24
3.2.8 III-III bismuth perovskites without Fe; BiMO ₃	26
3.2.9 III-III ferrite perovskites without Bi; AFeO ₃ , A = Y, La, Pr... Yb, Lu..	27
3.2.10 Solid solutions of BiFeO ₃ -ABO ₃ , A ≠ Bi, B ≠ Fe	27
3.3 Other multiferroic and magnetoelectric materials	28
3.3.1 Single phase compounds	28
3.3.2 Composites	29
3.4 Applications of BiFeO ₃	30
3.4.1 Magnetoelectric and multiferroic memories	30
3.4.2 Ferroelectricity and piezoelectricity	31
3.4.3 Optical properties	32
4 Experimental	33
4.1 Synthesis	33
4.1.1 Wet chemical synthesis of nano-crystalline BiFeO ₃	33
4.1.2 Synthesis of bulk materials by solid state reaction	35
4.2 Characterisation	37
4.2.1 X-ray diffraction	37
4.2.2 High temperature XRD	37
4.2.3 Rietveld refinements	38
4.2.4 Atomic pair distribution functions (PDF)	39
4.2.5 Determination of nanoparticle size	39
4.2.6 Thermogravimetry	40
4.2.7 Thermal analysis	40

4.2.8	Electrical conductivity.....	41
4.2.9	Vibrating Sample Magnetometry	42
5	Synthesis and stability.....	43
5.1	Introduction	43
5.2	Wet chemical synthesis	44
5.2.1	Results	44
5.2.2	Discussion	50
5.3	Solid state reaction.....	52
5.3.1	BiFeO ₃ formation from binary oxides.....	52
5.3.2	Stability of the secondary ternary phases Bi ₂₅ FeO ₃₉ and Bi ₂ Fe ₄ O ₉	55
5.4	Thermodynamic stability and chemical compatibility.....	62
5.4.1	Peritectic decomposition	62
5.4.2	Thermodynamic stability.....	64
5.4.3	Chemical compatibility	65
5.5	Conclusions	65
6	Phase transitions.....	67
6.1	Introduction	67
6.2	The antiferromagnetic to paramagnetic transition.....	68
6.3	Polymorphic transitions.....	73
6.4	Discussion.....	84
6.4.1	The Néel transition.....	84
6.4.2	The ferroelectric transition and the paraelectric polymorph	84
6.4.3	The cubic polymorph	89
6.4.4	Comparison of the effect of temperature and pressure on BiFeO ₃	91
6.5	Conclusions	92
7	Oxygen hyperstoichiometric BiFe _{1-x} Mn _x FeO _{3+δ}	95
7.1	Introduction	95
7.2	Results	95
7.2.1	Oxygen stoichiometry	95
7.2.2	Crystal structure at ambient temperature.....	96
7.2.3	Phase transitions.....	99
7.2.4	Electrical conductivity.....	104
7.2.5	Solubility	109
7.3	Discussion.....	111
7.3.1	Defect Chemistry.....	111
7.3.2	Crystal Structure.....	112
7.3.3	Phase diagram	114
7.3.4	Ferroelectric transition	115
7.3.5	Transition to cubic structure.....	116
7.3.6	Antiferromagnetic transition	117
7.3.7	Solubility of Mn in BiFeO ₃	119
7.3.8	Conductivity and device applications.....	119
7.4	Conclusions	120
8	La-substituted BiFeO ₃ : Bi _{1-x} La _x FeO ₃	121
8.1	Introduction	121
8.2	Results	123
8.2.1	Composition and structure	123

8.2.2 High temperature behaviour.....	131
8.3 Discussion.....	139
8.3.1 Structure and solubility	139
8.3.2 Chemical pressure and critical temperatures of the <i>R3c</i> phase	139
8.3.3 Solution thermodynamics and phase diagram.....	140
8.3.4 Metastable morphotropic phase boundaries	143
8.4 Conclusions	144
9 Size-dependent properties of BiFeO ₃ nanocrystallites.....	145
9.1 Introduction	145
9.2 Results	146
9.3 Discussion.....	154
9.3.1 Phenomenological interpretation of finite size effects	154
9.3.2 Local structure and structural coherence.....	156
9.3.3 Structure-property relationships in BiFeO ₃ nanoparticles.....	158
9.4 Conclusions	160
10 Outlook	161
10.1 Stability and compatibility.....	161
10.2 Crystal structure and chemical bonding	161
10.3 Phase transitions	162
10.4 The BiFeO ₃ -LaFeO ₃ and BiFeO ₃ -BiMnO ₃ phase diagrams	163
10.5 Origins of finite size effects.....	164
11 References.....	165

List of acronyms

AFM	Antiferromagnetic
DSC	Differential scanning calorimetry
DTA	Differential thermal analysis
EG	Ethylene glycol
FE	Ferroelectric
FeRAM	Ferroelectric random access memory
FM	Ferromagnetic
FWHM	Full width at half maximum
GMR	Giant magnetoresistance
HS	High spin
HTXRD	High temperature X-ray diffraction
LS	Low spin
MERAM	Magnetolectric random access memory
MPB	Morphotropic phase boundary
NPD	Neutron powder diffraction
$p(\text{O}_2)$	Partial pressure of oxygen
PDF	Pair distribution function
PZT	$\text{PbZr}_{1-x}\text{Ti}_x\text{O}_3$
RAM	Random access memory
SXRD	Synchrotron X-ray diffraction
TEM	Transmission electron microscopy
TGA	Thermogravimetical analysis
VSM	Vibrating sample magnetometry
XAFS	X-ray absorption fine structure
XRD	X-ray diffraction

1 Background

Information technology is a cornerstone of modern society, being an enabling technology in virtually all fields of science, engineering, business and administration, as well as public and private entertainment. There is an ever increasing demand for improved computer performance in terms of speed and data storage capacity. The information technology industry has so far been able to keep up with the evolution predicted by the famous Moore's law, which states that the performance of computers will double every other year.¹⁻² At the heart of information technology and computer performance lies materials science and engineering. Silicon in transistors and integrated circuitry has been equally important for human technology as other materials giving names to historical periods in human history, e.g. stone age, bronze and iron age. Data, represented by bits, "0" and "1" in the binary number system must be physically stored, switched and read. The dominating physical representation of bits have been magnetisation of ferromagnetic materials, where "0" and "1" correspond to magnetisation in opposite directions. Ferroelectric Random Access Memories (FeRAM) where bits are represented by opposite directions of ferroelectric polarisation display comparable speed to ferromagnetic memories, but bits can be stored in smaller domains, enabling a higher data storage capacity.³⁻⁷ FeRAM possess the advantage of being non-volatile; a power failure will not lead to loss of data not stored on a hard disk. Data bits can also be stored in resistivity based memories⁸⁻¹⁴ or memories based on phase change materials.¹⁵ In addition to data storage, progress in materials science has enabled faster writing and reading of bits, e.g. Giant MagnetoResistance (GMR), which the Nobel Prize of physics was awarded for in 2007.¹⁶⁻¹⁷ In future memory storage concepts, like e.g. "race track memories"¹⁸⁻¹⁹ or other spintronic concepts,²⁰⁻²¹ fundamental understanding of materials at the nano-scale will be core knowledge, enabling technological advancements. Physical representation of bits must be switchable, readable and preferably non-volatile, hence ferroic properties like ferromagnetism and ferroelectricity are already being exploited industrially, and are at the forefront of scientific research.

Multiferroic materials possess simultaneously two or more ferroic orders like ferroelectricity, ferromagnetism and ferroelasticity.²² Coexistence of e.g. ferroelectricity and ferromagnetism enables "four-state memories" based of magnetoresistance and electroresistance, due to the four different combinations of magnetisation and polarisation, which could dramatically enhance the data storage density.²³⁻²⁴ Even more interesting is the possibility of a magnetoelectric²⁵ memory,²⁶⁻²⁷ which display strong, linear coupling between ferroelectricity and ferromagnetism. Such a device would combine the best qualities of ferroelectric and magnetic memories. Writing bits represented through ferroelectric polarisation is faster than writing ferromagnetic bits, but ferroelectric bits are harder to read non-destructively than ferromagnetic, although recent progress has been made.²⁸⁻³⁰ An ideal concept for a memory based on magnetoelectric materials would hence be writing bits ferroelectrically and reading the bits through their associated ferromagnetic state. Both writing ferroelectric bits and reading ferromagnetic bits are mature technologies, but hitherto no materials combining *room temperature* ferroelectricity, ferromagnetism and strong magnetoelectric coupling are known.

Improvements of magnetoelectric multiferroic materials are so vast that this field the recent few years has become one of the hottest of materials science, inspiring numerous reviews the last few years,³¹⁻³⁸ only surpassed by the intense attention to high-temperature superconductors after their discovery in 1986.³⁹

Most multiferroic materials investigated are oxides, particularly hexagonal manganites and Bi-containing perovskites. Perovskite oxides are compatible with Si and SiO₂, the two materials the information technology industry is based on, and thus one of the most promising classes of materials for technological applications. Bismuth ferrite,⁴⁰ BiFeO₃, is the hitherto most studied multiferroic compound as it is so far the only known single compound exhibiting room temperature multiferroism.

BiFeO₃ belongs to a larger family of oxides with strongly correlated electrons,⁴¹⁻⁴³ also including e. g. high temperature superconductors,⁴⁴⁻⁴⁷ Colossal MagnetoResistant (CMR) materials,⁴⁷⁻⁴⁸ materials exhibiting metal-insulator transitions⁴⁸ and heterostructures with 2D electron gases at epitaxial interfaces.⁴⁹⁻⁵² In addition to their obvious potential future and present technological applications, these materials exhibit interesting and complex physics. Several fundamental questions still remain unsolved, with the most famous being the mechanism of high temperature superconductivity in cuprates.⁵³⁻⁵⁵ Thermodynamics and chemical compability of these materials are crucial for fabricating and integrating these materials into devices and electronic circuitry, as illustrated by Schlom and co-worker's reports on the thermodynamic stability and compabitibility of dielectric gate material oxides with respect to silicon.⁵⁶⁻⁵⁷ Mapping the phase diagrams of multiferroic materials will thus provide important insight into both the stability of the ferroic ordering phenomena and the underlying mechanisms responsible for multiferroism and magnetoelectric coupling. Such insight is vital to the search for new and improved material systems. Moreover, understanding the behaviour of ferroic ordering phenomena at the nano-scale is of outmost importance to the ever ongoing miniaturisation of electronic devices.

2 Aim of work

The initial aim of this work was to study finite size effects in multiferroic materials with BiFeO_3 as our compound of choice, being the hitherto only known single phase room-temperature multiferroic material. Wet chemical synthesis routes (chapters 4 and 5) yielding phase pure nanoparticles were developed to study finite size effects (chapter 9).

The high temperature behaviour of bulk BiFeO_3 was poorly understood at the start of the present work, and considerable effort was spent to study the structure, phase transitions and properties at elevated temperatures (chapter 6). Difficulties encountered during initial high temperature characterisation lead us to study the thermodynamic stability of BiFeO_3 as a function of temperature and chemical composition (chapter 5).

During high temperature characterisation of Mn-substituted BiFeO_3 the influence of defect chemistry due to oxygen hyperstoichiometry in $\text{BiFe}_{1-x}\text{Mn}_x\text{O}_{3+\delta}$ on structure and critical temperatures became obvious, and was investigated systematically (chapter 7). Finally, isovalent substitution with La on the A site was studied in search of a morphotropic phase boundary (chapter 8).

The research reported in this work can be classified into four related topics:

1. Synthesis and thermodynamic stability (chapter 5).
2. Phase transitions and properties of polymorphs (chapter 6).
3. Isovalent chemical substitution on the B and A site (chapters 7 and 8).
4. Finite size effects of nanoparticles (chapter 9).

3 Introduction

3.1 Ferroic ordering phenomena and multiferroism

3.1.1 Ferroelectricity

Ferroelectric materials⁵⁸⁻⁵⁹ are dielectrics which possess a switchable spontaneous electric polarisation P_S in absence of an external electric field. The direction of the polarisation can be switched by an oppositely aligned external electric field larger than the coercive field E_C . The non-linear behaviour of polarisation \mathbf{P} as a function of electric field is characterised by a hysteresis loop, as shown in Figure 3.1 (b).

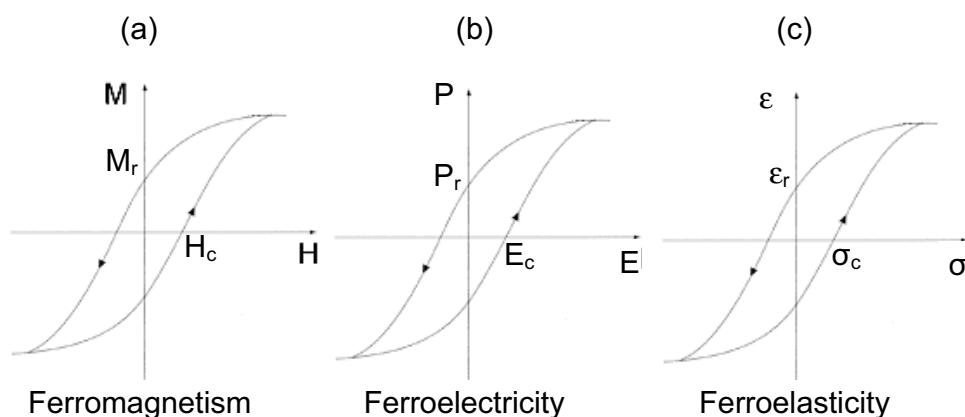


Figure 3.1 Hysteresis loops characteristic for the ferroic properties (a) ferromagnetism, (b) ferroelectricity and (c) ferroelasticity.

Polarisation will saturate at sufficiently large fields, and a remanent polarisation P_r , or spontaneous polarisation, prevails in zero electric field. Ferroelectricity is an ordering phenomenon which disappears at a critical temperature called the Curie temperature, T_C , above which the material is paraelectric. The dielectric constant ϵ , or electrical susceptibility $\chi = \epsilon - 1$, is large in ferroelectric materials, and diverges at the Curie temperature, when the polarisation is most susceptible to applied electric fields. The dielectric constant is a measure of the polarisability of the material; $\mathbf{P} = \epsilon_0 \chi \mathbf{E}$, where ϵ_0 is the dielectric constant in vacuum.

The symmetry of the crystallographic point groups imposes restrictions on the possibility of ferroelectricity in a crystal. There are 32 crystallographic point groups out of which 21 are *non-centrosymmetric*. Twenty of these 21 point groups exhibit piezoelectricity; mechanical stress can induce polarisation, and vice versa: an electric field can induce strain. Piezoelectricity is a strong, linear coupling between electric polarisation and mechanical stress, opposed to the weak, quadratic electrostriction effect found in all dielectric materials. Ten of the twenty non-centrosymmetric point groups possess one unique polar axis and hence exhibit pyroelectricity; a change of temperature will induce a change of polarisation. All pyroelectric materials are also piezoelectric, but piezoelectric materials without one

unique polar axis are not pyroelectric. All ferroelectric materials are pyroelectric, but not all pyroelectrics are ferroelectric. The distinguishing feature is whether the spontaneous polarisation can be switched by an external field or not, a feature which must be tested experimentally as it can not be predicted *a priori* from symmetry considerations.

Ferroelectrics can be classified as proper or improper, depending on the origin of the polarisation. In displacive ferroelectrics the spontaneous polarisation arises from displacements of cations with respect to the anion sublattice, creating electric dipoles which are aligned in one direction, breaking the inversion symmetry. In contrast with conventional displacive ferroelectrics, also known as *proper* ferroelectrics, polarisation in improper ferroelectrics is not the primary order parameter. In *improper* ferroelectrics polarisation results as a secondary effect from a lattice distortion, e.g. in magnetic spin spiral induced ferroelectrics, see chapter 3.2.1. Polarisation can also arise from ordering of the orientation of anion groups, charge ordering (electronic ferroelectrics),⁶⁰⁻⁶² orbital ordering,⁶³⁻⁶⁵ cooperative tilting of polyhedra (geometric ferroelectrics),⁶⁶ or layered ordering in asymmetric superlattices.⁶⁷ Long range Coulombic forces are responsible for the alignment of electric dipoles in one direction in displacive ferroelectrics, while short range Coulombic forces (e.g. ionic bonds) favour centrosymmetry; ferroelectricity thus requires long-range forces to dominate over short range forces. Partial covalent bonding is the common mechanism for stabilising ferroelectric dipoles by off-centering of cations relative to the anion sublattice, as discussed further below.

Perovskite oxides are the most important ferroelectric materials from both a scientific and a technological perspective. The generic formula of perovskite oxides is ABO_3 , where the sum of the valence of the A and B site must be +VI for charge neutrality in stoichiometric materials. This yields three principal types of perovskites based on cation valence distribution; I-V, II-IV and III-III perovskites. The simple, cubic perovskite structure is shown in Figure 3.2; the larger A cation resides in a 12-coordinated dodecahedron, while the smaller B cation is octahedrally coordinated.

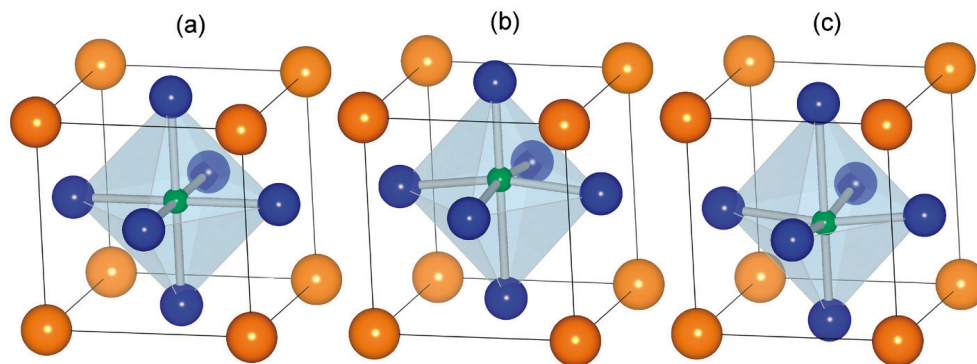


Figure 3.2. Unit cells of paraelectric cubic (a) and ferroelectric tetragonal perovskite with polarisation up (b) and down (c). A cations, B cations and oxygen anions are situated in the corners, centres and faces of the unit cells, respectively.

In the prototype ferroelectrics BaTiO₃ and PbTiO₃, the centrosymmetric, high-temperature cubic structure transforms to a tetragonal, polar structure below the Curie temperatures of 123 and 490 °C, respectively. The Ti⁴⁺ cation is displaced towards an apical oxygen along the long c-axis of the tetragonal unit cell, breaking inversion symmetry and providing electric dipoles along the [001] direction. Partial covalent bonding between empty *d* orbitals of Ti⁴⁺ and O 2*p* orbitals stabilises the off-centering of Ti⁴⁺ relative to the inversion symmetry centre of the TiO₆ octahedron, as shown by first principles calculations by Cohen,⁶⁸ and verified experimentally by Kuroiwa *et al.*⁶⁹ The substantially higher *T*_C, tetragonality (unit cell distortion *c/a*) and spontaneous polarisation of PbTiO₃ than BaTiO₃ shows the importance of the 6*s*² lone pair of Pb²⁺, as it takes part in partial covalent bonding with O 2*p* orbitals (Figure 3.3). Partial covalent bonding between O 2*p* and 4*d* orbitals of Nb⁵⁺ have also been identified in KNbO₃,⁷⁰ thus partial covalent bonding is not restricted to the titanate perovskites.

Materials with antiparallel dipoles are known as antiferroelectric, and thus exhibit no spontaneous polarisation as the moments from the two oppositely oriented sublattices cancel each other. The number of simple ferro- and antiferroelectric perovskites is restricted by the prerequisite of a narrow B-O π*-band to stabilise off-centering of B cations to create dipoles, antiparallel as well as parallel.⁷¹ Hence, (anti)ferroelectric perovskites have B cations from the early part of the transition metal block of the periodic table of elements, typically Ti⁴⁺, Nb⁵⁺, Mo⁶⁺, W⁶⁺. Partial covalent bonding between a 6*s*² lone pair on the A site and O 2*p* can stabilise ferroelectricity at room temperature, even if the B cation has non-zero *d*-electrons.

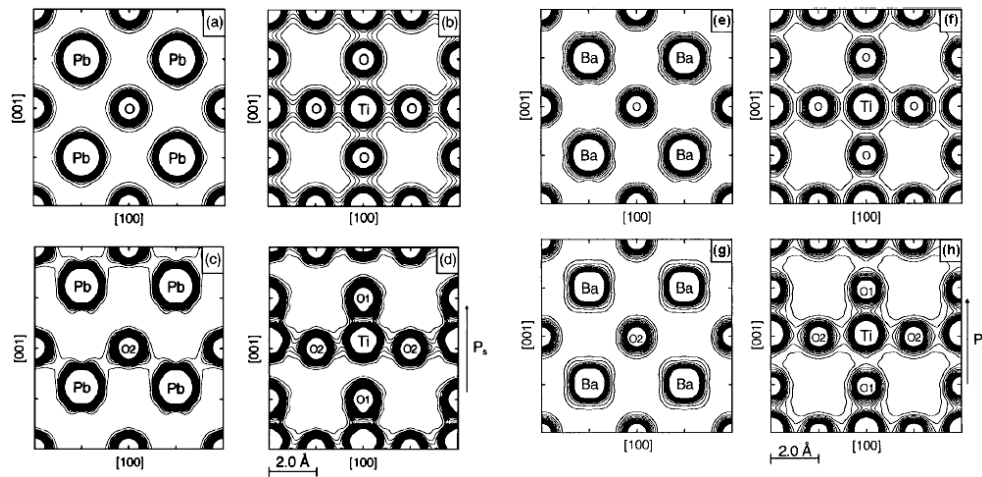


Figure 3.3. Electron density maps of PbTiO₃ (a-d) and BaTiO₃ (e-h) inferred from maximum entropy method analysis of synchrotron X-ray data, adapted from Kuroiwa *et al.*⁶⁹ (a-b) Cubic PbTiO₃ at 527 °C, (c-d) tetragonal PbTiO₃ at 27 °C, (e-f) cubic BaTiO₃ at 300 °C and (g-h) tetragonal BaTiO₃ at 27 °C.

Within ferroelectric domains all the dipoles are aligned in the same direction. Across ferroelectric domain walls the magnitude of the dipoles change gradually from one direction to the other along the polar axis over a few perovskite unit cells (180 ° walls). In tetragonal perovskites the ferroelectric domain walls are either 90 and 180 °, while more possibilities exist for perovskites with lower symmetry (see chapter 3.2.6 for domains in BiFeO₃). The scalar magnitude of ferroelectric dipoles can in principle vary continuously, while the direction of the polarisation vector is restricted by the crystal symmetry.

3.1.2 Ferro- and antiferromagnetism

Ferromagnetism is the existence of a spontaneous magnetisation which can be reversed by an opposite magnetic field, and is perfectly analogous to ferroelectricity, Figure 3.1. Ferromagnetic moments arise from ordering of the spins of unpaired electrons in *d* or *f* orbitals. Ferromagnets become paramagnetic above the ferromagnetic Curie temperature T_C of the material. The magnetic susceptibility χ follows a Curie-Weiss law; $\chi(T) = C/(1-\theta_{CW})$, where C is the Curie constant and θ_{CW} is the Curie-Weiss temperature. The metals Fe, Co and Ni are the most typical examples of ferromagnetic materials.

Although there are many examples of ferromagnetic spinels and other oxides, ferromagnetism is less common in perovskites, especially the III-III class. Some examples are SrRuO₃, La_{1-x}Sr_xCoO_{3- δ} ($x > 0.3$) and La_{1-x}Ca_xMnO₃ ($0.2 \leq x \leq 0.5$), which all display itinerant electrons.⁷² In perovskites ferromagnetic superexchange can take place between the e_g orbitals of $3d$ metals through O $2p$ orbitals; between half-filled and empty e_g orbitals ($e_g^1 - O - e_g^0$), and between half-filled and filled e_g orbitals ($e_g^1 - O - e_g^2$).⁷¹⁻⁷²

Antiferromagnetism, analogous to antiferroelectricity, is however abundant in III-III perovskites, e.g. LaMnO₃, LnCrO₃ and LnFeO₃, Ln = La, Pr, ..., Yb, Lu.⁷² Although not strictly a ferroic property, antiferromagnetic ferroelectrics are regarded as multiferroics. Antiferromagnets become paramagnetic above the Néel temperature T_N , where the magnetic susceptibility passes through a maximum, as the sublattice antiparallel to the magnetic field is most susceptible to reorientation by a field at T_N .⁷³ The spins on the B cations couple through oxygen anions by a virtual electron transfer mechanism known as superexchange.⁷³ Intra-atomic interactions cause the spins on each B cation to align parallel, obeying Hund's rule. Degeneracy of the *d* orbitals is lifted in an octahedral crystal field. Superexchange (interatomic interactions) between half-filled orbitals by 180 °, $e_g^1 - O - e_g^1$, yields antiparallel alignment of the spins on the two B cations.⁷¹ Superexchange (Figure 3.4) between e_g orbitals (σ interactions) is stronger than superexchange between t_{2g} orbitals (π interactions). This is demonstrated by the higher T_N of LaFeO₃ than LaCrO₃, 477 and 7 °C, respectively. For perovskites with tilted BO₆ octahedra the B-O-B angle is reduced to 180- θ °, implying less overlap of the O $2p$ and B *d* orbitals. The Néel temperature thus scales with the B-O-B angle 180 - θ ° by⁷⁴

$T_N \propto \cos^2 \theta$. In antiferromagnets with localised electrons T_N is thus expected to increase with hydrostatic pressure as the orbital overlap increases; $dT_N/dp > 0$. In contrast, $dT_N/dp < 0$ for itinerant antiferromagnets.⁷⁵ Similarly, chemical pressure by chemical substitution also affects T_N ; reducing the A cation radius in LnCrO_3 and LnFeO_3 reduces T_N in analogy with negative hydrostatic pressure.⁷¹

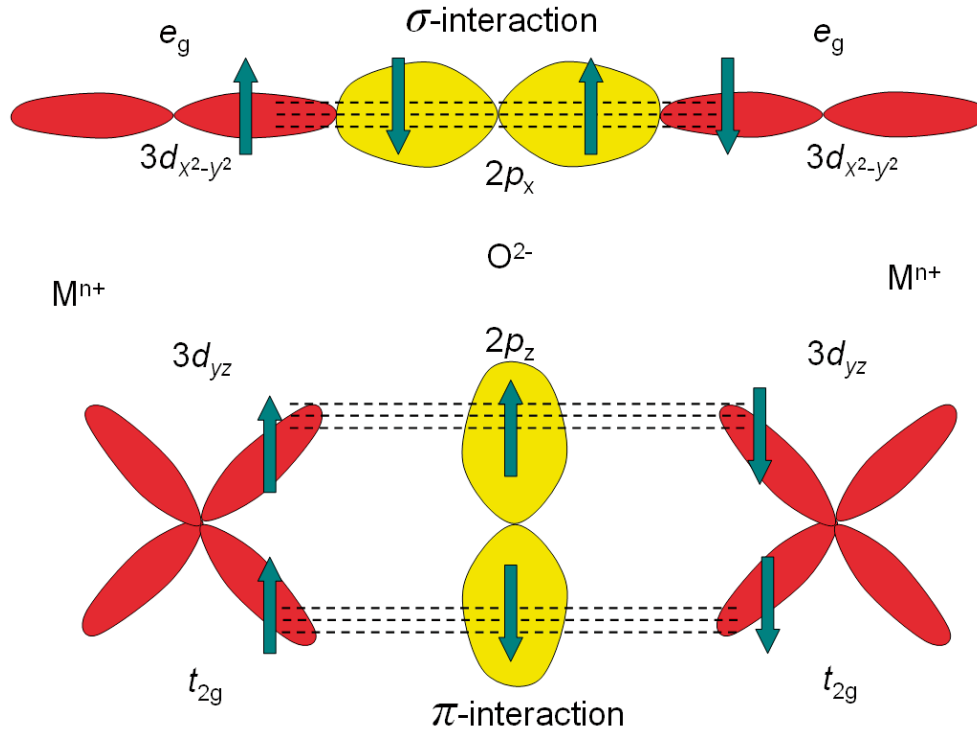


Figure 3.4. Schematic illustration of 180° antiferromagnetic superexchange; σ - and π -interactions.

Magnetic domain walls (Bloch walls) are broader than ferroelectric domains walls. The scalar magnitude of the spins is fixed, while the direction is not restricted as in the case of ferroelectric dipoles. Thus the direction of spin moments rotate continuously across a magnetic domain wall.⁷³

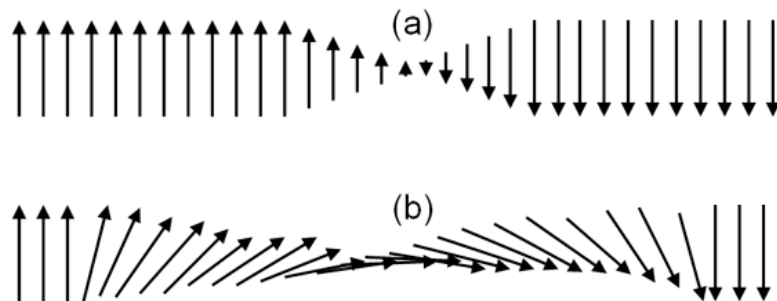


Figure 3.5. Sketch of (a) ferroelectric and (b) ferromagnetic 180° domain walls.

3.1.3 Ferroelasticity

Ferroelastic materials also display a hysteresis loop with macroscopic strain ε as a function applied mechanical stress σ , Figure 3.1 (c). Ferroelasticity disappears above a critical temperature T_C associated with a structural phase transition to a paraelastic phase. The low-symmetry ferroelastic phase must display lattice strain and exhibit two or more switchable domain states to enable the lattice strain to be reoriented by an applied stress.⁷⁶ Ferroelastic behaviour of LaCoO_3 and LaFeO_3 -based perovskites have been extensively studied at NTNU.⁷⁷⁻⁹⁰ Ferroelastic domain reorientation can also act as a mechanism of strain relaxation, as shown in Figure 3.6 (a), averaging out macroscopic strain by twinning.

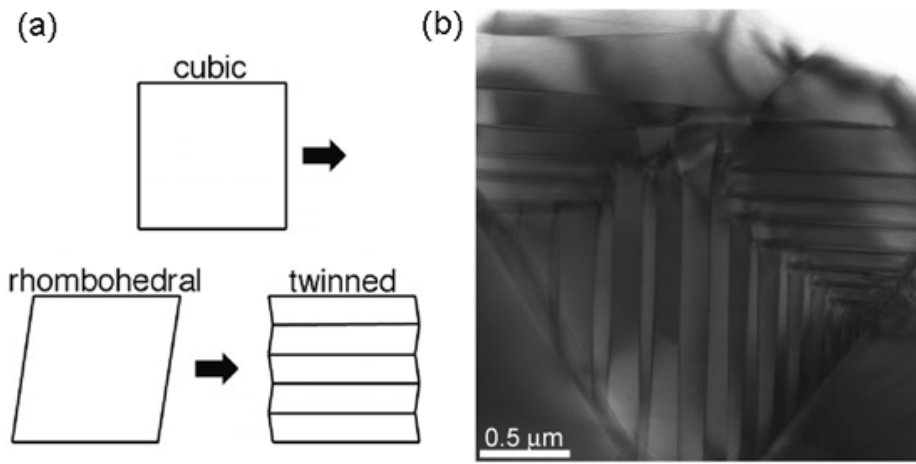


Figure 3.6. (a) Domain formation by twinning for stress relaxation and (b) TEM micrograph of ferroelastic domains in LaCoO_3 , adapted from references⁷⁷ and⁷⁹.

3.1.4 Multiferroism

It may appear somewhat arbitrary which materials are regarded as multiferroics. The definition proposed by Hans Schmid that “crystals can be defined as multiferroic when two or more of the primary ferroic properties ferromagnetism, -electricity and -elasticity are united in the same phase”³⁴ is not the one commonly used. Antiferromagnetic ferroelectrics are counted as multiferroic, while neither ferromagnetic nor antiferromagnetic ferroelastics like SrRuO_3 and LaFeO_3 , respectively, are. Ferroelastic ferroelectrics like the prototype materials BaTiO_3 and PbTiO_3 are not regarded multiferroic, thus ferroelasticity seems to be overlooked when counting multiferroic materials. A definition of multiferroic materials coherent with the current practice in literature may be “materials displaying simultaneous ferroelectricity and magnetic ordering, either ferro-, antiferro- or ferrimagnetism.” In addition to the three primary ferroic orders, ferrotoroidicity⁹¹⁻⁹³ is also regarded as sufficient to term a material multiferroic if combined with either ferroelectricity or magnetic ordering.

The coupling between ferroic orders is described by tensors, e.g. the piezoelectric coefficient d_{ijk} , which describes the coupling between mechanical

stress σ_{jk} and electric polarisation P_i .^{22, 37} Figure 3.7 (a) illustrates the tensors coupling primary ferroic orders with applied fields. The linear magnetoelectric effect (green arrows in Figure 3.7) is given by the tensor α_{ij} , which describes the induced polarisation P_i from an applied magnetic field H_j and vice versa; $P_i = \alpha_{ij}H_j$ and $M_i = \alpha_{ji}E_j$, respectively.

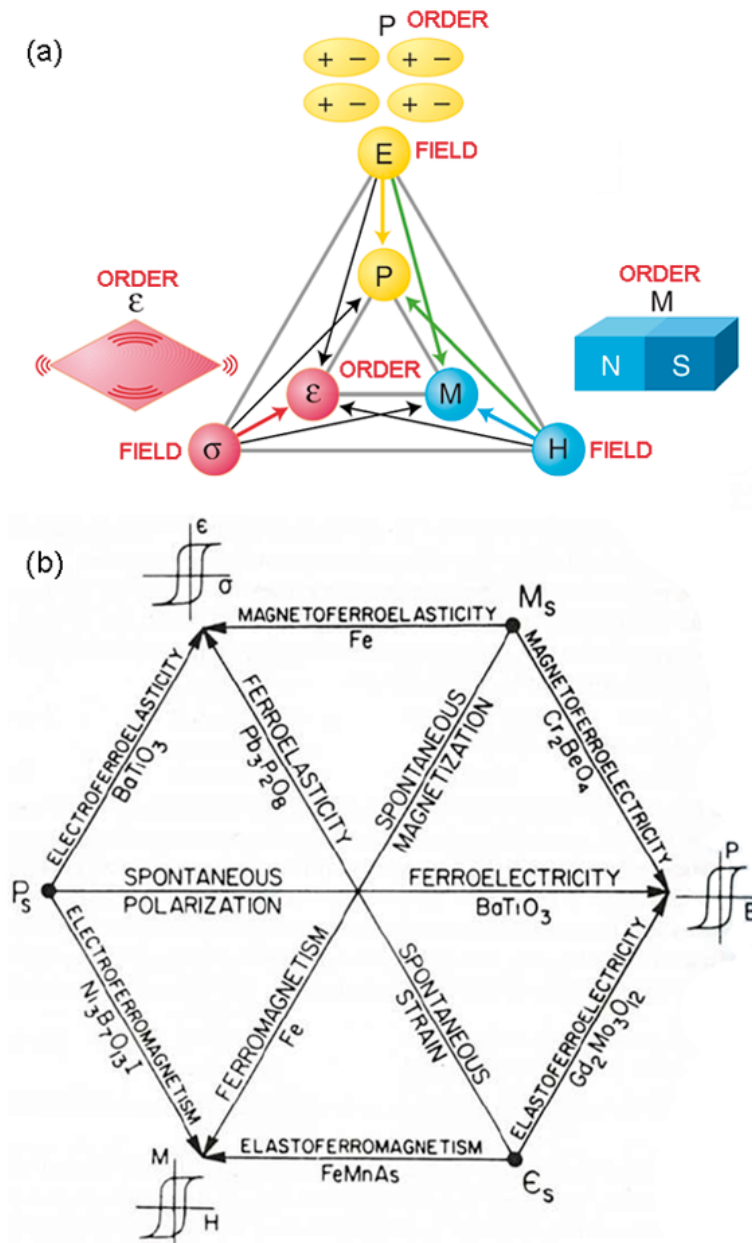


Figure 3.7. (a) Coupling between ferroic orders and fields. (b) Proper and improper ferroics. Adapted from references⁹⁴ and⁹⁵, respectively.

In primary ferroics, the electric fields \mathbf{E} controls the polarisation \mathbf{P} , the magnetic field \mathbf{H} the magnetisation \mathbf{M} and stress $\boldsymbol{\sigma}$ controls the strain $\boldsymbol{\varepsilon}$. Magnetoelectric coupling between the magnetic field \mathbf{H} and the polarisation \mathbf{P} , and between the electric field \mathbf{E} and the magnetisation \mathbf{M} , is depicted by green arrows in Figure 3.7. Piezoelectric coupling is represented by the arrows between stress $\boldsymbol{\sigma}$ and polarisation \mathbf{P} , and between electric field \mathbf{E} and strain $\boldsymbol{\varepsilon}$. Piezomagnetic and magnetoelastic coupling is illustrated by similar arrows.

Improper ferroics results from coupling between different ferroic phenomena rather than e.g. the direct coupling between ferromagnetism and magnetic field. Proper ferroics are along the diagonals, while improper ferroics lie on the edges of the hexagon.

It is important to note that multiferroism in a single compound does not necessarily imply magnetoelectric coupling, nor is magnetoelectric coupling restricted to multiferroic compounds. Different classes of materials with ferroic orders and magnetoelectric coupling are summarised in the Venn-diagram in Figure 3.8.

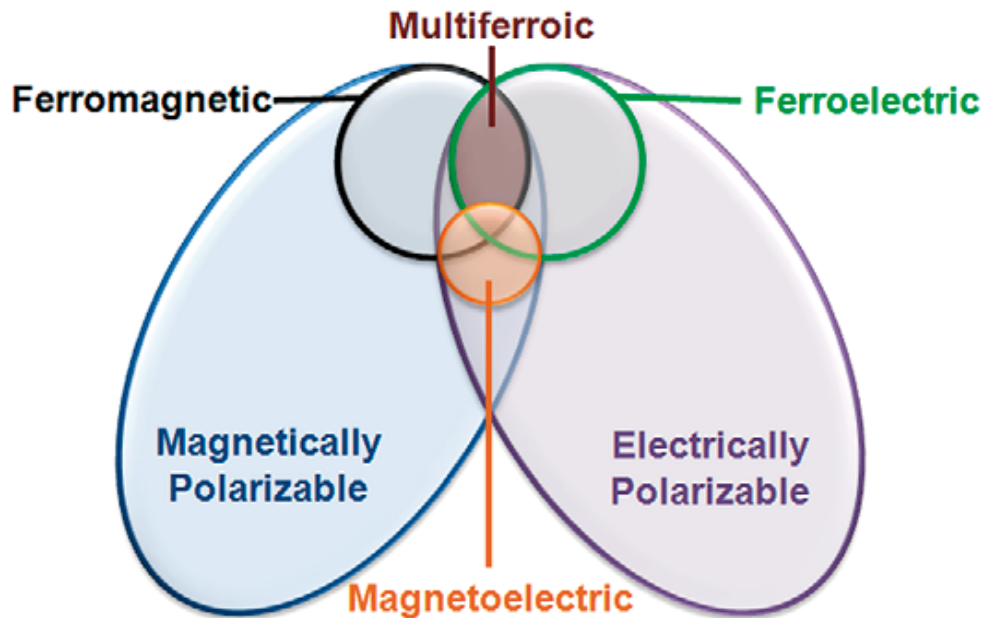


Figure 3.8. A schematic Venn-diagram showing the relations between multiferroic and magnetoelectric materials. Adapted from Martin *et al.*³³

The ideal compound for magnetoelectric multiferroic memories is found in the area common to multiferroic and magnetoelectric materials in Figure 3.8, with a large magnetoelectric tensor at room temperature. Hitherto no compound is known to exhibit strong ferroelectricity and ferromagnetism, and strong magnetoelectric coupling at room temperature. BiFeO_3 is ferroelectric and magnetoelectric, but not ferromagnetic.

In the late 90's Nicola Hill (now Spaldin) started to investigate why there are so few magnetic (ferro- or antiferro-) ferroelectric perovskites.⁹⁶⁻⁹⁸ Polarisation requires displacement of cations from their centrosymmetric positions with respect to the oxygen sublattice. In perovskites like BaTiO₃ and KNbO₃ the stabilising mechanism is partial covalent bonding between empty *d* orbitals of the B cation and O *2p* orbitals. On the other hand, magnetism requires unpaired electrons in *d* orbitals of the B cations, which is detrimental to partial covalent bonding between B cations and oxygen, as it inhibits electron density donation from O *2p* to B *d*. Unpaired spins in *f* orbitals of rare earth A cations can indeed order to give a magnetic moment, but only at too low temperatures for technological applications. Other mechanisms than partial covalent bonding between B *d*⁰ and O *2p* orbitals can stabilise ferroelectric dipoles, thus magnetic and ferroelectric order is not mutually exclusive. Lone pairs of Tl⁺, Pb²⁺ and Bi³⁺ can order and give partial covalent bonding with O *2p* orbitals. The role of the 6*s*² lone pair was extensively studied for BiMnO₃ by Seshadri and Hill.⁹⁹ Charge ordering (electronic ferroelectricity)^{60, 62} and “geometric ferroelectricity”, as in YMnO₃,⁶⁶ are other microscopic mechanisms that can stabilise ferroelectric dipoles in magnetic materials.

3.2 Properties of BiFeO₃

Table 3.1 summarises the most important structural and physical properties of BiFeO₃, out of which some are elaborated below.

Table 3.1. Structural and physical properties of BiFeO₃.

Property	Value	Ref.
Crystal system ^a	Trigonal	100
	$a_{\text{rh}} = 5.6343 \text{ \AA}$, $\alpha_{\text{rh}} = 59.348^\circ$	100-102
	$a_{\text{hex}} = 5.5787 \text{ \AA}$, $c_{\text{hex}} = 13.8688 \text{ \AA}$	
	$a_{\text{pc}} = 3.965 \text{ \AA}$, $\alpha_{\text{pc}} = 89.35^\circ$	
Space group	$R3c$, 161	100
Tolerance factor ^b	$t = 0.890$	
Polyhedral volume ratio	$V_{\text{A}}/V_{\text{B}} = 4.727$	103
Density	8.40 g/cm^3	
Thermal expansion	Non-linear and anisotropic	104-105
Ferroelectricity	$T_{\text{C}} = 820\text{-}830^\circ\text{C}$	106-107
Polarisation ^c	$90\text{-}100 \mu\text{C/cm}^2$	108-112
Dielectric constant	$\epsilon_{\text{r}} = 30$	113
Antiferromagnetism	Canted G-type, $T_{\text{N}} = 370^\circ\text{C}$	102
Piezoelectricity	$D_{33} = 15\text{-}60 \text{ pm/V}$	108, 111-112

^aTrigonal crystals can be represented with rhombohedral, hexagonal or pseudocubic unit cell axes and lattice parameters.

^bAssuming six-coordinated high spin Fe³⁺ and eight-coordinated Bi³⁺ with ionic radii from Shannon.¹¹⁴

^cInferred from measurements on thin films, single crystals, bulk ceramics and Berry phase calculations.

3.2.1 Crystal structure

The crystal structure of BiFeO₃ is a rhombohedrally distorted perovskite. The ideal, cubic perovskite structure, also known as the aristotype, is shown in Figure 3.2 (a). The space group of the aristotype perovskite is $Pm\bar{3}m$. The perovskite structure can be viewed as 3D network of corner-sharing BO₆ octahedra with 12-coordinated A cations in voids between the BO₆ octahedra. The relative sizes of the A and B cations is important for the geometric¹¹⁵⁻¹¹⁶ and thermodynamic stability¹¹⁷ of the perovskite structure, and assuming hard spheres it can be quantified by the Goldschmidt tolerance factor t :¹¹⁸

$$t = \frac{r_{\text{A}} + r_{\text{O}}}{\sqrt{2}(r_{\text{B}} + r_{\text{O}})} \quad (3.1)$$

where r_{A} , r_{B} and r_{O} are the ionic radii of the A cation, B cation and O²⁻ anion, respectively. For t close to unity the cubic perovskite structure is stable, e.g. in

SrTiO₃. For $1.0 < t < 1.065$ tetragonal perovskites with space group $P4mm$ often form, accommodating the small size of the B cation by allowing it to be displaced towards an apical oxygen in the BO₆ octahedron, thus creating an electric dipole and providing ferroelectricity and spontaneous polarisation, as in PbTiO₃, BaTiO₃ and KNbO₃.⁷¹ When the A cation is too large and for tolerance factors of about 1.07 and higher, hexagonal polytype structures form. Oversized A cations are accommodated by face-sharing BO₆ octahedra. Different polytypes form depending on the size mismatch, e.g. in SrMnO₃ and BaMnO₃.⁷¹ Tolerance factors larger than unity are commonly found in I-V and II-IV perovskites.

When the A cation is too small to fill the 12-coordinated void between BO₆ octahedra the perovskite structure accommodates this size mismatch by tilting the octahedra to reduce the size of the dodecahedron, and simultaneously the primary coordination number of the A cation. Tolerance factors less than unity is commonly found in II-IV and III-III perovskites. Typically the crystal system changes from cubic to rhombohedral and then orthorhombic with decreasing tolerance factor.⁷¹ For tolerance factors less about 0.86 the perovskite structure becomes unstable towards the hexagonal YMnO₃-structure, where the A cation is 7-coordinated and situated between layers of 5-coordinated B cations in bipyramides.¹¹⁹⁻¹²⁰

An equivalent way of describing the geometric stability of the perovskite structure is the polyhedral volume ratio V_A/V_B , which quantifies the size mismatch of the AO₁₂ dodecahedron relative to the BO₆ octahedron.^{103, 121-123} For $t = 1$ in the cubic perovskite structure, $V_A/V_B = 5.0$, which is thus regarded as the ideal value. The volume of BO₆ octahedron, V_B , is related to the cubic lattice parameter by $a^3/6$, and since the volume of the unit cell is a^3 , V_A must be $5a^3/6$ and hence $V_A/V_B = 5.0$. The calculation becomes increasingly difficult with decreasing crystal symmetry.¹²⁴ From geometric considerations, V_A/V_B remains 5.0 also in untilted perovskites with tolerance factor larger than unity, thus the V_A/V_B concept is more useful for perovskites with a tolerance factor of less than unity. The most common space groups encountered when V_A/V_B decreases from 5.0 in $Pm\bar{3}m$ in III-III perovskites is $R\bar{3}c$ (rhombohedral), $R3c$ (rhombohedral), $Immb$ (orthorhombic) and $Pbnm$ (orthorhombic) in decreasing order.¹²⁴ Other space groups like $I4/mcm$ (tetragonal), C_2/m (monoclinic) and $P2_1/m$ (monoclinic) are also commonly found. Perovskite structures can not be predicted with certainty from ionic radii or polyhedral volume ratios, but the empirical trends observed for various material systems provide important background knowledge for understanding the mechanisms of phase transitions induced by temperature, pressure, epitaxial strain or chemical composition.

Tilting of BO₆ octahedra is usually described within the Glazer tilt system.¹²⁵ The tilt system $a^0a^0a^0$ corresponds to the ideal cubic perovskite. The letters denote the relative size of the unit cell axes in terms of number of primitive lattice constants. Both a cubic unit cell with ~ 4 Å lattice parameters and a rhombohedral with $2^{1/2} \times 4$ Å have a Glazer tilt system with the letters aaa , while an orthorhombic unit cell with dimensions $4 \times 2^{1/2} \times 8$ Å would be described by the letters abc . The superscript refers to whether the tilting is ferrodistorive, “+”, or antiferrodistorive, “-“, along the three crystal axes. The Glazer tilt system $a^+a^-a^-$ would thus

correspond to a unit cell with $a = b = c$ with antiferrodistortive octahedral tilting along all three principal crystal axes, as found in BiFeO_3 with space group $R3c$.

Rhombohedral perovskites are commonly found within the four different space groups listed in Table 3.2. The space group $R3m$ results from cooperative displacements of the A and B cation along the $[111]$ pseudocubic axis, breaking the inversion symmetry, as illustrated in Figure 3.9. Elongation of the primitive unit cell along the $[111]$ axis makes the rhombohedral angle less than 60° , which is the value for the ideal cubic perovskite unit cell. Absence of octahedral tilting implies that the Glazer tilt system remains $a^0a^0a^0$ and V_A/V_B remains 5.0 by definition in the space group $R3m$. This distortion corresponds to condensation of an Γ -point optical phonon in the centre of the Brillouin zone.

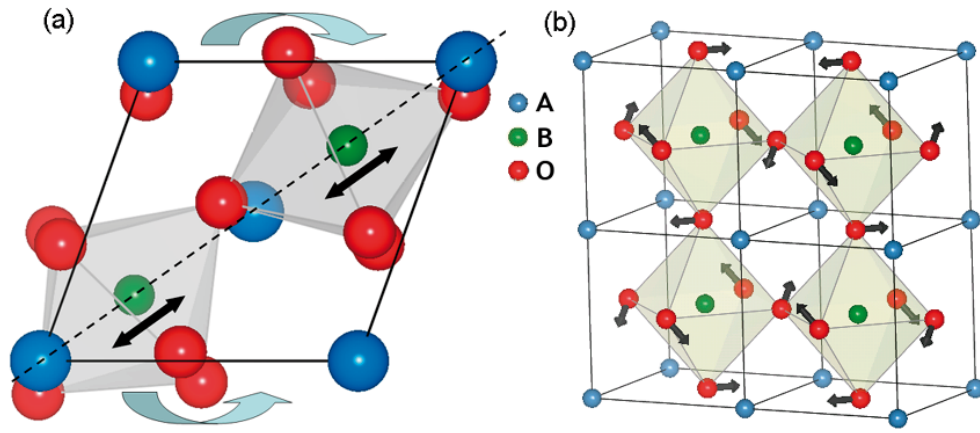


Figure 3.9. (a) Polar (black arrows) and antiferrodistortive (pale blue arrows) modes in rhombohedral perovskites. Oxygen octahedra can rotate antiparallel about the $[111]_{\text{cub}}$ axis by an angle of ω . Cations can be displaced parallel to the $[111]_{\text{cub}}$ direction. (b) Displacement of oxygen from their ideal positions from antiferrodistortive tilting about the $[111]_{\text{cub}}$ axis. Panel (b) was adapted from reference ¹²⁶.

Table 3.2. Crystallographic properties of rhombohedral space groups

S. G.	#	s, t	ω	d	e	Tilt	V_A/V_B	α_{rh}
$R3m$	160	$\neq 0$	$= 0$	$\neq 0$	$= 0$	$a^0a^0a^0$	5.0	$< 60^\circ$
$R3c$	161	$\neq 0$	$\neq 0$	$\neq 0$	$\neq 0$	$\bar{a}\bar{a}\bar{a}$	4.7-4.9	$< 60^\circ$
$\bar{R}3m$	166	$= 0$	$= 0$	$= 0$	$= 0$	$a^0a^0a^0$	5.0	$\approx 60^\circ$
$\bar{R}3c$	167	$= 0$	$\neq 0$	$= 0$	$\neq 0$	$\bar{a}\bar{a}\bar{a}$	4.85-5.0	$> 60^\circ$

The space group $\bar{R}3c$ results from antiferrodistortive rotation of the BO_6 octahedra about the $[111]$ pseudocubic axis. The symbol “ c ” in the space group symbol refers to the glide axis along the c -axis in the hexagonal setting parallel to the $[111]$ pseudocubic axis (see explanation of unit cell definition further below), thus doubling the unit cell along this axis. The antiferrodistortive rotation corresponds to the condensation of the R_{25} acoustic zone boundary phonon.

Condensation at the zone boundary, $q = 2\pi/a$, implies that the distortion repeats for each primitive unit cell length a ; thus the rotation of the BO_6 octahedra rotate opposite ways for each primitive unit cell. Rotation of the octahedra in the absence of polar displacements yields a compression of the primitive unit cell along the pseudocubic $[111]$ direction; thus the rhombohedral angle becomes larger than 60° . The resulting Glazer tilt system is $\bar{a}\bar{a}\bar{a}$, and the V_A/V_B decreases below 5.0. Centrosymmetry is preserved under this symmetry-lowering operation.

The space group $R3c$ of BiFeO_3 arises when both the polar distortion giving $R3m$ and the antiferrodistortive distortion giving $\bar{R}3c$ are combined. Inversion symmetry is broken, yielding a polar space group, elongated along the pseudocubic $[111]$ axis, yielding a rhombohedral angle less than 60° . The resulting Glazer tilt system is $\bar{a}\bar{a}\bar{a}$ and V_A/V_B is less than 5.0.

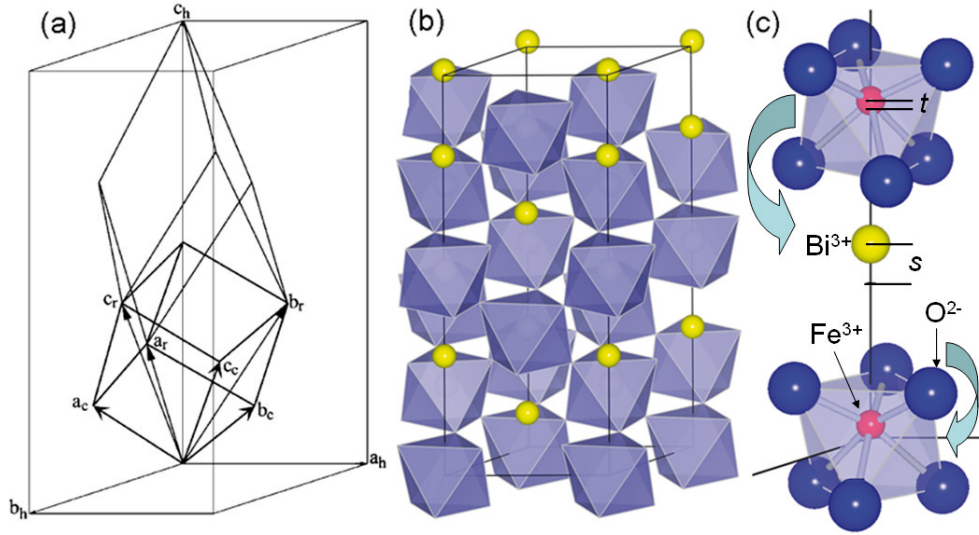


Figure 3.10. (a) Relation between pseudocubic, rhombohedral and hexagonal setting of the unit cell of BiFeO_3 with space group $R3c$. (b) Hexagonal unit cell of BiFeO_3 displayed with Bi^{3+} cations and FeO_6 octahedra. (c) Part of the hexagonal unit cell illustrating the atomic positions given in Table 3.3. The FeO_6 octahedra rotate antiparallel about the $[001]_{\text{hex}}$ axis.

The unit cell of the $R3c$ space group can be described with pseudocubic (pc), rhombohedral (rh) or hexagonal (h) axes, containing 1, 2 or 7 formula units, respectively, as shown in Figure 3.10 (a). The pseudocubic $[111]$ axis is the unique threefold axis and is parallel to the $[111]$ rhombohedral and $[001]$ hexagonal axis; $[111]_{\text{pc}} \parallel [111]_{\text{rh}} \parallel [001]_{\text{hex}}$. Rhombohedral and hexagonal lattice parameters are related by:¹²⁷

$$a_{\text{rh}} = \frac{a_{\text{h}}}{2 \sin\left(\frac{\alpha_{\text{rh}}}{2}\right)} \quad \text{and} \quad \alpha_{\text{rh}} = 2 \arcsin\left[\frac{3a_{\text{h}}}{2\sqrt{3a_{\text{h}}^2 + c_{\text{h}}^2}}\right]. \quad (3.2-3)$$

The pseudocubic angle α_{pc} is related to the rhombohedral angle by:¹²⁷

$$\alpha_{\text{pc}} = 90 + \arcsin\left(\frac{1 - 2 \cos \alpha_{\text{rh}}}{3 - 2 \cos \alpha_{\text{rh}}}\right). \quad (3.4)$$

The hexagonal representation is chosen for further quantitative description of the BiFeO₃ structure. The hexagonal unit cell of *R3c* contains 7 formula units and the polar displacements and spontaneous polarisation is along the *c*-axis. The rhombohedral angle of 59.35 ° implies a large unit cell distortion relative to the ideal cubic structure. For direct comparison with the aristotype structure the normalised lattice parameters $a_{\text{norm}} = 2^{-1/2} a_{\text{hex}}$ and $c_{\text{norm}} = 12^{-1/2} c_{\text{hex}}$ are useful. Since the polarisation is along the c_{hex} axis, the pseudotetragonality $c_{\text{hex}}/a_{\text{hex}}$ is a measure of the unit cell distortion along the polar axis, in analogy with prototype tetragonal ferroelectrics BaTiO₃ and PbTiO₃. The rhombohedral angle is related to the normalised lattice parameters by $\alpha_{\text{rh}} = 2 \arcsin\left[3a/2\sqrt{3a^2 + 6c^2}\right]$. Atomic positions in the space group *R3c* of BiFeO₃ are given in Table 3.3, following Megaw and Darlington.¹²⁷

Table 3.3. Atomic positions in the hexagonal setting of *R3c* (BiFeO₃).¹²⁷

atom/pos.	<i>x</i>	<i>y</i>	<i>z</i>
Bi ³⁺	0	0	1/4 + <i>s</i> = 0.30
Fe ³⁺	0	0	<i>t</i> = 0.02
O ²⁻	1/6 - 2 <i>e</i> - 2 <i>d</i> = 0.23	1/3 - 4 <i>d</i> = 0.34	1/12

The unit cell is anchored in the *z*-direction by the oxygen position fixed at 1/12 along the *c*-axis, as shown in Figure 3.10 (c). The displacement of Bi, *s*, is larger than the displacements of Fe, *t*. These displacements are cooperative, in the same direction, as parallel displacements are energetically strongly favoured compared to antiparallel due to electrostatic repulsion between the cations.¹⁰³ Alternatively, the unit cell could be anchored by placing Bi in *origo*, then the *z*-coordinate of Fe would be *s* - *t*. The oxygen position parameter *d* is related to the distortion of the FeO₆ octahedra parallel to the [001]_{hex} axis, while the parameter *e* is linked to the antiferrodistortive rotation of the octahedra by the angle ω about the [001]_{hex} axis by:¹²⁷

$$\omega = \arctan(2e\sqrt{3}). \quad (3.5)$$

Octahedral strain η is defined as:¹²⁷

$$\eta = \frac{c_{\text{hex}} \cos \omega}{a_{\text{hex}} \sqrt{6}}. \quad (3.6)$$

Bulk BiFeO₃ at ambient conditions possesses an antiferrodistortive rotation angle ω of $\sim 12^\circ$ and octahedral strain equal to 0.997. The polyhedral volumes of BiFeO₃ are $V_A = 51.587 \text{ \AA}^3$ for the BiO₁₂ dodecahedron and $V_B = 10.913 \text{ \AA}^3$ ratio for FeO₆ octahedron, thus $V_A/V_B = 4.727$.¹⁰³ V_A/V_B can be determined indirectly from the oxygen positions as it is related to the antiferrodistortive rotation angle by the approximation:¹⁰³

$$V_A/V_B = 6 \cos^2 \omega - 1. \quad (3.7)$$

The Fe-O-Fe angle $180 - \theta^\circ$ is smaller than 180° due to the distortions of the unit cell compared to the ideal cubic structure. This angle affects the overlap of Fe³⁺ 3d orbitals and O 2p orbitals, and is thus important for the magnetic and electronic properties of BiFeO₃, as discussed further below. The Fe – O – Fe angle can be estimated from the atomic position parameters by:¹²⁷

$$\cos(180 - \theta) = 1 - \frac{4}{3} \sin^2 \left(\frac{\omega}{2} \right) - 64t^2. \quad (3.8)$$

Lattice parameters and atomic positions are often given in the rhombohedral setting in the literature, hexagonal lattice parameters and atomic positions can be obtained from the rhombohedral by the following translation matrices:

$$\begin{pmatrix} 1 & -1 & 0 \\ 0 & 1 & -1 \\ 1 & 1 & 1 \end{pmatrix} \text{ and } \begin{pmatrix} 2/3 & -1/3 & -1/3 \\ 1/3 & 1/3 & 2/3 \\ 1/3 & 1/3 & 1/3 \end{pmatrix}, \quad (3.9)$$

respectively.¹²⁷

3.2.2 Ferroelectricity and Piezoelectricity

The spontaneous polarisation P_S is $\parallel [111]_{\text{rh}} \parallel [001]_{\text{hex}}$ in BiFeO₃, and is due to the cooperative displacements of Bi³⁺ by s and Fe³⁺ by t along this axis. The empirical relation found by Abrahams *et al.* in 1968,¹²⁸ $P_S = (258 \pm 9) \Delta z \mu\text{C cm}^{-2}$, predicts the P_S of bulk BiFeO₃ to be 98–108 $\mu\text{C/cm}^2$ at ambient conditions. Early direct measurements of polarisation did however yield a small value of 6 $\mu\text{C/cm}^2$.¹⁰⁶ Recent measurements on high quality thin films,¹¹² single crystals¹⁰⁸ and ceramic polycrystals¹¹¹ have shown that P_S is 90–100 $\mu\text{C/cm}^2$ along the polar axis, in agreement with the Abrahams *et al.*-relation. *Ab initio* studies by groups in Oslo¹¹⁰ and Santa Barbara¹⁰⁹ also found a large spontaneous polarisation in the order of 90–100 $\mu\text{C/cm}^2$. With a polarisation P_S of 90–100 $\mu\text{C/cm}^2$ along $[111]_{\text{cub}} \parallel [001]_{\text{hex}}$, the polarisation along $[110]_{\text{cub}} \parallel [104/110]_{\text{hex}}$ is $2^{-1/2} P_S$ and hence along $[001]_{\text{cub}} \parallel [012]_{\text{hex}}$ it is $3^{-1/2} P_S$, as demonstrated for epitaxial thin films of $(111)_{\text{cub}}$, $(110)_{\text{cub}}$ and $(100)_{\text{cub}}$ orientation, respectively.¹²⁹ The spontaneous ferroelectric polarisation of BiFeO₃ is larger than those of the prototype ferroelectrics BaTiO₃ and PbTiO₃,

in concordance with the more distorted crystal structure, larger polar displacements of cations and higher Curie temperature, the latter being 123 and 490 °C in BaTiO₃ and PbTiO₃, respectively.⁵⁸

3.2.3 Piezoelectricity and epitaxial strain in thin films

In contrast with the large polarisation, the piezoelectric coefficient d_{33} is substantially smaller in BiFeO₃, in the order of 15-60 pm/V,^{108, 111-112} than prototype ferroelectrics BaTiO₃, PbTiO₃ and PbZr_{1-x}Ti_xO₃, with 100-200 pm/V.¹³⁰ The room temperature dielectric constant of¹¹³ $\epsilon_r = \sim 30$ is also small compared to the mentioned prototype ferroelectrics. A high T_C and P_S , but a low d_{33} and ϵ_r all indicate that ferroelectric polarisation in BiFeO₃ is robust with respect to temperature and strain. The insensitivity of the polarisation to strain has been demonstrated in epitaxial thin films¹³¹ and inferred from *ab initio* calculations.¹³²⁻¹³³ This is in striking contrast with the prototype ferroelectric BaTiO₃ where compressive epitaxial strain can raise the T_C of 123 °C in bulk to > 677 °C in thin films, simultaneously increasing P_S by more than 250 %.¹³⁴⁻¹³⁵ Epitaxial tensile strain and compression can even induce a ferroelectric state in the bulk paraelectric, incipient ferroelectric SrTiO₃,¹³⁶ and large tensile strains are predicted to induce polarisation in CaTiO₃.¹³⁷ It should be noted that other reports indicate a strong strain dependence of the polarisation of BiFeO₃.¹³⁸

Epitaxial thin films of BiFeO₃ grown on substrates with a smaller lattice parameter than that of BiFeO₃, e.g. SrTiO₃, are subject to epitaxial compressive strain, while substrates with a larger lattice parameter induce tensile strain in epitaxial thin films. Compressive epitaxial strain can cause a distortion of the trigonal unit cell, inducing monoclinic or pseudo-tetragonal symmetry.¹³⁹⁻¹⁴¹ A record-high polarisation of 150 $\mu\text{C}/\text{cm}^2$ in tetragonal BiFeO₃ with $P4mm$ structure grown on Pt/TiO₂/SiO₂/Si substrates has been reported.¹⁴² A similar, strongly distorted monoclinic structure (resembling $P4mm$), epitaxially stabilised on a LaAlO₃ substrate, was recently found, but with $P_S = 75 \mu\text{C}/\text{cm}^2$ for 5 % Mn doping, similar to the value of bulk material.¹⁴¹ It thus appears that although the polarisation is insensitive to strain, the crystal symmetry is not. Ederer and Spaldin have discussed the apparent insensitivity of the polarisation to strain.¹³²⁻¹³³ The local structure and partial covalent bonding stabilising the off-centering of Bi³⁺ and Fe³⁺ is not necessarily sensitive to strain, although the unit cell symmetry is. Defect chemistry as a means of strain relaxation at epitaxial interfaces has only very recently attracted attention.¹⁴³⁻¹⁴⁴ Different substrate materials, -orientations and -miscuts have been explored for controlling the direction of the polarisation.¹⁴⁵⁻¹⁵¹

3.2.4 Electronic structure

Ferroelectric materials are dielectrics, as mobile charges would internally screen any induced polarisation. Like other III-III ferrite perovskites, the d electrons of HS Fe³⁺ are localised in BiFeO₃. It should be classified as a charge transfer insulator in the Zaanen, Sawatzky and Allen (ZSA)¹⁵²⁻¹⁵³ scheme; $p-d$ charge transfer transitions have smaller energies than $d-d$ transitions (Mott-Hubbard insulator).

The valence of Fe is important for the electronic structure, as e.g. $A^{II}Fe^{IV}O_3$ ($A = Ca, Sr$) with HS $d^4 Fe^{4+}$ is metallic with localised t_{2g} electrons and itinerant e_g electrons; $t_{2g}^3\sigma^{-1}$.⁷²

$BiFeO_3$ is a low bandgap semiconductor, but the term “bandgap” is ambiguous as different values can be obtained for spectroscopic and conductivity measurements, depending on the mechanisms involved. Reported values from spectroscopic studies vary from 2.2 to 2.8 eV. There is not yet consensus whether this bandgap is direct or indirect, and an indirect bandgap of 1.3-1.8 eV has also been reported.¹⁵⁴⁻¹⁵⁷ Bandgaps from *ab initio* calculations depend on the computational method used, and reported values are in the range of 1.9-2.8 eV.^{109, 158} $BiFeO_3$ has been reported to become metallic at high temperatures¹⁵⁹ and high pressures,¹⁶⁰ as discussed further in chapter 6.

In $BiFeO_3$ Bi^{3+} possesses a stereochemically active $6s^2$ lone pair due to hybridisation between $6s$ and $5p$ orbitals.¹¹⁰ Partial covalent bonding between the $6s^2$ lone pair and O $2p$ stabilises the displacement of Bi^{3+} towards the face of the FeO_6 octahedron along the $[001]_{hex}$ axis.¹⁰⁹⁻¹¹⁰ Fe^{3+} is a d^5 cation, which in octahedral coordination in oxides is high spin, thus the electronic configuration on the B site is $t_{2g}^3e_g^2$. If the chemical bonding in $BiFeO_3$ was purely ionic, it would have been centrosymmetric, as centrosymmetry maximises electrostatic attraction between anions and cations. Results from a theoretical study of chemical bonding in $BiFeO_3$ is shown in Figure 3.11. Although the bonding is primarily ionic, partial covalent bonding between Bi^{3+} and O^{2-} and between Fe^{3+} and O^{2-} is evident from the anisotropic valence electron charge distribution (a) and anisotropic charge transfer distribution (b).

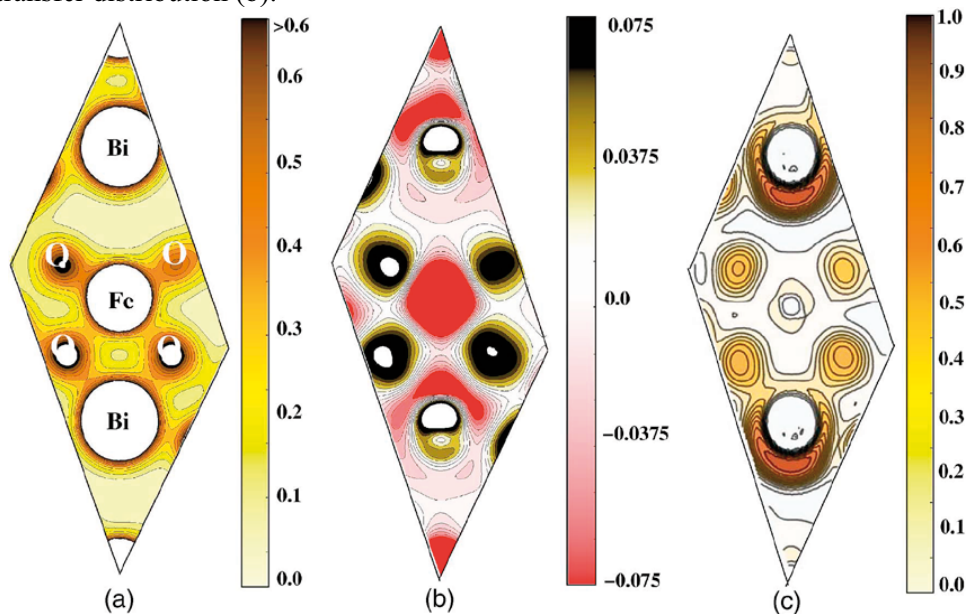


Figure 3.11. Chemical bonding in $BiFeO_3$ visualised from electron charge density maps from *ab initio* calculations. (a) valence electron charge density, (b) charge transfer and (c) electron localisation function. Adapted from Ravindran *et al.*¹¹⁰

3.2.5 Magnetic structure

BiFeO₃ is antiferromagnetic¹⁰² with G-type¹⁶¹ ordering, in analogy with the rock salt crystal structure; each Fe³⁺ with spin up is surrounded by six nearest neighbours with spin down, as shown in Figure 3.12 (a). The easy plane of magnetisation is the (001)_{hex} plane, perpendicular to the polar [111]_{hex} axis.¹⁶² Tilting of the FeO₆ octahedra reduces the Fe-O-Fe angle from 180 °, reducing the overlap of Fe *d* and O *2p* orbitals. The Fe-O-Fe angle is related to the atomic position parameters by eq. (3.8). At ambient temperature and pressure the Fe-O-Fe angle is 154-155 °. If the Fe-O-Fe angle was 180 ° one would expect collinear antiferromagnetism. The antiparallel magnetic sublattices are also canted caused by the Dzyaloshinskii-Moriya interaction,^{126, 163-164} a combination of exchange interaction and spin-orbit coupling. Canting of the sublattices yields a weak ferromagnetic moment, illustrated schematically in Figure 3.12 (b). On a local scale, BiFeO₃ thus possesses both ferroelectric polarisation and a weak ferromagnetic moment, the latter induced by the former; ferromagnetism induced by ferroelectricity.¹⁶⁵⁻¹⁶⁶ The weak ferromagnetic moment is however cancelled on average due to a spiral modulation, or spin cycloid, of the spin structure with a periodicity of 62 nm, incommensurate with the crystal lattice, see Figure 3.12 (c).¹⁶⁷

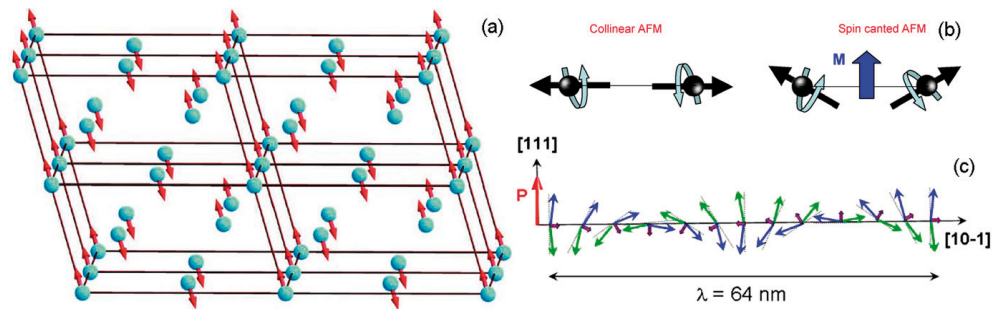


Figure 3.12. (a) G-type antiferromagnetic ordering. (b) Weak ferromagnetic moment induced by canted spin sublattices caused by the Dzyaloshinskii-Moriya interaction. (c) Cycloidal modulation of the spin structure, directions are given with pseudocubic indices. Adapted from references^{110, 126} and¹⁶⁸ respectively.

Several subtle, magnetic transitions at cryogenic temperatures have been reported the last two years.⁴⁰ Although ferromagnetism has been observed at low temperatures,¹⁶⁹⁻¹⁷⁰ there are hitherto no indications that true ferromagnetism is an intrinsic property of BiFeO₃, even at the lowest temperatures.^{108, 171}

3.2.6 Ferroelastic, ferroelectric and antiferromagnetic domains

The three different ferroic orders present in BiFeO₃ give rise to three different types of domains and domain walls; ferroelastic, ferroelectric and antiferromagnetic. The domains of these three orders are correlated, not independent. Ferroelectric domains are restricted by the ferroelastic strain states,

and the antiferromagnetic domains coincide with the ferroelectric domains, hence we start with the ferroelastic domain structure, which is analogous to other rhombohedral ferroelastic perovskites like LaCoO_3 .^{77, 85}

Since the rhombohedral $R\bar{3}c$ structure is elongated along the $[111]_{\text{cub}} \parallel [001]_{\text{hex}}$ axis, there are four different orientations of the unique threefold axis, as displayed in Figure 3.13. Four different domain states follows from the ratio of symmetry elements in the crystallographic point group of the parent aristotype structure and the ferroelastic h ettotype.⁷⁶ Although this relationship is derived under the assumption of a second order phase transition from the aristotype to the haettotype structure, which from symmetry considerations can not be the case in BiFeO_3 , the reasoning still holds. The point group of related ferroelastic LaCoO_3 -based materials with the isomorphous space group $R\bar{3}c$ is $\bar{3}m$ with 12 symmetry elements. As the point group $m\bar{3}m$ of the corresponding paraelastic phase with space group $Pm\bar{3}m$ has 48 symmetry elements, the number of different domain states for the point group $\bar{3}m$ is four. Thus the number of ferroelastic domain states in BiFeO_3 is four; R_1 , R_2 , R_3 and R_4 in Figure 3.13. The direction of the polarisation vector is constrained to the unique threefold axis of the rhombohedral unit cell. Removing centrosymmetry in the space group $R\bar{3}c$ with point group $\bar{3}m$ yields the polar space group $R3c$ of BiFeO_3 . The corresponding point group $3m$ has only 6 symmetry elements; $48/6$ yields 8 different domain states of BiFeO_3 when polarisation is taken into account. There are thus 8 different ferroelectric domain states, but these are not independent of the ferroelastic domain states. As illustrated in Figure 3.13; the ferroelectric domain states P_1^+ and P_1^- are restricted to the ferroelastic domain state R_1 , et.c.

Considering the intimate coupling between ferroelectric and ferroelastic domain states, only three different ferroelectric domain walls are possible. A domain with P_s in the direction $[111]_{\text{cub}}$ adjacent to a domain with P_s in the $[\bar{1}\bar{1}\bar{1}]_{\text{cub}}$ direction will be separated by a $\arccos(1/3) \sim 71^\circ$ domain wall. Domains with $[111]_{\text{cub}}$ and $[\bar{1}\bar{1}\bar{1}]_{\text{cub}}$ yield $\arccos(-1/3) \sim 109^\circ$ domain walls, while $\arccos(-1) = 180^\circ$ walls separate domains in the $[111]_{\text{cub}}$ and $[\bar{1}\bar{1}\bar{1}]_{\text{cub}}$ directions.¹⁷² Piezoelectric force microscopy (PFM) has been used by several groups to study the domain structure of thin films, single crystals and ceramics.^{108, 111, 162} 180° ferroelectric switching of domains hence does not require ferroelastic deformation of the crystal, but large displacements ($\sim 0.8\text{-}0.9 \text{ \AA}$ for Fe with Bi fixed in *origo*) of the cations along the unique threefold axis.¹⁰¹ 71° and 109° switching requires a change of the ferroelastic domain state as well as the ferroelectric, and requires deformation of the crystal.

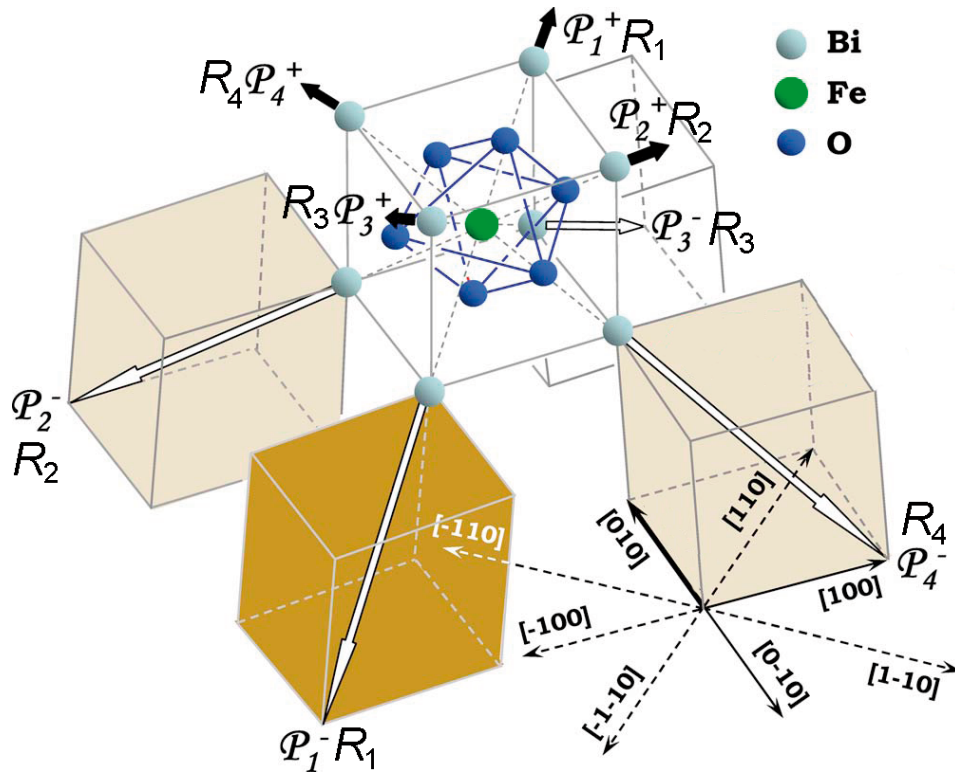


Figure 3.13. Ferroelectric and ferroelastic domain states in BiFeO_3 , the 8 ferroelectric domain states are restricted to the 4 ferroelastic domain states; P_1^+ and P_1^- to R_1 *et. c.* Switching the polarisation 180° between P_1^+ and P_1^- does not change the ferroelastic state R_1 , while e.g. 71° switching of the polarisation from P_1^+ to P_4^+ will change the ferroelastic state from R_1 to R_4 . Adapted from ref. ¹⁷³.

3.2.7 Magnetoelectric coupling

The cycloidal modulation of the spin structure prevents a macroscopic weak ferromagnetic moment, and also exploitation of the linear magnetoelectric effect. At large magnetic fields, above 20 T, the cycloidal modulation is suppressed and linear magnetoelectric coupling is possible. The origin of the cycloidal spin structure is believed to be the ferroelectric polarisation, as polarisation can couple to magnetisation gradients and induce the spin cycloid. This can be regarded as the opposite effect of the polarisation induced by spiral magnetic order in improper ferroelectric multiferroics (chapter 3.3.1).¹⁶⁵⁻¹⁶⁶

Given that BiFeO_3 is a proper ferroelectric with only weak ferromagnetism due to the Dzyaloshinskii-Moriya interaction, ferroelectric control of the magnetic structure is obviously more feasible than vice versa, as e.g. demonstrated in TbMnO_3 .¹⁷⁴ A theoretical study of BiFeO_3 found that the direction of the weak ferromagnetic moment can be reversed by switching the direction of antiferrodistortive rotation of the FeO_6 octahedra, but it is invariant under 180°

switching of the direction of polar displacements of the Bi^{3+} and Fe^{3+} cations.¹⁷⁵ 180° ferroelectric switching does not affect neither the ferroelastic state of the material, nor the easy plane of magnetisation. Switching the ferroelectric polarisation by 71° or 109° changes the ferroelastic strain state of the domains for the rhombohedral structure, also changes both the easy plane of magnetisation and the direction of the weak ferromagnetic moment. This has been experimentally verified in rhombohedral 600 nm thick films without cycloidal modulation of the magnetic structure, as illustrated in Figure 3.14. The antiferromagnetic domains coincide with the ferroelectric, illustrating the strong coupling of ferroelectric and magnetic order in BiFeO_3 . This was the first demonstration of electric voltage control of magnetic order at room temperature.¹⁶² Two independent neutron scattering studies of BiFeO_3 single crystals, with cycloidal spin structure, demonstrated that 71° switching of polarisation is accompanied by a 71° switching of the easy plane of magnetisation.^{168, 176-177}

The microscopic origin of magnetoelectric coupling is not fully understood, and is expected to attract considerable attention in near future. Based on observations of phonon anomalies at T_N , and coupling of magnetic order to the ferroelastic domain state, Rovillain *et al.* proposed that the magnetoelectric coupling in BiFeO_3 is mediated by magnetostriction and piezoelectricity.¹⁷⁸ Other phenomena observed at T_N are discussed in Chapter 6.

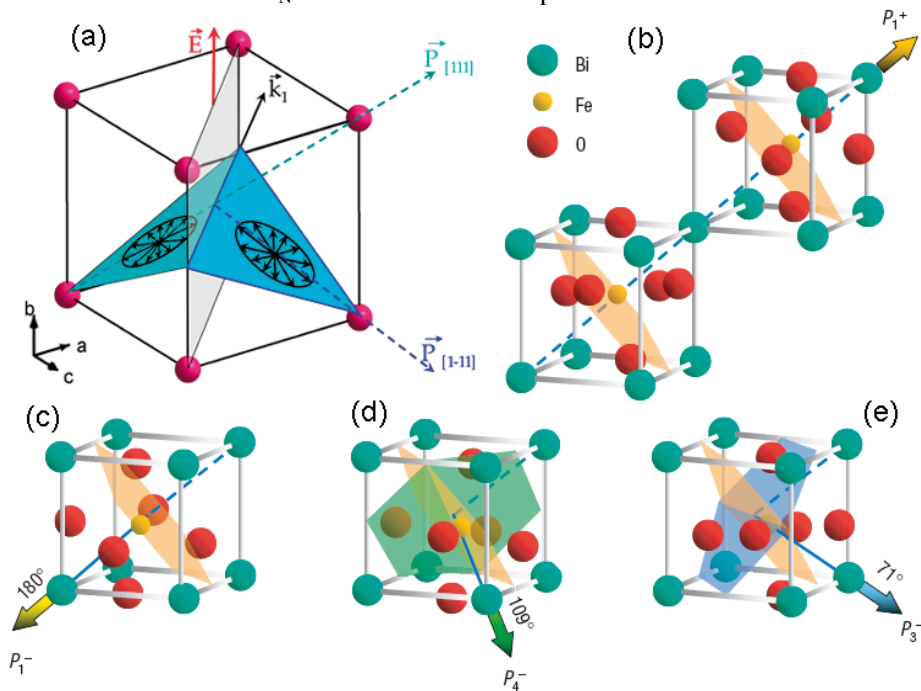


Figure 3.14. (a) 71° domain wall (light grey) and polarisation vectors with pseudocubic indices. The plane of spin rotation (Figure 3.12 (c)) is defined by the polarisation vector \vec{P} and the propagation vector \vec{k}_1 . (b-d) The antiferromagnetic plane is normal to the polarisation and does not change with 180° switching (b) \leftrightarrow (c), but rotates when the ferroelastic state is altered (d) and (e). Adapted from reference ¹⁶⁸ (a) and ¹⁶² (b-e).

3.2.8 III-III bismuth perovskites without Fe; BiMO₃

To illustrate the role of Fe³⁺ in BiFeO₃ the structures and properties of closely related Bi-based non-ferrite perovskites are presented here. Selected properties and structures of Bi-based perovskites are given in Table 3.4. It should be noted that all the other simple BiMO₃ materials are metastable at ambient conditions, hence they must be prepared by high pressure synthesis. BiMnO₃ and BiScO₃ can be stabilised by epitaxial strain when grown as thin films,¹⁷⁹⁻¹⁸⁰ and in the case of BiMnO₃ also by hydrothermal crystallisation.¹⁸¹⁻¹⁸² BiFeO₃ is also the only simple compound exhibiting multiferroism at ambient temperature. Five examples of mixed B site occupancy are also included in Table 3.4, three of them stable at ambient pressure.

Table 3.4. The compounds BiMO₃ and selected properties.

M	Space group ^a	Ferroelectricity ^b	Magnetism	Synthesis conditions ^c	Comments ^d	Ref.
Al	<i>R3c</i>	$T_C > 520$ $P_S = 9$	d^0	1000 6 GPa		183- 184
Ga	<i>Pcca</i>	Centrosym.	d^0	1200 6 GPa		184
In	<i>Pna2₁</i>	$T_C > 600$ $P_S = 18$	d^0	1000 6 GPa	P_S from PCM.	185
Sc	<i>C2/c</i>	Centrosym.	d^0	1140 6 GPa		186
Cr	<i>C2/c</i>	Centrosym.	$T_N = 109$ K AFM G-type	1380 6 GPa		187
Mn	<i>C2/c</i>	Centrosym.	$T_C = 100$ K FM	500-1110 4-6 GPa	Debated.	98-99, 188- 199
Co	<i>P4mm</i>	$T_C > 247$ $P_S = 175$	$T_N = 197$ AFM C-type	970 6 GPa	P_S from BPC.	200- 202
Ni	$P\bar{1}$	Centrosym.	$T_N = 27$ AFM	1000 6 GPa		203- 204
Cr _{0.5} Fe _{0.5}	<i>R3c</i>	T_C unkown $P_S = 63$	$T_N = 130$ K AFM	1000 6 GPa	P_S from PCM.	205
Ni _{0.5} Mn _{0.5}	<i>C2</i>	T_C unkown $P_S = 20$	$T_C = 140$ K FM	800 6 GPa	P_S from PCM	206
Mn _{2/3} Ni _{1/3}	<i>Pn2₁m</i>	T_C unkown $P_S = 60$	Short range order.	800 Ambient P	P_S from PCM	207
Ti _{3/8} Fe _{2/8} Ni _{3/8}	<i>R3c</i>		-	Multiple firing. Ambient P	Unsaturated Hysteresis loop.	208
Ti _{3/8} Fe _{2/8} Mg _{3/8}	<i>R3c</i>	$T_C = 730$ $P_S = 0.5$	-	Multiple firing. Ambient P	Unsaturated Hysteresis loop.	208

^a*Pcca*, *Pna2₁* and *Pn2₁m* are orthorhombic, *C2/c* monoclinic and $P\bar{1}$ is triclinic.

^bUnits for T_C and P_S are °C and $\mu\text{C}/\text{cm}^2$, respectively.

^cTemperatures are given in °C.

^dPCM = Point Charge Model, BPC = Berry Phase Calculations, other values of P_S were obtained by dielectric measurements.

3.2.9 III-III ferrite perovskites without Bi; AFeO₃, A = Y, La, Pr...Yb, Lu

To illustrate the significance of Bi³⁺ for BiFeO₃, the structure and properties of closely related ferrite perovskites are shortly summarised. The III-III ferrite perovskites are known as orthoferrites which crystallise in the centrosymmetric orthorhombic space group *Pbnm* at ambient conditions, illustrating the importance of the 6s² lone pair of Bi³⁺ for stabilizing BiFeO₃ in the polar *R3c* structure. The orthoferrites are also G-type antiferromagnets with high T_N of 350-467 °C.⁷¹ Rare earth Ln cations with unpaired *f* electrons have the possibility of magnetic exchange striction between Ln 4*f* orbitals and Fe 3*d* orbitals, which can induce a small polarisation. However, the magnetic ordering temperature of Ln is very low, 3.5 K in Dy in DyFeO₃, where a magnetic field can induce polarisation below 3.5 K.²⁰⁹ A similar effect has been observed in GdFeO₃, but here the small polarisation of 0.12 μC/cm² at 2 K is stable even in zero magnetic field.²¹⁰

3.2.10 Solid solutions of BiFeO₃-ABO₃, A ≠ Bi, B ≠ Fe

A few solid solution systems of BiFeO₃ with ferroelectric materials have been extensively studied, the earliest being BiFeO₃-PbTiO₃.²¹¹ From a fundamental point of view, simultaneous substitution on both the A site and B site can hinder interpretations of the significance of Bi³⁺ and Fe³⁺, thus substitution only on either the A or B site is a better proxy for this purpose, as investigated in chapters 7 and 8. Optimisations of functional properties has however been demonstrated, e.g. in (BiFeO₃)_{1-x}(Pb_{1-y}La_yZr_{1-z}Ti_zO₃)_x where simultaneous weak ferromagnetism and low ferroelectric polarisation was reported to occur at room temperature.²¹² Coexistence of ferroelectricity of ferromagnetism at room temperature, albeit weak, has been reported for (BiFeO₃)_{0.3}(BaTiO₃)_{0.7}.²¹³ (BiFeO₃)_{0.8}(BaTiO₃)_{0.2} ceramic materials with monoclinic *Cm* structure exhibit spontaneous polarisation and magnetisation at room temperature.²¹⁴ The crystal structure, morphotropic phase boundary and multiferroic properties of (BiFeO₃)_{1-x}(PbTiO₃)_x solid solutions have also recently been revisited.²¹⁵⁻²¹⁹

3.3 Other multiferroic and magnetoelectric materials

This subchapter provides a short overview of the vast and rapidly increasing number of multiferroic single-phase compounds and composites. As many questions still remain open even for the most studied compound, BiFeO₃, it is safe to claim that the field is immature.

3.3.1 Single phase compounds

Coupling of polarisation and magnetism in solids was anticipated by P. Curie already in 1894,²²⁰ but magnetoelectric coupling was not experimentally demonstrated until 1960 for Cr₂O₃.²²¹ Next to the Bi-based perovskites, the most important class of multiferroic materials are the hexagonal manganites with YMnO₃-structure.^{35, 119, 222} Hexagonal RMnO₃ (R = Y, In, Sc, Ho-Lu) are frustrated antiferromagnets with ferroelectric $T_C \gg T_N$, typically > 500 and < -150 °C, respectively. Weak magnetoelectric coupling follows from $T_C \gg T_N$. YMnO₃ is the most studied hexagonal manganite.^{66, 96, 120, 223-229} Orthorhombic manganites (perovskites with space group *Pbnm*) are not ferroelectric at room temperature, but RMnO₃ with R = Dy, Tb and Gd exhibit multiferroism below with $T_C < T_N$, which is typically about 27 K. Here ferroelectric polarisation originates from lattice distortions induced by magnetic frustration, yielding comparatively low values of polarisation.³⁵ The hexagonal and orthorhombic polymorphs are close in Gibbs energy for the RMnO₃ family. Hydrostatic pressure and high temperature can cause a reconstructive phase transition from hexagonal to the denser orthorhombic polymorph,²³⁰⁻²³¹ and the orthorhombic structure can also be stabilised by compressive epitaxial strain²³² or partial oxidation.²³³ Likewise, the hexagonal polymorph can be stabilised by epitaxial strain for TbMnO₃, thus increasing the T_C by several hundred degrees relative to the stable orthorhombic polymorph.²³⁴ TbMnO₃ is the most studied of the multiferroic orthorhombic manganites.^{174, 235-240}

The two different types of RMnO₃ materials illustrate the most obvious way of dividing multiferroics into two classes; those with polarisation induced by frustrated magnetic spiral order²⁴¹ (with low ferroelectric $T_C < 40$ K and $T_C < T_{\text{magnetic ordering}}$), and those where polarisation is stabilised by other mechanisms (usually with $T_C \gg 40$ K and $T_C \gg T_{\text{magnetic ordering}}$). Other important systems in the latter class are:

- PbB_{1-x}B'_xO₃ (R = Fe, Mn, Ni, Co (d^n $n \neq 0$); R' = Nb, W, Ta, d^0) where R yields magnetism and R' polarisation.^{31, 242}
- Polarisation induced by charge ordering,⁶⁰ e.g. LuFe₂O₄,⁶¹⁻⁶² Fe₃O₄²⁴³ and RMn₂O₅ (R = Y, Tb, Ho, Er, Tm).²⁴⁴⁻²⁴⁹
- Polarisation induced by ordering of both orbitals and charge, e.g. Pr_{1-x}Ca_xMnO₃^{64, 250} and Pr(Sr_{0.1}Ca_{0.9})₂Mn₂O₇.⁶⁵

Examples of multiferroic materials with polarisation induced by frustrated spiral spin ordering are Ni₃V₂O₈,²⁵¹⁻²⁵³ RCrO₂ (R = Li, Na, Cu, Ag)²⁵⁴⁻²⁵⁵ and CuRO₂ (R = Cr, Fe).²⁵⁵⁻²⁵⁶ Ca₃CoMnO₆ is an Ising chain magnets with inversion symmetry broken by ordering of Co and Mn, giving rise to ferroelectric

polarisation.²⁵⁷⁻²⁵⁸ The boracites, $M_3B_7O_{13}X$ ($M = Cr, Mn, Fe, Co, Ni, Cu$; $X = Cl, Br, I$), exhibit magnetic ordering only below 100 K and ferroelectricity above room temperature for some compositions.^{22, 259} Another example from last year is the hexaferrites, $(Ba_{1-x}Sr_x)_2R_2Fe_{12}O_{22}$ ($R = Mg, Zn$), where the polarisation can be controlled by a low magnetic field.²⁶⁰

The most intriguing recent discovery is arguably the comparatively high ferroelectric T_C of 230 K in the simple, binary compound CuO .²⁶¹⁻²⁶² This is the highest known T_C among the spin spiral induced ferroelectrics and a major advance towards room-temperature magnetoelectric multiferroic materials of this class.

A rare example of a multiferroic and magnetoelectric spinel is $CoCr_2O_4$.²⁶³ Among the spinels there are also examples of non-oxide chalcogenides, e.g. $CdCr_2S_4$.²⁶⁴ The $BaRF_4$ ($R = Mg, Mn, Fe, Co, Ni, Zn$) family has long been known to exhibit strong magnetoelectric coupling,^{31, 37} in addition to other fluoride structures.²⁶⁵ Finally, the $LiRPO_4$ ($R = Mn, Fe, Co, Ni$) compounds display strong magnetoelectric coupling and ferrotoroidicity.^{25, 91-93, 266}

3.3.2 Composites

Composites consisting of both a ferroelectric and ferromagnetic phase circumvent the challenge of finding a single-phase compound exhibiting room-temperature multiferroism, and may thus be candidates for 4-state memories. The disadvantage is that magnetoelectric coupling is restricted to interfaces only. An early approach was fabricating particulate composites of magnetostrictive ($CoFe_2O_4$) and piezoelectric ($BaTiO_3$) compounds; an applied magnetic field causes strain in the magnetostrictive phase and the resulting pressure causes polarisation in the piezoelectric compound. Due to the highly anisotropic nature of magnetostriction and piezoelectricity, laminar composites improve the magnetoelectric response (Figure 3.15). Magnetoelectric coupling in composites is limited by the mechanical, electrical and magnetic coefficients of the constituents, the thickness and number of the laminate layers, the bonding between the layers and the crystallographic orientation of the layers relative to the applied electric or magnetic fields.²⁵ Interface strain due to different elastic constants of the constituents must be controlled to exploit multiferroic coupling in vertical columnar nanocomposites.²⁶⁷

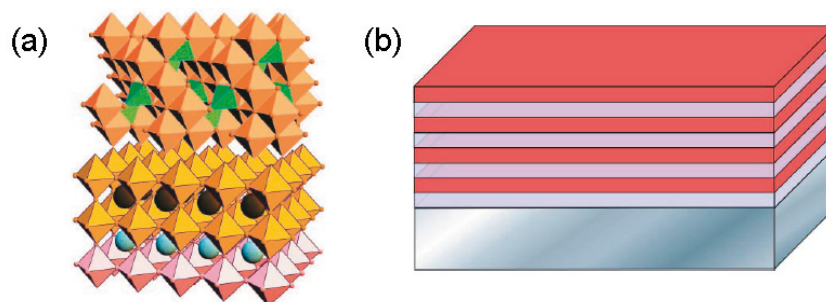


Figure 3.15. Examples of multiferroic composites of ferroelectric $BaTiO_3$ and ferromagnetic $CoFe_2O_4$. (a) superlattice and (b) layered composite. Adapted from reference²⁶⁸.

Composites of ferroelectric perovskites and ferromagnetic (or ferrimagnetic) spinels are the most studied composite systems, both for laminar and columnar geometries. Elastic interactions have been shown to mediate the magnetoelectric coupling in BaTiO₃-CoFe₂O₄ composites.²⁶⁸ BaTiO₃ has also been combined with CuFe₂O₄ and CuFe_{1.5}Cr_{0.4}O₄.²⁶⁹⁻²⁷⁰ Magnetoelectric coupling was found in bilayers of magnetostrictive La_{0.7}Sr_{0.3}MnO₃ and piezoelectric PZT.²⁷¹ In recent years BiFeO₃ has become the common choice for the ferroelectric perovskite constituent of perovskite-spinel composites. It has been combined with CoFe₂O₄,²⁷²⁻²⁷⁶ MnFe₂O₄,²⁷⁷ CuFe₂O₄,²⁷⁸ Ni_{0.75}Co_{0.25}Fe₂O₄,²⁷⁹ and NiFe₂O₄.²⁸⁰ This year (2009) two new concepts have emerged; PZT-magnetoplumbite (PbZr_{1-x}Ti_xO₃-PbFe₁₂O₁₉) composites have been proposed as a route to multiferroic ceramic composite,²⁸¹ and (BiFeO₃)_{0.5}-(Sm₂O₃)_{0.5} self-assembled composites have been demonstrated.²⁸²

3.4 Applications of BiFeO₃

3.4.1 Magnetoelectric and multiferroic memories

BiFeO₃ is a prime candidate for magnetoelectric memories, where bits can be written by an electric field, utilising the ferroelectric polarisation, and read from the associated magnetic field, avoiding destructive read-out of the ferroelectric state. Reading antiferromagnetic states is not straight-forward, and an obvious solution to this is to read the magnetism of a ferromagnetic layer in contact with antiferromagnetic BiFeO₃, exploiting the associated exchange bias.²⁸³ Exchange bias offsets and/or widens the magnetic hysteresis loops, and exchange bias between BiFeO₃ and several ferromagnetic materials has been reported,^{27, 284-286} see Figure 3.16 (a-b). Voltage control of an exchange biased ferromagnetic layer has been demonstrated.²⁷ A possible Magnetoelectric Random Access Memory (MERAM) element using BiFeO₃ is shown in Figure 3.16 (c). A voltage V controls the ferroelectric state of BiFeO₃, and given the strong coupling between the antiferromagnetic plane and ferroelectric polarisation, switching the ferroelectric polarisation by 71 or 109 ° can change the antiferromagnetic planes, and thereby flip the direction of the lower ferromagnetic (FM, blue) layer through exchange bias if the coupling is strong enough. In the FM-Metal-FM trilayer the alignment of the FM layers can thus be controlled to be parallel or antiparallel by the ferroelectric state of the green BiFeO₃ layer. Parallel FM layers give a lower resistance across the FM-Metal-FM trilayer, corresponding to the binary state “0”. Oppositely, antiparallel alignment of the FM layers give a higher resistance, corresponding to the binary state “1”, as in conventional read-out of bits utilising Giant Magnetoresistance.

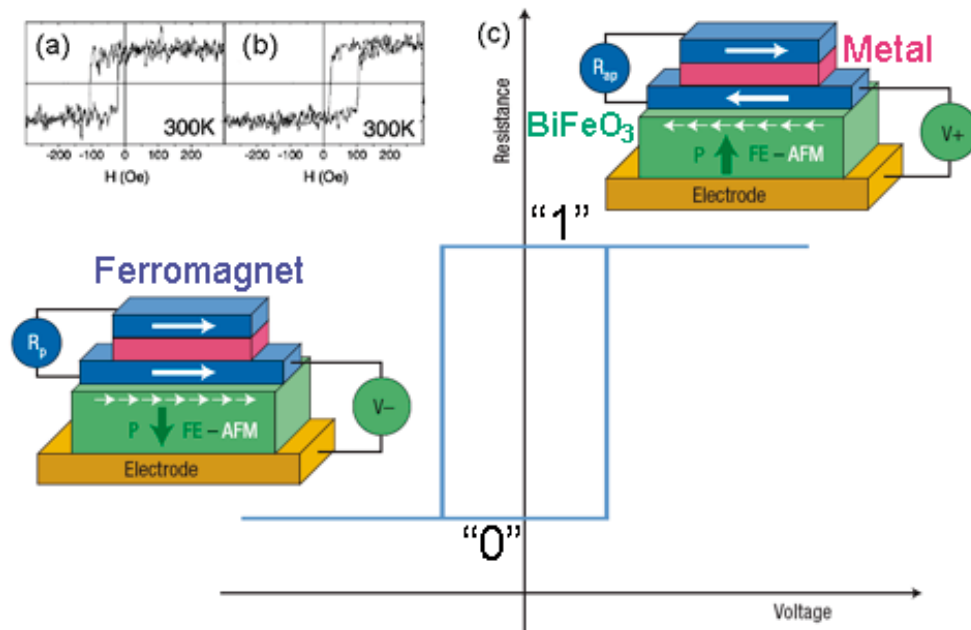


Figure 3.16. (a-b) Exchange biased magnetic hysteresis loops of ferromagnetic CoFeB (5 nm) grown on BiFeO₃ (35 nm) measured along opposite direction of ferroelectric polarisation in (a) and (b), adapted from reference²⁸⁴. (c) A concept for a MERAM element utilising BiFeO₃ (green FE-AFM layer, ferroelectric antiferromagnet). Modified from reference²⁶.

BiFeO₃ can also be used as a tunnelling barrier layer as it is ferroelectric down to 2 nm thickness.²⁸⁷ The ferroelectric state can control the direction of magnetisation in adjacent ferromagnetic layers, and thus the tunnelling magnetoresistance.^{32, 284} The direction of the polarisation can also directly control the tunnelling resistance, enabling non-destructive read-out of ferroelectric bits.^{28-30, 288} Four-state memories where both the polarisation and magnetisation can modulate the tunnelling resistance have been demonstrated.²³

3.4.2 Ferroelectricity and piezoelectricity

As BiFeO₃ is a lead-free, non-toxic ferroelectric with the highest switchable polarisation known among perovskites, it is a primary candidate for substituting PbZr_{1-x}Ti_xO₃ (PZT). It is possible to incorporate into Si and SiO₂ based circuitry, and can thus be used for FeRAM, which do not utilise the magnetic properties. Leakage currents must be controlled and minimised to utilise the ferroelectric polarisation, regardless of whether the magnetism is active as in MERAM or “passive” as in FeRAM concepts. Chemical compatibility, fatigue and voltage stressing are other challenges for BiFeO₃-based ferroelectric memories.⁴⁰

Pure BiFeO₃ has a too low piezoelectric coefficient to challenge PZT, but pulsed laser deposition (PLD) grown films of Bi_{1-x}Sm_xFeO₃ can exhibit a

piezoelectric coefficient d_{33} of > 100 pm/V at a morphotropic phase boundary, and are promising candidates for lead-free piezoelectrics.²⁸⁹⁻²⁹⁰

Emission of terahertz radiation from BiFeO₃ when illuminated with a femtosecond laser pulse is correlated with the ferroelectric state. THz emission has thus the potential of being a non-destructive and very fast way of reading ferroelectric bits. It has the further advantage that it is insensitive to leakage currents.²⁹¹⁻²⁹²

3.4.3 Optical properties

The optical bandgap of BiFeO₃ of 2.2-2.8 eV is interesting for applications utilising photoconductivity (sensors), the photovoltaic effect or the photocatalytic properties, and nanoparticles have been proposed as photocatalysts.²⁹³⁻³⁰⁰ Significant photoconductivity in BiFeO₃ thin films has been reported.¹⁵⁵ The semiconducting nature of BiFeO₃ can be exploited in diodes, which have been demonstrated to be sensitive to the ferroelectric state, as the direction of the diode can be flipped by switching the ferroelectric polarisation by an external electric field.¹⁵⁶ The diode effect is also associated with a photovoltaic current, with switchable direction determined by the ferroelectric state. Although BiFeO₃ is not likely to be applied as a conventional solar cell, it may be applied in future devices utilising not only ferroelectricity and magnetism, but also the optical and semiconducting properties.

4 Experimental

4.1 Synthesis

4.1.1 Wet chemical synthesis of nano-crystalline BiFeO₃

Wet chemical syntheses were performed with aqueous nitrate solutions as metal precursors. A bismuth nitrate precursor solution was prepared by dissolving Bi(NO₃)₃ · 5 H₂O (Fluka, >99%) in distilled water under addition of HNO₃ (Merck, 65%) to pH 1-2. An iron nitrate precursor solution was prepared by dissolving Fe(NO₃)₃ · 9 H₂O (Merck, >99%) in distilled water under addition of HNO₃ (Merck, 65%) to pH 0-1. The concentrations of metal cations in the nitrate solutions were determined by thermogravimetric analysis (TGA). The solutions were added to pre-heated porcelain crucibles and heat-treated for 24 h at 650 and 1000 °C for bismuth and iron nitrates, respectively. A low annealing temperature for the bismuth solution minimised the risk of loss of volatile bismuth oxide, and a low heating rate of 50 °C/h was used to avoid boiling.

A scheme of the synthesis route for BiFeO₃ is shown in Figure 4.1. Carboxylic acid (0.03 moles) was dissolved in distilled water (30 ml) in a pyrex beaker with a magnetic stirrer on a hot plate holding 50 °C. The carboxylic acids used were DL-tartaric acid (Acros Organics, 99.5%), DL-malic acid (Aldrich, 99%), succinic acid (Merck, >99%), maleic acid (Merck, >99%) and malonic acid (Fluka, 99%). The metal nitrate precursor solutions (0.015 moles of each) were weighed, mixed and then poured slowly into a beaker under stirring to ensure complexing of metal cations. All the solutions displayed a yellow to orange colour after addition of the nitrates, and turned darker upon further heating. Ethylene glycol (EG) (Acros Organics, >99.9%) in a molar ratio to the respective carboxylic acid of 1:1 was finally added to half of the syntheses as a polymerizing agent. Homogenous solutions were heated under stirring with the hot plate holding 150 °C. The solutions were finally transferred to crystallisation jars on the same hot plate to prepare a dry polymeric precursor. Polymeric precursors from syntheses with EG as a polymerising agent were more porous than those without. Typical examples of the physical appearance of polymeric precursors from syntheses with and without EG are shown in Figure 4.2, where malic acid was used as the complexing agent. After the precursor was completely dried, it was ground into a fine powder in an Agate mortar. Ground precursor powders were calcined in air with a heating rate of 400 °C/h, and kept for 2 h at different temperatures to obtain a series of different particle sizes.

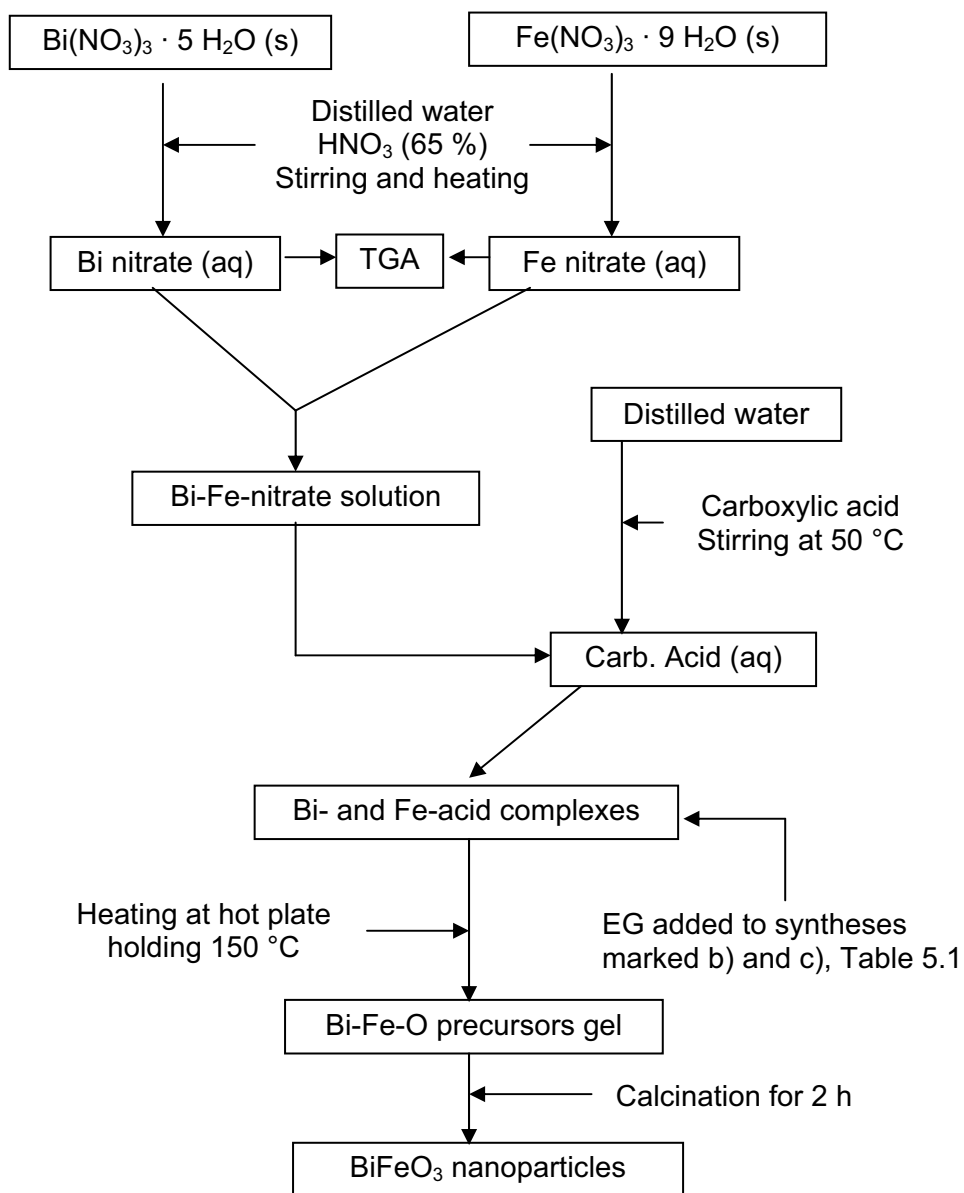


Figure 4.1. Scheme of wet chemical synthesis routes for BiFeO₃.

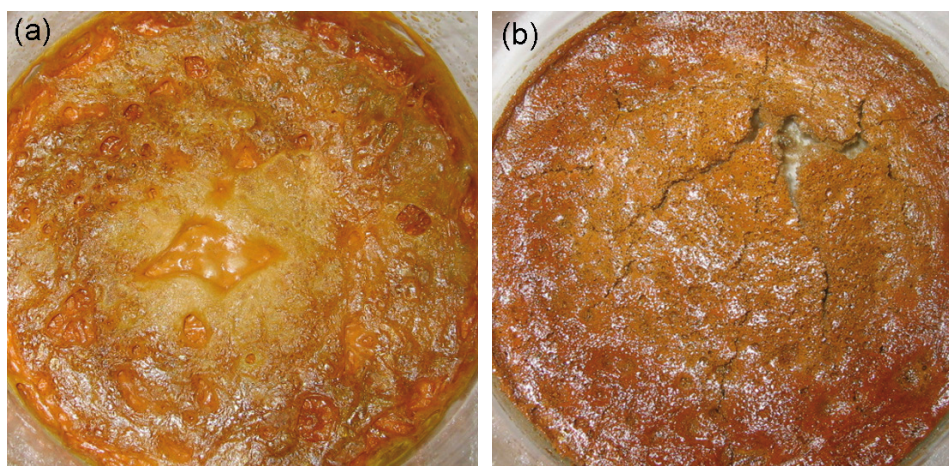


Figure 4.2. Photographs of polymeric precursor after drying on a hot plate at 150 °C, (a) malic acid and (b) malic acid and EG.

4.1.2 Synthesis of bulk materials by solid state reaction

Bulk BiFeO₃ powder was prepared by solid state reaction between Bi₂O₃ (Aldrich, >99.9%) and Fe₂O₃ (Merck, >99%). Precursor powders were dried for ~8 h at 600 °C and carefully weighed to control the nominal stoichiometry. The ideal starting point for solid state reaction synthesis is a homogenous mixture of small binary oxide particles. Several approaches to mix the binary oxides prior to firing were explored. The most successful with respect to time consumption, control of stoichiometry and reproducibility in terms of phase purity of the fired product was to mix the binary oxides in ethanol using an Agate mortar and a pestle. Ball milling in ethanol with yttria stabilised zirconia balls was less successful with respect to obtaining phase pure samples after firing. Ball milling inevitably introduces impurities to the system, which destabilise the perovskite phase (chapter 5). Complete separation of the milled powder from the zirconia balls also proved difficult, hindering control of the nominal stoichiometry.

Dried binary oxide mixtures were uniaxially cold-pressed with 20-40 MPa pressure into 5-20 mm diameter pellets of 1-10 mm thickness and placed on an alumina disk. Typical green densities were 55-60 % of the theoretical density. Pellets were covered in sacrificial powder to avoid evaporation of bismuth oxides (Bi₂O₃ and BiO). Test samples fired without sacrificial powder did however not show signs of loss of bismuth oxide. Sacrificial powder between the pellet and the alumina disk during firing is however imperative due to the chemical incompatibility of BiFeO₃ to Al₂O₃ (chapter 5). Considerable deviation from a Bi:Fe ratio of 1:1 is not in concordance with recent phase diagrams of the system Bi₂O₃-Fe₂O₃, showing that there is negligible intrinsic solid solubility in BiFeO₃.^{159, 301-302} This was confirmed by a series of BiFeO₃ samples with intentional deviation from a Bi:Fe ratio 1:1. These samples contained the expected secondary phases Bi₂Fe₄O₉ and Bi₂₅FeO₃₉ due to non-stoichiometry and no variation in lattice

parameters of BiFeO₃ with nominal composition was observed. A nominal Bi:Fe ratio close to unity was thus inferred for phase pure materials.

All samples were fired in air. The firing temperature is important, and discussed further in chapter 5. Empirically it was found that 825 °C was the minimum firing temperature necessary to obtain phase pure BiFeO₃, and 8 h was chosen as the soaking time. A heating and cooling rate of 400 °C/h was initially used. After the thermodynamics of the phase formation (chapter 5) was investigated, the chosen synthesis route was heating by 400 °C/h to 900 °C followed by quenching the sample in air after 5-10 min soaking time. No differences in the structural parameters of BiFeO₃ fired at 825 and 900 °C were found. Repeated firing with intermediate grinding between did not yield less secondary phases than after the first firing.

BiFeO₃ substituted with Mn were prepared by solid state reaction with Mn₂O₃, Fe₂O₃ and Bi₂O₃. Mn₂O₃ was prepared by calcining Mn(CH₃COO)₂·4H₂O (Riedel-de-Haën, >99.5%) at 700 °C for 8 h in air. The resulting Mn₂O₃ powder was phase pure within the detection limits of XRD. Mn-substituted samples were fired at different temperatures to obtain a variation in the oxygen stoichiometry, as described in chapter 7.

La-substituted BiFeO₃ samples were obtained from Bi₂O₃, Fe₂O₃ and La₂O₃ (Merck, >99%). La₂O₃ was dried overnight at 900 °C before weighing. Bi_{1-x}La_xFeO₃ samples with $x \leq 0.1$ were fired once for 10 min at 900 °C. Samples with $x > 0.1$ were fired once for 10 min at 900 °C and once for 10 min at 950 °C after intermediate grinding. The second firing did not change neither the phase composition nor the lattice parameters.

Substitution with Al, Ga, Cr and Co was attempted using Al₂O₃ (Merck, >99%), Ga₂O₃ (Aldrich, >99.99%), Cr₂O₃ (Merck, >99%) and Co₃O₄ (Aldrich, >99%), respectively. The samples were initially fired once for 8 h at 825 °C. Subsequent firing for 12 and 24 h at 825 °C with intermediate grinding did not substantially change the phase composition inferred from XRD patterns.

Solid state reaction synthesis of phase pure BiFeO₃-based materials is difficult, and with poor reproducibility, due to the sensitivity towards impurities, local and nominal off-stoichiometry and the intermediate temperature region of metastability described in chapter 5.

4.2 Characterisation

4.2.1 X-ray diffraction

X-ray diffraction (XRD) at ambient temperature was performed with two different instruments with Cu K α radiation in Bragg-Brentano geometry. A θ - θ Bruker AXS D8 ADVANCE diffractometer with a VANTEC-1 position sensitive detector (PDS) and a secondary monochromator was used for collecting XRD patterns of nanoparticles (Figure 5.2 and 9.1). Data were collected from 20 to 90 $^{\circ}2\theta$ with a step size of 0.016 $^{\circ}2\theta$, 1.2 sec. per step (total data collection time 1 h 29 min per sample) and 1 $^{\circ}$ fixed divergence slit. A θ - 2θ Bruker AXS D8 FOCUS diffractometer with a LynxEye PSD was used to collect XRD patterns of bulk materials (Figures 5.9, 5.11, 5.13, 7.1 and 8.1) at ambient temperature. Data were collected from 20 to 96 $^{\circ}2\theta$ with a step size of 0.014 $^{\circ}2\theta$, 3 sec. per step (total data collection time 4 h 41 min per sample) and 0.2 $^{\circ}$ fixed divergence slit. Samples with $x_{\text{Mn}} = 0.3$ (Figure 7.1) and $x_{\text{La}} = 0.1, 0.125$ and 0.25 (Figure 8.1) were measured with 10 sec. per step (total data collection time 15 h per sample).

4.2.2 High temperature XRD

High temperature XRD (HTXRD) was primarily performed with the Bruker D8 ADVANCE instrument described in 4.2.1. A high temperature stage from mri Physikalische Geräte GmbH was used. A circular alumina crucible supported the sample in a cavity with $\varnothing = 12$ mm and depth = 1 mm. Heat was provided by a platinum-rhodium heating mantle encapsulating the alumina crucible and the temperature was monitored by an S-type thermocouple placed in contact with the alumina crucible between the crucible and the heating mantle. Temperature calibration was performed with MgO and the estimated uncertainty in absolute temperature is ± 15 $^{\circ}\text{C}$.

Preliminary HTXRD patterns of BiFeO₃ in Figure 5.12 (a) were collected in air from 20 to 120 $^{\circ}2\theta$ with a step size of 0.016 $^{\circ}2\theta$, 3 sec. per step (total data collection time 5 h 15 min per temperature) and 0.2 $^{\circ}$ fixed divergence slit. The powder sample was held for 30 min at each temperature prior to data collection to ensure thermal equilibrium.

HTXRD patterns of a polished polycrystalline BiFeO₃ disk in Figure 6.2 and powder in Figure 6.8, respectively, were collected in air from 20 to 96 $^{\circ}2\theta$ with a step size of 0.016 $^{\circ}2\theta$, 3 sec. per step (total data collection time 4 h 2 min per temperature) and 0.2 $^{\circ}$ fixed divergence slit. The sample was held for 30 min at each temperature prior to data collection to ensure thermal equilibrium.

HTXRD patterns of BiFeO₃ powder in Figures 6.9 and 6.10 were collected in O₂ atmosphere from 20 to 96 $^{\circ}2\theta$ with a step size of 0.016 $^{\circ}2\theta$, 1.5 sec. per step (total data collection time 2 h 1 min per temperature) and V6 variable divergence slit. The powder was held for 15 min at each temperature prior to data collection to ensure thermal equilibrium.

HTXRD patterns of the $\text{BiFe}_{0.7}\text{Mn}_{0.3}\text{O}_3$ powder in Figure 7.3 were collected in air from 18 to 60 $^\circ 2\theta$ with a step size of 0.016 $^\circ 2\theta$, 1.6 sec. per step (total data collection time 1 h 13 min per temperature) and 0.1 $^\circ$ fixed divergence slit. The powder was held for 10 min at each temperature prior to data collection to ensure thermal equilibrium.

HTXRD patterns of $\text{Bi}_{0.9}\text{La}_{0.1}\text{FeO}_3$ and $\text{Bi}_{0.75}\text{La}_{0.25}\text{FeO}_3$ powders in Figures 8.2 and 8.3, respectively, were collected in air from 20 to 96 $^\circ 2\theta$ with a step size of 0.016 $^\circ 2\theta$, 1 sec. per step (total data collection time 1 h 16 min per temperature) and V6 variable divergence slit. The sample was held for 5 min at each temperature prior to data collection to ensure thermal equilibrium.

Preliminary HTXRD data of $\text{BiFe}_{0.7}\text{Mn}_{0.3}\text{O}_3$ (Figure 5.12 (b)) were collected with a Siemens D5005 θ - θ diffractometer with a high temperature camera (HTK 16, Anton Paar, GmbH) using Cu $K\alpha$ radiation and a primary monochromator. The powder sample was dispersed in ethanol and applied to a platinum strip used for heating. The temperature was monitored with an S-type thermocouple welded to the platinum strip and the measurement was done in air atmosphere. For each temperature, the data collection time was 5.1 h over the range 19 to 96 $^\circ 2\theta$. Prior to each subsequent scan the powder samples were held for 30 min at the temperature to establish thermal equilibrium.

4.2.3 Rietveld refinements

All Rietveld³⁰³ refinements were carried out using the software TOPAS R (Bruker AXS) version 2.1. The background intensity was accounted for using a Chebychev polynomial of the minimum order to account for the curvature. Sample displacements were refined, while zero errors were fixed. Peak shapes were refined using the peak profile functions Pearson VII or Thompson-Cox-Hastings modified pseudo-Voigt.³⁰⁴ The peak profile function giving the best fit to the experimentally observed data was chosen and kept for all patterns within a series of patterns with varying composition, temperature or crystallite size.

Refinements of diffraction patterns within the space group no. 161 ($R3c$) were done in the hexagonal setting with the unit cell anchored in $z_0 = 1/12$, space group no. 62 in the $Pbnm$ setting, and space group no. 221 ($Pm\bar{3}m$) with the A cation in *origo*. Further details of the space groups used are given in the following chapters.

Lattice parameters, background, displacement and peak profile parameters were allowed to converge before atomic positions were added to the refinement. Systematically, the position parameters of the heaviest atom in the unit cell were refined to convergence before subsequently adding lighter atoms to the refinement. Isotropic thermal displacement parameters were added to the refinement after convergence of atomic positions, and finally anisotropic thermal displacement parameters.

For the La-substituted two-phase samples described in chapter 8 the La occupancy of the A site was initially inferred from mass balance requirements. La occupancies of the $R3c$ and $Pbnm$ phases were subsequently added to the refinement after convergence of the thermal displacement parameters. Attempts to

refine the B site occupancy of oxygen hyperstoichiometric samples in chapter 7 were unsuccessful.

4.2.4 Atomic pair distribution functions (PDF)

Atomic pair distribution functions (PDF) for BiFeO₃ nanoparticles (Figure 9.11) were obtained from synchrotron XRD patterns collected at the 11-ID-C beamline at Argonne National Laboratory, IL, USA. X-rays with an energy of 115.232 keV ($\lambda = 0.1076 \text{ \AA}$) were used and patterns were collected in transmission geometry using a large area detector (General Electric). The patterns were corrected for background intensity and Fourier transformed to real space PDFs. A recent review by Petkov describes the fundamentals of this method.³⁰⁵

4.2.5 Determination of nanoparticle size

Crystallite sizes of nanoparticles (chapter 9) were determined using the Scherrer³⁰⁶ equation:

$$d_{\text{XRD}} = \frac{K\lambda}{\beta \cos \theta} \quad (4.1)$$

The factor K was set to 1.0, the radiation wavelength $\lambda = 1.5418 \text{ \AA}$, the Full Width at Half Maximum (FWHM) of the Bragg reflection is depicted by β and θ is the angle of the chosen Bragg reflection. FWHM values were obtained using the EVA software (Bruker AXS). The (024) reflection (hexagonal setting, (111) with pseudocubic indices) at approximately $45^\circ 2\theta$ was chosen due to the high relative intensity and absence of adjacent reflections. The FWHM, β , was corrected for instrumental broadening with a Cauchy profile (linear subtraction) using a diffraction pattern of a NIST Standard Reference Material® 660a LaB₆ powder recorded with identical X-ray optics.

Surface area was measured by nitrogen adsorption using the five-point BET isotherm (Micromeritics Tristar Surface Area and Porosity Analyzer and a Micromeritics VacPrep 061 Sample Degas System). The particle size, d_{BET} , was calculated from the measured surface area using the relation

$$d_{\text{BET}} = \frac{6}{\rho_{\text{cryst}} \cdot A_{\text{BET}}} \quad (4.2)$$

where ρ_{cryst} is the crystallographic density of BiFeO₃ (8.34 g cm^{-3}) and A_{BET} is the surface area according to the BET isotherm.³⁰⁷

Transmission electron microscopy (TEM) was performed using a JEM 2100 microscope with a point to point resolution of 0.23 nm. The microscope was equipped with an energy dispersive X-ray spectroscopic (EDS) detector, operated at an accelerating voltage of 200 kV. The powder samples investigated were ball

milled for 1 h in ethanol before the powder was retrieved on a holey carbon grid for high resolution TEM observations.

4.2.6 Thermogravimetry

Thermogravimetry (TGA) to determine the oxygen nonstoichiometry, δ in $\text{BiFe}_{1-x}\text{Mn}_x\text{O}_{3+\delta}$ (chapter 7) was performed for each sample on three parallels of fine-crushed powders by annealing for 30 min at 850 °C in flowing 5.0 N₂ to reduce manganese to +III. The samples were cooled at 200 °C/h to ambient temperature in N₂ atmosphere. It is assumed that the content of Mn⁴⁺ is negligible at this condition, corresponding to $\delta = 0$. One test series with non-substituted BiFeO₃ samples verified that weight loss was due to reduction of the Mn⁴⁺ and not evaporation of Bi₂O₃.

TGA of polymeric precursor gels (chapter 5) was performed with a Netzsch STA 449 C *Jupiter* in synthetic air using a heating rate of 10 °C/min up to 600 °C. TGA during *in situ* coarsening of nanoparticles (chapter 9) was in done synthetic air on two powder samples heat treated for 2 h at 425 and 500 °C, with initial crystallite sizes of 13.3 ± 1 and 20.4 ± 2 nm, respectively. The samples were heated to 400 °C with a rate of 10 °C min⁻¹ and held for 8 h to remove adsorbed water, and further heated to 600 °C at the same rate and held for 8 h to measure mass loss/gain due to reduction/oxidation during crystallite growth.

4.2.7 Thermal analysis

Differential scanning calorimetry (DSC) was performed with a Perkin Elmer DSC 7, PE Thermal Analysis Controller TAC 7/DX and Pyris v. 3.81 software. Samples of 20-100 mg were encapsulated in aluminium sample pans and the measurements were done in air with 40 or 10 °C/min heating and cooling rates in the temperature region 25-550 °C. Néel temperatures were determined as the temperatures of the maximum value of the calorimetric peaks.

Differential thermal analysis (DTA) was done with a Netzsch STA 449 C *Jupiter* in synthetic air, 5.0 N₂ and 5.0 O₂ atmospheres, with heating and cooling rates of 10-50 °C/min, 10 °C/min rates were applied unless otherwise stated. Alumina crucibles were used. First order phase transitions were determined as the onsets of the thermal events.

Dilatometric traces were recorded in synthetic air or 5.0 O₂ (chapter 6) atmospheres with a Netzsch DIL 402 C dilatometer, using a heating rate of 2-5 °C/min heating and cooling rates. The fastest heating rate and O₂ atmosphere was used for measurements in the vicinity of the peritectic decomposition temperature.

4.2.8 Electrical conductivity

Electrical conductivity measurements were performed on dense, polycrystalline ceramic bars (>93 % of crystallographic density) prepared by solid state reaction method. Bars polished with SiC paper to a cross sectional area of 0.15-0.2 cm² were attached to platinum wires with platinum paint. A home-built stage for conductivity measurements with controlled atmosphere and temperature was used, as illustrated in Figure 4.3.

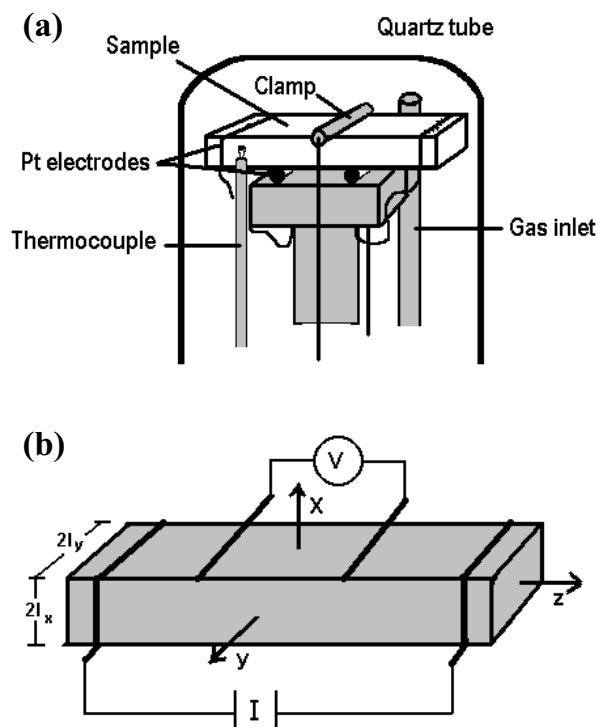


Figure 4.3. (a) The experimental set-up for electrical conductivity measurements. (b) The orientation of the sample and a visual guide to where the electrodes are attached. Adapted from Wærnhus³⁰⁸

An S-type thermocouple calibrated against the melting temperature of gold adjacent to the sample bar was used for monitoring the sample temperature. The 4-point method allows the current I and the voltage V to be individually measured (Keithley D500) with two wires passing a current through the sample and two wires $d = 5$ mm apart measuring the voltage drop across the sample. The conductivity was calculated from:

$$\sigma = \frac{Id}{VA} \quad (4.3)$$

where A is the cross sectional area normal to the current. An Al_2O_3 clamp secured the sample onto the Al_2O_3 stage. The sample and stage was placed inside a sealed quartz tube and heated under controlled atmosphere, using synthetic air, 5.0 N_2 or 5.0 O_2 with a low flow rate of 5 ml/min to minimise evaporation from the sample. Heating and cooling rates used were 3 or 5 $^\circ\text{C}/\text{min}$, the latter for measurements in the vicinity of the peritectic decomposition temperature.

4.2.9 Vibrating Sample Magnetometry

Vibrating sample magnetometry (VSM) was done with a Quantum Design MPMS SQUID VSM dc Magnetometer from 300 to 700 K, collecting data every 0.2 K, using a 50 Oe magnetic field. The polycrystalline sample pellet was supported by copper foil.

5 Synthesis and stability

5.1 Introduction

The pseudo-binary phase diagram^{159, 301-302} of the system $\text{Bi}_2\text{O}_3\text{-Fe}_2\text{O}_3$ in Figure 5.1 contains three ternary phases at room temperature; sillenite with composition $\text{Bi}_{25}\text{FeO}_{39}$, the perovskite BiFeO_3 and mullite with composition $\text{Bi}_2\text{Fe}_4\text{O}_9$. The formation of the sillenite and mullite phases is a challenge during ceramic and chemical synthesis routes to obtain BiFeO_3 , and is the first main topic of this chapter.

According to the phase diagram, BiFeO_3 is a stable compound up to the peritectic decomposition temperature of 930-934 °C, where BiFeO_3 melts incongruently (Figure 5.1). In contrast with the phase diagram, which per definition depicts the equilibrium thermodynamic properties, BiFeO_3 has frequently been claimed to be metastable at high temperatures, above 750-830 °C.^{40, 309-310} This obvious contradiction deserves further attention, and it is the second main topic of this chapter.

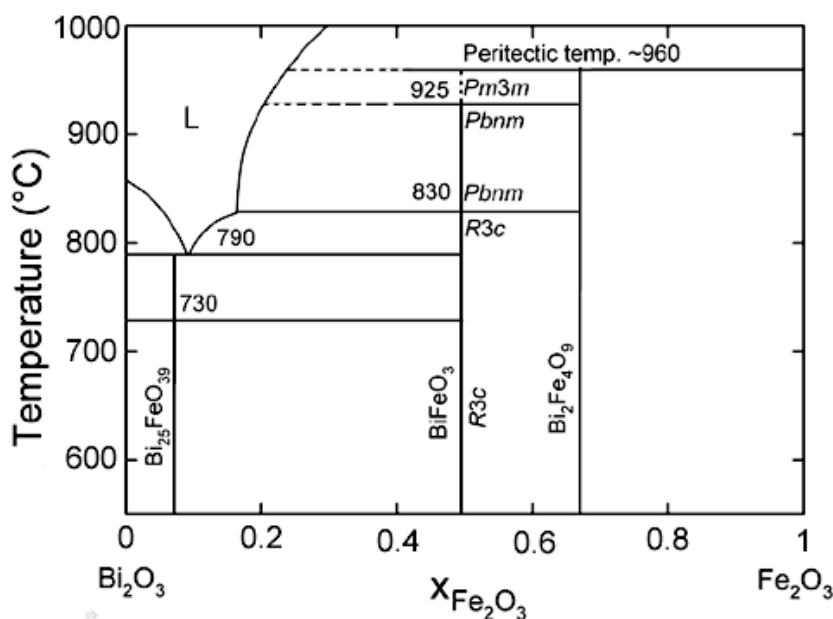


Figure 5.1. Binary phase diagram of the system $\text{Bi}_2\text{O}_3\text{-Fe}_2\text{O}_3$, based on references 159, 301-302, 311

Solid state reaction between Bi_2O_3 (s) and Fe_2O_3 (s) at high temperature is in principle the simplest way to prepare BiFeO_3 . In practice it has however proven challenging to avoid formation of the other two ternary phases in the $\text{Bi}_2\text{O}_3\text{-Fe}_2\text{O}_3$ system. An early approach applied by Achenbach *et al.* was to use a 100 % excess of Bi_2O_3 to suppress formation of $\text{Bi}_2\text{Fe}_4\text{O}_9$ during firing, with subsequent multiple leaching steps with diluted HNO_3 to dissolve the remaining $\text{Bi}_{25}\text{FeO}_{39}$ in order to obtain phase pure BiFeO_3 .³¹² A more recent approach is the "rapid liquid phase

sintering” method.³¹³ This method involves rapid heating and firing for 7.5 min of a stoichiometric Bi₂O₃-Fe₂O₃ mixture at 880 °C, which is above the melting temperature of Bi₂O₃ (~790 °C).³¹⁴ A major advance for the understanding of the solid state reaction synthesis of BiFeO₃ was obtained through a systematic study of the influence of impurities by Valant *et al.*³¹⁴ The presence of the impurities Al₂O₃ or SiO₂, which are more soluble in Bi₂₅FeO₃₉ or Bi₂Fe₄O₉ than BiFeO₃, reduces the stability of BiFeO₃.

Soft chemistry synthesis methods have the great advantage over the solid state reaction method that the precursor solution, gel or polymer precursor is homogenous on an atomic scale prior to crystallisation, in contrast with a heterogeneous mixture of Bi₂O₃ and Fe₂O₃. The most elegant way to obtain phase pure BiFeO₃ would be decomposition and crystallisation of a bimetallic organic molecule, e.g. an alkoxide.³¹⁵ Hydrothermal crystallisation^{295, 316-322}, molten salt synthesis³²³ and α -alanine-nitrate combustion routes³²⁴⁻³²⁵ to prepare BiFeO₃ have been reported. Combustion routes have the possible disadvantage of Bi vapourisation due to high local temperatures. Several polymer precursor routes, based on modifications of the Pechini method,³²⁶ have been developed since the first report by Ghosh *et al.*³²⁷⁻³³¹

Other routes to obtain phase pure BiFeO₃ are single crystal growth³³²⁻³³³ and various methods to prepare thin films like pulsed laser deposition (PLD),¹¹² metal-organic chemical vapour deposition (MOCVD),³³⁴ molecular beam epitaxy (MBE)³³⁵⁻³³⁶ sputtering,³³⁷ chemical solution deposition (CSD)^{315, 338} and liquid phase epitaxy (LPE).³³⁹ The stability range of BiFeO₃ in terms of pO_2 and substrate temperature has been studied with respect to MBE and PLD of thin films.^{157, 340-341}

5.2 Wet chemical synthesis

A systematic investigation of the effect of temperature, type of carboxylic acids to complex Bi³⁺ and Fe³⁺ cations and ethylene glycol (EG) on the formation of BiFeO₃ by wet chemical method was performed. The synthesis route is described in detail in chapter 4.1.1.

5.2.1 Results

An overview of syntheses and products identified by XRD after annealing at 600 °C is presented in Table 5.1, X indicates presence of a phase, while (X) indicates that only trace amounts of the phase were present in the XRD patterns, which were compared with JCPDS Card No. 86-1518 (BiFeO₃), 72-1832 (Bi₂Fe₄O₉) and 46-0416 (Bi₂₅FeO₃₉).[§] Syntheses 1 c), 2 a), 2 b) and 4 b) are new wet chemical routes yielding phase pure BiFeO₃, synthesis 1 a) was reproduced after Ghosh *et al.*³²⁷ for comparison.

[§]JCPDS Card No. 46-0416 denotes Bi₂₅FeO₄₀, with 24 Bi³⁺ and one Bi⁵⁺, introducing a new chemical degree of freedom. The formula Bi₂₅FeO₃₉ implies that all Bi is present as Bi³⁺, thus this formula is used here.

Table 5.1. Syntheses and product phases identified by XRD after annealing of the polymeric precursor at 600 °C for 2 h.

Synth.	CA	EG	BiFeO ₃	Bi ₂ Fe ₄ O ₉	Bi ₂₅ FeO ₃₉	Unknown
1 a)	Tartaric	-	X	(X) ^a		
1 b)	Tartaric	EG	X	X		
1 c)	Tartaric	EG	X			
2 a)	Malic	-	X			
2 b)	Malic	EG	X			
3 a)	Succinic	-	X	X	X	
3 b)	Succinic	EG	X	(X)	(X)	
4 a)	Maleic	-	X	X	X	X
4 b)	Maleic	EG	X			
5 a)	Malonic	-	X		X	X
5 b)	Malonic	EG	X	(X)	(X)	

^aPrecipitation of white crystals, possibly Bi(NO₃)₃, on the walls of the beaker at the liquid-air interface was observed during evaporation of the solution, and may explain the trace amounts of Bi₂Fe₄O₉ after calcination.

All the carboxylic acids in Table 5.1 complexed the metal cations, as no precipitates were observed during evaporation. The syntheses yielding phase pure BiFeO₃, displayed more porous precursor after drying than those who resulted in multiphase samples. The original Pechini method³²⁶ with citric acid and EG was also tested, but did not yield BiFeO₃ (not shown). Syntheses with EG as a polymeriser produced more porous polymeric precursor powder than those without. Powders from syntheses 1 a), 1 c), 2 b), 3 a) and 5 a) displayed completely amorphous XRD patterns before calcination, while XRD of the other as-prepared powders showed various weak unidentified Bragg reflections. All the weak reflections disappeared upon heat treatment, as the polymeric precursor decomposes. Apparently, there is no relation between the crystallinity of the as-prepared powder and the phase composition of the final calcined powder. The solution with tartaric acid in synthesis 1 a) wetted the surface of the beaker and white crystals precipitated on the walls of the beaker during evaporation of the solution. Synthesis 1 b) with tartaric acid and EG ignited during TGA at 210 °C, and probably also during calcination. The powder from the identical synthesis 1 c) was hence subjected to intermediate 2 h calcinations at 200 °C and subsequently 250 °C to avoid ignition. In synthesis 4 a) using maleic acid, the precursor gel ignited during drying on the hot plate.

XRD patterns of as-prepared powders and powders after calcinations at various temperatures from synthesis 2 a) with malic acid and synthesis 4 b) with maleic acid and EG are shown in Figure 5.2 (a) and (b), respectively. An XRD pattern of phase pure bulk materials is included in Figure 5.2 (a) as a reference. XRD patterns of powders calcined at 600 °C from the other syntheses are shown in Figure 5.2 (c). Crystallisation and crystallite growth of BiFeO₃ was evidenced by the XRD patterns recorded with increasing calcination temperature (Figure 5.2). The crystallisation rate or temperature shows minor variations for the different syntheses. For synthesis 2 a) the powder is amorphous after calcination at 400 °C, while for synthesis 4 b) the powder is partly crystallised.

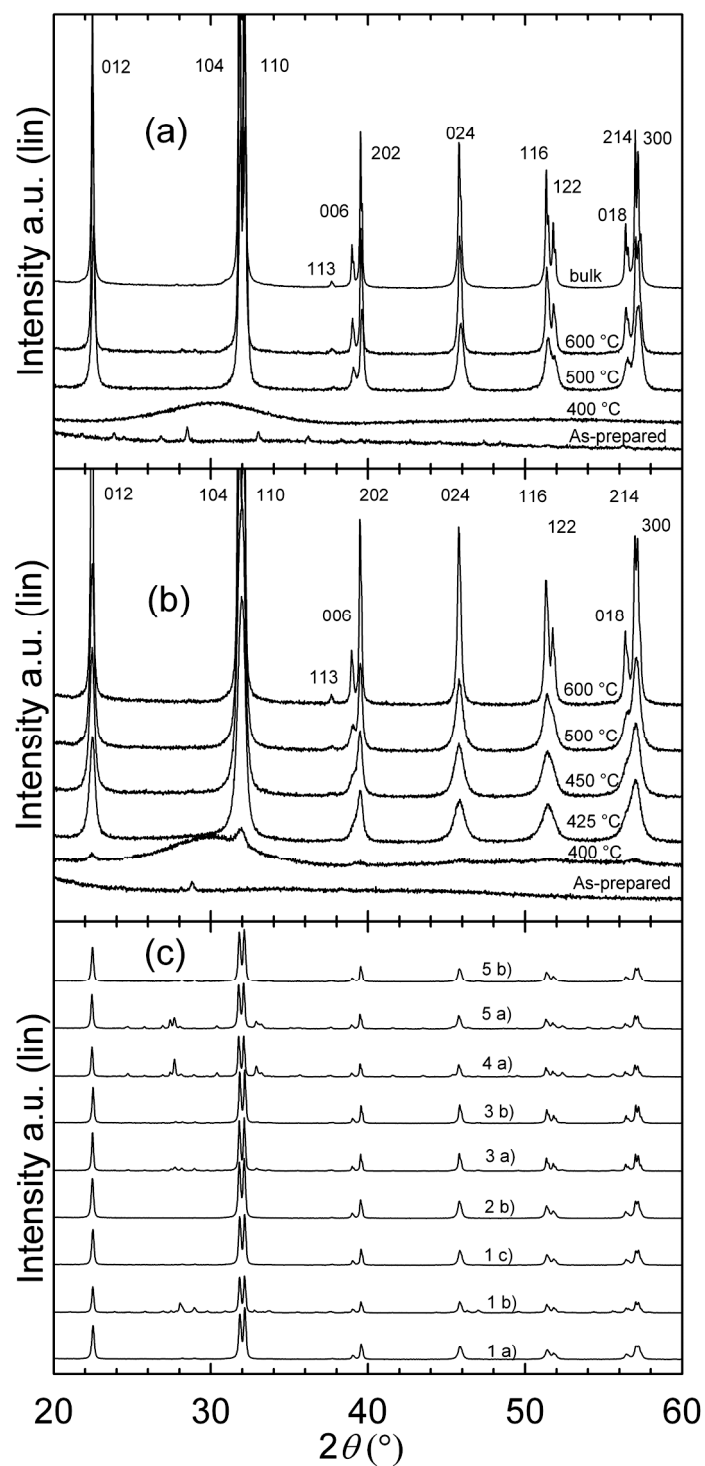


Figure 5.2. XRD patterns of powders from (a) syntheses 2 a) and (b) syntheses 4 b), respectively, labels refer to calcination temperatures (2 h). (c) All syntheses but 2 a) and 4 b) after calcination at 600 °C for 2 h.

TGA of the powder from synthesis 4 b) demonstrate that the precursor powder is completely decomposed at 450 °C when heated with 10 °C/min, see Figure 5.3. Precursor powders from the other syntheses do not differ significantly, except the powder from synthesis 1 b) which was shown to ignite at approximately 200 °C, indicated by the drop in the mass accompanied by a sharp exothermic peak. The low weight loss above 400 °C was also confirmed in separate subsequent calcinations at 400, 500 and 600 °C.

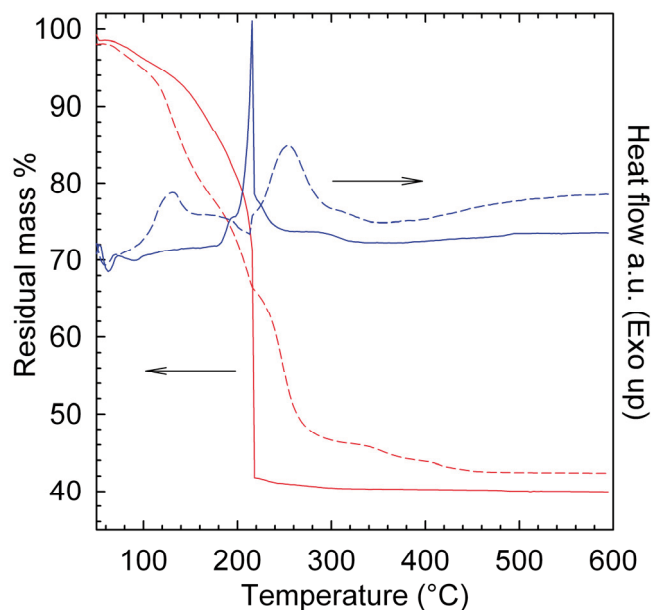


Figure 5.3. Thermogravimetical analysis (TGA) and DTA traces (heat flow) of powders from syntheses 1 b) and 4 b), depicted by solid and dashed lines, respectively.

Powder from synthesis 2 b) precalcined for 2 h at 400 °C was completely amorphous by XRD analysis, and negligible weight loss after further calcinations at higher temperatures, indicated that negligible amounts of organic residuals were present in the amorphous oxide. Crystallisation of the amorphous powder was observed by DSC (Figure 5.4). Two separated exothermic peaks are evident, and the peaks are shifted to higher temperatures with increasing heating rate. As discussed later these peaks correspond to nucleation and growth of crystallites.

The ordering temperature, T_N , for the antiferromagnetic to paramagnetic second order phase transition was determined from the maximum of the endothermic peaks by numerical differentiation of DSC traces, Figure 5.5. The obtained value of 372 ± 1.5 °C is in accordance with previous reports.¹⁰²

Mean crystallite sizes estimated from XRD data of phase pure samples are shown in Figure 5.6. Particle sizes calculated from surface area for powders from synthesis 4 b) are included for comparison. An increase in crystallite size with increasing calcination temperature is evident. Comparing d_{XRD} with d_{BET} , the increasing difference with increasing calcination temperature is attributed to an

increased degree of agglomeration. The TEM micrograph in Figure 5.7 shows a typical agglomerate and a single nanocrystallite in the inset. Lattice parameters refined by the Rietveld method are given in Table 5.2, the values were in accordance with literature values for bulk BiFeO_3 .¹⁰¹

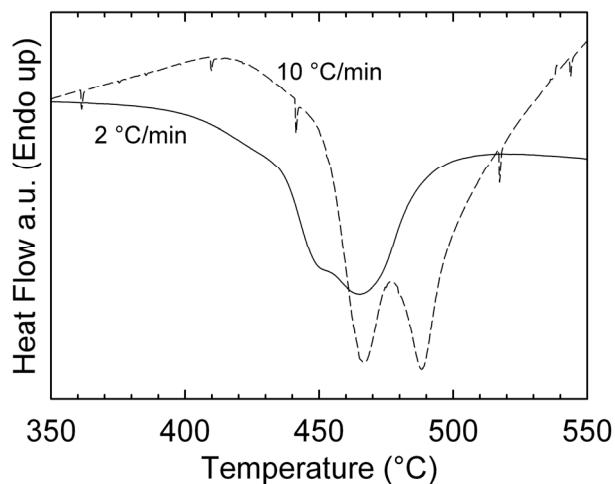


Figure 5.4. Crystallisation of amorphous powder observed by DSC. Minor peaks due to noise are present.

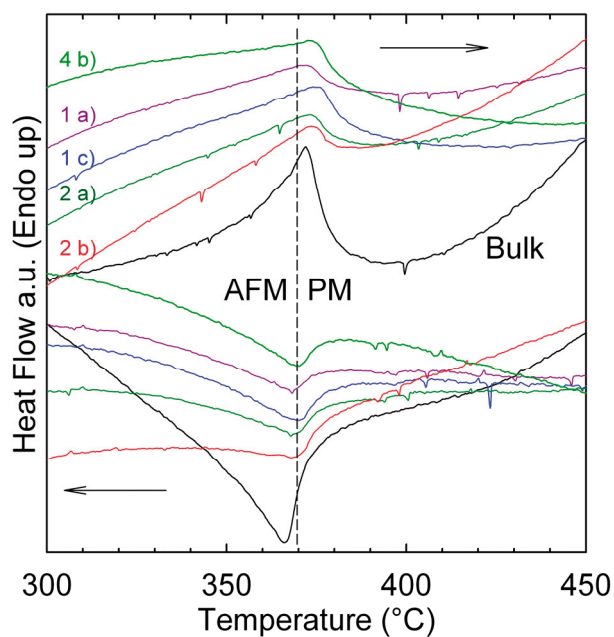


Figure 5.5. DSC traces of powders calcined for 2 h at 600 °C (labels refer to syntheses in Table 1) and from solid state method (bulk). The vertical dotted line is a guide to the eye, separating the antiferromagnetic (AFM) and paramagnetic (PM) region.

Table 5.2. Refined lattice parameters for powders from synthesis 4 b) and the solid state method.

Sample	a (Å)	c (Å)	R_{wp}
Single crystal data, ref. ¹⁰¹	5.57874	13.8688	
Bulk powder from SSM	5.578(5)	13.868(5)	7.06
4 b), $d_{XRD} = 70$ nm.	5.578(9)	13.866(9)	4.43

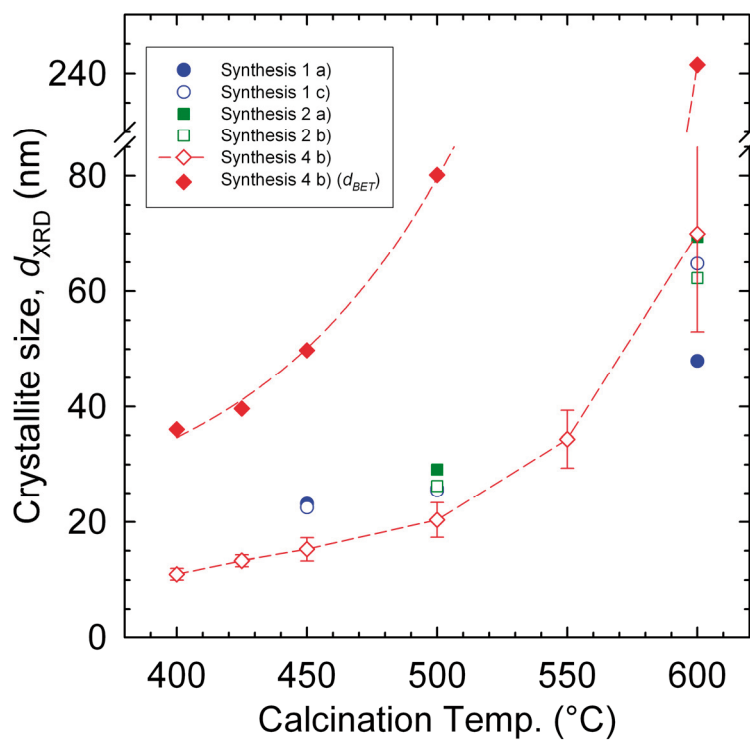


Figure 5.6. Crystallite sizes (XRD) for different calcination temperatures (2 h soaking time) for powders prepared by wet chemical syntheses, labels refer to Table 5.1. Typical error estimates for the crystallite sizes from synthesis 4 b) are shown. One series with particle sizes measured by nitrogen adsorption (d_{BET}), from synthesis 4 b), is also shown.

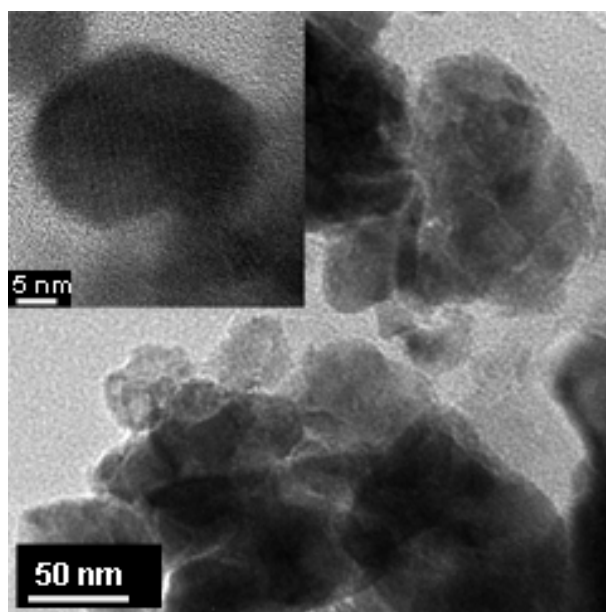


Figure 5.7. Transmission electron micrograph of BiFeO₃ powder calcined for 2 h at 450 °C, showing nanocrystallites in agglomerates. Inset shows dimensions and morphology of a typical individual nanocrystallite.

5.2.2 Discussion

Four new aqueous metal nitrate based routes for preparation of phase pure BiFeO₃ have been demonstrated by syntheses 1 c), 2 a), 2 b) and 4 b) in Table 5.1. Lattice parameters and Néel temperatures of the powders calcined for 2 h at 600 °C show that these materials display bulk properties. The syntheses without EG were successful for tartaric and malic acid, but not for neither succinic, maleic nor malonic acid. The structure of the organic molecules used in the syntheses are shown in Figure 5.8. A requirement for the formation of a homogenous polyester precursor without segregation of cations is thus proposed to be COOH-groups for complexing of Bi³⁺ and Fe³⁺, and OH-groups for polyesterification with COOH-groups. Bi³⁺ has been reported to form nine-coordinated complexes with tartaric and maleic acid.³⁴² The addition of equimolar amounts of EG with respect to the carboxylic acids also caused the synthesis with maleic acid to yield phase pure BiFeO₃. The syntheses with succinic and malonic acid without EG were not successful. Succinic and malonic acid lack OH-groups on the main branch, which also only contains single bonds, allowing the COOH-groups to rotate independently, while maleic acid displays a double bond between the carbon atoms in the main branch, fixing the relative orientations of the COOH-groups as *cis*. A rigid 3D network can form by polymerisation of OH-groups, on either EG or the main branch of the carboxylic acid molecule, and COOH-groups. The influence of impurities and temperature is discussed separately in chapter 5.3.

Precursor powder from synthesis 1 b) with equimolar amounts of tartaric acid and ethylene glycol ignited during calcination, while synthesis 2 b) and 4 b)

with tartaric acid substituted by malic and maleic acid, respectively, did not. The ratio of fuel (carboxylic acids and EG) to oxidisers (NO_3 -groups) may determine a critical heating rate for ignition. We propose that Fe^{3+} may catalyse the ignition. Detection of the iron rich phase $\text{Bi}_2\text{Fe}_4\text{O}_9$, but not $\text{Bi}_{25}\text{FeO}_{39}$, in the XRD pattern from synthesis 1 b) is attributed to high local temperatures and evaporation of volatile Bi_2O_3 . The two exothermic events during heating (Figure 5.4), and the diffractogram of the powder from synthesis 4 b) calcined at $400\text{ }^\circ\text{C}$ (Figure 5.2 (b)), suggests that the amorphous BiFeO_3 goes through a nucleation and growth process to form crystalline BiFeO_3 . The shift towards higher temperatures with higher heating rate signifies that the events are thermally activated. Crystallite growth is also evident from XRD and BET (Figure 5.2 and 5.6) in the same temperature region as the second peak in the DSC curves. The present findings show that nano-crystalline BiFeO_3 can be obtained below approximately $450\text{ }^\circ\text{C}$ by the present wet chemical route.

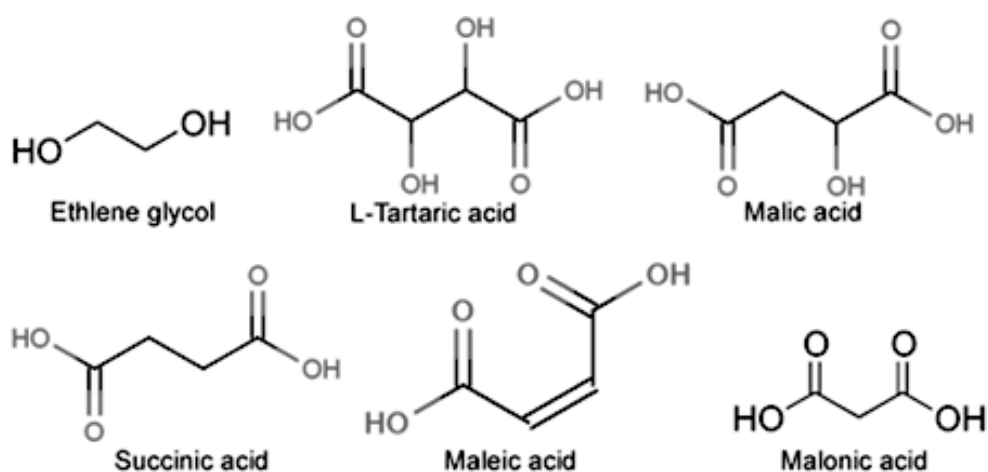


Figure 5.8. Ethylene glycol and the carboxylic acids used as complexing agents.

5.3 Solid state reaction

5.3.1 BiFeO₃ formation from binary oxides

Preparation of phase pure BiFeO₃ from Bi₂O₃ and Fe₂O₃ is difficult, with poor reproducibility. Trace amounts of the secondary ternary compounds Bi₂₅FeO₃₉ and Bi₂Fe₄O₉ are frequently detected by XRD. Deviation from the nominal 1:1 stoichiometric ratio of Bi:Fe results in formation of either Bi₂₅FeO₃₉, Bi₂Fe₄O₉ or even both in addition to BiFeO₃. A low intrinsic solid solubility (a low tolerance for vacancies in the cation sublattices) implies that the nominal stoichiometry must be carefully controlled. For soft chemical synthesis methods homogeneity on an atomic level is obtained, while in solid state reaction synthesis individual particles of Bi₂O₃ and Fe₂O₃ are present prior to firing. A homogenous Bi₂O₃-Fe₂O₃ precursor mixture with small particles is thus important for suppressing formation of Bi₂₅FeO₃₉ and Bi₂Fe₄O₉. The influence of grain size of the binary oxides has been systematically studied by Yuan *et al.*³⁴³ Finally, the temperature of firing is also important, and empirically we have found that 825 °C is the minimum temperature for obtaining phase pure BiFeO₃, with 8 h soaking time and heating and cooling rates of 400 °C/min. An XRD pattern of BiFeO₃ prepared by this method is shown in Figure 5.9, showing that it is phase pure within the detection limits of laboratory XRD.

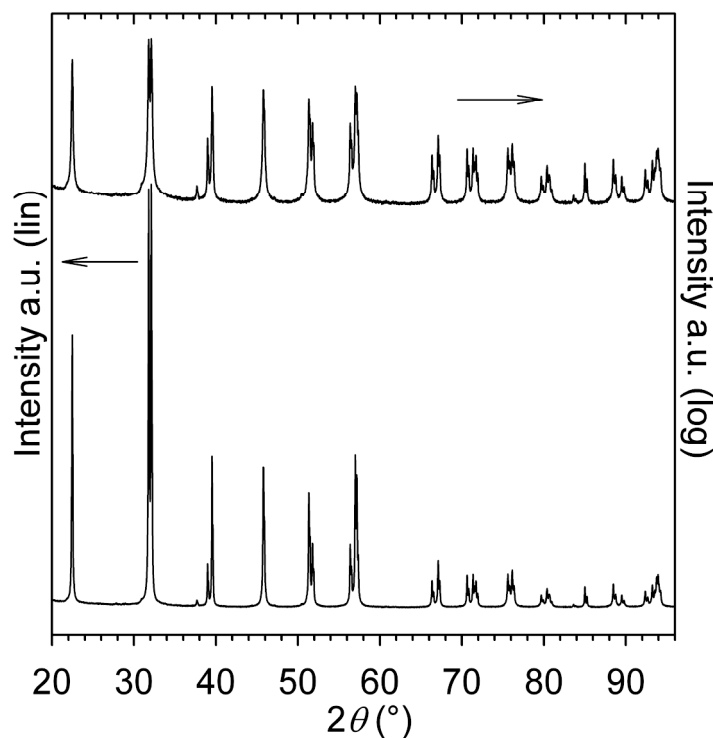
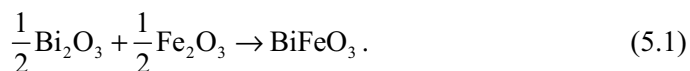


Figure 5.9. XRD patterns of bulk BiFeO₃ prepared by solid state reaction, plotted on a linear and logarithmic scale.

The formation reaction from the binary oxides is:



Based on solution calorimetry data provided by Phapale *et al.*³⁴⁴ the enthalpy of reaction (5.1), $\Delta_{\text{f,ox}}H_m^\circ$, is -70.75 ± 3.40 kJ/mol at 298.15 K. The difficulties in obtaining phase pure BiFeO₃ is thus not due to a low thermodynamic stability relative to the binary oxides, as e.g. phase pure LaFeO₃, which is less stable, is readily obtained by solid state reaction.³⁴⁵ BiFeO₃ also falls within the perovskite region of formability maps obtained from geometric considerations¹¹⁵⁻¹¹⁶ and the bond-valence model.³⁴⁶ Yokokawa *et al.*¹¹⁷ first pointed out the relation between $\Delta_{\text{f,ox}}H_m^\circ$ for perovskites and the Goldschmidt tolerance factor, t .¹¹⁸ Increasing tolerance factor implies straightening of bond angles and optimisation of attractive Coulombic forces, stabilising the structure, with an associated more negative $\Delta_{\text{f,ox}}H_m^\circ$. BiFeO₃ follows this trend, as shown in Figure 5.10. For direct comparison, a coordination number (CN) of 9 was used for all A cations, as the radii of 12 coordinated cations are not available for many lanthanides and Bi³⁺. The ionic radii of a 6s² lone pair cation like Bi³⁺ is not straight forward, and depends on the stereochemical activity of the lone pair.¹¹⁴ Hence an uncertainty in terms of t is included in Figure 5.10, spanning from the values obtained for CN = 8 for Bi³⁺ to that for CN = 9 for the almost equally large cation La³⁺.

The trend in Figure 5.10 suggests that isovalent substitution with a larger cation on the A site or a smaller cation on the B site would increase the stability of BiFeO₃ with respect to the binary oxides, and possibly also with respect to the Bi₂Fe₄O₉ mullite and Bi₂₅FeO₃₉ sillenite phases. Substitution of a more acidic cation on the B site or a more basic cation on the A site is also expected to stabilise the perovskite phase.³⁴⁷ La³⁺ is almost the same size as Bi³⁺, and although the space group changes with high substitution levels, perovskite phase is obtained for all values of x in Bi_{1-x}La_xFeO₃.³⁴⁸ Nd³⁺, Sm³⁺ and Gd³⁺ are smaller than Bi³⁺, but more basic cations, and solid solutions prepared at ambient pressure have been reported up to 15-20 % substitution.³⁴⁹⁻³⁵¹ Mn³⁺ is the only cation reported to substitute Fe³⁺ by substantial amounts (30 %) with solid state reaction synthesis at ambient pressure.³⁵² Al³⁺, Ga³⁺, Cr³⁺ and LS Co³⁺ are all smaller than HS Fe³⁺, but they can not be substituted by 1-20 % at ambient pressure, resulting in mullite and sillenite phases, as shown in Figure 5.11. BiAlO₃, BiGaO₃, BiCrO₃ and BiCoO₃ can however be prepared by high pressure synthesis.^{184, 187, 353}

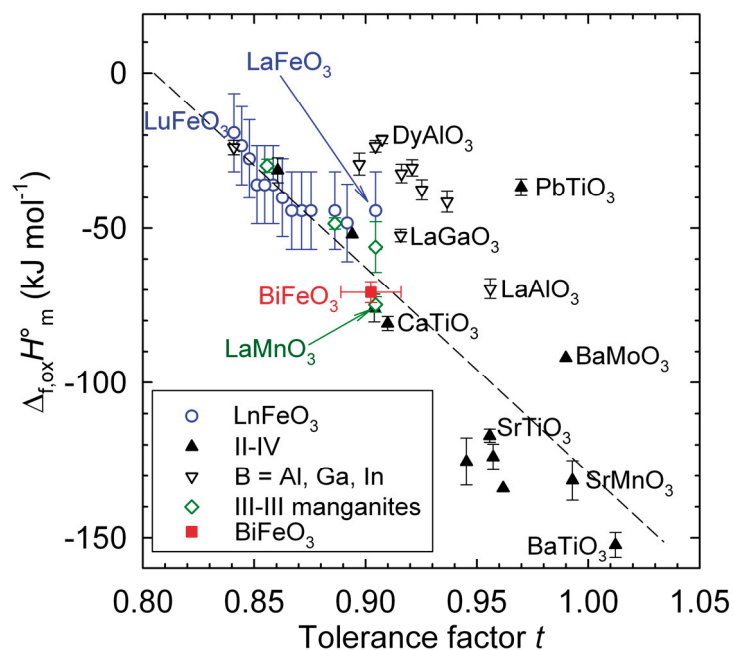


Figure 5.10. Standard enthalpies of formation for perovskites from binary oxides plotted as a function of the Goldschmidt tolerance factor. For direct comparison, all tolerance factors were calculated for nine-coordinated A cations. The dashed line is a guide to the eye. Thermodynamic data were adopted from references ^{347, 354-359}

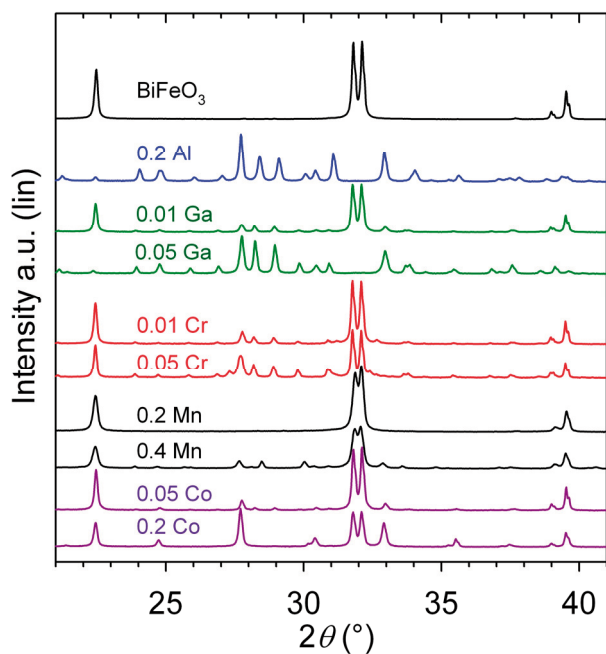


Figure 5.11. XRD patterns of pure and B site cation substituted BiFeO_3 prepared by solid state reaction. Labels refer to x and M in $\text{BiFe}_{1-x}\text{M}_x\text{O}_3$.

5.3.2 Stability of the secondary ternary phases $\text{Bi}_{25}\text{FeO}_{39}$ and $\text{Bi}_2\text{Fe}_4\text{O}_9$

During HTXRD of BiFeO_3 formation of $\text{Bi}_{25}\text{FeO}_{39}$ (x) and $\text{Bi}_2\text{Fe}_4\text{O}_9$ (o) was observed at 878 K,[§] as shown in Figure 5.12 (a). The two main peaks of BiFeO_3 are shown as unlabelled bars at 31.78° and 32.10° 2θ . The relative intensities of the Bragg reflections demonstrate the growth of $\text{Bi}_{25}\text{FeO}_{39}$ and $\text{Bi}_2\text{Fe}_4\text{O}_9$ at the expense of BiFeO_3 up to 1090 K. At higher temperatures the Bragg reflections of $\text{Bi}_{25}\text{FeO}_{39}$ and $\text{Bi}_2\text{Fe}_4\text{O}_9$ disappear, implying that these phases react back to the perovskite phase. The volatility of bismuth rich compounds cannot explain these observations since this would result in residual Fe_2O_3 or $\text{Bi}_2\text{Fe}_4\text{O}_9$. In contradiction with previous reports,³⁰⁹ we do not observe decomposition of BiFeO_3 between 1090 and 1199 K, even at long data collection times. Thus BiFeO_3 is a thermodynamically stable compound in the paraelectric state up to the peritectic decomposition temperature³⁰² of 1207 K. The same thermal evolution of the diffractograms is seen for $\text{BiFe}_{0.7}\text{Mn}_{0.3}\text{O}_3$ in Figure 5.12 (b), with nucleation of $\text{Bi}_2\text{Fe}_{4-y}\text{Mn}_y\text{O}_9$ and $\text{Bi}_{25}\text{Fe}_{1-z}\text{Mn}_z\text{O}_{39}$ around 873 K and subsequent increasing amounts up to 1023 K. At 1073 K the intensities of the reflections due to secondary ternary oxides have decreased, as the secondary phases have reacted back to the perovskite phase.

Ex situ XRD of isothermally heat treated Bi_2O_3 - Fe_2O_3 mixture and phase pure BiFeO_3 are shown in Figure 5.13. Substantial amounts of $\text{Bi}_{25}\text{FeO}_{39}$ and $\text{Bi}_2\text{Fe}_4\text{O}_9$ are evident at 927 K, while minor amounts are present at 1048 and 1123 K. Larger amounts of mullite and sillenite phase are observed in the initially phase pure and fine-grained material from a wet chemical route than the initial Bi_2O_3 - Fe_2O_3 mixture. From the annealing experiments of phase pure BiFeO_3 at 927 K it was shown that the amount of $\text{Bi}_{25}\text{FeO}_{39}$ and $\text{Bi}_2\text{Fe}_4\text{O}_9$ was increasing with time in line with a recent report.³⁶⁰

[§] Kelvin is chosen as the temperature unit in this subchapter since it contains thermodynamic calculations.

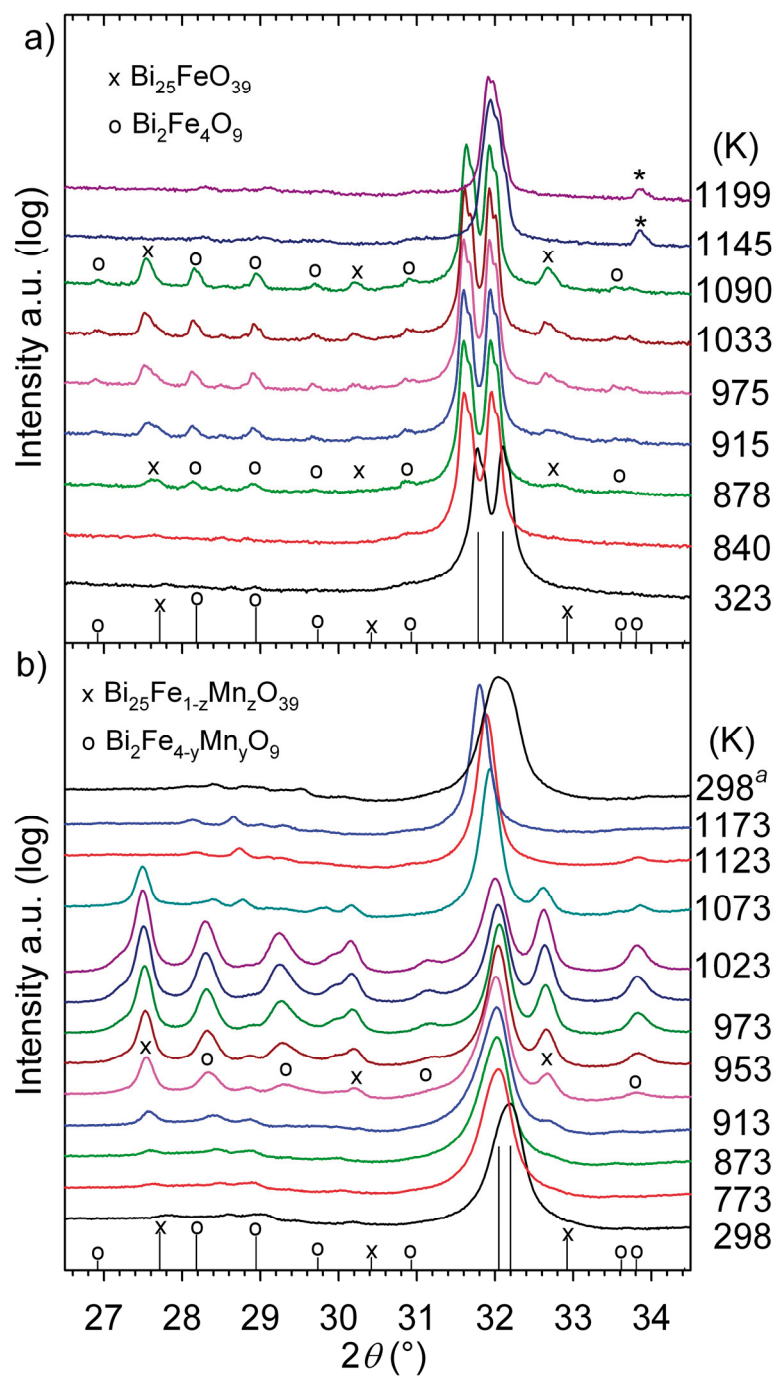


Figure 5.12. HTXRD patterns of a) BiFeO_3 and b) $\text{BiFe}_{0.7}\text{Mn}_{0.3}\text{O}_3$. Secondary phases $\text{Bi}_{25}\text{FeO}_{39}$ (x) (JCPDS 46-0416) and $\text{Bi}_2\text{Fe}_4\text{O}_9$ (o) (JCPDS 72-1832) form at the expense of the perovskite phase above 873 K, but reacts back to the perovskite phase at higher temperatures. The diffractogram labelled 298^a in b) was recorded after cooling from 1173 K to 298 K. Reflections labelled * are from the paraelectric polymorph, see Chapter 6.

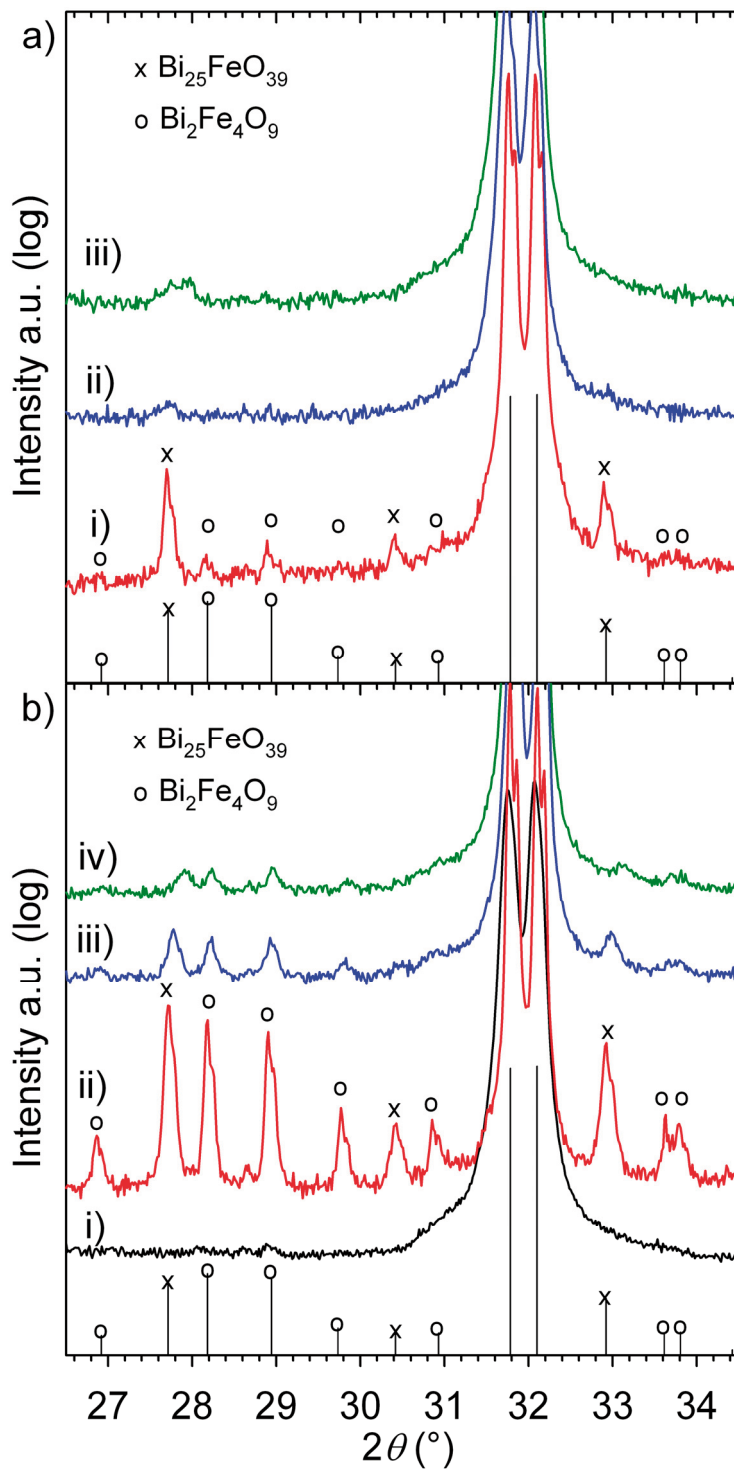
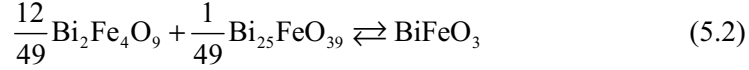


Figure 5.13. Ex situ XRD patterns of isothermally heat treated $\text{Bi}_2\text{O}_3\text{-Fe}_2\text{O}_3$ mixture (a) and initially phase pure BiFeO_3 (b). The labels i), ii), iii) and iv) refer to 1123, 1048, 973 and 298 K (before heat treatment), respectively.

The chemical reaction observed during HTXRD of BiFeO₃ in Figure 5.12 a) is³⁶⁰



In the following, only the case on BiFeO₃ will be discussed, as the same principles also will apply to BiFe_{0.7}Mn_{0.3}O₃. In line with Gibbs' phase rule the three phases can coexist with zero degrees of freedom, as the number of components is two, since the oxidation state of Fe does not change, and the system can be described as the pseudo-binary system Bi₂O₃-Fe₂O₃. Given that BiFeO₃ is stable above 1040 K, the molar Gibbs energy of reaction (5.2), $\Delta_{r,(5.2)}G_m^\circ$, must change sign from positive to negative at 1040 K. According to

$$\Delta_{r,(5.2)}G_m^\circ = \Delta_{r,(5.2)}H_m^\circ - T\Delta_{r,(5.2)}S_m^\circ, \quad (5.3)$$

both $\Delta_{r,(5.2)}H_m^\circ$ and $\Delta_{r,(5.2)}S_m^\circ$ must thus be positive. Solution calorimetry data from Phapale *et al.*¹⁰ gives an enthalpy of reaction at ambient temperature close to zero: $\Delta_{r,(5.2)}H_m^\circ = -4.91 \pm 2.93$ kJ/mol, hence reaction (5.2) is weakly exothermic at room temperature. $\Delta_{r,(5.2)}G_m^\circ$ may change sign from positive to negative at 1040 K if both $\Delta_{r,(5.2)}H_m^\circ$ and $\Delta_{r,(5.2)}S_m^\circ$ also change signs from negative to positive at temperatures lower than 1040 K. To examine this scenario we apply the difference in molar heat capacity for reaction (5.2), $\Delta_{r,(5.2)}C_{p,m}^\circ$, derived from $C_{p,m}^\circ$ reported³⁴⁴ for BiFeO₃, Bi₂Fe₄O₉ and Bi₂₅FeO₃₉ weighted according to the stoichiometry of reaction (5.2):

$$\Delta_{r,(5.2)}C_{p,m}^\circ(T) = 2.74 + 1.96 \cdot 10^{-3}T - 9.4797 \cdot 10^4 T^{-2} \quad \text{J/Kmol}. \quad (5.4)$$

At $T_{\text{eq}} \approx 1040$ K, $\Delta_{r,(5.2)}G_m^\circ = 0$ and $\Delta_{r,(5.2)}H_m^\circ(T_{\text{eq}}) = T_{\text{eq}}\Delta_{r,(5.2)}S_m^\circ(T_{\text{eq}})$, where

$$\Delta_{r,(5.2)}H_m^\circ(T_{\text{eq}}) = \Delta_{r,(5.2)}H_m^\circ(298.15) + \int_{298.15}^{T_{\text{eq}}} \Delta_{r,(5.2)}C_p^\circ dT \quad (5.5)$$

and

$$\Delta_{r,(5.2)}S_m^\circ(T_{\text{eq}}) = \Delta_{r,(5.2)}S_m^\circ(298.15) + \int_{298.15}^{T_{\text{eq}}} \frac{\Delta_{r,(5.2)}C_p^\circ}{T} dT. \quad (5.6)$$

$\Delta_{r,(5.2)}S_m^\circ(298.15)$ is expected to be negative and close to zero, in line with the value of $\Delta_{r,(5.2)}H_m^\circ(298.15)$, and the more open and disordered crystal structures of Bi₂Fe₄O₉ and Bi₂₅FeO₃₉ relative to BiFeO₃.³⁶¹⁻³⁶² Since $\Delta_{r,(5.2)}C_{p,m}^\circ(T)$ is positive

for $T > 300$ K, $\Delta_{r,(5.2)}H_m^\circ(T)$ and $\Delta_{r,(5.2)}S_m^\circ(T)$ will increase with temperature. $\Delta_{r,(5.2)}G_m^\circ(T) = \Delta_{r,(5.2)}H_m^\circ(T) - T\Delta_{r,(5.2)}S_m^\circ(T)$ with $\Delta_{r,(5.2)}H_m^\circ(298.15) = -4.91 \pm 2.93$ kJ/mol is plotted in Figure 5.14, demonstrating the small difference in Gibbs energy of reaction (5.2). $\Delta_{r,(5.2)}G_m^\circ(T)$ is sensitive to the value of $\Delta_{r,(5.2)}S_m^\circ(298.15)$ and as the inset of Figure 5.14 illustrates, with a value of -3.62 J/Kmol (solid line) $\Delta_{r,(5.2)}G_m^\circ(T)$ evolves in concordance with the XRD data in Figures 5.12 and 5.13. $\Delta_{r,(5.2)}G_m^\circ(T) > 0$ for approximately $720 \text{ K} < T < 1040 \text{ K}$ with $\Delta_{r,(5.2)}H_m^\circ(298.15) = -1.98$ kJ/mol and $\Delta_{r,(5.2)}S_m^\circ(298.15) = -3.62$ J/Kmol. In this temperature interval $\text{Bi}_2\text{Fe}_4\text{O}_9$ and $\text{Bi}_{25}\text{FeO}_{39}$ are weakly more stable (thermodynamically) than BiFeO_3 . Observation of the partial decomposition in this temperature interval was only possible due the long HTXRD data collection times, owing to the small thermodynamic driving force, and the low ionic mobility in the lower end of the temperature interval in question. The apparent contradiction that BiFeO_3 is seemingly metastable up to 1090 K in the HTXRD data compared to 1040 K in the ex situ XRD data follows from the small thermodynamic driving force for reaction (5.2) in this temperature region, thus the reaction back to perovskite is slow. Influence of impurities as suggested by Valant *et al.*³¹⁴ may also effect the observation as discussed further below.

BiFeO_3 is the energetically stable ternary compound at temperatures higher than 1040 K, but $\Delta_{r,(5.2)}G_m^\circ(T)$ is close to zero. The XRD data in Figures 5.12 and 5.13 and the thermodynamic analysis in Figure 5.14 explains why firing a Bi_2O_3 - Fe_2O_3 precursor at lower temperatures than 1040 K yields substantial amounts of $\text{Bi}_2\text{Fe}_4\text{O}_9$ and $\text{Bi}_{25}\text{FeO}_{39}$.^{313, 363-364} In terms of obtaining single phase perovskite during solid state reaction synthesis, rapid heating of a Bi_2O_3 - Fe_2O_3 precursor prevents initial formation of $\text{Bi}_2\text{Fe}_4\text{O}_9$ and $\text{Bi}_{25}\text{FeO}_{39}$, and fast cooling prevents the decomposition of BiFeO_3 shown in Figure 5.12. In addition the importance of pure precursors, small reactant powder particles and precursor homogeneity has been pointed out earlier.^{314, 343, 365}

The influence of impurities on reaction (5.2) needs particular attention. It might be tempting to argue that the addition of several new chemical components (impurities) may lead to coexistence between the three pure phases BiFeO_3 , $\text{Bi}_2\text{Fe}_4\text{O}_9$ and $\text{Bi}_{25}\text{FeO}_{39}$ (In terms of the Gibbs phase rule the number of independent components does increase). However, the coexistence of the pure phases is only possible when the Gibbs energy of reaction (5.2) is equal to zero (which only occurs at two specific temperatures, see Figure 5.14). On the other hand, if the solubility of the impurities is larger in $\text{Bi}_2\text{Fe}_4\text{O}_9$ or $\text{Bi}_{25}\text{FeO}_{39}$ than in BiFeO_3 the Gibbs energy of reaction (5.2) will be influenced and thereby effect the stability of BiFeO_3 relative to the $\text{Bi}_2\text{Fe}_4\text{O}_9$ and $\text{Bi}_{25}\text{FeO}_{39}$ solid solutions. Tentative phase diagrams provided by Valant *et al.*³¹⁴ discuss this in detail (narrow three phase region consisting of BiFeO_3 in equilibrium with $\text{Bi}_{25}\text{Fe}_{1-x}\text{A}_x\text{O}_{39}$ and $\text{Bi}_2\text{Fe}_{1-x}\text{A}_x\text{O}_9$ where AO_y is the impurity oxide). A higher solubility of impurities in $\text{Bi}_2\text{Fe}_4\text{O}_9$ and/or $\text{Bi}_{25}\text{FeO}_{39}$ will cause a thermodynamic destabilisation of BiFeO_3 resulting in a shift upwards in the Gibbs energy curve for reaction (5.2) shown in

Figure 5.14. The effect of the impurities is to increase the temperature interval where $\text{Bi}_2\text{Fe}_4\text{O}_9$ and $\text{Bi}_{25}\text{FeO}_{39}$ are stable (destabilising BiFeO_3 in accordance with Valant *et al.*³¹⁴). To summarise, the strong influence of impurities is caused by the small Gibbs energy difference between the reactants and products in reaction (5.2). Impurities will therefore have a strong effect on the phase equilibrium and result in poor reproducibility if the impurity level, for example alumina or silica from crucibles etc, is not well controlled.

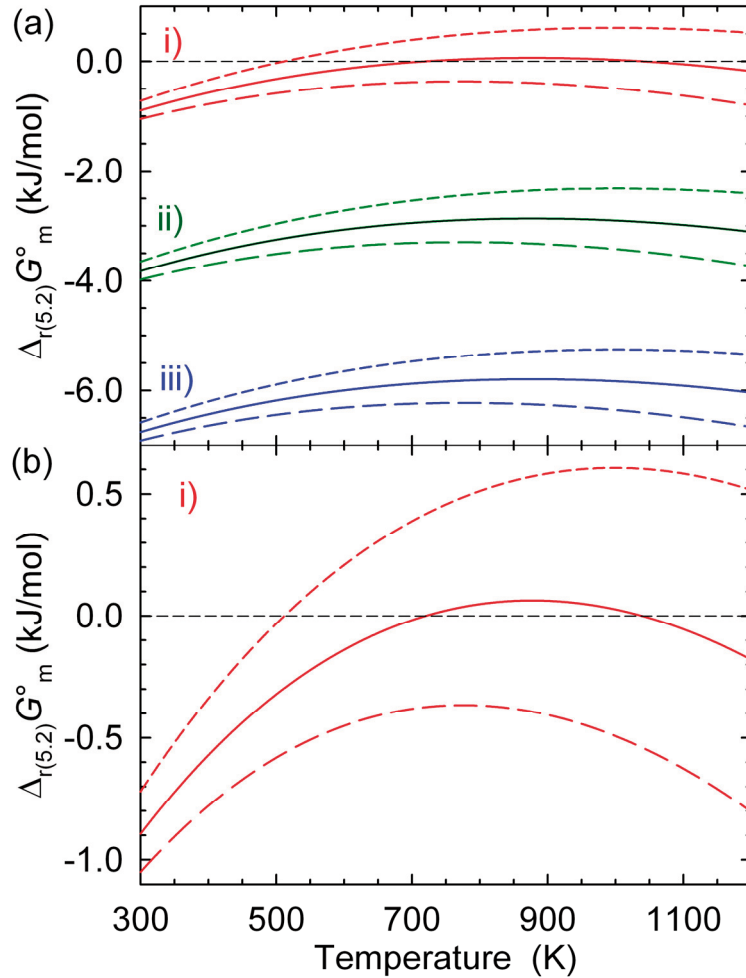


Figure 5.14. (a) Gibbs energy (for one mole of BiFeO_3) of reaction (5.2), $\Delta_{r(5.2)}G_m^\circ(T)$ with $\Delta_{r(5.2)}H_m^\circ(298.15) = -1980$ i), -4910 ii) and -7840 J/mol iii) respectively, and $\Delta_{r(5.2)}S_m^\circ(298.15) = -3.62$ (solid line), -4.2 (long dash) and -3.1 (short dash) J/Kmol, respectively. (b) $\Delta_{r(5.2)}G_m^\circ(T)$ with $\Delta_{r(5.2)}H_m^\circ(298.15) = -1980$ J/mol, implying that BiFeO_3 is metastable with respect to $\text{Bi}_2\text{Fe}_4\text{O}_9$ and $\text{Bi}_{25}\text{FeO}_{39}$ for $720 \text{ K} < T < 1040 \text{ K}$ as $\Delta_{r(5.2)}G_m^\circ(T) > 0$, in line with the XRD data in Figures 5.12 and 5.13.

The influence of temperature and chemical homogeneity is illustrated schematically in Figure 5.15. The three ternary oxides are in equilibrium according to Gibbs' phase rule when $\Delta_{r,(5.2)}G_m^\circ(T_{eq})=0$, where the Gibbs energy curve of BiFeO_3 has a common tangent with the Gibbs energy curves of $\text{Bi}_2\text{Fe}_4\text{O}_9$ and $\text{Bi}_{25}\text{FeO}_{39}$. For $T > T_{eq}$ the Gibbs energy curve of BiFeO_3 is lower than the $\text{Bi}_2\text{Fe}_4\text{O}_9$ - $\text{Bi}_{25}\text{FeO}_{39}$ tangent line and BiFeO_3 is the stable compound. Deviation from 1:1 Bi_2O_3 : Fe_2O_3 stoichiometry will result in equilibrium between BiFeO_3 and one of the secondary ternary oxides. Moreover, the influence of pressure on reaction (5.2) is self-evident from the crystal structure of perovskite being denser than the mullite and sillenite structures of $\text{Bi}_2\text{Fe}_4\text{O}_9$ and $\text{Bi}_{25}\text{FeO}_{39}$, respectively.³⁶¹⁻³⁶² The volume change of reaction (5.2) is hence large and negative, $\Delta_{r,(5.2)}V_m = -5.14 \text{ cm}^3/\text{mol}$. The perovskite phase is thus favoured by pressure and possibly compressive strain in thin films relative to the sillenite and mullite phase, and the $\Delta_{r,(5.2)}G_m^\circ(T)$ curves in Figure 5.14 will be shifted toward more negative values with increasing pressure.

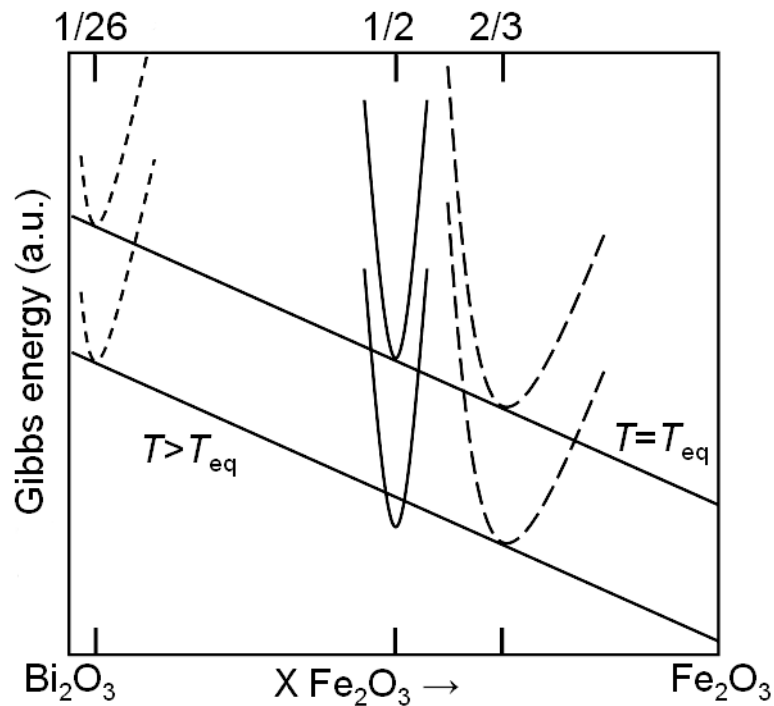


Figure 5.15. Schematic illustration of the Gibbs energy (a.u.) of BiFeO_3 (solid), $\text{Bi}_{25}\text{FeO}_{39}$ (short dash) and $\text{Bi}_2\text{Fe}_4\text{O}_9$ (long dash) as a function of nominal composition. At $T_{eq} = 1040 \text{ K}$ the tangent shows that the three phases are in equilibrium in line with Gibbs' phase rule. At $T > 1040 \text{ K}$ BiFeO_3 ($x = 1/2$) has lower Gibbs energy than $\text{Bi}_{25}\text{FeO}_{39}$ ($x = 1/26$) and $\text{Bi}_2\text{Fe}_4\text{O}_9$ ($x = 2/3$) which are in equilibrium, as their common tangent line lies higher in Gibbs energy than the Gibbs energy curve of BiFeO_3 .

We now revisit the effect of chemical substitution. The energetics of the chemical equilibria (5.1) and (5.2) determine the formability of the perovskite phase. Equilibrium (5.1) is strongly shifted towards the right, favouring BiFeO₃ formation. As $\Delta_{r(5.2)}G_m^\circ$ is close to zero, equilibrium (5.2) is the critical for obtaining phase pure perovskite phase. The configurational entropy contribution from chemical substitution to $\Delta_{r(5.2)}G_m^\circ$ determines which way equilibrium (5.2) is shifted:

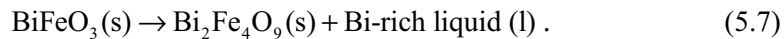
- Substitution with elements *more* soluble in BiFeO₃ than Bi₂₅FeO₃₉ or Bi₂Fe₄O₉ shifts equilibrium (5.2) towards the *right* hand side, favouring the formation of pure, single phase perovskite. La³⁺ and other Ln³⁺ cations are more soluble in BiFeO₃ than Bi₂₅FeO₃₉ and Bi₂Fe₄O₉, and shift the $\Delta_{r(5.2)}G_m^\circ$ curves in Figure 5.14 towards *more* negative values.
- Substitution with elements *less* soluble in BiFeO₃ than Bi₂₅FeO₃₉ or Bi₂Fe₄O₉ shifts equilibrium (5.2) towards the *left* hand side, disfavoring formation of pure, single phase perovskite. Al³⁺, Ga³⁺, Cr³⁺ and Co³⁺ are more soluble in Bi₂₅FeO₃₉ and/or Bi₂Fe₄O₉ than BiFeO₃, and shift the $\Delta_{r(5.2)}G_m^\circ$ curves in Figure 5.14 towards *less* negative values, in analogy with the presence of impurities like Al₂O₃ and SiO₂.

Due to the large negative value of $\Delta_{r(5.2)}V_m$, high pressure can shift equilibrium (5.2) towards the right hand side, enabling formation of single phase perovskite with chemical compositions which are not stable at ambient pressure. Thus, even if the ambient pressure solubility of Al³⁺, Ga³⁺, Cr³⁺ and Co³⁺ is limited, high pressure will enable full solid solubility. Substitution with Mn and La is treated separately in chapters 7 and 8, respectively.

5.4 Thermodynamic stability and chemical compatibility

5.4.1 Peritectic decomposition

DTA traces recorded in different atmospheres are shown in Figure 5.16. Peritectic decomposition of BiFeO₃ in air gives rise to the largest endothermic peak, with onset at 940 °C, T_p (Figure 5.16 (a)). The decomposition at the peritectic temperature involves partial melting of the solid, thus the large amount of heat associated with this reaction. The enhanced mass loss above T_p can be explained by the considerable higher vapour pressure of Bi₂O₃ above the Bi₂O₃-rich liquid formed at T_p and possible reduction of Fe³⁺ to Fe²⁺ in this acidic liquid. An approximate equation for the peritectic decomposition reaction is:



The influence of atmosphere on the peritectic decomposition is shown in Figure 5.16 (b). An increase of the onset temperature of peritectic decomposition in O₂ atmosphere was observed and reproduced. Although a subtle endothermic peak is

observed just above T_{trs} (polymorphic phase transition, see chapter 6) for both measurements in O_2 , it is too small to correspond to peritectic decomposition. In O_2 atmosphere the peritectic decomposition starts at approx. 960°C , which has also been reported as the decomposition temperature of $\text{Bi}_2\text{Fe}_4\text{O}_9$.¹⁵⁹ The weight loss and the shift in the peritectic temperature point to a partly thermal reduction of the oxidation state of Fe at the peritectic decomposition. T_{trs} refers to a polymorphic transition, see chapter 6.

During electrical conductivity measurements described in chapter 6 (Figures 6.13-6.14) it was also observed that O_2 atmosphere stabilises BiFeO_3 towards decomposition relative to the behaviour in N_2 atmosphere.

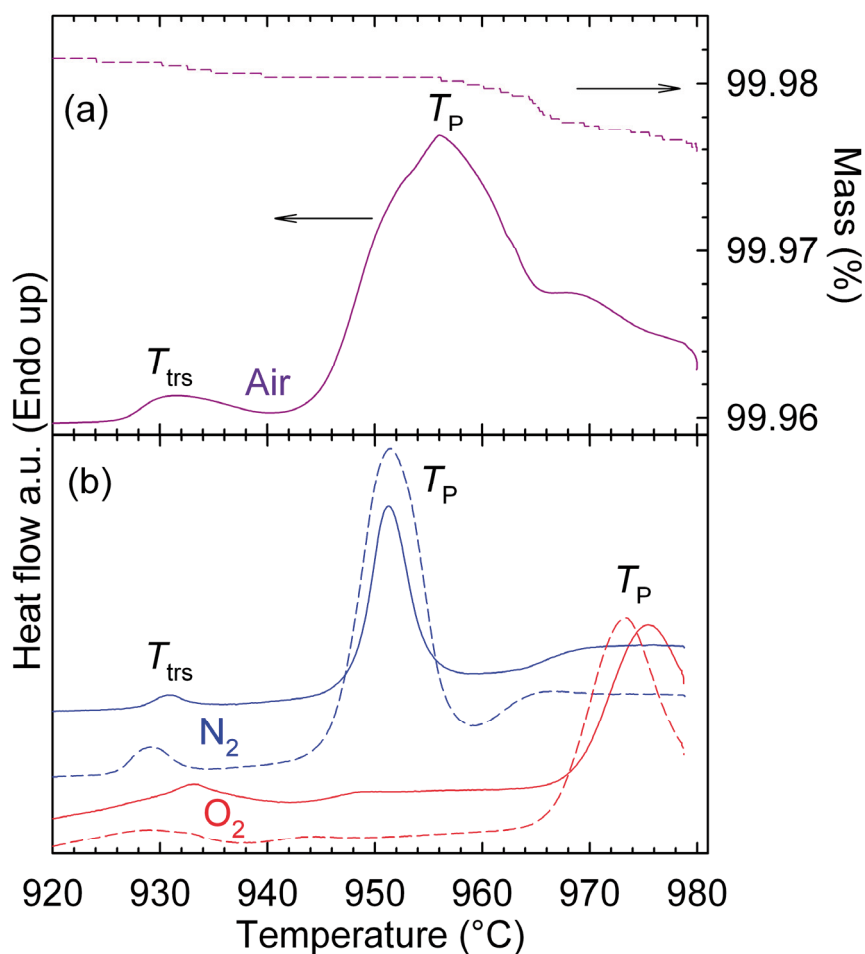


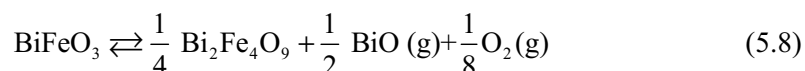
Figure 5.16. (a) Differential thermal analysis (DTA) and thermogravimetry (TGA) of BiFeO_3 bulk powder in air. (b) DTA traces of BiFeO_3 bulk powder in N_2 and O_2 atmospheres (two samples measured in each atmosphere).

5.4.2 Thermodynamic stability

High temperature studies of BiFeO₃ have proven difficult, with poor reproducibility between different laboratories and experimental setups, and decomposition below the peritectic temperature of 935 °C has been frequently reported in the literature.^{40, 301, 311, 366-367} Results from DTA (Figure 5.16) and electrical conductivity measurements (Figure 6.13 and 6.14) suggest that BiFeO₃ is more stable in O₂ than in air and N₂ atmospheres. Thus a higher partial pressure of oxygen stabilises BiFeO₃, in agreement with a titration study by Li and MacManus-Driscoll.³⁶⁸

BiFeO₃ is stable towards decomposition to the binary oxides Bi₂O₃ and Fe₂O₃ as the enthalpy of formation from oxides, $\Delta_{f,ox} H_m^{\circ}$ is -70.75 ± 3.40 kJ/mol at 298.15 K. To state the obvious; BiFeO₃ would not form from Bi₂O₃ and Fe₂O₃ during solid state reaction synthesis if it were unstable at the temperature of firing. The “rapid liquid phase sintering” method³¹³ which involves firing a Bi₂O₃-Fe₂O₃ mixture for 7.5 minutes at 880 °C, would not be successful if BiFeO₃ were unstable towards decomposition into Bi₂O₃ and Fe₂O₃. For Bi₂Fe₄O₉, $\Delta_{f,ox} H_m^{\circ}$ is -255.8 ± 3.6 kJ/mol (-86.47 kJ/mol when normalised to a 5 atom unit cell) and for Bi₂₅FeO₃₉ it is 7.3 ± 11.8 kJ/mol, from thermodynamic data provided by Phapale *et al.*³⁴⁴ Thus Bi₂Fe₄O₉ rather than Fe₂O₃ is the energetically preferred decomposition product in the presence of Bi₂O₃. The Gibbs energy of reaction (5.2), $\Delta_{r(5.2)} G_m^{\circ}$, is close to zero, but increasingly negative with increasing temperature above 800 °C. Ignoring mass loss through evaporation of bismuth oxides, BiFeO₃ is stable towards decomposition to Bi₂Fe₄O₉ and Bi₂₅FeO₃₉ below the peritectic decomposition temperature.

Evaporation of bismuth oxides from BiFeO₃ would yield coexistence of BiFeO₃ and Bi₂Fe₄O₉ according to the phase diagram. BiO is the dominant gaseous bismuth oxide species above 800 °C. The vapour pressure of BiO (g) can be estimated by the thermodynamics of the chemical equilibrium:



Thermodynamic calculations with FactSage³⁶⁹ show that the vapour pressure of BiO (g) over pure Bi₂O₃ (l) is less than 10⁻⁶ atm at 1200 K. The presence of iron oxide in the system will reduce the activity of BiO, hence the vapour pressure of BiO (g) is therefore significantly lower above solid BiFeO₃ than the vapour pressure above pure liquid Bi₂O₃. However, in experiments using powder or thin films, where the mass is relatively small and the surface area large, evaporation of BiO (g) may occur, particularly if the sample is exposed to a gas flow, resulting in the formation of Bi₂Fe₄O₉. For bulk material however the loss of Bi through BiO (g) evaporation should be less pronounced. Equilibrium (5.8) explains the stabilisation of BiFeO₃ from peritectic decomposition in O₂ relative to N₂ atmosphere³⁶⁸ by the le Chatelier principle.

5.4.3 Chemical compatibility

Since $\Delta_{r(5.2)} G_m^\circ$ is close to zero the equilibrium (5.2) is sensitive to the presence of impurities, and minor amounts of Al_2O_3 or SiO_2 drives reaction (5.2) towards left, as Al_2O_3 and SiO_2 is more soluble in $\text{Bi}_2\text{Fe}_4\text{O}_9$ and $\text{Bi}_{25}\text{FeO}_{39}$, respectively, than in BiFeO_3 . Unfortunately, Al_2O_3 and SiO_2 are primary constituents of refractory materials commonly in contact with BiFeO_3 during high temperature experiments. Hence decomposition of BiFeO_3 at $\text{BiFeO}_3/\text{Al}_2\text{O}_3$ and $\text{BiFeO}_3/\text{SiO}_2$ interfaces must be anticipated. Interface reactions between SiO_2 and BiFeO_3 was pointed out as a problem already by Bucci *et al.* in 1972,¹⁰⁴ but this was largely forgotten in the following decades. Decomposition from 700 °C was observed during a high temperature neutron diffraction study by Palewicz *et al.* where the BiFeO_3 sample was encapsulated by a vanadium container.³⁶⁷ SiO_2 was used for sample containment by Arnold *et al.* who observed traces of $\text{Bi}_2\text{Fe}_4\text{O}_9$ from 810 °C and complete decomposition at 870 °C.³¹¹ Moreover, platinum is often used for electrodes for electrical contact or heating strips in HTXRD experiments with Bragg-Brentano geometry. The binary Pt-Bi phase diagram³⁷⁰ displays several intermetallic phases, demonstrating affinity between Bi and Pt, suggesting that interface reactions will occur at high temperatures, as reported by Yakovlev *et al.*³⁷¹ Based on this reasoning, we propose that decomposition of BiFeO_3 below the peritectic temperature is due to *chemical incompatibility* towards the materials in contact with the sample rather than *intrinsic thermodynamic instability*. E. g. alloying of Bi in contact with Pt at high temperatures requires reduction of Bi from +III to 0, thus a high $p\text{O}_2$ stabilises BiFeO_3 from interface reaction with Pt towards higher temperatures, as shown in Figure 6.15 and 6.16 in the next chapter. Finding materials chemically inert towards BiFeO_3 would substantially ease high temperature studies. This is equally important for the integration of BiFeO_3 into electronic circuitry, and thus a technological challenge as much as a means towards fundamental understanding of the high temperature behaviour.

5.5 Conclusions

Four new wet chemical routes to obtain phase pure BiFeO_3 have been demonstrated, and the materials exhibit bulk lattice parameters and T_N after calcination for 2 h at 600 °C. Only minor amounts of secondary phases after 2 h at 600 °C were present in materials obtained by the routes initially not deemed successful. This may be related to the purity of the carboxylic acids used as complexing agents, and that BiFeO_3 is metastable with respect to sillenite and mullite at 600 °C. The modified Pechini method developed can thus be regarded as a more general approach than initially thought to obtain phase pure materials which are difficult to prepare by solid state reaction.

BiFeO_3 has been observed by HTXRD to be metastable with respect to $\text{Bi}_{25}\text{FeO}_{39}$ and $\text{Bi}_2\text{Fe}_4\text{O}_9$ between 600 and 770 °C. The Gibbs energy of the reaction from $\text{Bi}_{25}\text{FeO}_{39}$ and $\text{Bi}_2\text{Fe}_4\text{O}_9$ to BiFeO_3 is close to zero, with a maximum value larger than zero at about 630 °C. Thermodynamic calculations imply that BiFeO_3 is metastable between 450 and 770 °C, and is thus kinetically stabilised in the lower

end of this temperature range. The small difference in Gibbs energy between BiFeO_3 and the secondary ternary compounds makes the equilibrium reaction sensitive to the presence of impurities. BiFeO_3 is destabilised by impurities more soluble in $\text{Bi}_{25}\text{FeO}_{39}$ or $\text{Bi}_2\text{Fe}_4\text{O}_9$ than the perovskite phase, and vice versa. The optimum strategy for obtaining phase pure BiFeO_3 by solid state reaction is thus to rapidly heat a well-mixed fine-grained Bi_2O_3 - Fe_2O_3 mixture to a high temperature just below the peritectic decomposition temperature, followed by quenching after a short soaking time. As BiFeO_3 is denser than $\text{Bi}_{25}\text{FeO}_{39}$ and $\text{Bi}_2\text{Fe}_4\text{O}_9$, high pressure will favour perovskite formation, even for stoichiometries not obtainable at ambient pressure.

In contrast to almost 50 years of claims that BiFeO_3 is metastable at high temperatures, it is here proposed that BiFeO_3 is a thermodynamically stable compound below the peritectic decomposition temperature. BiFeO_3 is stable relative to Bi_2O_3 and Fe_2O_3 , and thermodynamic calculations and HTXRD measurements show that it is increasingly more stable towards $\text{Bi}_{25}\text{FeO}_{39}$ and $\text{Bi}_2\text{Fe}_4\text{O}_9$ with increasing temperature. Decomposition below the peritectic temperature can be rationalised from the *chemical incompatibility* of BiFeO_3 towards adjacent materials rather than *intrinsic thermodynamic instability*. Precautions must thus be taken during both synthesis and characterisation at high temperatures to avoid decomposition at interfaces.

6 Phase transitions

6.1 Introduction

Structural phase transitions are abundant in perovskites. Perovskites with tilted octahedra usually go through one or more structural transitions before reaching the cubic aristotype structure. Some compounds decompose before the cubic structure is reached, e.g. LiNbO_3 .³⁷²⁻³⁷³ An early work by Ismailzade found at least eight phase transition in BiFeO_3 between room temperature and $850\text{ }^\circ\text{C}$.¹⁰⁵ Albeit the real number has proven to be smaller, the phase transitions of BiFeO_3 has been a subject of debate in the literature also during the course of the present work, with many contradicting reports regarding both the nature and order of the transitions and the structure and properties of the polymorphs.

BiFeO_3 is an antiferromagnet with a Néel temperature of $370\text{ }^\circ\text{C}$.¹⁰² The sublattice magnetisation inferred from high temperature neutron powder diffraction (HTNPD)^{367, 374} and Mössbauer³⁷⁵ spectroscopy goes continuously to zero when approaching T_N , but the magnetic transition has been reported to be first order with discontinuous volume.^{104-105, 376} The unit cell distortion along the $[111]_{\text{cub}}$ direction reaches its maximum value closely above T_N , which may be due spin-lattice coupling. Phonon anomalies across T_N have been observed by Raman and IR spectroscopy.^{113, 178, 376-383}

The ferroelectric transition occurs at $820\text{-}830\text{ }^\circ\text{C}$ and is first order from the non-zero $\Delta_{\text{trs}}V$ and $\Delta_{\text{trs}}H$.^{159, 301, 366} The space group of the paraelectric phase has however been under debate throughout the course of this work. Theoretical and experimental studies of Raman and IR phonon spectra pointed to a displacive phase transition with incomplete phonon softening.³⁸⁴⁻³⁸⁵ Loss of Raman signal above T_C at $820\text{ }^\circ\text{C}$ implied that the paraelectric phase is the cubic $Pm\bar{3}m$.^{376, 378-380} A Raman signature consistent with orthorhombic symmetry was observed by Palai *et al.*¹⁵⁹ who proposed a simple orthorhombic paraelectric unit cell with space group with untilted octahedra. A tetragonal paraelectric polymorph with space group $I4/mcm$ was inferred from finite temperature Monte Carlo simulations,³⁸⁶ and a similar structure with a small monoclinic distortion giving the space group $P2_1/m$ was determined from HTXRD by Haumont *et al.*³⁰¹ The present author suggested the centrosymmetric $R\bar{3}c$ structure as the paraelectric space group.³⁶⁶

A 2nd order transition from orthorhombic $P2mm$ to cubic $Pm\bar{3}m$ at $925 \pm 5\text{ }^\circ\text{C}$ was reported by Palai *et al.*,¹⁵⁹ and the cubic polymorph was suggested to be metallic based on optical reflectivity and electrical resistivity measurements. Decomposition of the sample before the cubic polymorph was reached was observed in other reports.^{301, 366-367}

The purpose of this chapter is to characterise the thermodynamic order and nature of the phase transitions of BiFeO_3 , and to investigate the structure and properties of the polymorphs.

6.2 The antiferromagnetic to paramagnetic transition

The antiferromagnetic to paramagnetic phase transition at T_N is evident from the cusp in the calorimetric trace obtained by DSC, shown in Figure 6.1 (a). The enthalpy of the transition is small and in the range of 3 ± 0.3 kJ/mol. The magnetic susceptibility diverges at T_N (Figure 6.1 (b)), which is typical of the behaviour across an antiferromagnet transition.

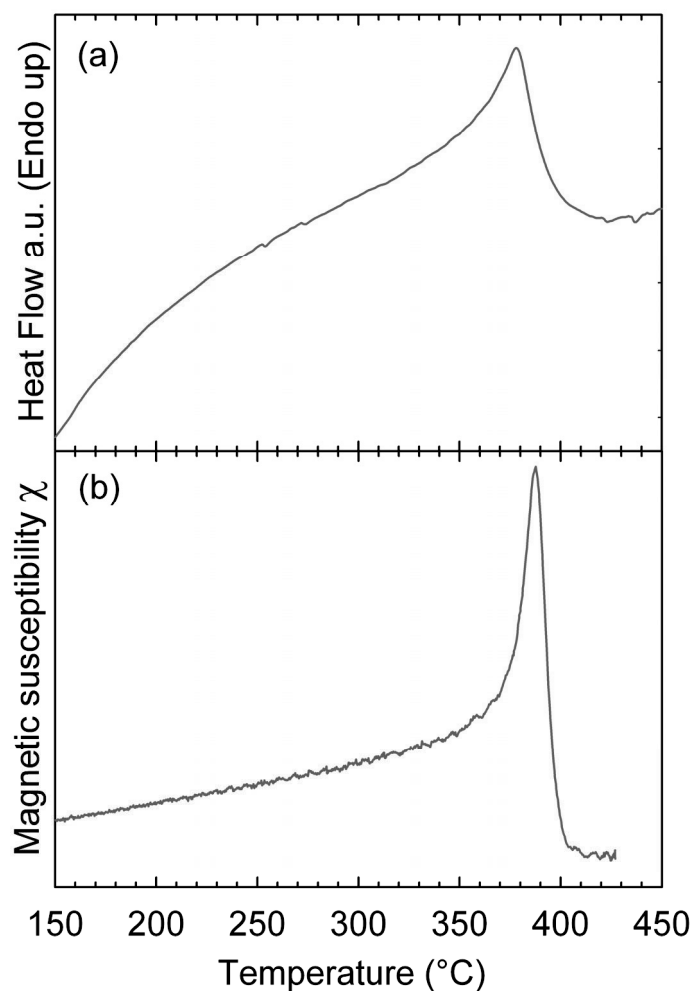


Figure 6.1. The antiferromagnetic to paramagnetic phase transition in bulk BiFeO_3 measured by (a) DSC and (b) vibrating sample magnetometry (VSM).

In order to elucidate structural anomalies associated with the loss of antiferromagnetic order, HTXRD patterns were collected with small temperature steps across T_N . No abrupt changes in the XRD patterns were observed across T_N , as shown in Figure 6.2. Rietveld refinement of the HTXRD patterns revealed that the thermal expansion of BiFeO_3 is both anisotropic and non-linear across T_N . The loss of antiferromagnetic order is associated with expansion in both the ab-plane

and along the c -axis of the hexagonal unit cell, superimposed on the thermal lattice expansion, as shown in Figure 6.3 (a). The unit cell distortion quantified by the rhombohedral angle α_{rh} and pseudotetragonality c/a in Figure 6.3 (b) evolves continuously across T_N . A maximum unit cell distortion about 70 °C above T_N is in accordance with previous reports.¹⁰² No abrupt changes in cation positions can be identified within the uncertainty of the refinement (Figure 6.3 (c)). As the uncertainty of refined oxygen positions (not shown) is larger than that of cations from laboratory XRD data, higher quality data is required to resolve whether the loss of antiferromagnetic ordering is accompanied by abrupt changes in atomic positions.

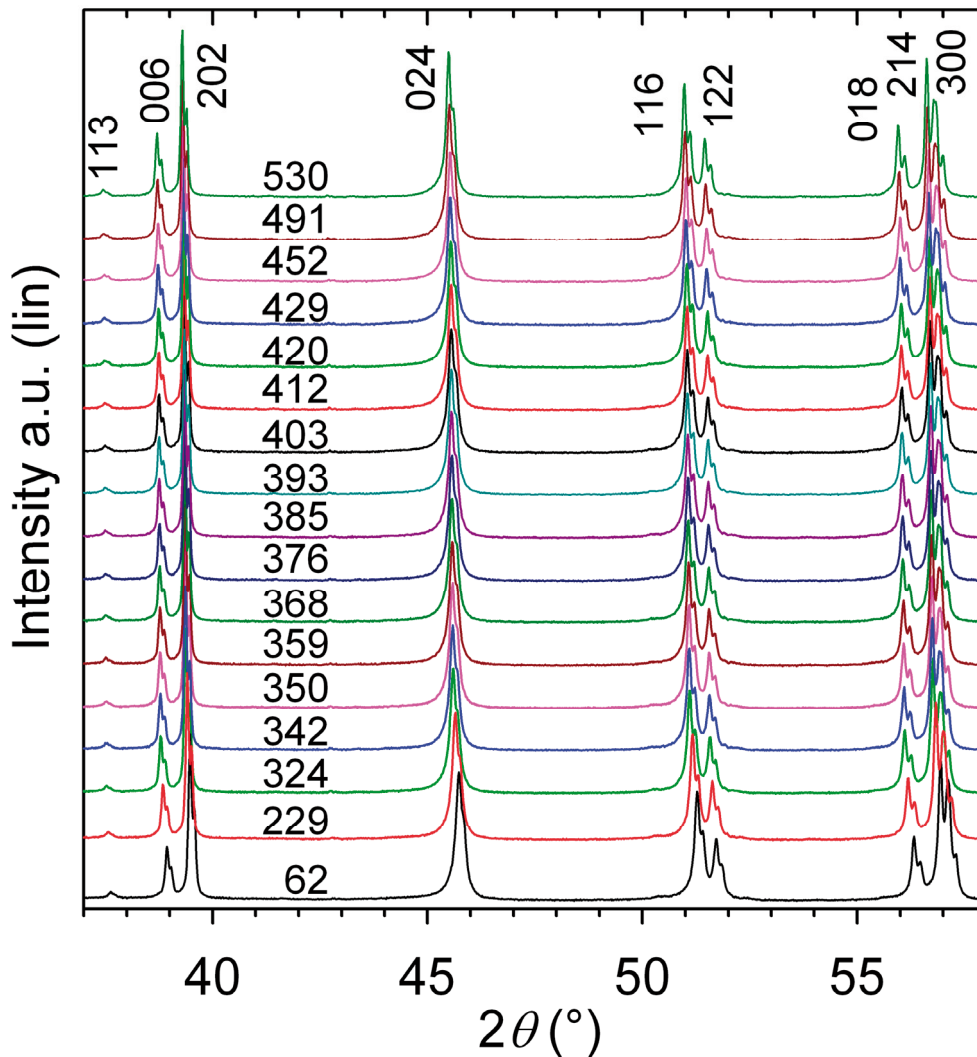


Figure 6.2. HTXRD pattern of a BiFeO_3 polycrystalline sample (> 93 % dense) across $T_N = 370$ °C.

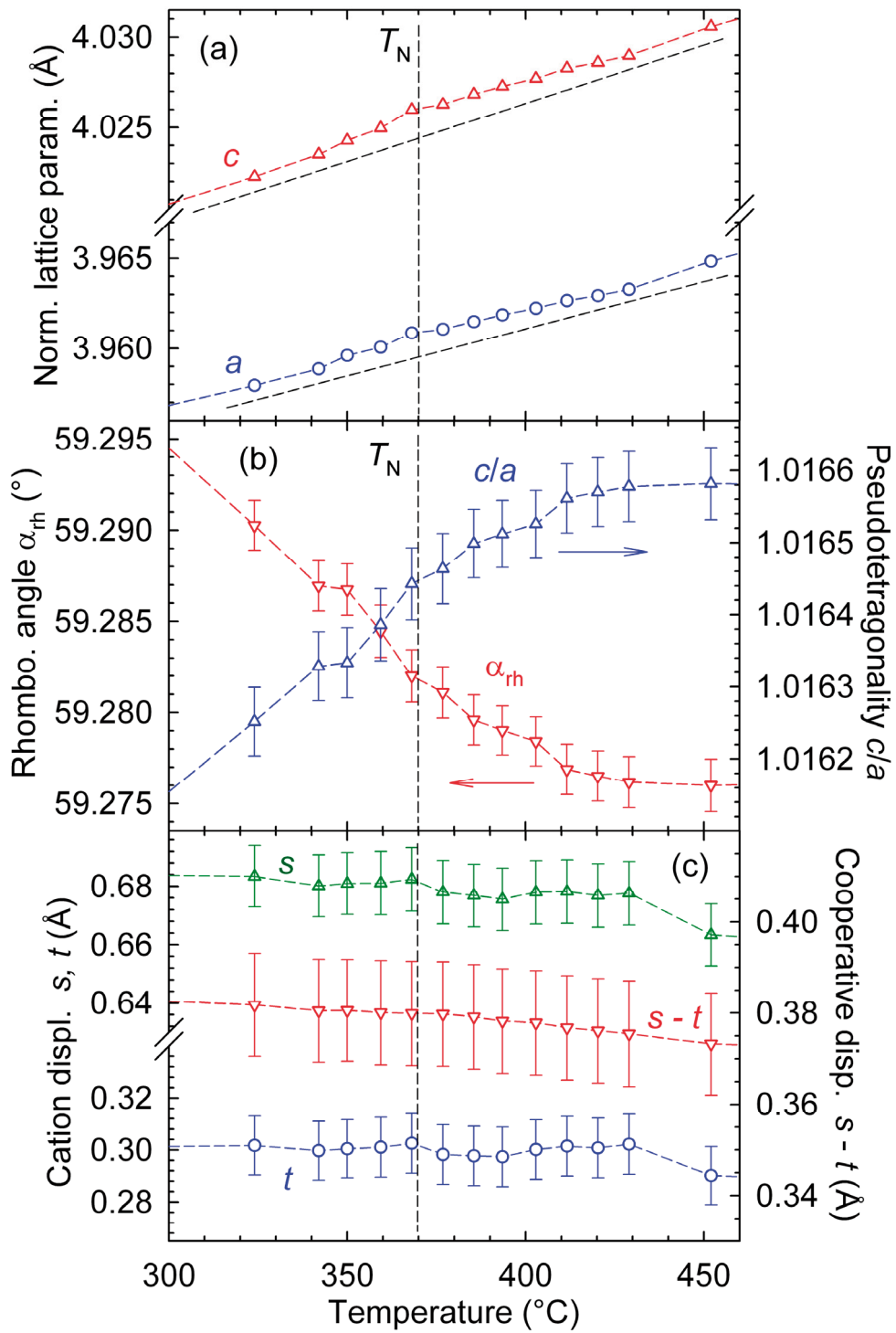


Figure 6.3. Structural parameters of a BiFeO₃ polycrystalline disk (> 93 % dense) across T_N . Dashed lines are guides to the eye.

As the preceding HTXRD investigation was done with a stepwise change in temperature, dilatometry of a polycrystalline samples was performed as a continuous probe of thermal expansion across T_N . The dilatometric trace in Figure 6.4 (a) confirms that the molar volume is continuous across T_N , but with additional continuous expansion, due to the magnetic transition, superimposed on the crystallographic thermal expansion. Just below T_N a cusp is evident in the differential thermal expansion, Figure 6.4 (b).

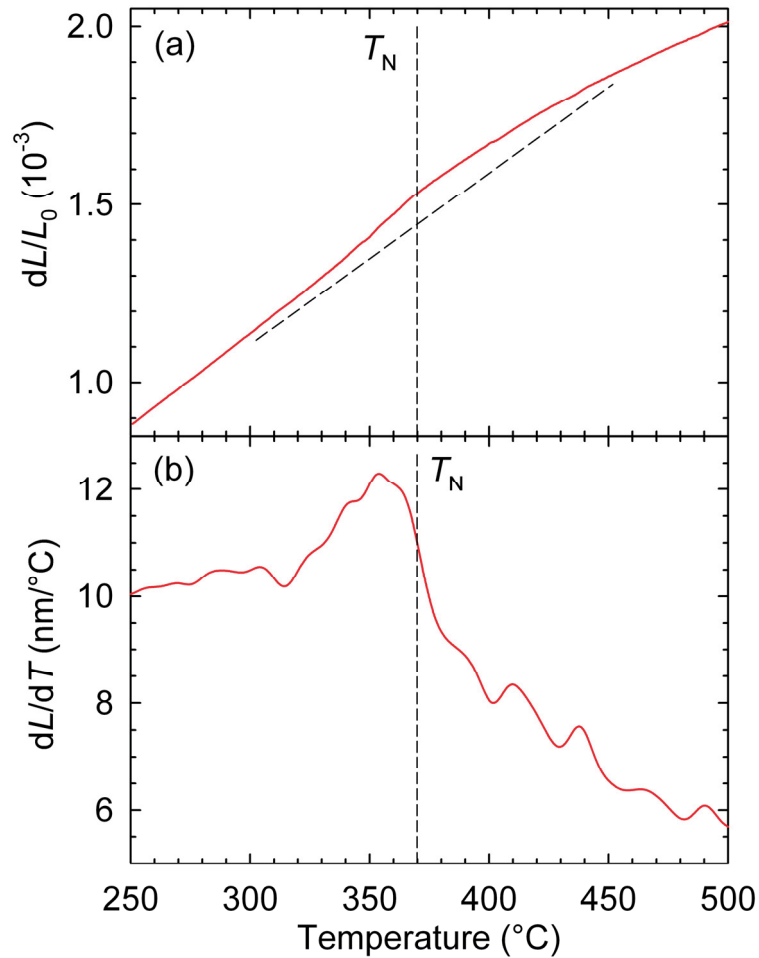


Figure 6.4. (a) Thermal expansion of a BiFeO_3 polycrystalline sample bar (> 93 % dense) across and (b) differential thermal expansion across T_N . The dashed lines are guides to the eye.

Figure 6.5 (a) shows that the electrical conductivity of a polycrystalline sample bar is continuous across T_N upon both heating and cooling, indicating that there are no abrupt structural changes at T_N . Differentiation of the electrical conductivity gives the activation energy of electrical conduction, E_a , Figure 6.5 (b). Upon both heating and cooling, E_a passes through a maximum at T_N , resembling the behaviour of the differential thermal expansion in Figure 6.4 (b).

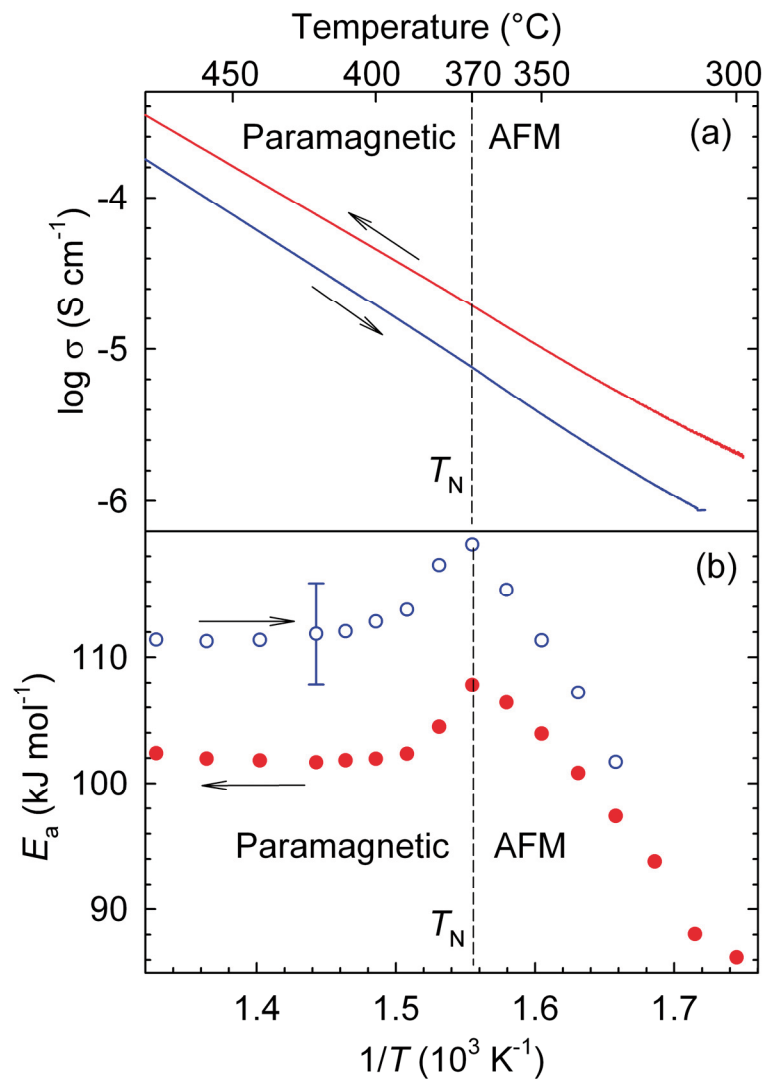


Figure 6.5. (a) Electrical conductivity of a BiFeO_3 polycrystalline sample bar (> 93 % dense) in air and (b) activation energy E_a for conduction across T_N . The dashed line is a guide to the eye.

6.3 Polymorphic transitions

Differential thermal analysis (DTA) in different atmospheres identified three thermal events, with onsets at 830 ± 5 , 925 ± 5 and $940\text{-}970$ °C in Figure 6.6. The temperature of the ferroelectric transition T_C at 830 °C is in good accordance with previous studies.^{159, 301, 311} The endothermic peak at 925 °C is interpreted as the temperature of the transition from the paraelectric to the cubic polymorph, T_{cub} . An endothermic peak at about $925\text{-}930$ °C has also previously been reported.^{159, 301} The distinct thermal signature points to a first order phase transition. Peritectic decomposition gives rise to the largest endothermic peak, with onset at $940\text{-}970$ °C, T_p . The decomposition at the peritectic temperature involves partial melting of the solid, thus the large amount of heat associated with this reaction. Given that the transition at T_C is strongly first order, the relative magnitudes of the endothermic events point to a less abrupt first order transition at T_{cub} . Neither T_C nor T_{cub} is sensitive to the atmosphere, and no systematic difference in T_C nor T_{cub} was found. The lack of influence of the atmosphere demonstrates clearly that these phase transitions are not accompanied by possible thermal reduction of the oxidation state of Fe. An increase in the onset temperature of peritectic decomposition in O_2 atmosphere was observed and reproduced. Although a subtle endothermic peak is observed just above T_{cub} for both measurements in O_2 , it is too small to correspond to peritectic decomposition. In O_2 atmosphere the peritectic decomposition starts at approx. $960\text{-}970$ °C, which has also been reported as the decomposition temperature of $\text{Bi}_2\text{Fe}_4\text{O}_9$.¹⁵⁹

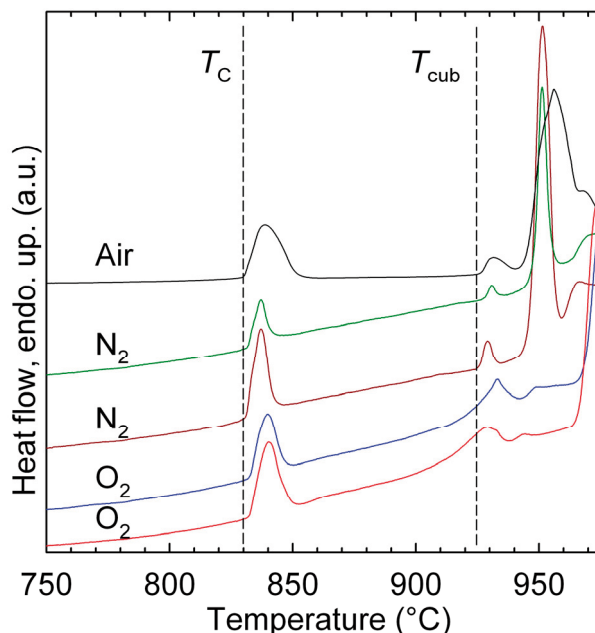


Figure 6.6. DTA trace of BiFeO_3 bulk powder in air, N_2 and O_2 atmospheres. The ferroelectric Curie temperature and transition to cubic phase are denoted as T_C and T_{cub} , respectively. Dashed lines are guides to the eye.

At T_C the volume of transition, $\Delta_{\text{trs}}V$, is large and negative, as shown by dilatometry of a dense ($> 93\%$) ceramic polycrystal in Figure 6.7. At T_{cub} the thermal expansion anomaly identifies $\Delta_{\text{trs}}V$ as positive. Both discontinuous volume and thermal hysteresis, as shown in the inset of Figure 6.7, is consistent with a first order phase transition at T_{cub} . Thermally induced creep and possibly sintering is superimposed on the crystallographic thermal expansion resulting in an apparent volume decrease between T_C and T_{cub} , and the difference in thermal expansion upon heating and cooling. Absolute values of $\Delta_{\text{trs}}V$ could not be determined from the dilatometer data, but the sign and relative magnitudes of the thermal expansion anomalies at T_C and T_{cub} unambiguously show that $\Delta_{\text{trs}}V_{T_C} < 0$, $\Delta_{\text{trs}}V_{T_{\text{cub}}} > 0$ and $|\Delta_{\text{trs}}V_{T_C}| \gg |\Delta_{\text{trs}}V_{T_{\text{cub}}}|$. The steep rise in volume upon cooling through T_C is probably related to the geometry of the dilatometric measurement setup, and the relatively fast heating and cooling rates of $5\text{ }^\circ\text{C}/\text{min}$. Discontinuous expansion of the sample gives sharper signals than discontinuous contraction.

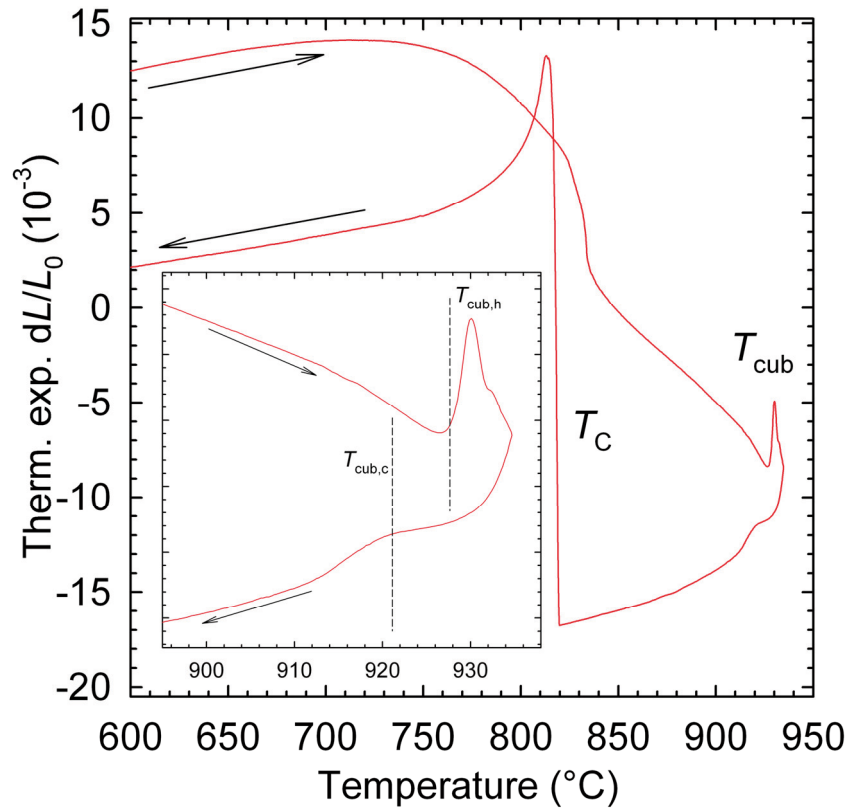


Figure 6.7. Dilatometric trace of a dense BiFeO₃ polycrystal in air. Inset: zoom-in on the transition to cubic phase, T_{cub} . Subscripts “h” and “c” refer to the transition upon heating and cooling, respectively.

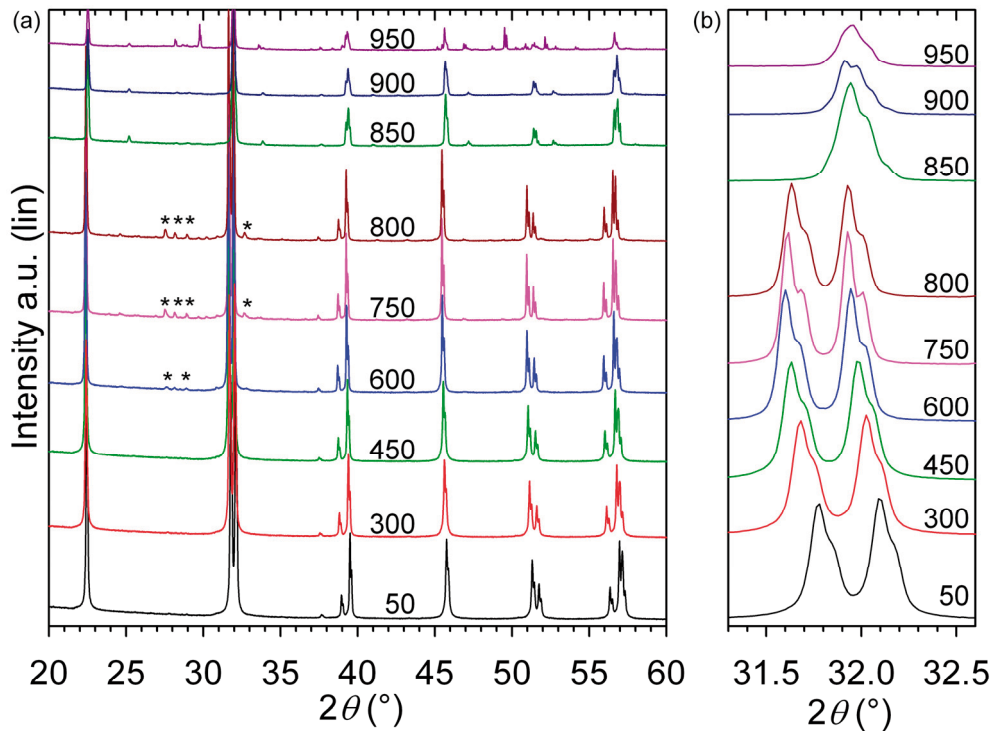


Figure 6.8. (a) HTXRD patterns of bulk BiFeO_3 powder in air, labels refer to the temperature in $^\circ\text{C}$. Asterisks (*) denote reflections from the secondary phases $\text{Bi}_{25}\text{FeO}_{39}$ and $\text{Bi}_2\text{Fe}_4\text{O}_9$. (b) Zoom-in on the $(110)_{\text{cub}}$ reflection.

HTXRD was performed to investigate the symmetry of the paraelectric phase and to confirm that the phase transition at T_{cub} really corresponds to a transition to a cubic aristotype structure $Pm\bar{3}m$. Below T_C there are no evident changes in the XRD patterns in Figure 6.8 (a), in accordance with previous reports.³⁶⁷ The ferroelectric transition occurs between 800 and 850 $^\circ\text{C}$, in concordance with DTA and dilatometry measurements. The paraelectric phase has a distinct different XRD pattern with new superreflections appearing at 850 $^\circ\text{C}$. At 950 $^\circ\text{C}$ the sample has partially decomposed as the peritectic temperature has been exceeded. The presence of weak reflections due to $\text{Bi}_{25}\text{FeO}_{39}$ and $\text{Bi}_2\text{Fe}_4\text{O}_9$ in the 600–800 $^\circ\text{C}$ temperature interval is explained in chapter 5.3. A large negative $\Delta_{\text{trs}}V$ is evident from the shift of the $(110)_{\text{cub}}$ reflection towards higher 2θ values above T_C , and the less pronounced splitting of this reflection points to a less distorted unit cell.

A second and third series of HTXRD patterns recorded in the temperature range 800–925 $^\circ\text{C}$ are displayed together in Figure 6.9. Superreflections denoted with asterisks (*) prevail up to the highest temperature reached before complete decomposition (a log scale is used in Figure 6.9 (a) for plotting to highlight these reflections). At 917 $^\circ\text{C}$ one single reflection due to partial decomposition appears at 28.8 $^\circ 2\theta$, more reflections appear at 921 $^\circ\text{C}$ and at 925 $^\circ\text{C}$ all the reflections due to decomposition can be indexed according to the pattern of mullite, $\text{Bi}_2\text{Fe}_4\text{O}_9$.

(JCPDS 72-1832). In addition, the curved background of the pattern, increasing from 917 to 925 °C, shows the existence of a liquid phase at these temperatures. Decomposition of BiFeO₃ into Bi₂Fe₄O₉ and a bismuth oxide rich liquid is in accordance with recent phase diagrams.^{159, 301-302} Zoom-in on the (110)_{cub} reflection evidences the triplet splitting in the paraelectric phase. The combination of a triplet (110)_{cub} reflection and the super-reflections (*) points to GdFeO₃-type paraelectric structure with space group *Pbnm* and Glazer tilt system $a^-a^-b^+$, which was first identified through a HTNPD study by Arnold *et al.*³¹¹

The pure cubic phase was thus not reached before the decomposition was initiated, as the triplet splitting of the (110) pseudo-cubic reflection did not disappear at 925 °C, as highlighted by an arrow. Close examination of the thermal evolution of the Bragg reflection in Figure 6.9 (b) shows anomalous shift of both 2θ position and FWHM from 921 to 925 °C. We suggest that the origin of this anomaly is the presence of two phases at this temperature, orthorhombic *Pbnm* and cubic *Pm $\bar{3}m$* , accounting for the increased FWHM. The latter polymorph is expected to display a higher unit cell volume at T_{cub} than the former due to straightening of Fe-O-Fe bonds, hence the shift towards a lower 2θ value. Observation of two phases across the ferroelectric transition, T_C , is demonstrated in Figure 6.9 (c). The signature of the ferroelectric *R3c* polymorph is still visible at 840 °C, and does not fully disappear before at 850 °C. Thermal gradients in the sample is an experimental artefact which can be difficult to detect and control, and which would explain the observation of the ferroelectric polymorph well above T_C . Coexistence of the ferroelectric and paraelectric polymorph about T_C has been suggested⁴⁰ as the explanation of the apparently monoclinic paraelectric phase reported by Haumont *et al.*³⁰¹

Rietveld refinement of the HTXRD pattern in Figure 6.10 recorded at 889 °C confirmed the paraelectric structure to belong to the space group *Pbnm*. The space group *Pbnm* allows reconstruction of both splitting of the strong Bragg reflections as well as the position and intensity of the reflections from oxygen planes due to octahedral tilting. Attempts to refine the pattern recorded at 889 °C using other space groups like e.g. *P2₁/m*, *C2/m*, *Cmcm*, *I4/mcm*, *Ibmm*, *P4bm*, *Pbcm* and *Pna2₁* were unsuccessful, as not all the weak reflections could be reconstructed properly. Structural details of the refinement presented in Table 6.1 are in good accordance with those reported by Arnold *et al.*,³¹¹ but the lattice parameters are systematically 0.07-0.09 % smaller.

Table 6.1 Refined structural parameters from an XRD pattern recorded at 889 °C within the space group *Pbnm*, GOF = 2.12, $R_{\text{exp}} = 1.03$ and $R_{\text{wp}} = 2.18$.

Latt. param.	a (Å)	B (Å)	c (Å)	V (Å ³)
	5.6114(80)	5.6427(42)	7.9675(99)	252.28(71)
Atom	Site	x	y	z
Bi	4c	0.998(5)	0.024(2)	¼
Fe	4a	½	0	0
O(1)	4c	0.05(8)	0.48(8)	¼
O(2)	8d	0.71(3)	0.29(7)	0.03(8)

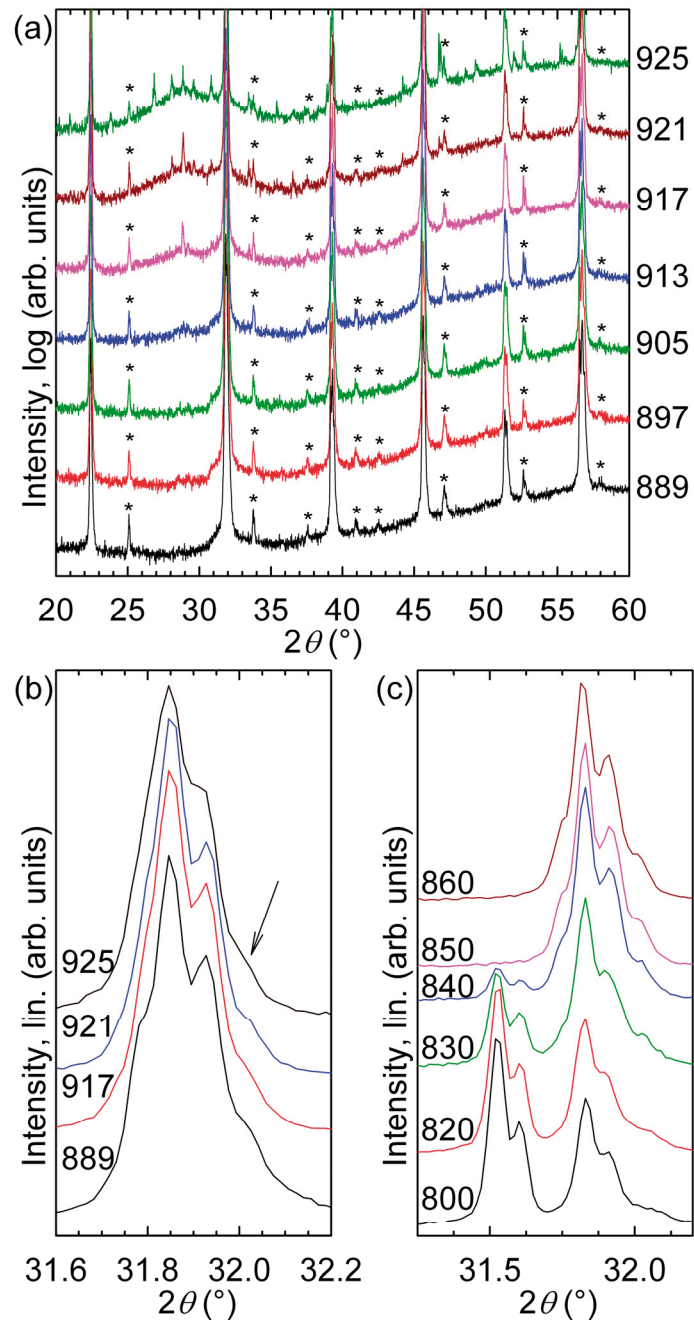


Figure 6.9. HTXRD patterns of BiFeO₃ at selected temperatures, from two different measurements. (a) Plotted on a common log scale to highlight the superstructure reflections (*) and the reflections due to partial decomposition to mullite (Bi₂Fe₄O₉) and liquid when approaching the peritectic temperature. (b) The pseudo-cubic (110) reflection from panel (a) plotted on a linear scale. The arrow shows the splitting of this reflection into a triplet. (c) The pseudo-cubic (110) reflection from a second measurement to display coexistence of two phases in the vicinity of $T_C = 820\text{-}830$ °C.

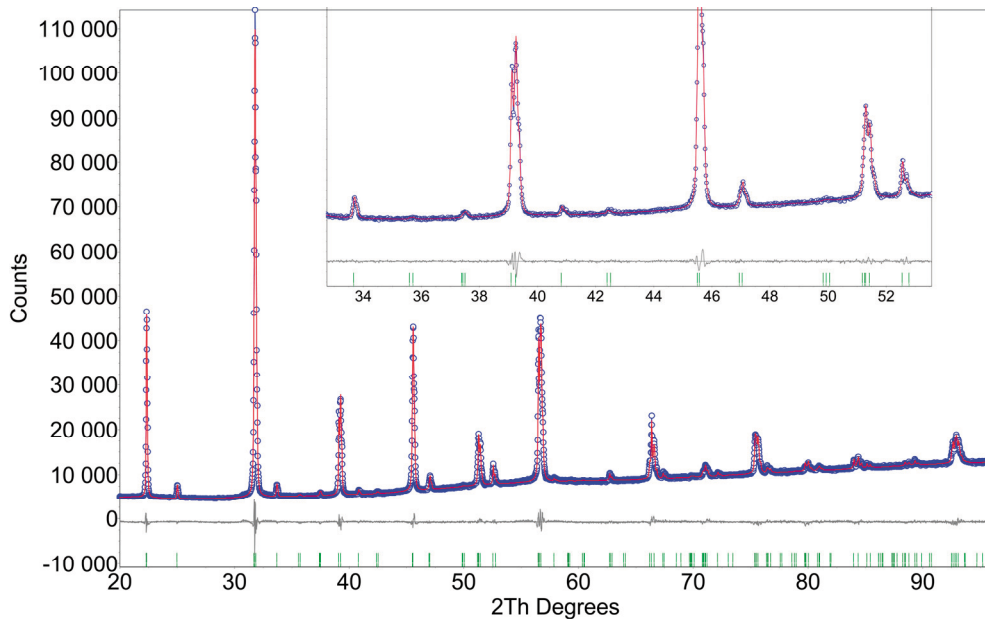


Figure 6.10. Rietveld refinement within the space group $Pbnm$ of an XRD pattern of BiFeO_3 recorded at $889\text{ }^\circ\text{C}$. Refined structural details are given in Table 6.1.

Refined lattice parameters in Figure 6.11 (a) show that the thermal expansion in the ferroelectric polymorph is both anisotropic and strongly non-linear, in accordance with HTPND studies.^{311, 367} In contrast with the prototype ferroelectric perovskite PbTiO_3 ,³⁸⁷ the unit cell of BiFeO_3 expands along polar axis of BiFeO_3 with increasing temperature up to about $100\text{ }^\circ\text{C}$ below T_C . The c -axis expands faster with temperature than the a -axis, and the maximum unit cell distortion c/a , or minimum rhombohedral angle α_{th} , occurs at about $450\text{ }^\circ\text{C}$, as shown in Figure 6.11 (b). The primitive unit cell volume of $\sim 64\text{ \AA}^3$ at T_C decreases by $\sim 1.5\%$ into the paraelectric phase. The unit cell distortion of the paraelectric structure also decreases with increasing temperature. The cooperative cation displacements $s - t$ decreases weakly with temperature towards T_C , but retain a large finite value just below T_C . At $925\text{ }^\circ\text{C}$ refinement of the pattern within the $Pbnm$ space group yields an anomalous shift in lattice parameters and unit cell distortion towards a metrically cubic structure. This is in concordance with the interpretation that the HTXRD pattern recorded at $925\text{ }^\circ\text{C}$ contains both the paraelectric $Pbnm$ polymorph and a fraction of the cubic $Pm\bar{3}m$ polymorph, in addition to the products from partial peritectic decomposition. A cubic phase was shown by HTXRD at $880\text{--}900\text{ }^\circ\text{C}$ of $\text{BiFe}_{0.7}\text{Mn}_{0.3}\text{O}_3$ in chapter 7, implying that the polymorph reached at $925\text{ }^\circ\text{C}$ belongs to the cubic aristotype structure with space group $Pm\bar{3}m$. Mn-substitution stabilises the cubic polymorph to lower temperatures and over a larger temperature interval compared to pure BiFeO_3 .³⁸⁸

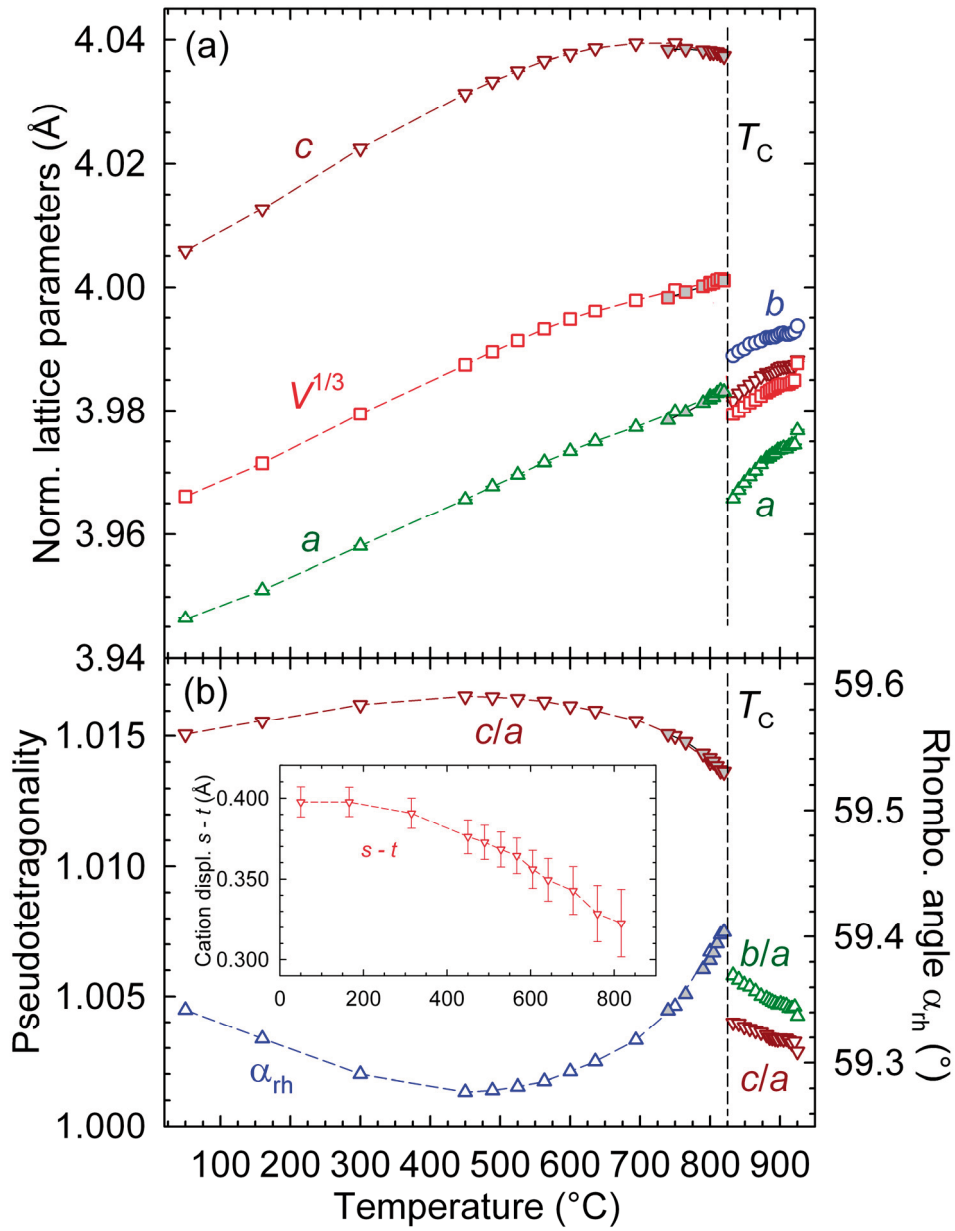


Figure 6.11. (a) Refined normalised lattice parameters and unit cell volume of BiFeO_3 . Grey-filled symbols are from an additional series of measurements close to T_C . (b) Unit cell distortion quantified by the rhombohedral angle α_{rh} and unit cell distortions c/a and b/a . Inset: cooperative cation displacements in the $R3c$ phase.

Normalised lattice parameters ($a_{\text{norm}} = 2^{-1/2} a_{\text{ortho}}$, $b_{\text{norm}} = 2^{-1/2} b_{\text{ortho}}$ and $c_{\text{norm}} = 1/2 c_{\text{ortho}}$) and atomic positions of the orthorhombic $Pbnm$ polymorph are displayed in Figure 6.12 (a). Refined atomic positions within the $Pbnm$ structure are displayed in Figure 6.12 (b-d). Scattered oxygen positions are due to the insensitivity of oxygen to X-rays.

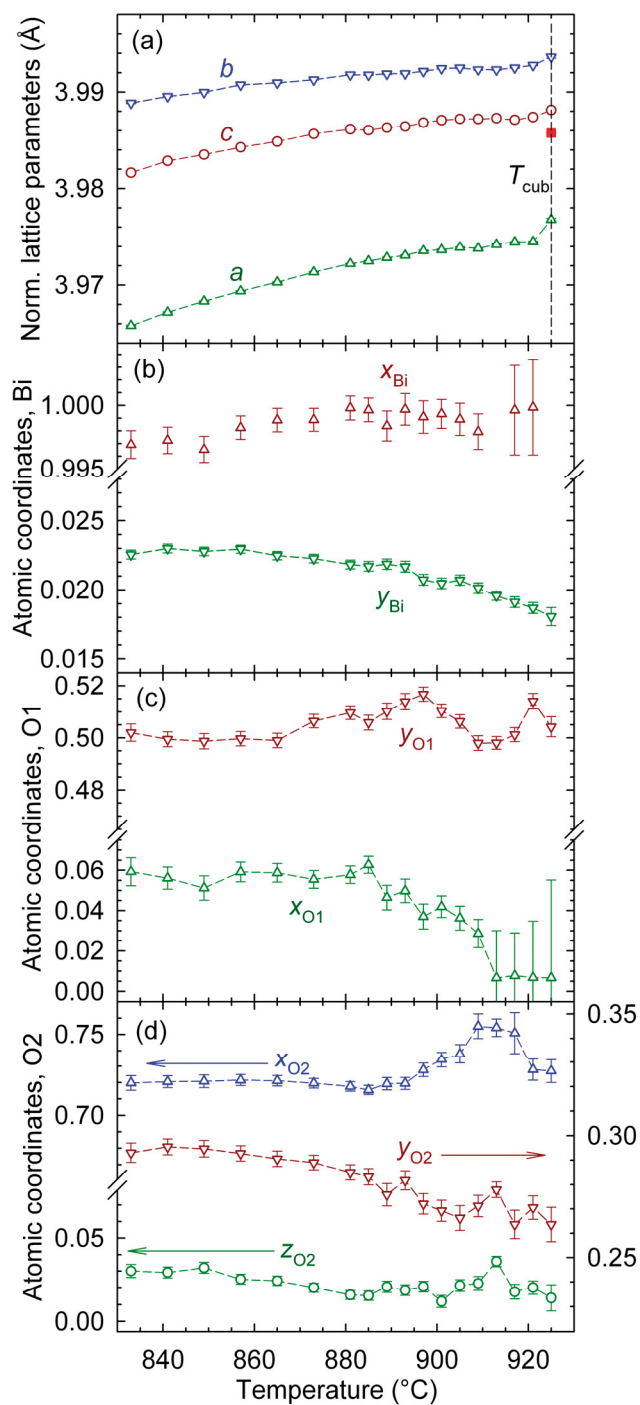


Figure 6.12. (a) Refined normalised lattice parameters in the paraelectric *Pbnm* polymorph. Parameters refined within the cubic structure at 925 °C are depicted with a filled square. Atomic coordinates for (b) Bi, (c) O1 and (d) O2. Atomic coordinates in *Pbnm*: Bi ($x_{Bi}, y_{Bi}, 1/4$), Fe ($1/2, 0, 0$), O1 ($x_{O1}, y_{O1}, 1/4$) and O2 (x_{O2}, y_{O2}, z_{O2}). Filled symbols are from this study, open symbols from ref. ³¹¹.

The electrical conductivity of a dense polycrystal was measured in O₂ atmosphere since DTA indicated higher stability in O₂ than air (Figure 5.16 (b)). The discontinuous increase in conductivity seen in Figure 6.13 (a) across T_C is in accordance with the negative sign of $\Delta_{\text{trs}} V_{T_C}$.³⁶⁶

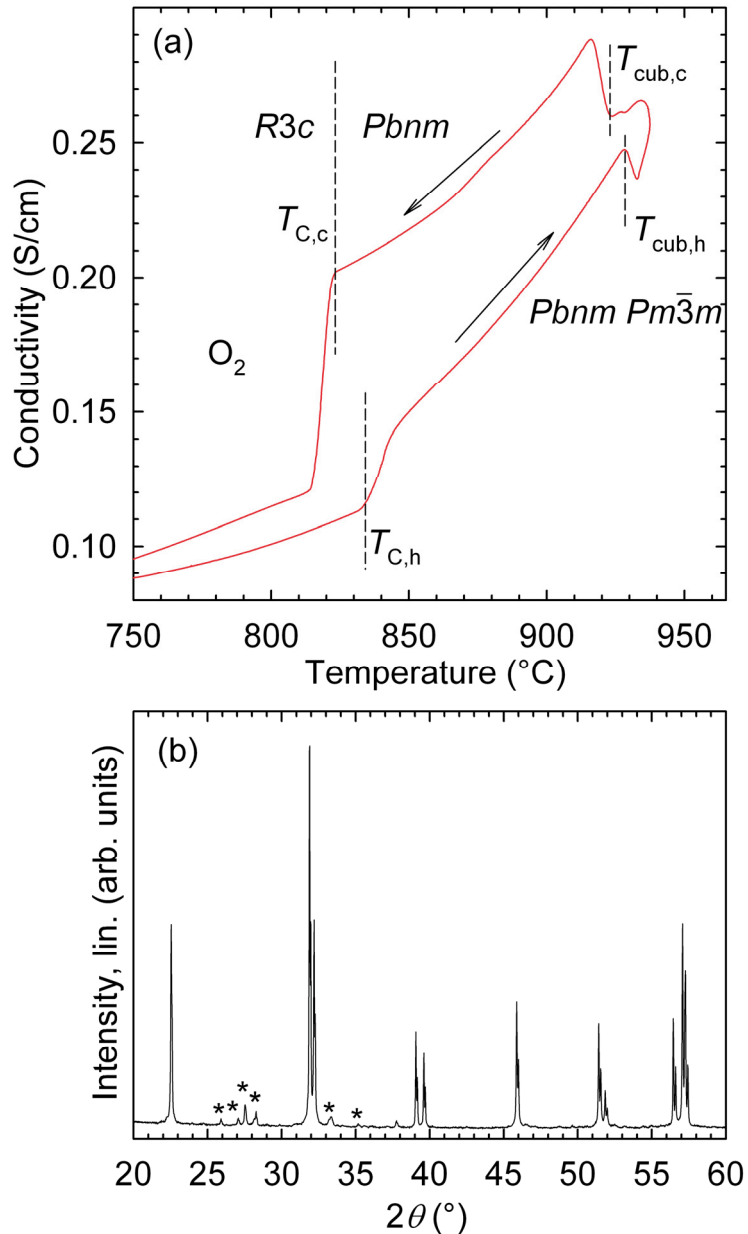


Figure 6.13. (a) Electrical conductivity of a dense BiFeO₃ polycrystalline bar in O₂ atmosphere. $T_{C,h}$ and $T_{C,c}$ denote T_C upon heating and cooling, respectively. (b) XRD pattern of a crushed part of the sample after the measurement, asterisks (*) denote Bragg reflections from silenite and mullite phases due to partial decomposition.

At T_{cub} there is a change of the slope $d\sigma/dT$ from positive to negative, which was also observed by Palai *et al.*,¹⁵⁹ who interpreted this as an insulator to metal transition. Upon increasing temperature the slope $d\sigma/dT$ changes sign again to positive, and upon cooling the same feature appears. The cubic phase, with larger molar volume, is less conducting than the denser *Pbnm* polymorph. When entering the *Pbnm* phase region upon cooling the conductivity increases abruptly, consistent with the smaller unit cell volume of this phase compared to the cubic. The sign and magnitude of the discontinuous conductivity anomalies at T_C and T_{cub} reflect the sign and magnitude of the thermal expansion anomalies found by dilatometry in Figure 6.7. A finite, narrow temperature interval with negative $d\sigma/dT$ slope is therefore only observed due to the kinetics of the phase transition and does not reflect a transition to an intermediate structure.

The difference in conductivity upon heating and cooling is related to possible creep and minor deformation of the sample. Some interface reaction between the Pt electrodes and the sample is also expected.³⁷¹ Ex-situ XRD of a crushed part of the polycrystalline sample after the conductivity measurement revealed negligible partial decomposition into mullite ($\text{Bi}_2\text{Fe}_4\text{O}_9$) and sillenite ($\text{Bi}_{25}\text{FeO}_{39}$), as shown in Figure 6.13 (b).

The conductivity measurement in O_2 was repeated on a pristine polycrystalline BiFeO_3 sample (Figure 6.14 (a)) and the findings in Figure 6.13 (a) were reproduced. Thermal hysteresis and discontinuous electrical conductivity confirms the first order nature of this reversible, first order phase transition. The influence of the atmosphere on the electrical conductivity was investigated by *in-situ* change of the atmosphere from O_2 to N_2 at 850 °C. BiFeO_3 is thermodynamically stable relative to mullite and sillenite at 850 °C, and equilibration due to change of atmosphere is expected to occur in the time scale of the experiment since cation mobility is relatively fast (the solid state reaction synthesis of BiFeO_3 from Bi_2O_3 and Fe_2O_3 is completed in minutes at this temperature).³⁸⁹ Heating in N_2 atmosphere (Figure 6.14 (b)), demonstrates that the absolute conductivity is higher than in O_2 atmosphere. Anomalies associated with T_{cub} is not observed before 933 °C, with a change of the slope $d\sigma/dT$ from positive to negative, as observed in O_2 atmosphere. At 936 °C a steep rise in conductivity is observed, followed by irregular conductivity behaviour, similar to that observed by Palai *et al.*¹⁵⁹ Since this feature was not reproduced upon cooling, we interpret this as partial peritectic decomposition with concomitant formation of a liquid phase. *Ex situ* XRD of a crushed part of the pellet after the conductivity measurement showed substantial decomposition of BiFeO_3 into $\text{Bi}_2\text{Fe}_4\text{O}_9$ and $\text{Bi}_{25}\text{FeO}_{39}$ (Figure 6.14 (c)).

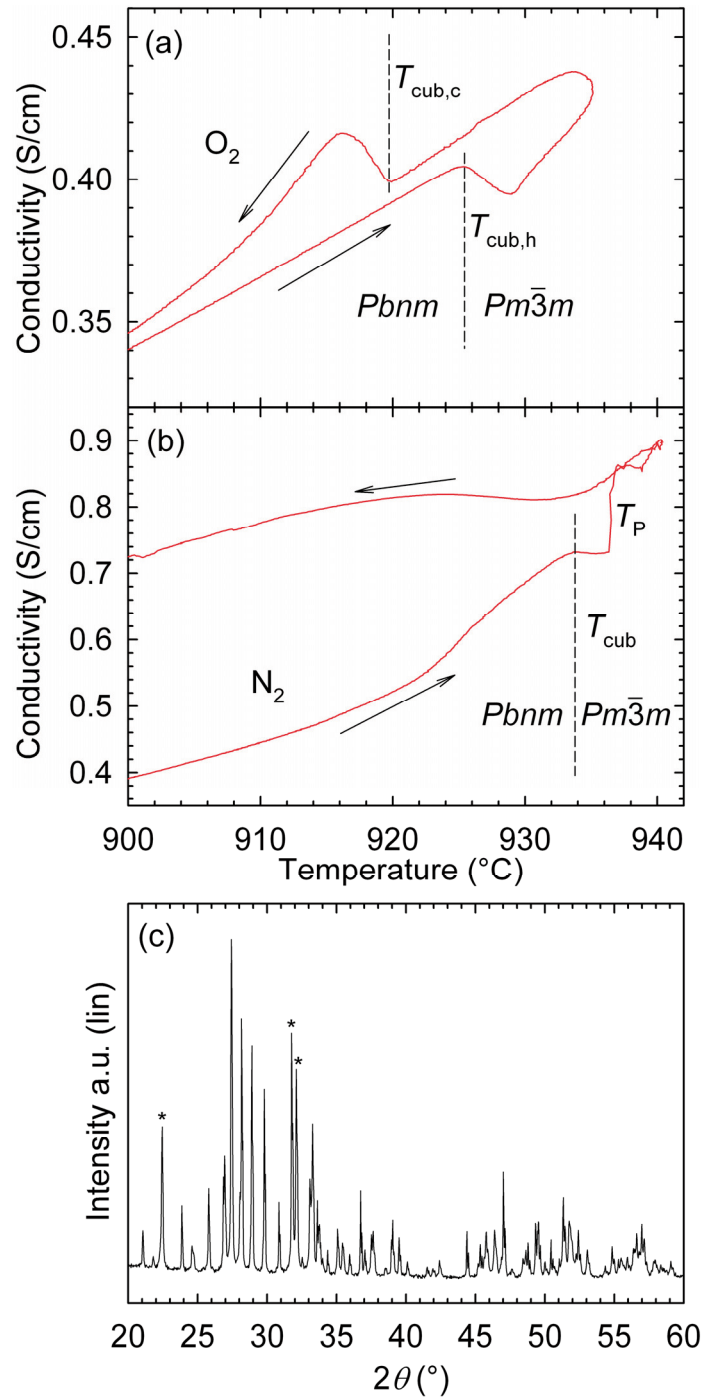


Figure 6.14. (a) Electrical conductivity of a dense BiFeO₃ polycrystalline bar in O₂ atmosphere. $T_{C,h}$ and $T_{C,c}$ denote T_C upon heating and cooling, respectively. (b) Conductivity of the same sample bar after *in-situ* change of atmosphere to N₂ followed by 1 h equilibration at 850 °C. (c) XRD pattern of a crushed part of the sample after the measurement in N₂ atmosphere, asterisks (*) denote Bragg reflections from residual perovskite BiFeO₃ after partial peritectic decomposition.

6.4 Discussion

6.4.1 The Néel transition

The structural evolution, thermal expansion, calorimetric trace, magnetic susceptibility and electrical conductivity across T_N all point to a continuous transition, meaning a second order transition. In first order transitions

$$\frac{\partial G}{\partial T} = -S \quad \text{and} \quad \frac{\partial G}{\partial P} = V \quad (6.1)$$

are both discontinuous, while in second order transitions the first derivative of Gibbs energy is continuous. Second order transitions are defined by discontinuities in the second derivative of Gibbs energy:

$$\frac{\partial^2 G}{\partial T^2} = \left(-\frac{\partial S}{\partial T} \right)_P = -\frac{C_p}{T}, \quad \frac{\partial^2 G}{\partial P^2} = \left(\frac{\partial V}{\partial P} \right)_T = -\beta V \quad \text{and} \quad \frac{\partial^2 G}{\partial P \partial T} = \left(\frac{\partial V}{\partial T} \right)_P = \alpha V \quad (6.2)$$

where β is the isothermal compressibility and α the isobaric thermal expansivity. A continuous structural evolution across T_N is in disagreement with previous work,¹⁰⁴⁻¹⁰⁵ and it is proposed that the non-linear expansion superimposed on the thermal expansion across T_N is the origin of this discrepancy. The nearly isotropic lattice expansion is accompanied by a cusp in the activation energy for electrical conduction, which can be attributed to a larger conduction bandgap as the unit cell expands, or larger hopping distance in a polaron picture.

In the related material BiMnO₃ the magnetisation goes continuously to zero at the ferromagnetic T_C , where anisotropic, continuous lattice anomalies occur.¹⁹³ Cusps in the thermal expansion coefficients at T_N have also been observed at T_N in HoMnO₃.³⁹⁰ Lattice anomalies and spin-lattice coupling is not restricted to multiferroic or magnetoelectric materials. Magnetoelastic coupling is known to occur in RTiO₃ (R = La, Nd, Sm, Gd, Y), represented by continuous anomalies in the dielectric constant and lattice parameters.³⁹¹ Thermal expansion anomalies and continuous lattice expansion similar to the present work was also reported for RTiO₃, indicating that the anomalies observed at T_N for BiFeO₃ is mainly due to the loss of magnetic ordering and not multiferroicity or magnetoelectric coupling. However, it should be noted that the magnitude of the phonon anomalies at T_N were an order of magnitude larger for BiFeO₃ than the magnetically similar paraelectric EuFeO₃, where Fe³⁺ is in a centrosymmetric position.³⁷⁸ Fe³⁺ in BiFeO₃ is displaced from the centrosymmetric position, and loss of antiferromagnetic ordering, and loss of Dzhyaloshinskii-Moriya interaction is anticipated to affect the atomic positions.

6.4.2 The ferroelectric transition and the paraelectric polymorph

The paraelectric polymorph has been confirmed by the present work to belong to the orthorhombic GdFeO₃-structure with space group $Pbnm$ and Glazer tilt system

$a^-a^+b^+$. Centrosymmetry implies that the $Pbnm$ structure is paraelectric, thus the $R3c \leftrightarrow Pbnm$ at $T_C = 820\text{-}830$ °C is indeed the ferroelectric transition of BiFeO_3 . The space group $Pbnm$ is the most abundant among III-III perovskites.^{124, 346} A transition from $R3c$ to $Pbnm$ at 697 ° was also recently reported for $\text{Bi}_{0.91}\text{La}_{0.05}\text{Tb}_{0.04}\text{FeO}_3$.³⁹² The structure of the paraelectric polymorph is displayed in Figure 6.17.

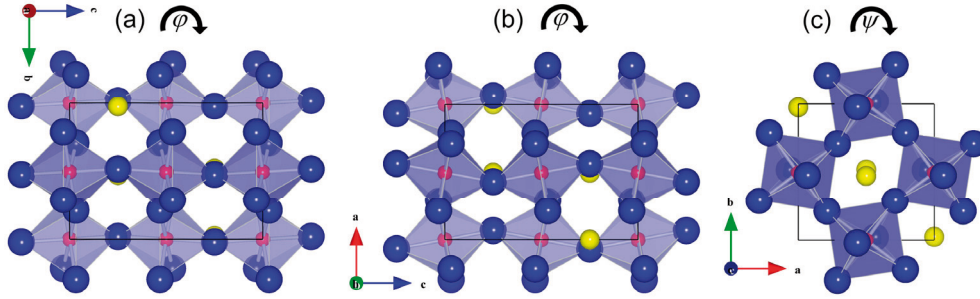


Figure 6.15. Structure of the paraelectric, ferroelastic polymorph of BiFeO_3 with space group $Pbnm$ seen along (a) the a -axis, (b) the b -axis and (c) the c -axis. Bi^{3+} , Fe^{3+} and O^{2-} are represented by yellow, red and blue spheres, respectively.

The octahedral tilt system changes across T_C , followed by a change of ferroelastic domain structure. The tilt angles do however not change substantially across T_C . At 830 °C the antiferrodistortive tilt angle φ along the a - and b -axis is about 10.8 °, while the ferrodistortive tilt angle ψ along the c -axis is about 8.8 °.³¹¹ The atomic position of O(2) (Table 6.1) in the $Pbnm$ unit cell can be given as $(3/4 - u, 1/4 + v, w)$, where $u = v = w = 0$ would correspond to untilted octahedra.³⁹³ The antiferrodistortive tilt angle φ about the a - and b -axis can then be calculated from:

$$\varphi = \arctan\left(4\sqrt{2}w\right). \quad (6.3)$$

The ferrodistortive tilt angle ψ about the c -axis is given by:

$$\psi = \arctan\left(2(u + v)\right). \quad (6.4)$$

The temperature dependence of the ferro- and antiferrodistortive tilt angles are shown in Figure 6.16. Although the values are somewhat scattered, with large uncertainties due to the insensitivity of X-rays to oxygen positions, both tilt angles decrease with increasing temperature, towards a less distorted unit cell. It appears that the antiferrodistortive tilt angle φ decreases faster with temperature than the ferrodistortive ψ , but higher quality diffraction data are necessary to determine this feature with certainty.

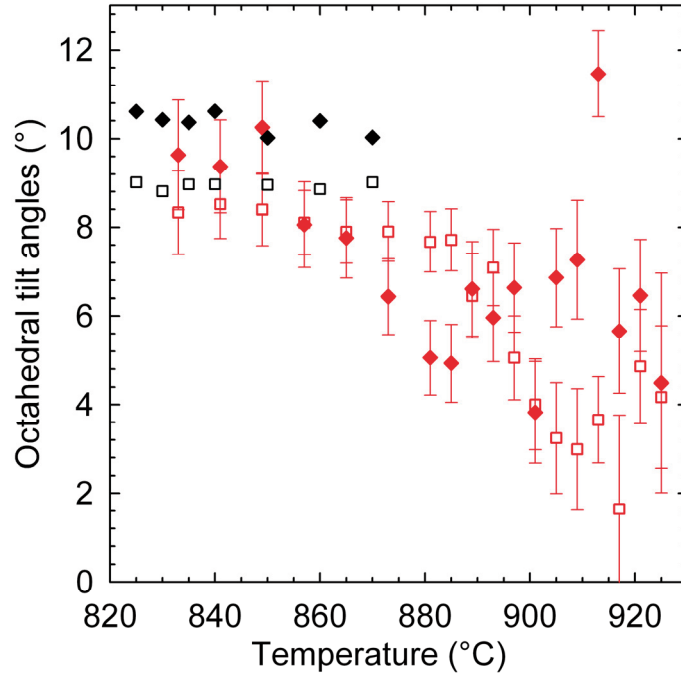


Figure 6.16. Octahedral tilt angles in the *Pbnm* polymorph of BiFeO_3 , diamonds depict the antiferrodistortive tilt angle ϕ and squares the ferrodistortive tilt angle ψ . Red symbols are from this work, black symbols from literature.³¹¹

The ferroelectric $R3c \leftrightarrow Pbnm$ is shown to be first order from non-zero $\Delta_{\text{us}}V_{T_c}$ and $\Delta_{\text{us}}H_{T_c}$, in addition to discontinuous electrical conductivity. A continuous second order phase transition is forbidden from Landau theory in terms of symmetry restrictions as there is no group-subgroup relationship between $R3c$ and $Pbnm$. The higher conductivity of the *Pbnm* polymorph can be rationalised from the smaller unit cell volume compared to the ferroelectric polymorph, implying a shorter hopping distance in terms of polarons, or smaller bandgap in a band structure picture.

Lattice parameters increase faster with temperature in the *Pbnm* phase than the *R3c* polymorph. In the *R3c* phase the thermal expansion of the chemical bonds and decreasing octahedral tilts³⁶⁷ are partly counteracted by decreasing cation displacements. The combination of straightening bond angles through decreasing octahedral tilt angles (Figure 6.16) and increasing bond lengths in the *Pbnm* phase explains the steeper rise in unit cell volume with temperature.³⁹⁴

The ferroelectric transition is not soft-mode driven, but the exact microscopic mechanism of this phase transition has not been conclusively determined. Although BiFeO_3 is arguably a proper displacive ferroelectric, opposed to improper or order-disorder ferroelectrics, the ferroelectric transition is neither simply displacive, as in PbTiO_3 ,^{68, 387} nor order-disorder, as in LiNbO_3 .³⁷²⁻³⁷³ The robust ferroelectricity of BiFeO_3 has very little in common with the weak ferroelectricity induced by magnetic ordering in the improper ferroelectric multiferroics with $T_C < T_N$. To the

author's knowledge, no other perovskite with a $R3c \leftrightarrow Pbnm$ ferroelectric transition is known. Based on finite temperature Monte Carlo simulations Kornev and Bellaiche suggested that the ferroelectric transition of BiFeO_3 is neither proper nor improper, but belongs to a rare trigger-type transition.³⁹⁵ Unfortunately their simulations predicted a tetragonal paraelectric phase with space group $I4/mcm$, thus the relevance of their suggestions is difficult to assess. Here follows an alternative interpretation of the ferroelectric transition.

Below T_C the polar c -axis begins to contract, as shown in Figure 6.11 (a), suggesting that the ferroelectric order is beginning to weaken. Cation positions from two HTNPD studies, shown in the inset of Figure 6.17, also point to decreased ferroelectric order just below T_C , resembling incomplete softening of a Γ -mode. In terms of polyhedral volume ratios,^{103, 121-122} V_A/V_B , the ferroelectric space group $R3c$ is stable for larger values than the paraelectric space group $Pbnm$.¹²³⁻¹²⁴ Polyhedral volume ratios can be calculated from the formulas^{103, 124}

$$R3c: \quad \frac{V_A}{V_B} \approx 6 \cos^2(\omega) - 1 \quad (6.5)$$

$$Pbnm: \quad \frac{V_A}{V_B} \approx 6 \cos^2(\varphi) \cos(\psi) - 1 \quad (6.6)$$

or

$$\frac{V_A}{V_B} = -1 + \frac{3}{2(3 - 4x_{O(2)})(y_{O(2)} - 4y_{O(1)}z_{O(2)}) - 4z_{O(2)}(4x_{O(2)} - 2x_{O(1)} - 3) + 2x_{O(2)} - 1} \quad (6.7)$$

where the atomic positions in eq. (6.7) refer to the labels in Table 6.1. Eq. (6.7) was preferred for the calculation of V_A/V_B in the $Pbnm$ polymorph. The estimate in eq. (6.6) gives approximately the same values as eq. (6.7), and the same evolution with temperature. V_A/V_B increases slowly towards T_C in the $R3c$ and decreases abruptly across the ferroelectric transition (Figure 6.17). The c -axis and the polar displacements of the cations (inset in Figure 6.17) decrease towards T_C , the polyhedral volume ratio inferred from oxygen positions increases slowly, meaning that the BiO_{12} dodecahedron expands relative to the FeO_6 octahedron. Upon approaching T_C , Bi^{3+} moves away from the face of the closest FeO_6 octahedron along the c -axis until the polar $R3c$ structure becomes unstable at T_C . Destabilisation of the polar cation displacements cause the BiO_{12} and FeO_6 polyhedra to contract, and the V_A/V_B ratio decreases abruptly. We suggest that this may be the instability that drives the ferroelectric transition: thermal destabilisation of the cation displacements drives the transition with concomitant change of tilt system yielding the $Pbnm$ structure, not opposite.

The displacement of Bi^{3+} is larger than that of Fe^{3+} in the $R3c$ polymorph, the room temperature value 4.73 of V_A/V_B is on the border of the stability regions of the $Pbnm$ structure (below) and $R\bar{3}c$ (above).¹²³⁻¹²⁴ The large volume contraction at T_C implies contraction of both the BiO_{12} dodecahedron and the FeO_6 octahedron, and given the larger displacement of Bi^{3+} , the former polyhedron will contract more than the latter, yielding a smaller V_A/V_B ratio in the paraelectric phase. In retrospect, based on this reasoning, $Pbnm$ could have been predicted as the paraelectric structure of BiFeO_3 . Compared to YFeO_3 and LnFeO_3 ($\text{Ln} = \text{La}, \dots, \text{Lu}$), all with $Pbnm$ structure, the stereochemical activity of the Bi^{3+} $6s^2$ lone pair distinguishes BiFeO_3 . At the temperature T_C , which this partial covalent bonding no longer stabilises the polar displacement of Bi^{3+} , BiFeO_3 becomes isostructural with YFeO_3 and LnFeO_3 .

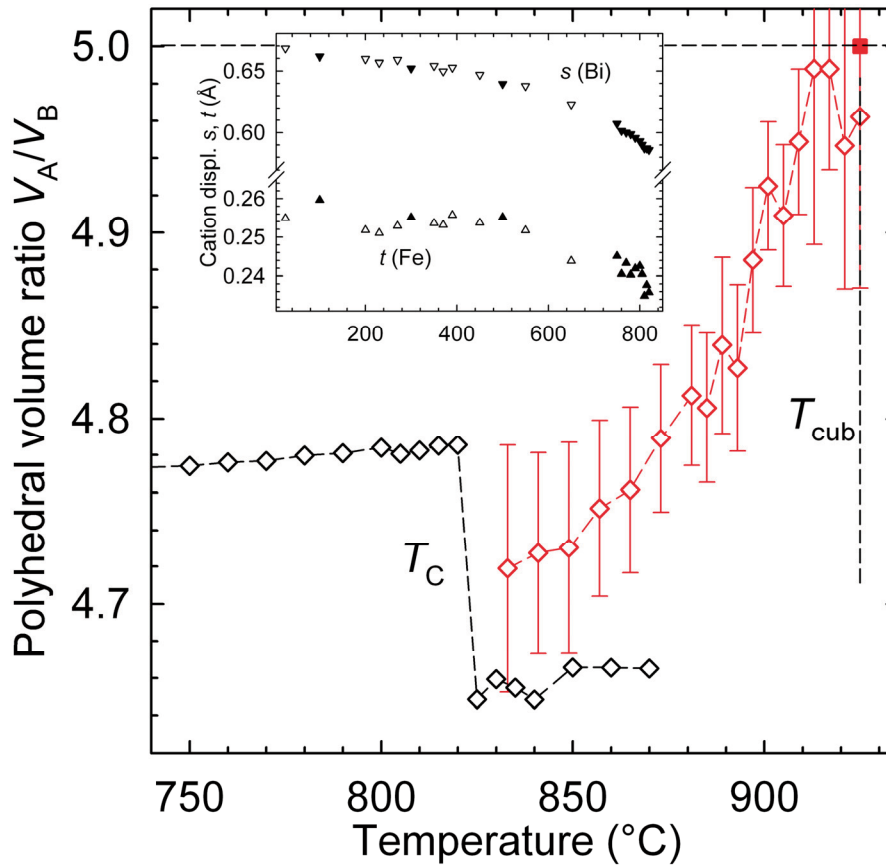


Figure 6.17. Polyhedral volume ratio V_A/V_B . Red diamond symbols represent values obtained from this study and powder neutron diffraction data from ref.³¹¹ are represented by black diamonds. The filled, red square denotes the value of V_A/V_B for cubic perovskite $Pm\bar{3}m$, which is 5.0 by definition,^{103, 123} and also depicted by a horizontal dashed line. Inset: cation displacements from references³¹¹ (filled symbols) and³⁶⁷ (open symbols).

6.4.3 The cubic polymorph

Attempts to observe pure BiFeO₃ as cubic single phase by HTXRD were unsuccessful, but isostructural BiFe_{0.7}Mn_{0.3}O₃ was shown to become cubic at high temperature (chapter 7).³⁸⁸ The transition to the cubic polymorph is first order, evidenced from non-zero $\Delta_{\text{trs}}H_{T_{\text{cub}}}$ and $\Delta_{\text{trs}}V_{T_{\text{cub}}}$ and discontinuous electrical conductivity. In contrast with the large negative $\Delta_{\text{trs}}V_{T_{\text{C}}}$, $\Delta_{\text{trs}}V_{T_{\text{cub}}}$ is smaller and positive. The sign and magnitude of the discontinuous decrease of electrical conductivity across T_{cub} is consistent with the sign and magnitude of the increase across T_{C} . A positive $\Delta_{\text{trs}}V_{T_{\text{cub}}}$ follows from the discontinuous straightening of the Fe-O-Fe angles from the $Pbnm$ structure with tilt system $\bar{a}\bar{a}b^+$ to the $Pm\bar{3}m$ structure with tilt system $a^0a^0a^0$. For the transition $Pbnm \leftrightarrow Pm\bar{3}m$ a zero or negative $\Delta_{\text{trs}}V_{T_{\text{cub}}}$ could hypothetically occur if the transition was accompanied by a transition from HS to LS Fe³⁺, but no experimental data points to a HS to LS transition induced by temperature in BiFeO₃. A HS to LS transition is unlikely to be induced by increasing temperature.

There is no smooth transition from $Pbnm$ to $Pm\bar{3}m$ with neither increasing temperature nor increasing Goldschmidt tolerance factor.³⁹⁶⁻³⁹⁷ Centrosymmetric $R\bar{3}c$ is a commonly found intermediate polymorph between $Pbnm$ and $Pm\bar{3}m$ in perovskites, e.g. LaGaO₃ and La_{1-x}Sr_xFeO_{3- δ} .^{345, 398} The absence of an intermediate polymorph before reaching the cubic phase is novel, and the transition sequence $R\bar{3}c \leftrightarrow Pbnm \leftrightarrow Pm\bar{3}m$ is hitherto unique in perovskites. Recently, a first order insulator to metal transition with $\Delta_{\text{trs}}V < 0$ from $Pbnm$ to either $Pbnm$ (isostructural) or $Immb$ at $925 \pm \text{ }^\circ\text{C}$ was suggested.³⁹⁹ Polyhedral volume ratios calculated from the atomic positions inferred from HTXRD in this study show an increasing trend towards 5.0 (Figure 6.17), which is the value for the cubic polymorph $Pm\bar{3}m$, indirectly supporting a direct transition to $Pm\bar{3}m$.

A second order, or nearly second order transition, at T_{cub} was reported by both Palai *et al.*¹⁵⁹ and Redfern *et al.*,³⁹⁹ but a second order transition from $Pbnm$ to $Pm\bar{3}m$ is not allowed from the symmetry restrictions imposed by Landau theory, as there is no group-subgroup relationship between $Pm\bar{3}m$ and $Pbnm$. To obtain the $Pbnm$ structure from $Pm\bar{3}m$, two phonon modes must freeze, at the M_3 and R_{25} points of the Brillouin zone. Although a direct second order transition from $Pbnm$ to $Pm\bar{3}m$ is not allowed, two consecutive second order transitions are possible, from $Pbnm$ to $P4/mcm$ to $Pm\bar{3}m$, as shown in Figure 6.18. Neither the present data, not available literature suggest two consecutive second order transitions, all the available evidence points to one first order transition from $Pbnm$ to $Pm\bar{3}m$.

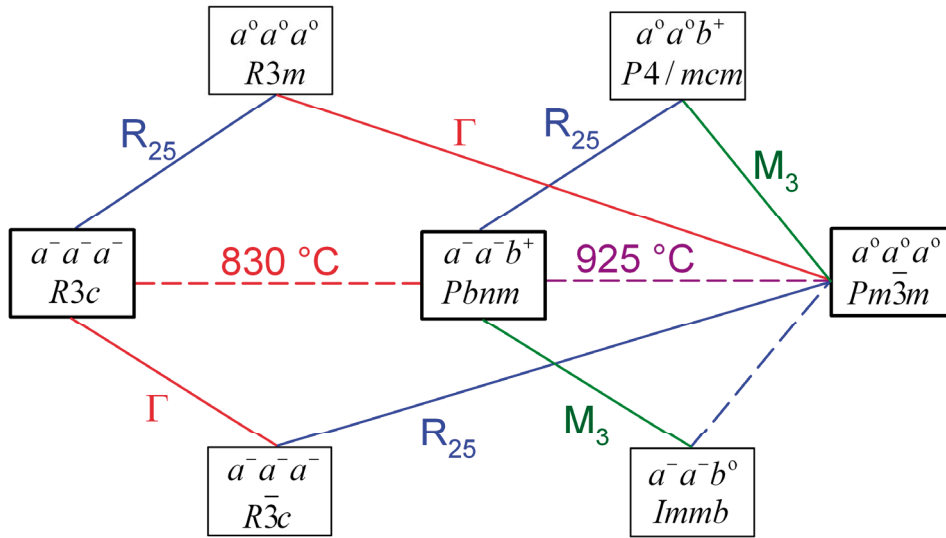


Figure 6.18. Symmetry relations between the space groups of the polymorphs of BiFeO_3 (boxes with thick lines) and other related space groups. Solid lines depict transitions which are allowed to be second order from group theory, while second order transitions are forbidden by Landau theory for the transitions denoted by dashed lines, and must hence be first order. Red lines contain at least one polar Γ -mode, blue lines correspond to antiferrodistortive R_{25} -modes while green lines denote ferrodistortive M_3 -modes. Based on references⁴⁰⁰⁻⁴⁰³.

The cubic polymorph with the aristotype perovskite structure with space group $Pm\bar{3}m$ can not be ferroelastic, and thus no ferroic ordering is present in this phase. All the three polymorphs of BiFeO_3 exhibit semiconductivity, in disagreement with previous experimental reports and theoretical studies suggesting a metallic or semimetallic cubic polymorph.^{40, 158-159, 399} A positive $\Delta_{\text{ts}} V_{T_{\text{cub}}} > 0$ makes the typical Mott transition^{48, 404-406} an unlikely scenario. An insulator to metal transition originating from straightening of the Fe-O-Fe angle and change of even number to an odd number of electrons per unit cell was proposed by Redfern *et al.*, implying that BiFeO_3 is a band insulator below T_{cub} .³⁹⁹ BiFeO_3 is probably better described as a charge-transfer insulator than a Mott-Hubbard insulator in the Zaanen, Sawatzky and Allen scheme.^{152-153, 160, 407} Related perovskite III-ferrites like LaFeO_3 are charge transfer insulators.^{72, 408} All the lanthanide III-ferrites (Fe^{3+} is $t_{2g}^3 e_g^2$) are known to be insulators at ambient pressure, while alkaline earth IV-ferrates can undergo metal insulator transitions (Fe^{4+} from $t_{2g}^3 e_g^1$ to $t_{2g}^3 \sigma^{*1}$ where t_{2g} electrons are localised and e_g electrons itinerant in a σ^* band).⁷² CaFeO_3 becomes metallic at -158 °C while SrFeO_3 is metallic until it is thermally reduced due to formation of Fe(III).⁴⁰⁹ Conducting $\text{Bi}_{0.9}\text{Ca}_{0.1}\text{FeO}_{3-\delta}$ was recently demonstrated,⁴¹⁰ where δ is 0.05 for $x_{\text{Ca}} = 0.1$ given that Fe is predominantly present as +III. In pure BiFeO_3 however, δ has been found to be less than 0.01 at 800 °C,³⁶⁸ and the present data show that BiFeO_3 remains semiconducting in both oxygen and inert

atmosphere (Figure 6.13-14). The data show that +III is the stable oxidation state of Fe in BiFeO₃ until thermal reduction will occur at significantly lower partial pressure of oxygen ($< 10^{-11}$ bar at 900 °C) as observed for SrFeO_{3- δ} ($\delta > 0.5$).⁴¹¹

6.4.4 Comparison of the effect of temperature and pressure on BiFeO₃

The behaviour of BiFeO₃ under high pressure has received less attention than the high temperature behaviour, and at present there is no consensus regarding the sequence of phase transitions and the symmetry of the high pressure polymorphs. A transition to the paraelectric *Pbnm* structure at 13 GPa was theoretically predicted by Ravindran *et al.*,¹¹⁰ and also found experimentally at 10 GPa by Haumont *et al.*, who also found a monoclinic bridging phase with space group *C2/m* at 3.5 GPa.⁴¹² Redfern *et al.* reported the same structural transition sequence with pressure as with temperature, $R3c \leftrightarrow Pbnm \leftrightarrow Pm\bar{3}m$, with transitions occurring at 10 and 47 GPa, respectively.³⁹⁹ A rhombohedral high pressure phase was reported by Gavriluk *et al.*,¹⁶⁰ and $R\bar{3}c$ was found to be the high pressure phase in independent theoretical studies by Zinenko and Pavlovskii⁴¹³⁻⁴¹⁴ and González-Vázquez and Íñiguez.⁴⁰⁷ Different behaviour under compression and decompression was recently reported by Belik *et al.*,⁴¹⁵ who also found a different transition sequence where the orthorhombic structures *Cmmm* and *Ibam* appeared at 4 and 7 GPa, respectively. One of the reasons of the contradicting reports on the high pressure polymorphs may be ferroelastic behaviour and domain reorientation under anisotropic pressure (diamond anvil cells), which could yield diffractograms indicating a higher symmetry than the “actual” under isotropic hydrostatic pressure.

The structural response of a perovskite to high temperature does not necessarily correspond to the response to high pressure. The presence of both an antiferrodistortive mode and a polar, ferroelectric mode makes the comparison non-trivial. Centrosymmetric perovskites with a tolerance factor *t* of less than unity have A-O bonds under tension and B-O bonds under compression, implying that $dt/dP > 0$, thus pressure favours higher symmetry. Zone-boundary distortions (antiferrodistortive) generally increase with pressure, while zone-centre distortions decrease.⁴¹⁶ Re-examination of this rule of thumb explained that if the A-O bonds in III-III perovskites are stiffer than the B-O bonds, dt/dP will be negative, implying that pressure favours lower symmetry.⁴¹⁷⁻⁴¹⁸ The BiO₁₂ dodecahedron is more “expanded” relative to a centrosymmetric state than the FeO₆ octahedron ($s > t$), thus pressure should be expected to decrease the V_A/V_B ratio, eventually favouring the paraelectric *Pbnm* structure. The monoclinic bridging state found by Haumont *et al.*⁴¹² may be a stress-relaxation mechanism related to monoclinic nanodomains found in the rhombohedral ferroelastic LaCoO₃-based perovskites.⁷⁹ Such a monoclinic bridging phase is however not anticipated at the ambient pressure ferroelectric transition. A pressure-induced HS to LS transition for Fe³⁺ was found both experimentally and theoretically to be accompanied by metallic behaviour. The temperature induced transition to cubic structure is accompanied by a positive $\Delta_{\text{trs}} V_{T_{\text{cub}}}$, making a HS to LS transition highly unlikely. There is thus not necessarily a contradiction between a temperature-driven transition to an insulating

cubic phase and a pressure-driven transition to a metallic cubic phase if the HS to LS transition is necessary to make pure BiFeO₃ metallic. The related orthoferrites LaFeO₃ and PrFeO₃ show gradual transitions from HS to LS from 50 GPa. Onset of a metallic state in LaFeO₃ was observed at 120-170 GPa, and a normal metal was extrapolated to occur at 240 GPa.⁴¹⁹

In terms of thermodynamics, $\Delta_{\text{trs}}H$ must be negative upon cooling as the high temperature polymorph will have higher entropy than the low temperature polymorph, the transitions are endothermic upon heating. Opposite signs of $\Delta_{\text{trs}}V_{T_c}$ and $\Delta_{\text{trs}}V_{T_{\text{cub}}}$ thus imply that the Clapeyron slopes of the two transitions are opposite;

$$\frac{dp}{dT_c} = \frac{\Delta_{\text{trs}}H_{T_c}}{T_c\Delta_{\text{trs}}V_{T_c}} < 0 \quad \text{and} \quad \frac{dp}{dT_{\text{cub}}} = \frac{\Delta_{\text{trs}}H_{T_{\text{cub}}}}{T_{\text{cub}}\Delta_{\text{trs}}V_{T_{\text{cub}}}} > 0. \quad (6.8)$$

This is in agreement with the observation of the paraelectric *Pbnm* polymorph at ambient temperature and high pressure. The positive Clapeyron slope of the transition from *Pbnm* to *Pm $\bar{3}m$* initially suggests that the cubic polymorph can not be reached by high pressure. Three theoretical studies found *R $\bar{3}c$* as the high pressure polymorph,^{407, 413-414} and *R $\bar{3}c$* is a commonly observed transitional polymorph when going from *Pbnm* to *Pm $\bar{3}m$* by chemical pressure, hydrostatic pressure and temperature in e.g. LnNiO₃ and LnCoO₃.³⁹⁶⁻³⁹⁷ A theoretical study of the structural stability of BiFeO₃ under pressure found that *Pbnm*, *I2/a* (monoclinic) and *R $\bar{3}c$* are all more stable than the *Pm $\bar{3}m$* structure.¹¹⁰ The related compound LaFeO₃ was found to transform to a tetragonal polymorph at 40 ± 10 GPa,⁴¹⁹ but direct comparison with BiFeO₃ is difficult as the 6s² lone pair of Bi³⁺ makes this cation asymmetric, more polarisable and possibly more compressible than La³⁺. In the pressure-induced paraelectric *Pbnm* phase, the Fe-O bonds may be more compressible than the Bi-O bonds, as observed for A-X and B-X bonds in some other III-III perovskites.⁴¹⁷ More compressible Fe-O bonds translates to an increasing effective tolerance factor and V_A/V_B ratio with pressure, and the possibility of a HS to LS transition renders a pressure-induced *Pbnm* to *Pm $\bar{3}m$* transition hypothetically possible. The *P-T* phase diagram of BiFeO₃ is not by far fully understood, and much experimental work remains.

6.5 Conclusions

The antiferromagnetic to paramagnetic transition at $T_N = 370$ °C has been shown to be continuous second order, evidenced by DSC, magnetic susceptibility, crystal structure and expansion and electrical conductivity. The transition is associated with continuous nearly-isotropic lattice expansion superimposed on the baseline thermal expansion. A peak in the activation energy of electrical conduction at T_N was found.

In the ferroelectric polymorph with space group $R3c$ the thermal expansion is both anisotropic and non-linear. The ferroelectric to paraelectric phase transition at $T_C = 830$ °C is strongly first order with non-zero $\Delta_{\text{trs}}H_{T_C}$ and large $\Delta_{\text{trs}}V_{T_C} < 0$. The electrical conductivity increases discontinuously across T_C , as a consequence of the smaller unit cell volume. The paraelectric crystal structure is confirmed to GdFeO_3 -type with the centrosymmetric space group $Pbnm$ and tilt system $a^-a^-b^+$. The paraelectric polymorph is also a ferroelastic semiconductor, and the unit cell distortion and octahedral tilting decreases with increasing temperature. Loss of polar cation displacements at T_C is suggested as the driving mechanism of the ferroelectric transition, causing a change of the tilt system to the $Pbnm$ structure which is stable for lower polyhedral volume ratios than $R3c$.

The structural transition $Pbnm \leftrightarrow Pm\bar{3}m$ at $T_{\text{cub}} = 925$ °C must be first order evidenced from non-zero $\Delta_{\text{trs}}H_{T_{\text{cub}}}$ and $\Delta_{\text{trs}}V_{T_{\text{cub}}} > 0$, as also predicted from Landau theory. The aristotype cubic perovskite structure is paraelastic, thus no ferroic orders are retained in the cubic polymorph. BiFeO_3 remains a semiconductor also in the cubic polymorph, and no experimental evidence in favour of the previously proposed metallic state was found. The sign and magnitude of the discontinuous changes in electrical conductivity across T_C and T_{cub} correspond to the sign and magnitude of the $\Delta_{\text{trs}}V$ of these first order phase transitions.

7 Oxygen hyperstoichiometric $\text{BiFe}_{1-x}\text{Mn}_x\text{FeO}_{3+\delta}$

7.1 Introduction

Manganese is the only element which can be substituted on the B-site of BiFeO_3 by more than 10 % at ambient pressure. Mn substitution does not alter the space group of $\text{BiFe}_{1-x}\text{Mn}_x\text{O}_3$ for $x \leq 0.3$,^{352, 420} thus the multiferroic properties can be tailored by the Mn content.^{352, 420-421} Correlating structural changes with the Mn content also gives insight to the importance of Fe for the unique properties of BiFeO_3 . The ambient pressure solubility limit is close to $x = 0.3$,⁴²⁰ and high pressure is necessary to form phase pure perovskite for $x > 0.3$.³⁵³ The other end member of the pseudo-binary system BiFeO_3 - BiMnO_3 is also termed a multiferroic material, although it has been debated whether it is polar or antipolar.^{189-190, 193, 195, 197} Oxygen nonstoichiometry has only recently been systematically quantified and shown to change the crystal symmetry and magnetic properties of BiMnO_3 ,⁴²²⁻⁴²³ but has also been reported to influence the high temperature behavior.¹⁹² Manganese is known to readily adopt the oxidation states of +3 and +4 in perovskites, e.g. in paraelectric $\text{LaMnO}_{3+\delta}$.⁴²⁴⁻⁴²⁶ Oxygen nonstoichiometry in pure $\text{BiFeO}_{3+\delta}$ is however < 0.01 at 800 °C.³⁶⁸ Both the ferroelectric T_C and the T_N as well as the unit cell distortion have previously been reported to decrease with Mn substitution,^{352-353, 420-421} but a systematic investigation has been lacking. The influence of the oxygen nonstoichiometry on Mn-substituted BiFeO_3 has not been investigated previously. This chapter presents a systematic study of the effect of Mn substitution and oxygen hyperstoichiometry on the crystal structure, electrical conductivity and phase transition temperatures.

7.2 Results

7.2.1 Oxygen stoichiometry

Oxygen hyperstoichiometry (δ) found by thermogravimetric analysis of $\text{BiFe}_{1-x}\text{Mn}_x\text{O}_{3+\delta}$ samples with different thermal histories is summarised in Table 7.1. The oxygen stoichiometry is determined by the thermal history of the materials due to the possible variation of the valence state of Mn (Mn^{3+} and Mn^{4+}). Samples annealed in N_2 were assumed to be stoichiometric with respect to oxygen. Two significant trends were found: 1) air-quenched samples display less excess oxygen than air cooled samples with equal Mn substitution, 2) oxygen hyperstoichiometry increases with increasing Mn content under equal thermal history. More reducing conditions at higher temperatures yields less excess oxygen in accordance with the predominance diagram of the Mn-O binary system.⁴²⁷

Table 7.1. Thermogravimetric analysis of $\text{BiFe}_{1-x}\text{Mn}_x\text{O}_{3+\delta}$ with different thermal histories.

x	T (°C)	Time (h)	Atm.	History	δ	$x_{\text{Mn(IV)}}$	$\text{Mn}^{4+}/(\text{Mn})$
0.0	900	0.1	Air	Quench (q)	0.00 ± 0.01^a	-	-
0.1	900	0.1	Air	Quench (q)	0.015 ± 0.005	0.030 ± 0.010	0.30
0.1	825	8.0	Air	400°C/h (c)	0.028 ± 0.005	0.056 ± 0.010	0.56
0.2	900	0.1	Air	Quench (q)	0.016 ± 0.005	0.031 ± 0.010	0.16
0.2	825	8.0	Air	400°C/h (c)	0.037 ± 0.005	0.074 ± 0.010	0.37
0.3	900	0.1	Air	Quench (q)	0.030 ± 0.005	0.060 ± 0.010	0.20
0.3	825	8.0	Air	400°C/h (c)	0.059 ± 0.005	0.118 ± 0.010	0.39
0.3	850	0.5	N ₂	400°C/h (c)	0.00^b	0^b	0^b

^aFrom reference ³⁶⁸.

^bAssuming negligible amounts of Mn^{4+} after annealing in N₂.

7.2.2 Crystal structure at ambient temperature

Room temperature X-ray diffraction patterns for all samples could be indexed with the space group $R3c$, thus the ground state space group does not change within the range of Mn substitution and oxygen hyperstoichiometry investigated here. Selected Bragg reflections from XRD shown in figure 7.1 illustrate the effect of Mn substitution (x) and oxygen hyperstoichiometry (δ). The observed splitting of the pseudocubic (110) reflection into $(104)_{\text{hex}}$ and $(110)_{\text{hex}}$ reflections is due to the rhombohedral distortion of the unit cell. This splitting, and the analogous decrease of the splitting of the (111) pseudocubic reflection into $(006)_{\text{hex}}$ and $(202)_{\text{hex}}$ reflections, with increasing Mn content (x) and excess oxygen (δ) reveal that the unit cell becomes less distorted.

Normalised lattice parameters $a = 2^{-1/2}a_{\text{hex}}$, $c = 12^{-1/2}c_{\text{hex}}$ and primitive unit cell volume obtained by Rietveld refinement of the XRD patterns as a function of Mn substitution are shown in Figure 7.2 (a). The lattice parameter c , parallel to the spontaneous polarisation, decreases more rapidly with Mn substitution than the lattice parameter a , implying that the unit cell becomes less distorted, consistent with the evolution of the splitting of the $(110)_{\text{cub}}$ reflection in Figure 7.1. Air cooled samples with more excess oxygen (open symbols in Figure 7.2 (a), see also Table 7.1) display substantially smaller lattice parameters and unit cell volumes than the quenched samples (grey-filled symbols). Filled symbols represent oxygen stoichiometric material with $x = 0.3$ annealed in N₂. Lattice parameters and unit cell volume decrease with increasing Mn substitution also for oxygen stoichiometric materials.

Polar cation displacements (Figure 7.2 (b)) confirm that both Mn substitution and excess oxygen gives a less distorted crystal structure. The displacement of Bi on the A site is more sensitive to Mn substitution and excess oxygen than the displacement of Fe and Mn on the B site, where the substitution takes place. The quantity $s - t$ is the relative displacement of Bi and Fe/Mn, or equivalently the displacement of Fe/Mn from its centrosymmetric position with the unit cell fixed with Bi in *origo*.

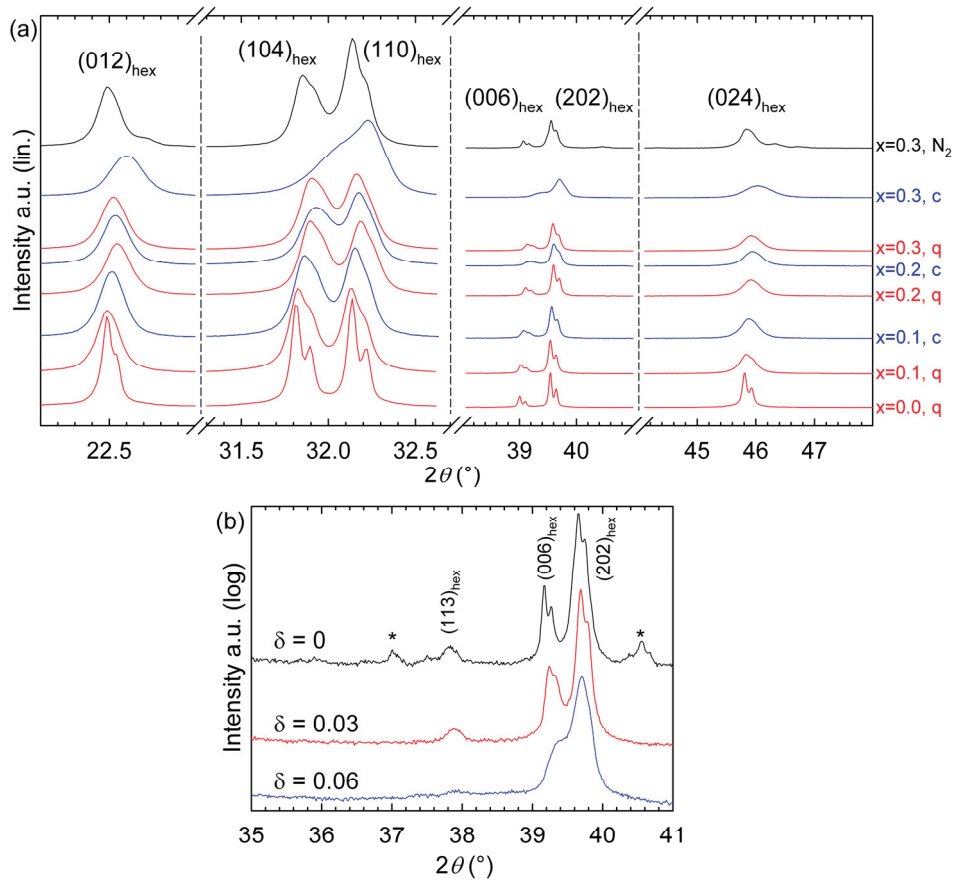


Figure 7.1 (a) X-ray diffractograms displaying selected Bragg peaks reflecting the influence of Mn-substitution (x in $\text{BiFe}_{1-x}\text{Mn}_x\text{O}_{3+\delta}$) and thermal history on the crystal structure. From left to right the reflections are: (100), (110), (111) and (200) in pseudo-cubic indices. Patterns labelled “q” are for materials quenched in air, patterns labelled “c” for materials cooled at $400\text{ }^\circ\text{C h}^{-1}$ in air, and the pattern labelled “N₂” is for material annealed in flowing N₂ atmosphere (see Table 1). (b) The (113)_{hex} reflection distinguishes the space group $R3c$ from e.g. $R3m$. Asterisks (*) denote reflections from impurity phases.

Oxygen positions, which are linked to the antiferrodistortive rotation of oxygen octahedra about the $[001]_{\text{hex}}$ axis, did not converge during the refinements and are not reported, thus higher quality diffraction data are required for a detailed study of the influence of Mn substitution and excess oxygen on this structural feature. Oxygen positions obtained from neutron data reported by Sosnowska *et al.* show that the antiferrodistortive rotation of the oxygen octahedra decreases with increasing Mn substitution.⁴²⁸ The rhombohedral angle α_{rh} (Figure 7.2 (c)) increases with increasing Mn substitution and increasing δ from the value 59.35° in pure BiFeO_3 .

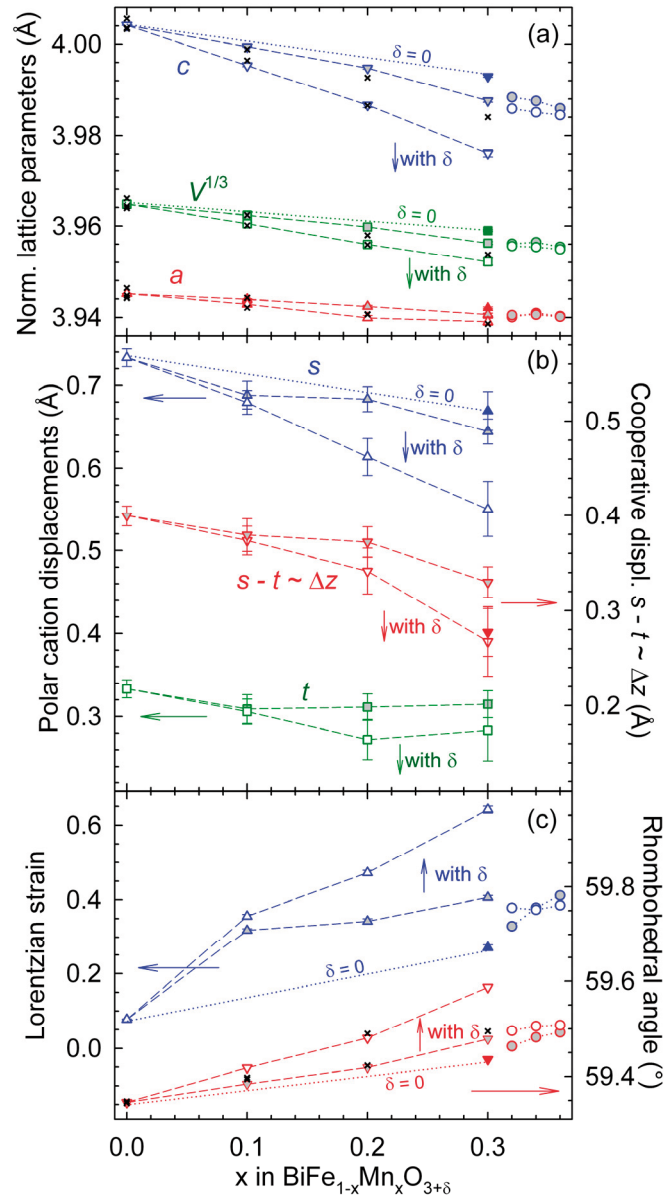


Figure 7.2 Crystallographic properties obtained from Rietveld refinement of XRD patterns in Figure 7.1. Grey-filled symbols are for quenched samples, open symbols for samples cooled with $400\text{ }^{\circ}\text{C h}^{-1}$ and filled symbols for the $x = 0.3$ sample fired in N_2 . Circles refer to the samples in Figure 7.13 with grey-filled and open symbols corresponding to samples fired at 900 and $800\text{ }^{\circ}\text{C}$, respectively. (a) Normalised lattice parameters ($a = 2^{-1/2} a_{\text{hex}}$ and $c = 12^{-1/2} c_{\text{hex}}$) and primitive unit cell volume. (b) Polar cation displacements s (Bi) and t (Fe/Mn) and cooperative polar displacements $s - t$. (c) Refined Lorentzian strain and rhombohedral angle of the unit cell in rhombohedral setting. Literature values from References⁴²⁰ and⁴²⁸ are denoted as \mathbf{x} .

Refined Lorentzian strain increases with increasing Mn substitution and oxygen excess, in concordance with the systematic broadening of the Bragg reflections in Figure 7.1 (a). The Full Width at Half Maximum (FWHM) of the Bragg reflections increases with both increasing x and δ . The FWHM is substantially larger for the sample “0.3, c” than the “0.3, N₂” sample (see caption of Figure 7.1 (a)). The influence of excess oxygen, which has not been accounted for in previous reports on Mn substituted BiFeO₃, is the likely origin of the spread in literature values from references ⁴²⁰ and ⁴²⁸, denoted by \mathbf{x} in Figure 7.2.

7.2.3 Phase transitions

The structural phase transition sequence in BiFe_{0.7}Mn_{0.3}O_{3+ δ} and BiFeO₃ is $R3c \leftrightarrow Pbnm \leftrightarrow Pm\bar{3}m$, evidenced by the HTXRD patterns recorded in air, displayed in Figure 7.3. The intermediate $Pbnm$ polymorph is evident from the combination of superreflections, Figure 7.3. (a), and the triplet splitting of the (110)_{cub} reflection, Figure 7.3 (b), as in BiFeO₃. At 880 and 900 °C the absence of superreflections and splitting of the (110)_{cub} reflection (other than from $K\alpha_1$ and $K\alpha_2$) identifies this phase as the aristotype perovskite structure $Pm\bar{3}m$. This is supported by a significant reduction in the FWHM of the Bragg reflections from 860 to 880 °C, as shown in Figure 7.3 (c). Attempts to refine the patterns collected at 880 and 900 °C within the commonly found space groups $R3m$, $B2mm$, $P2mm$ and $P4mm$ without octahedral tilting resulted in cubic lattice parameters. Mn-substitution stabilises the cubic polymorph at lower temperatures and over a larger temperature interval than in pure BiFeO₃. The 2θ positions of the (110)_{cub} reflections confirm that $\Delta_{\text{trs}}V_{T_c} < 0$ and $\Delta_{\text{trs}}V_{T_{\text{cub}}} > 0$, in accordance with the dilatometric trace in Figure 6.7.

Decomposition into Bi₂₅Fe_{1-y}Mn_yO_{39+ δ} (sillenite) and Bi₂Fe_{4-z}Mn_zO_{9+ δ} (mullite) at intermediate temperatures (750 °C in Figure 7.3 (a)), and reaction back to perovskite at higher temperatures (840 °C), is explained in chapter 5.3. At 920 °C the sample decomposed peritectically to a non-perovskite phase and a liquid phase envisaged by a curved baseline. The measurement was terminated manually.

Lattice parameters in Figure 7.4 (a) for the $R3c$ and $Pbnm$ polymorphs of BiFe_{0.7}Mn_{0.3}O_{3+ δ} behave qualitatively in line with BiFeO₃ in Figure 6.11 (a) and earlier reports.^{159, 301, 311, 366-367} As shown in the inset of Figure 7.4 (a), the primitive unit cell volume increases by 0.5 % from 62.98 Å³ (860 °C, $Pbnm$) to 63.30 Å³ (880 °C, $Pm\bar{3}m$), thus $\Delta_{\text{trs}}V_{T_{\text{cub}}} > 0$, as in pure BiFeO₃. The unit cell distortion c/a and α_{th} behave qualitatively as for BiFeO₃, and the maximum unit cell distortion occurs at 100-200 °C (Figure 7.4 (b)). The unit cell distortions b/a and c/a decreases in the $Pbnm$ phase with increasing temperature, as for BiFeO₃.

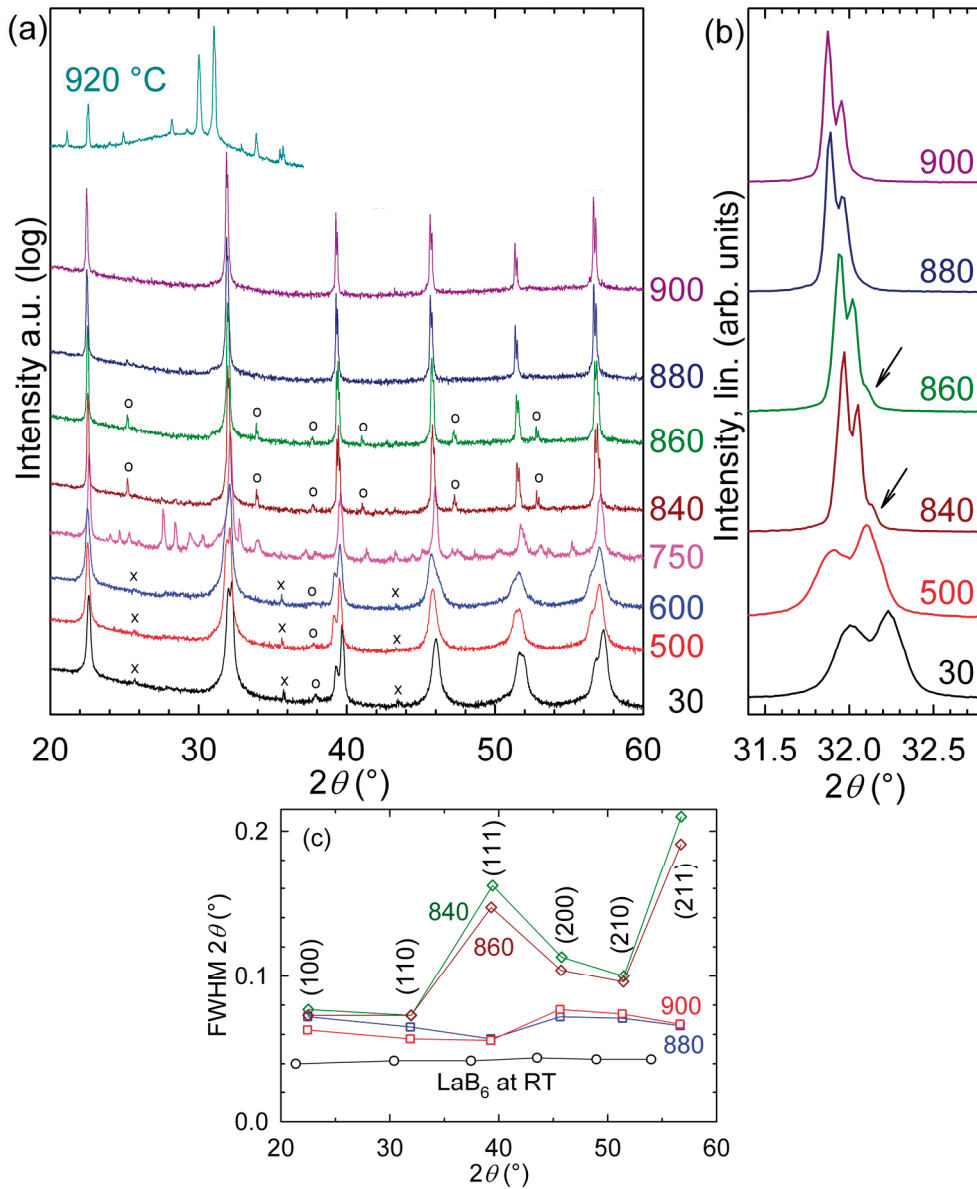


Figure 7.3. HTXRD patterns of $\text{BiFe}_{0.7}\text{Mn}_{0.3}\text{O}_{3+\delta}$ at selected temperatures. (a) Superreflections identifying the $R3c$ and the $Pbnm$ phases are denoted by o , while x denotes (012), (104) and (113) corundum reflections of the Al_2O_3 sample holder, which are not present at ambient temperature measurements with conventional sample holders. (b) Thermal evolution of the (110) pseudocubic reflection (linear scale), the arrows highlight the splitting into a triplet for the orthorhombic $Pbnm$ phase. (c) FWHM of Bragg reflections recorded below and above the $Pbnm$ to $Pm\bar{3}m$ transition. Bragg reflections are given with pseudocubic indices. FWHM for a LaB_6 NIST standard material at ambient temperature with identical optics is included for comparison.

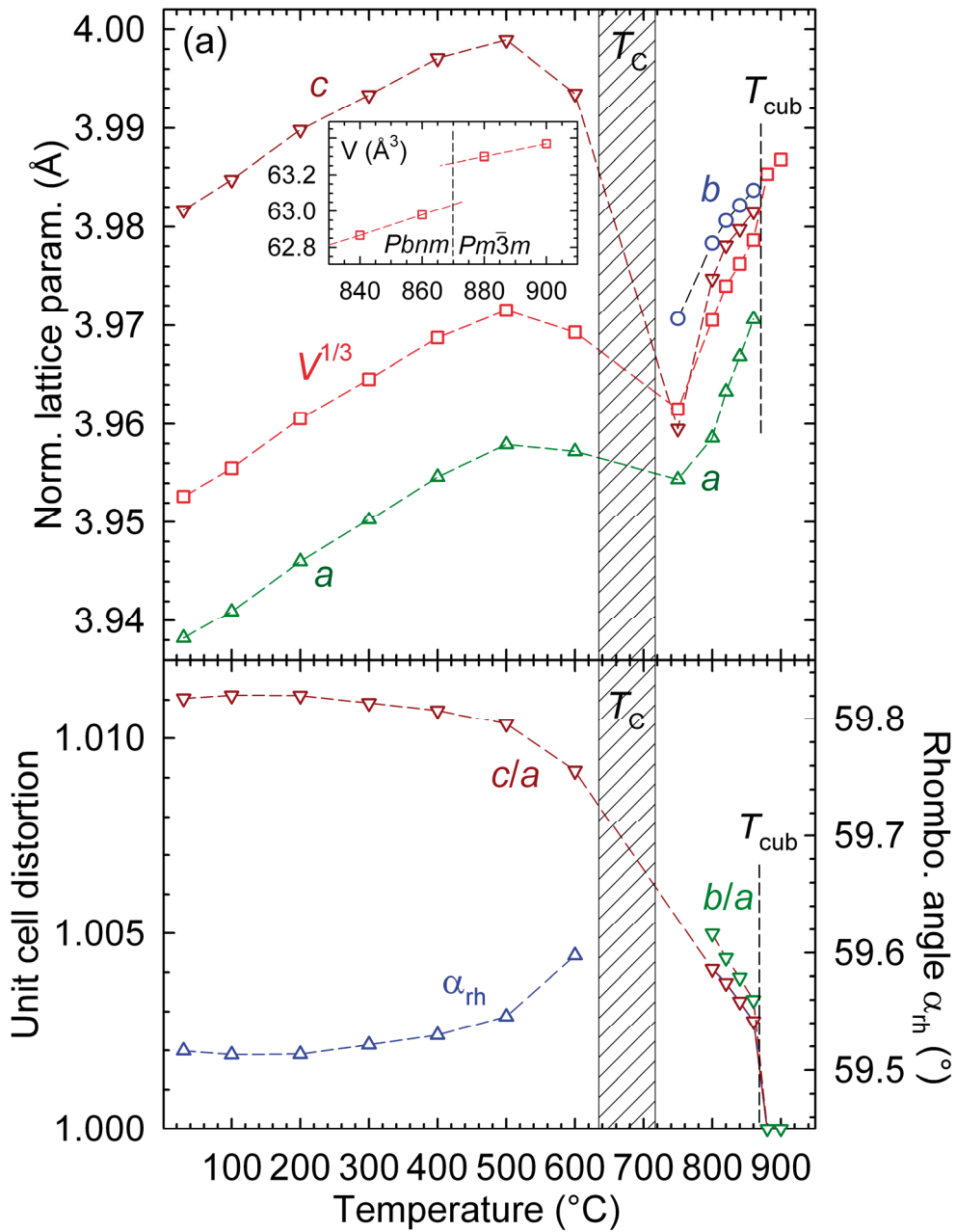


Figure 7.4. (a) Refined lattice parameters of $\text{BiFe}_{0.7}\text{Mn}_{0.3}\text{O}_{3+\delta}$ for the $R3c$, $Pbnm$ and $Pm\bar{3}m$ polymorphs. Inset: primitive unit cell volume across the $Pbnm$ to $Pm\bar{3}m$ transition. (b) Unit cell distortions c/a and b/a , and rhombohedral angle α_{rh} .

The effect of Mn substitution x and oxygen hyperstoichiometry δ on the structural phase transitions measured by DTA is displayed in Figure 7.5 (a). Quenched samples with less excess oxygen were measured in N_2 atmosphere, while air cooled samples with more excess oxygen were measured in synthetic air to retain the

difference in oxygen stoichiometry during the measurements. The ferroelectric Curie temperature, T_C , is substantially lowered by Mn substitution, in agreement with previous reports.⁴²⁰ From the four $x = 0.3$ samples in Figure 7.5 (b) it is also evident that δ affects T_C , which is discussed further below. Substitution with Mn increases the temperature interval of the $Pbnm$ polymorph, and also stabilises the $Pm\bar{3}m$ polymorph at lower temperatures. The dashed lines show that T_{cub} is less influenced by Mn substitution than T_C . Oxygen hyperstoichiometry lowers T_{cub} compared to oxygen stoichiometric Mn substituted materials.

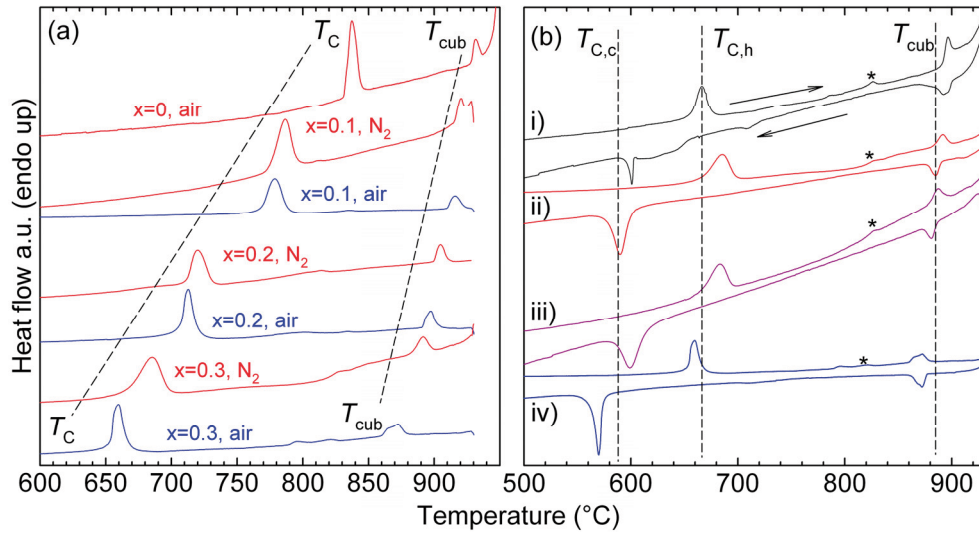


Figure 7.5 (a) DTA traces identifying the transitions to the paraelectric phase (T_C) and the paraelastic, cubic phase (T_{cub}). Labels refer to x in $BiFe_{1-x}Mn_xO_{3+\delta}$ and the atmosphere used during the measurements. Quenched samples (red traces) were measured in flowing N_2 atmosphere, cooled samples (blue traces) were measured in synthetic air. (b) DTA traces of $BiFe_{0.7}Mn_{0.3}O_{3+\delta}$ i) N_2 -cooled from $850^\circ C$ ($\delta = 0$) measured in N_2 , ii) quenched in air from $900^\circ C$ ($\delta = 0.03 \pm 0.005$) measured in N_2 and iii) air, and iv) cooled from $850^\circ C$ in air ($\delta = 0.06 \pm 0.005$) and measured in air. $T_{C,h}$ and $T_{C,c}$ denotes the Curie temperature upon heating and cooling, respectively. Asterisks (*) denote minor peaks attributed to the T_m of sillenite.

Dilatometric traces in Figure 7.6 (a) recorded on polycrystalline bars confirm the phase transition temperatures found by calorimetry. Across the ferroelectric transition at T_C the volume of transition, $\Delta_{trs}V_{T_C}$ is large and negative for all x , but decreases with increasing x . Thermal expansion anomalies across T_N are envisaged by the differential traces in the inset of Figure 7.6 (a). Measurements at higher temperatures on a well densified $BiFe_{0.7}Mn_{0.3}O_{3+\delta}$ polycrystalline bar confirm that $\Delta_{trs}V_{T_{cub}} > 0$, in line with the unit cell volumes found from HTXRD (Figure 7.4 (a)). At elevated temperatures the effects of creep, sintering and chemical expansion⁴²⁹

are superimposed on the crystallographic thermal expansion, thus absolute values for $\Delta_{\text{trs}}V_{T_C}$ and $\Delta_{\text{trs}}V_{T_{\text{cub}}}$ could not be determined from dilatometry. The relative magnitude of the thermal expansion anomalies at T_C and T_{cub} correspond to the magnitude of the calorimetric signatures.

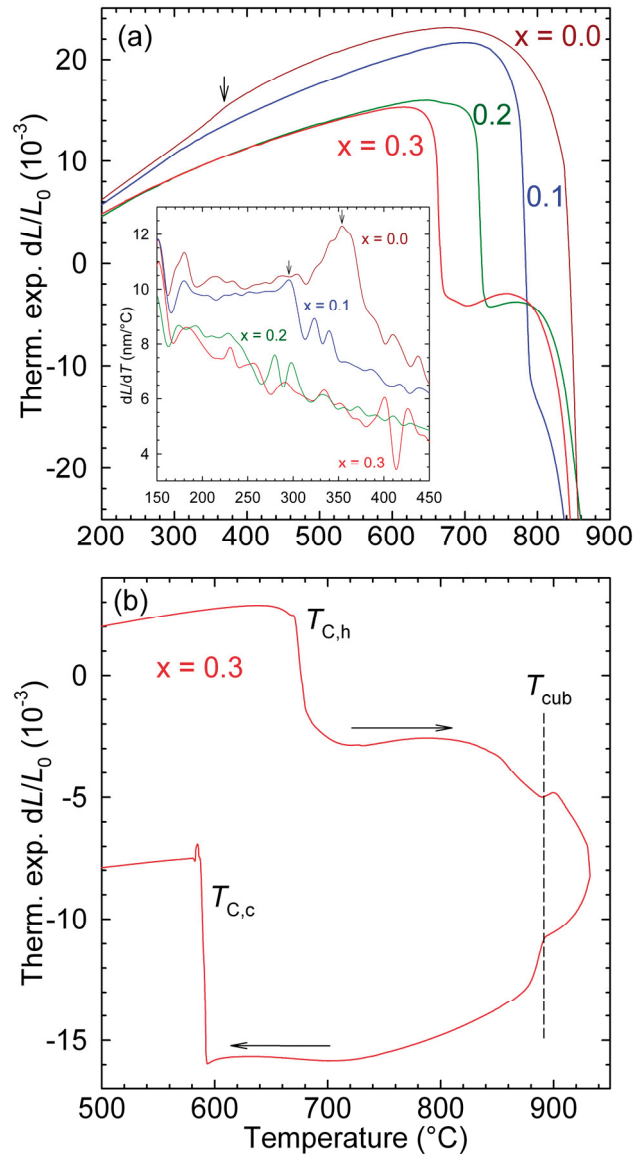


Figure 7.6 (a) Dilatometric traces measured in synthetic air on polycrystalline bars, labels refer to x in $\text{BiFe}_{1-x}\text{Mn}_x\text{O}_{3+\delta}$. The arrow denotes the continuous expansion anomaly associated with the Néel transition at T_N . Inset: differential thermal expansion around T_N . (b) Dilatometric trace for an air-quenched $\text{BiFe}_{0.7}\text{Mn}_{0.3}\text{O}_{3+\delta}$ ceramic bar measured in air.

Differential scanning calorimetry (DSC) traces reveal the Néel temperature as an endothermic peak (Figure 7.7). The Néel temperature decreases substantially with both x and δ compared to the pure BiFeO_3 sample with $T_N = 370$ °C. The endothermic peaks become less sharp with increasing x and δ , suggesting that the transition becomes smeared out over a larger temperature interval, possibly reflecting structural disorder. It was not possible to identify with certainty the Néel temperature in $\text{BiFe}_{0.7}\text{Mn}_{0.3}\text{O}_{3.06}$ and materials with $x > 0.3$ by DSC.

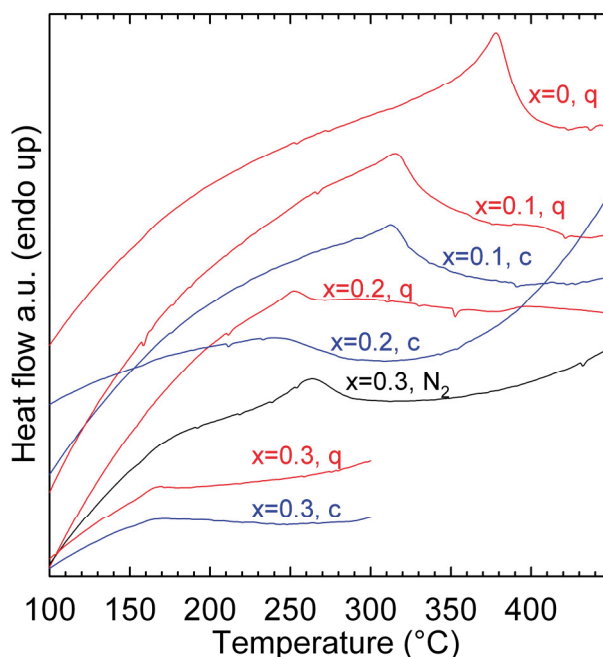


Figure 7.7 Differential scanning calorimetry (DSC) traces identifying the Néel temperature of $\text{BiFe}_{1-x}\text{Mn}_x\text{O}_{3+\delta}$. Labels refer to the thermal history of the samples as explained in Table 7.1.

7.2.4 Electrical conductivity.

Electrical conductivity measured in synthetic air is displayed in Figure 7.8, showing that $\text{BiFe}_{1-x}\text{Mn}_x\text{O}_{3+\delta}$ displays semiconductivity for all temperatures, x and δ investigated. The conductivity increases with Mn substitution, while the $\log \sigma$ vs $1/T$ slope decreases, indicating a lower activation energy of conduction. The conductivity anomaly due to the ferroelectric phase transition is related to the large volume contraction going from the ferroelectric to the paraelectric polymorph. The transition temperatures are in good accordance with the DTA and dilatometry traces in Figure 7.5 and 7.6. With increasing x and decreasing T_C , the discontinuity in conductivity associated with T_C becomes smaller. This feature can be rationalised from the smaller volume of transition with increasing x , demonstrated in Figure 7.6.

Thermal hysteresis of the conductivity traces, associated with the first order nature of the ferroelectric transition, increases with Mn substitution, thus the paraelectric structure becomes metastable to lower temperatures upon cooling compared to the transition temperature upon heating. Increasing thermal hysteresis about T_C with increasing substitution level is opposite of the behavior reported for the ferroelectric model system $\text{PbZr}_{1-x}\text{Ti}_x\text{O}_3$ (PZT).⁴³⁰ In PZT both Zr and Ti have stable oxidation states of 4+, while Mn is found as 3+ and 4+ in $\text{BiFe}_{1-x}\text{Mn}_x\text{O}_{3+\delta}$, depending on the oxygen stoichiometry. This additional chemical degree of freedom in the $\text{BiFe}_{1-x}\text{Mn}_x\text{O}_{3+\delta}$ system allows two solids to coexist with a gas phase in line with Gibbs phase rule, explaining the increasing thermal hysteresis with increasing x in $\text{BiFe}_{1-x}\text{Mn}_x\text{O}_{3+\delta}$.

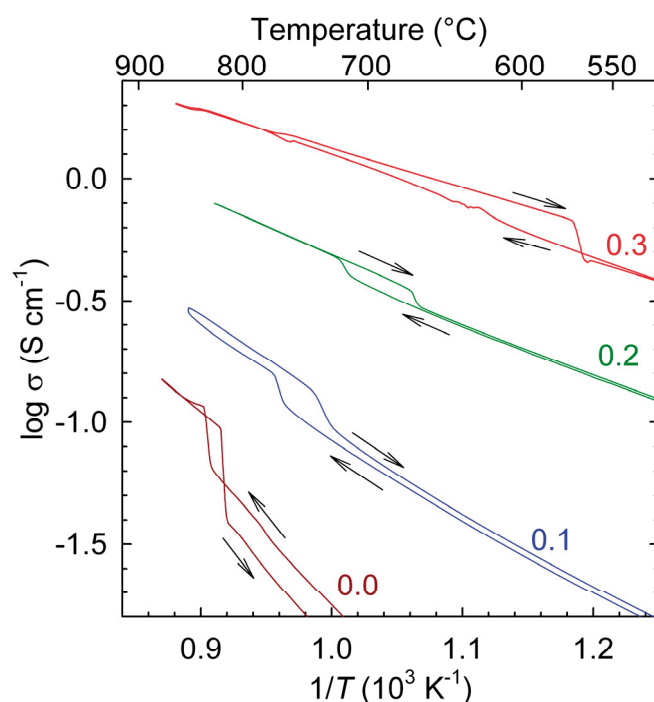


Figure 7.8 Electrical conductivity traces measured in synthetic air on polycrystalline bars. The labels refer to x in $\text{BiFe}_{1-x}\text{Mn}_x\text{O}_{3+\delta}$. Arrows depict traces upon heating and cooling.

The conductivity of $\text{BiFe}_{0.7}\text{Mn}_{0.3}\text{O}_{3+\delta}$ in different atmospheres is investigated further in the following. Electrical conductivity anomalies similar to those observed in pure BiFeO_3 are evident at both structural transitions in air, Figure 7.9. Anomalies associated with the transition $Pbnm \leftrightarrow Pm\bar{3}m$ are shown in the inset of Figure 7.9. The conductivity of the cubic polymorph is lower than the orthorhombic, as in pure BiFeO_3 .

The influence of oxygen nonstoichiometry on the electrical conductivity was investigated on a fresh sample in N_2 and O_2 atmospheres. After heating the pristine sample in air for 30 min at 829 °C, *in-situ* switching to N_2 atmosphere was

followed by an isothermal conductivity relaxation stabilizing after ~50 min as shown in Figure 7.10.

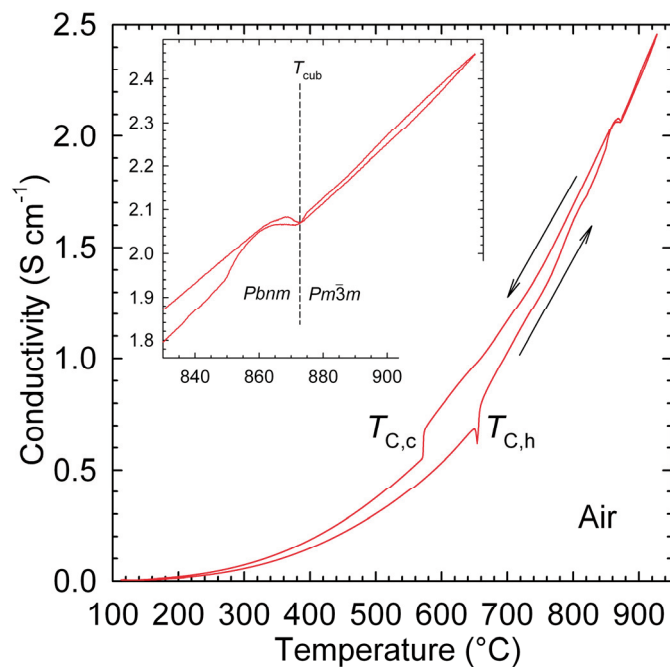


Figure 7.9. Electrical conductivity trace of $\text{BiFe}_{0.7}\text{Mn}_{0.3}\text{O}_{3+\delta}$ in with 5 °C/min heating and cooling rate. Inset: zoom in the transition to cubic structure.

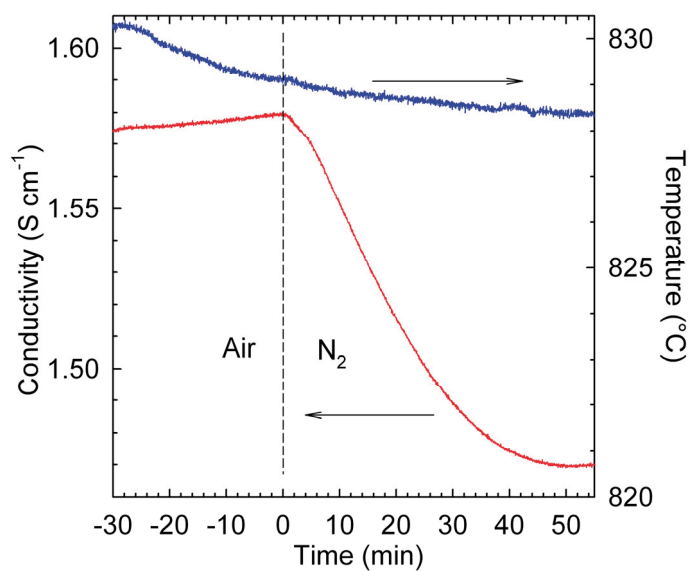


Figure 7.10. Conductivity relaxation of $\text{BiFe}_{0.7}\text{Mn}_{0.3}\text{O}_{3+\delta}$ upon in situ change of atmosphere from air to N_2 .

Figure 7.11 shows the conductivity during heating and cooling across T_{cub} in N_2 atmosphere. During ~ 15 min at 913°C the conductivity decreased, possibly due to further loss of excess oxygen (Figure 7.11 (a)). Cation diffusion is known to be slow in related perovskites at these temperatures,⁴³¹ preventing equilibrium conditions in a ceramic sample bar on the time scale of the experiment. An anomaly associated with the $Pbnm$ to $Pm\bar{3}m$ transition can be seen at $886\text{--}891^\circ\text{C}$ in Figure 7.11 (b), corresponding to the calorimetric peak at 896°C of sample iv) with $\delta = 0$ in Figure 7.5 (b). The conductivity decreased across T_{cub} upon both heating and cooling in N_2 atmosphere, in contrast with the behaviour in air, O_2 atmosphere (as shown below) and that of pure BiFeO_3 , and the positive $\Delta_{\text{trs}}V_{T_{\text{cub}}}$ upon heating. No further attention is given to this exception.

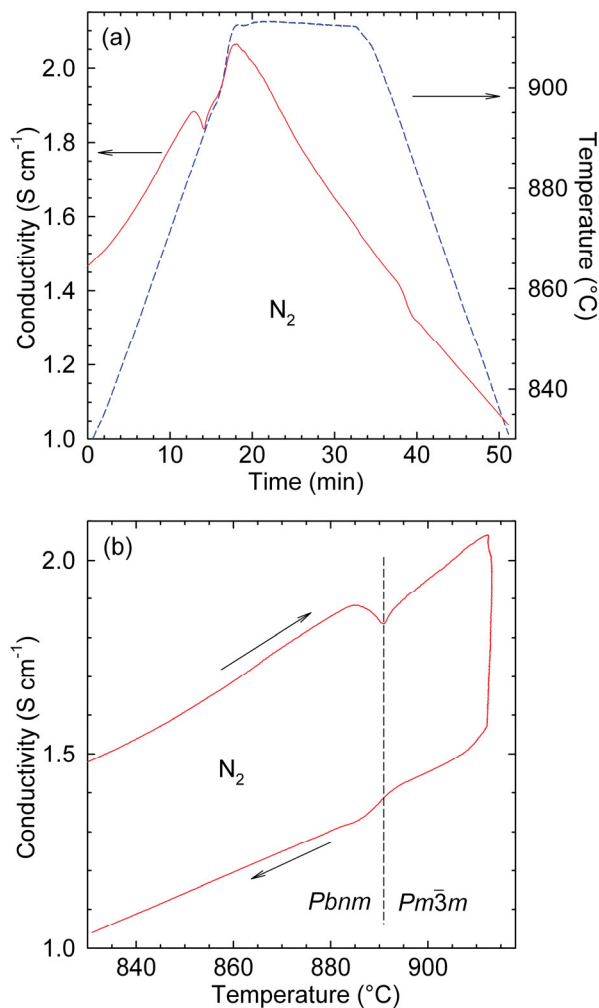


Figure 7.11. (a) Electrical conductivity of $\text{BiFe}_{0.7}\text{Mn}_{0.3}\text{O}_{3+\delta}$ in N_2 atmosphere as a function of time and temperature. (b) Electrical conductivity of $\text{BiFe}_{0.7}\text{Mn}_{0.3}\text{O}_{3+\delta}$ in N_2 atmosphere as a function of temperature.

After cooling to 829 °C in N₂ atmosphere and subsequent equilibration for 30 min, the same sample was subjected to *in-situ* change of atmosphere from N₂ to O₂, and the electrical conductivity is shown in Figure 7.12 (a).

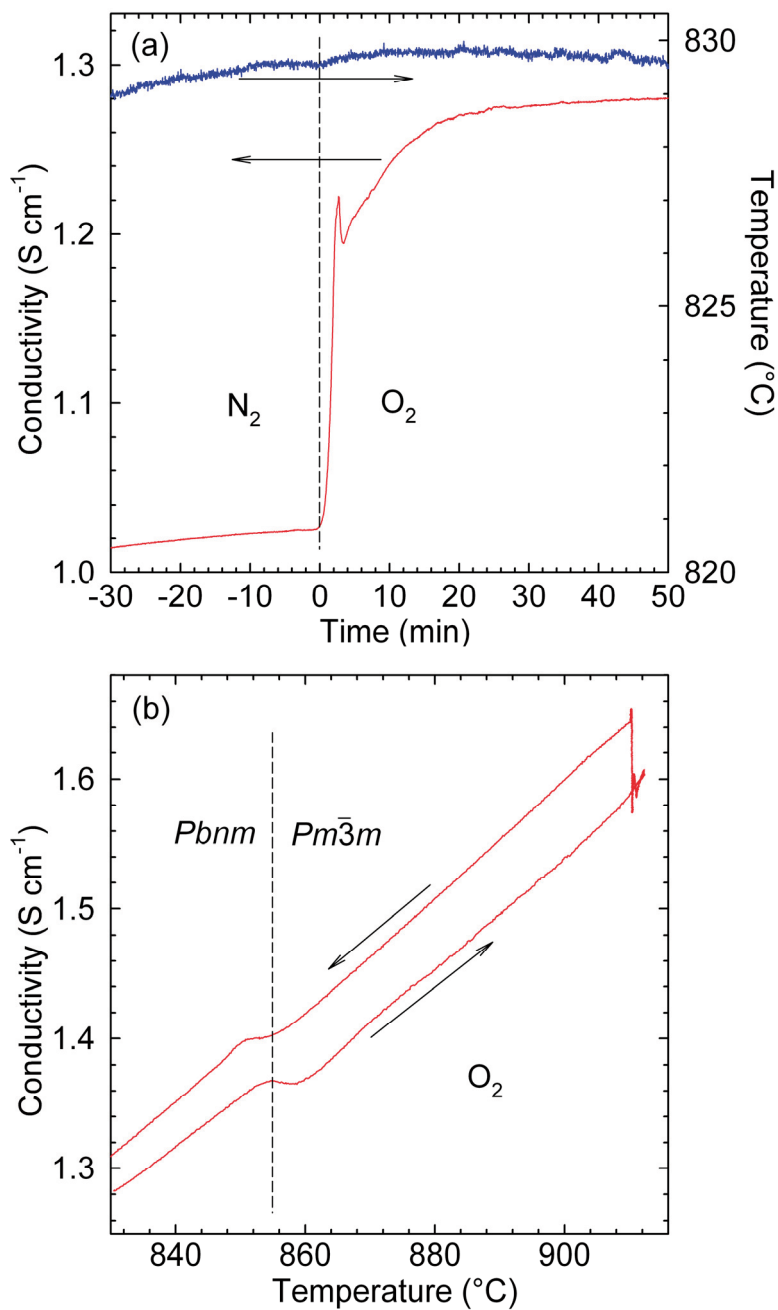


Figure 7.12. (a) Electrical conductivity of BiFe_{0.7}Mn_{0.3}O_{3+δ} relaxation upon in situ change of atmosphere from N₂ to O₂. (b) Conductivity of BiFe_{0.7}Mn_{0.3}O_{3+δ} in O₂ atmosphere as a function of temperature.

Increasing conductivity in O₂ atmosphere at isothermal conditions is complementary to the decreasing conductivity observed after in-situ change from air to N₂ atmosphere in Figure 7.10. Both observations point to BiFe_{0.7}Mn_{0.3}O_{3+δ} being a *p*-type semiconductor. The relatively steeper change of conductivity with time at the same temperature when switching from N₂ to O₂ atmosphere relative to switching from air to N₂ follows from the larger difference in *p*O₂. After an unexplained cusp in the isothermal conductivity 2-3 minutes after switching to O₂ atmosphere, the conductivity follows a relaxation behaviour before stabilizing after 30-40 minutes.

A small decrease in the conductivity associated with the *Pbnm* to *Pm* $\bar{3}m$ transition is observed at 855-859 °C upon heating in O₂ atmosphere, a significantly lower temperature than the calorimetric peak at 872 °C for sample iv) with $\delta = 0.06$ in Figure 7.5 (b). This suggests that δ is larger than 0.06 at these conditions. When kept isothermally at 910 °C in O₂, the increasing conductivity supports a *p*-type semiconducting cubic phase, as does the increasing conductivity decreased when kept isothermally at 913 °C in N₂ atmosphere.

7.2.5 Solubility

To elucidate the solid solubility limit, and the origins of the limited solubility of Mn in BiFeO₃ at ambient pressure, three samples with compositions $x = 0.32, 0.34$ and 0.36 were characterised. The ambient pressure solid solubility limit is reported as being close to $x = 0.3$, while high pressure synthesis enables complete solid solution.³⁵²⁻³⁵³ In Figure 7.13 (a) XRD patterns are displayed on log scale to highlight any secondary phases found in these samples. All reflections due to secondary phases could be indexed according to the patterns of Bi₂₅Fe_{1-y}Mn_yO_{39+δ} (sillenite, Bi₂₅FeO₃₉, JCPDF 46-0416) and Bi₂Fe_{4-z}Mn_zO_{9+δ} (mullite, Bi₂Fe₄O₉, JCPDF 72-1832). Materials fired at 900 °C clearly contain less secondary phases than the samples fired at 800 °C. This suggests that the solubility of Mn increases with increasing temperature. If exceeding the solid solubility limit simply led to Mn going into the secondary phases sillenite and mullite, one would expect the structural phase transition temperatures of the perovskite phase to be equal for the three compositions with $x > 0.3$. However, as shown in Figure 7.13 (b), both T_C and T_{cub} for the materials fired at 900 °C decrease with increasing x while the melting temperature of the sillenite secondary phase does not change, implying that the solid solubility limit at ambient pressure is larger than 0.3, in agreement with the systematic decrease in lattice parameter c for $x > 0.3$ (Figure 7.2 (a)).

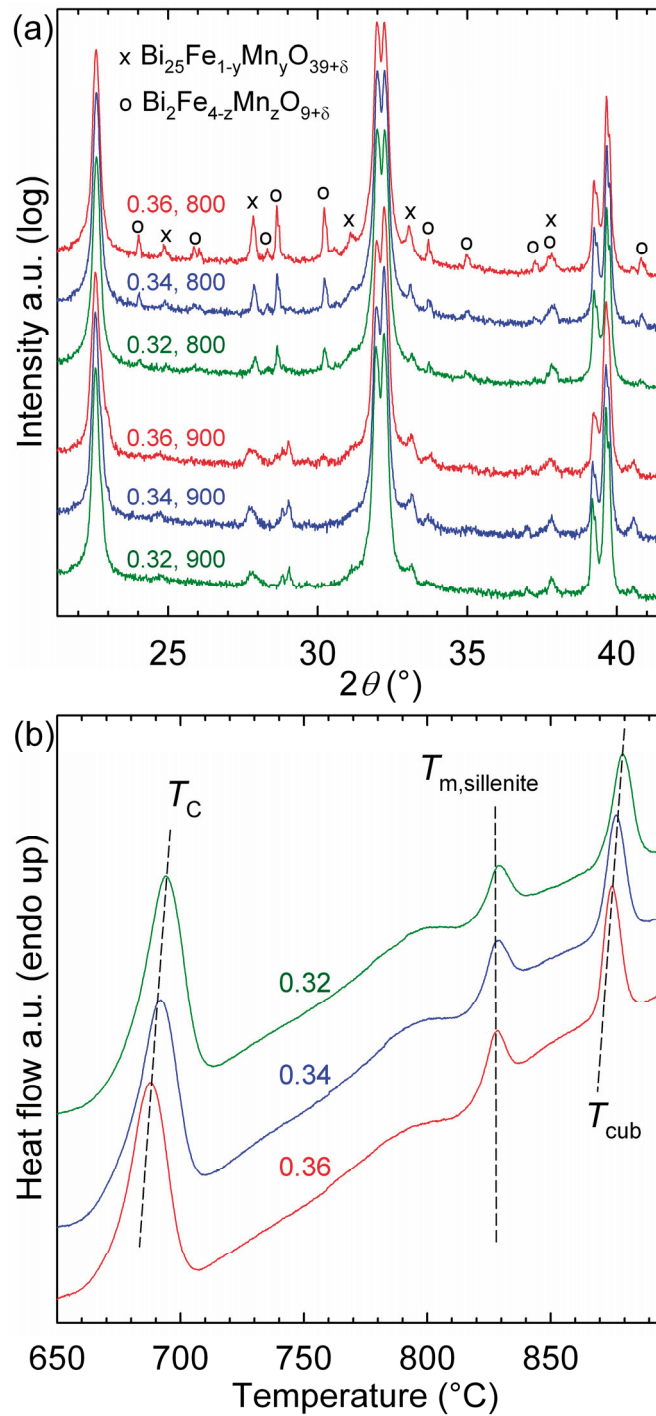


Figure 7.13 (a) XRD patterns of samples with compositions beyond the ambient pressure solid solubility limit. Labels refer to x in $\text{BiFe}_{1-x}\text{Mn}_x\text{O}_{3+\delta}$ and the firing temperature. (b) DTA traces for samples fired at 900 $^{\circ}\text{C}$, measured in flowing N_2 atmosphere.

7.3 Discussion

7.3.1 Defect Chemistry

Oxygen deficiency is well known in perovskite materials, while oxygen hyperstoichiometry is far less common. Excess oxygen can not be accommodated as interstitial ions in perovskites as the crystal structure is too close-packed.⁴²⁶ To retain charge equilibrium excess oxygen is compensated by cation vacancies. Addition of excess oxygen to $\text{BiFe}_{1-x}\text{Mn}_x\text{O}_3$ can be described by the Kröger-Vink point defect equilibrium:



Cation vacancies in the Bi and Fe/Mn sublattices are denoted as $V_{\text{Bi}}^{\prime\prime}$ and $V_{\text{Fe,Mn}}^{\prime\prime}$, respectively. Holes, h^\bullet , appear when Mn^{3+} is oxidised to Mn^{4+} ; $\text{Mn}^{4+} \rightleftharpoons \text{Mn}^{3+} + h^\bullet$. The ratio $\text{Mn}^{4+}:\delta$ is 2:1, and the fraction of manganese ions present as Mn^{4+} is $2\delta/x$. Nonsubstituted $\text{BiFeO}_{3+\delta}$ is stoichiometric within $\delta < 0.01$,³⁶⁸ and iron has been shown to exist in the +III oxidation state in BiFeO_3 .⁴³² Oxygen hyperstoichiometry is thus predominantly charge compensated by oxidation of Mn^{3+} to Mn^{4+} in $\text{BiFe}_{1-x}\text{Mn}_x\text{O}_{3+\delta}$. A more correct formula for oxygen hyperstoichiometric Mn substituted BiFeO_3 is therefore $\text{Bi}_{1-\delta/3}(\text{Fe}_{1-x}\text{Mn}_x)_{1-\delta/3}\text{O}_3$.

The defect equilibrium (7.1) accounts for the observed relations between electrical conductivity and atmosphere. When $p\text{O}_2$ is reduced, excess oxygen is removed from $\text{BiFe}_{0.7}\text{Mn}_{0.3}\text{O}_{3+\delta}$ by shifting the equilibrium (7.1) towards the left hand side, reducing the number of charge carrying holes h^\bullet , equivalently reducing the average oxidation state of Mn. Increasing $p\text{O}_2$ will increase the average oxidation state of Mn and thus also the concentration of charge carrying holes h^\bullet . This defect model explains the p -type semiconductivity observed in both the paraelectric $Pbnm$ and cubic $Pm\bar{3}m$ polymorphs of $\text{BiFe}_{0.7}\text{Mn}_{0.3}\text{O}_{3+\delta}$.

Excess oxygen compensated by cation vacancies and mixed Mn valence of 3+/4+ have also been reported for the related systems $\text{BiMnO}_{3+\delta}$, $\text{LaMnO}_{3+\delta}$ and $\text{La}_{0.5}\text{Bi}_{0.5}\text{Mn}_{0.5}\text{Fe}_{0.5}\text{O}_{3.09}$.^{422-424, 426, 433} A larger concentration of vacancies at the A site than the B site, $\text{Bi}_{1-y}(\text{Fe}_{1-x}\text{Mn}_x)_{1-z}\text{O}_3$ with $y > z$, is known to occur in $\text{La}_{1-y}\text{Mn}_{1-z}\text{O}_3$.⁴³⁴⁻⁴³⁵ The samples studied in the present investigation would not reveal if significant cation non-stoichiometry is possible in Mn-substituted BiFeO_3 .

7.3.2 Crystal Structure

Decreasing unit cell volume (Figure 7.2 (a)) with increasing x and δ is in line with the decreasing polar displacement of Bi^{3+} , s (Figure 7.2 (b)). The lattice parameter c is parallel to the polar cation displacements, and is also the most sensitive to x and δ . However, the lattice parameter a , normal to the polarisation, also decreases with x and δ . Both c and a are smaller for oxygen stoichiometric $\text{BiFe}_{0.7}\text{Mn}_{0.3}\text{O}_3$ than for pure BiFeO_3 . Substantially smaller unit cell volumes with increasing excess oxygen arises naturally from the smaller ionic radii¹¹⁴ of Mn^{4+} than Mn^{3+} and Fe^{3+} . Chemical expansion is well established in perovskites with oxygen nonstoichiometry compensated by multiple cation valences.^{429, 436} The influence of the oxidation state of manganese is demonstrated in Figure 7.14, where lattice parameters, rhombohedral angle and Bi displacement are all shown to correlate well with the fraction of Mn^{4+} inferred from δ in $\text{BiFe}_{1-x}\text{Mn}_x\text{O}_{3+\delta}$. Given that the antiferrodistortive rotation of oxygen octahedra decreases with x ,⁴²⁸ one would expect the lattice parameter a to increase with x since the Shannon radii of Fe^{3+} and Mn^{3+} are equal. Decreasing the antiferrodistortive rotation of oxygen octahedra alone should increase the lattice parameter,³⁹⁴ thus it appears that Mn^{3+} possesses a smaller ionic radius than Fe^{3+} in $\text{BiFe}_{1-x}\text{Mn}_x\text{O}_{3+\delta}$. Decreasing unit cell volume with increasing δ is also known from $\text{LaMnO}_{3+\delta}$.⁴³⁷

The combination of decreasing unit cell distortion and increasing Lorentzian strain (Figure 7.2 (c)) implies that lattice strain and/or structural disorder is introduced by both Mn substitution and excess oxygen. The oxygen stoichiometric $x = 0.3$ sample (filled symbol, Figure 7.2 (c)) shows that Mn substitution causes some lattice strain even for oxygen stoichiometric samples. Comparison of the three different oxygen stoichiometries for $x = 0.3$ relative to the influence of Mn content indicates that excess oxygen causes larger lattice strain than the introduction of Mn alone. Inhomogenous oxygen stoichiometry throughout the sample, and associated gradients in the concentration of Mn^{4+} , must be anticipated, as cation diffusion is slow in perovskites.⁴³¹ The apparent discontinuity in lattice parameters between the series of quenched samples with $x \leq 0.3$ (grey-filled symbols, Figure 7.2 (b)) and the series with $x > 0.3$ is probably due to the sensitivity of the crystal structure to the thermal history, as these samples were fired in separate series (possibly with different quench rates).

The polar displacement of the A cation Bi^{3+} is far more sensitive to x than the displacement of the B cations, even though substitution takes place on the B site. These displacements are coupled, and the electrostatic energy strongly favours unidirectional displacement along the polar axis.¹⁰³ The substantial decrease in displacement of Bi may thus reflect disorder introduced on the B site with Mn, as Mn^{3+} is a HS d^4 Jahn-Teller active cation opposed to HS d^5 Fe^{3+} . Excess oxygen also contributes to B site disorder, as it is compensated by both vacancies and d^3 Mn^{4+} , resulting in four different occupants of the B site; Fe^{3+} , Mn^{3+} , Mn^{4+} and vacancy. B site disorder is a likely origin of the increasing broadening of the Bragg reflections with increasing x and δ in Fig. 1, and the increasing Lorentzian strain in Figure 7.2 (c).

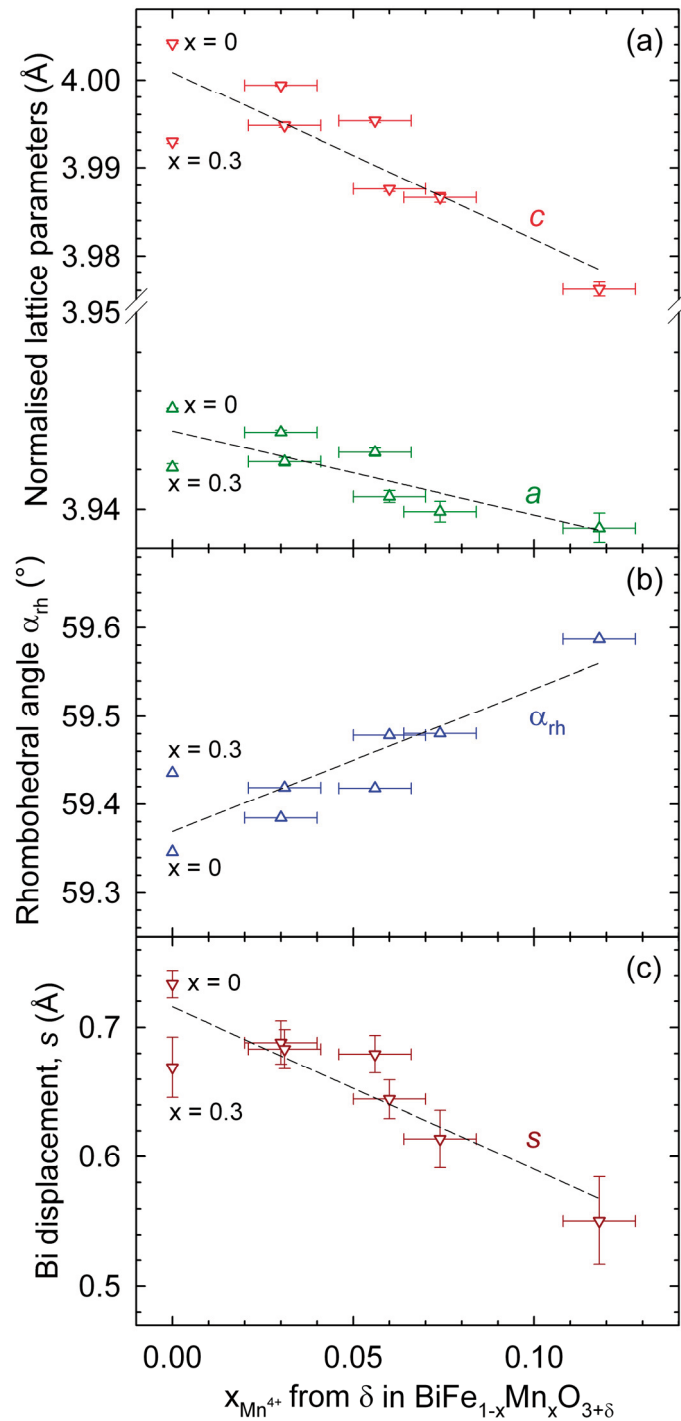


Figure 7.14 (a) Normalised lattice parameters of $\text{BiFe}_{1-x}\text{Mn}_x\text{O}_{3+\delta}$ as a function of Mn^{4+} content inferred from δ . (b) Rhombohedral angle and (c) polar displacement of Bi (s) and as a function of Mn^{4+} . Dashed lines are guides to the eye.

7.3.3 Phase diagram

The phase diagram shown in Figure 7.15 is the main conclusion of this chapter, demonstrating the stability range of regions with three, two, one or zero ferroic orders in terms of temperature, manganese content and excess oxygen. Each of the transitions associated with the onset of a ferroic order are discussed below.

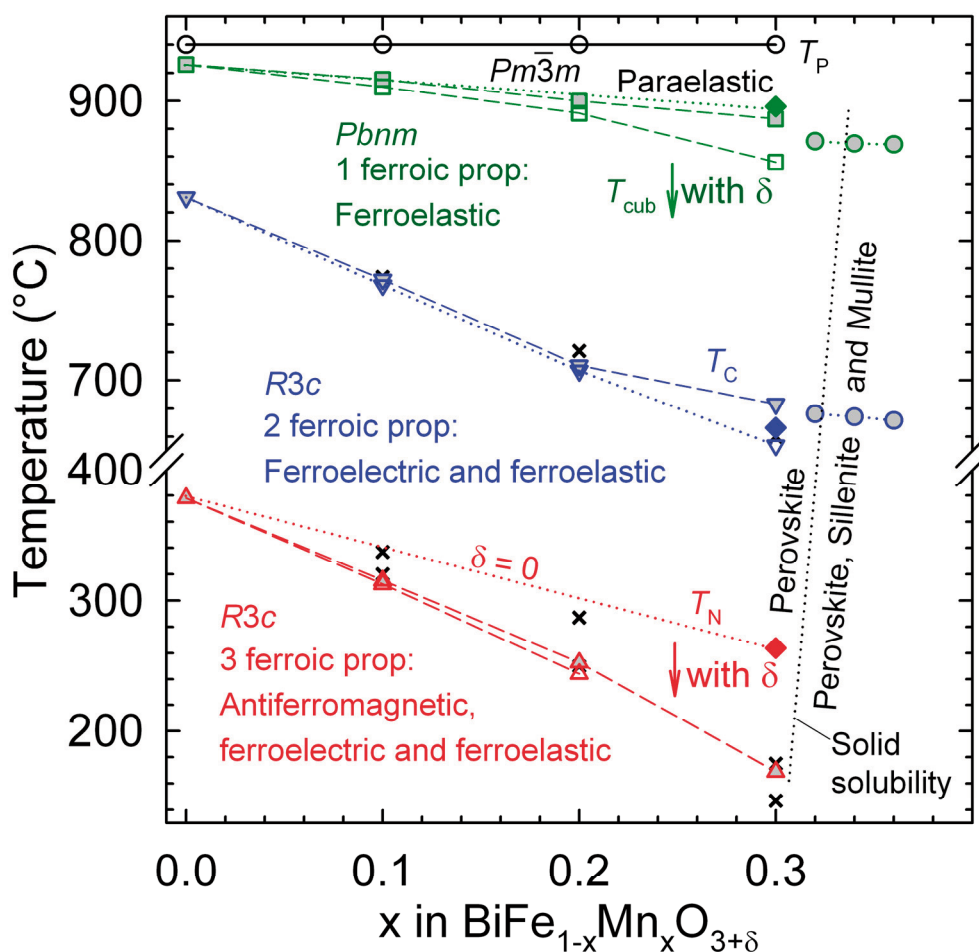


Figure 7.15 Phase diagram of the pseudo-binary system $\text{BiFeO}_3\text{-BiMnO}_{3+\delta}$ at ambient pressure showing the stability regions of three, two, one and zero ferroic properties as a function of Mn substitution (x) and the influence of oxygen hyperstoichiometry (δ). T_N , T_C , T_{cub} and T_P denote the antiferromagnetic Néel, ferroelectric Curie, transition to cubic and the peritectic decomposition temperature, respectively. Filled symbols are for the $x = 0.3$ sample annealed in N_2 , grey-filled symbols for quenched samples and open symbols for samples cooled with 400 °C/h . The dotted, almost vertical, line is an estimate for the ambient pressure solid solubility limit of Mn. Circles are phase transition temperatures based on DTA traces in Figure 7.13 (b). Literature values^{352, 420, 428} are denoted as **x**.

7.3.4 Ferroelectric transition

Ferroelectricity is a cooperative phenomenon, and chemical substitution, defects and finite size effects are known to influence both the spontaneous polarisation and Curie temperature of ferroelectric materials.⁵⁸ In perovskites with B cations with non-zero number of d -electrons, ferroelectricity can occur due to partial covalent bonding between O $2p$ orbitals and a $6s^2$ lone pair on the A cation.^{96, 109} Even though the $6s^2$ lone pair of Bi^{3+} is considered the primary driving force for ferroelectricity,^{96, 109-110} the substantial decrease in T_C of 5-6 °C per % Mn substituted demonstrates the importance of the B site. Six coordinated high-spin (HS) Fe^{3+} and HS Mn^{3+} are equal in size according to their Shannon radii (0.645 Å), although it appears that Mn^{3+} occupies a smaller volume than Fe^{3+} , as previously mentioned. The main difference between HS Fe^{3+} and Mn^{3+} is the number of e_g electrons, 2 and 1, respectively. The e_g orbitals of Mn^{3+} possess higher energy than those of Fe^{3+} due to smaller effective nuclear charge. Thus, partial covalent bonding between Fe $3d$ and O $2p$ orbitals may be more important to ferroelectricity in BiFeO_3 than commonly recognized. Partial covalent bonding between Ti $3d$ and O $2p$ orbitals stabilises the ferroelectric phase in BaTiO_3 and PbTiO_3 ,⁶⁸ and partial covalency was also found between Fe $3d$ and O $2p$ orbitals in a theoretical study of BiFeO_3 by Ravindran *et al.*¹¹⁰ The observed structural disorder and loss of structural coherence caused by Mn substitution, as evidenced by increasing FWHM of Bragg reflections (Figure 7.1 (a)) and lattice strain (Figure 7.2 (c)), may thus destabilise the ferroelectric phase. Site disorder is detrimental to a cooperative phenomenon as ferroelectricity. Based on this, B site disorder is proposed to be important for both the decreasing polar displacements of Bi and the observed decrease of T_C . In analogy, substitution of Sc for Mn in BiMnO_3 has been reported to disrupt the short range order of the crystal lattice.¹⁹⁹ This substitution also affected the long-range order of the structure where correlations between Mn^{3+} and Bi^{3+} are important, and not only the ordering of the Bi^{3+} $6s^2$ lone pairs. Systematic studies of the effects of substitution thus may shed light on the chemical bonding and the origins of multiferroic behavior in BiFeO_3 and BiMnO_3 , and their solid solutions.

Abrahams *et al.* reported a simple, empirical relation between Curie temperature and polar cation displacements Δz relative to a centrosymmetric reference structure; $T_C = (\kappa/2k_B)(\Delta z)^2$, where κ is a force constant and k_B the Boltzmann's constant.¹²⁸ For the polar space group $R3c$, the quantity Δz in the Abrahams *et al.* relation corresponds to $s - t$, where the unit cell is anchored by $z_A = 0$. A plot of T_C vs $(s - t)^2 \sim (\Delta z)^2$ indicates two regions of linearity with a crossover between $x = 0.1$ and 0.2 , as shown in Figure 7.16. The ferroelectric polymorph is destabilised by Mn substitution with respect to temperature, and according to the proposed P - T phase diagram,⁴⁰ one would expect that Mn substitution also destabilises the $R3c$ phase with respect to pressure. High pressure studies of $\text{BiFe}_{1-x}\text{Mn}_x\text{O}_{3+\delta}$ could improve the understanding of the high pressure behaviour of pure BiFeO_3 .

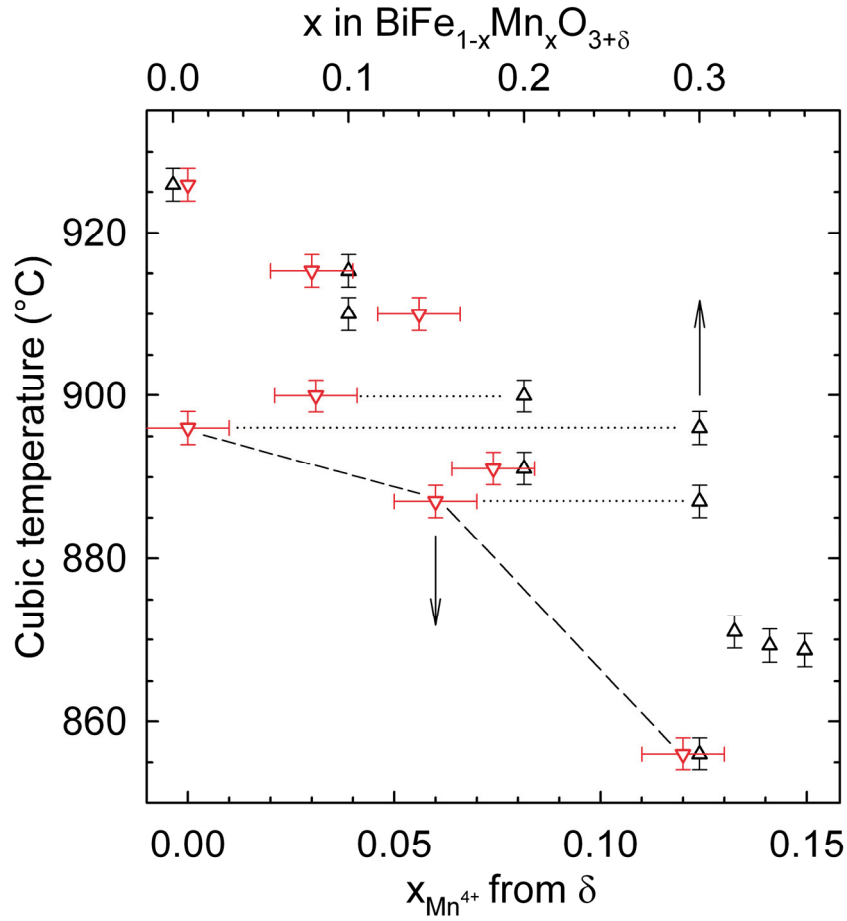


Figure 7.17 The temperature of transition to the, ideal, cubic aristotype structure as a function of x in $\text{BiFe}_{1-x}\text{Mn}_x\text{O}_{3+\delta}$ (filled symbols, upper x -axis) and as a function of content of oxidised Mn^{4+} due to oxygen hyperstoichiometry δ (open symbols, lower x -axis). The three horizontal dotted lines connect the same data points plotted on the two different x -axes. The dashed line highlights the influence of the content on Mn^{4+} for three different materials with $x = 0.3$ and different oxygen stoichiometry δ .

7.3.6 Antiferromagnetic transition

The B cations present in $\text{BiFe}_{1-x}\text{Mn}_x\text{O}_{3+\delta}$ in this study are Fe^{3+} (d^5 HS), Mn^{3+} (d^4 HS) and Mn^{4+} (d^3), thus the number of e_g electrons are 2, 1 and 0, respectively. According to the Goodenough-Kanamori rules,⁴³⁸ Fe^{3+} - Fe^{3+} superexchange interactions ($e_g^1 - \text{O} - e_g^1$) are antiferromagnetic, Fe^{3+} - Mn^{3+} interactions ($e_g^1 - \text{O} - e_g^1$ and $e_g^1 - \text{O} - e_g^0$) antiferromagnetic and ferromagnetic, and Fe^{3+} - Mn^{4+} interactions ($e_g^1 - \text{O} - e_g^0$) ferromagnetic. Hence, Removing e_g electrons by increasing x and δ yields fewer antiferromagnetic superexchange interactions and more frustrated

antiferromagnetic order, accounting for the decreasing Néel temperature observed by DSC (Figure 7.7). Experimentally, T_N scales with the average number of e_g electrons on the B site, as shown in Figure 7.18. Complex magnetic behavior at cryogenic temperatures is anticipated in materials with high x and/or δ , in analogy with $\text{BiMnO}_{3+\delta}$ and $\text{LaMnO}_{3+\delta}$.^{422-423, 439-441} Pure BiFeO_3 has been reported to display spin glass behaviour and several low temperature magnetic phase transitions,⁴⁰ but hitherto there are no reports on the influence of oxygen stoichiometry on the magnetic structure of Mn substituted BiFeO_3 below room temperature. We note that the Néel transition is associated with a continuous, positive thermal expansion anomaly for $x = 0.0$ and 0.1 , as evident from the inset in Figure 7.6 (a). With increasing x , and more frustrated antiferromagnetic order, thermal expansion anomalies associated with T_N could not be observed. More frustrated antiferromagnetic order may also lead to weaker spin-lattice coupling. Although it is not clear whether the maximum unit cell distortion at ~ 450 °C (Figure 6.11 (b)) in pure BiFeO_3 is related to the T_N at 370 °C, it should be noted that the maximum unit cell distortion in $\text{BiFe}_{0.7}\text{Mn}_{0.3}\text{O}_{3+\delta}$ occurs between 100 and 200 °C, and thus at a lower temperature compared to the T_N of ~ 150 °C compared to pure BiFeO_3 .

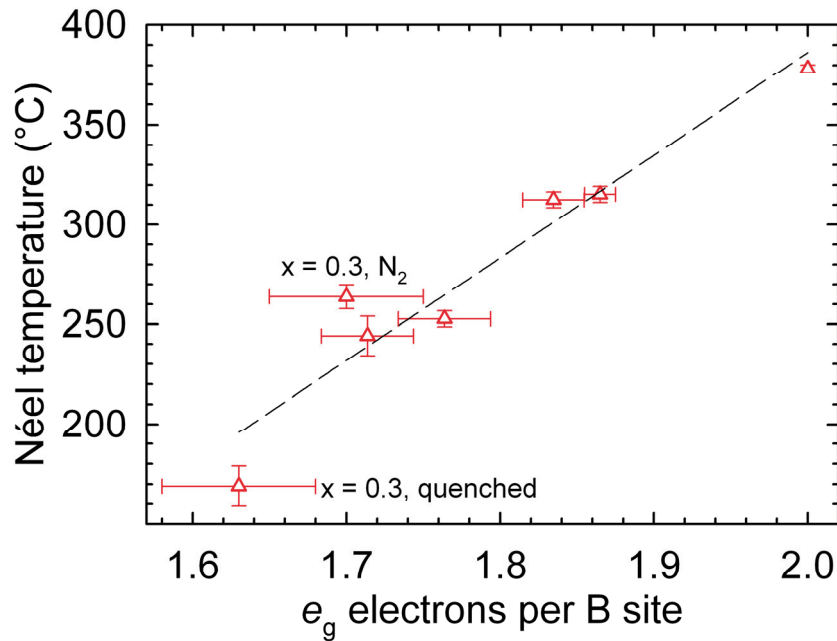
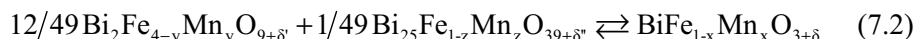


Figure 7.18 The Néel temperature of $\text{BiFe}_{1-x}\text{Mn}_x\text{O}_{3+\delta}$ displays a correlation with the number of e_g electrons on the B-site.

7.3.7 Solubility of Mn in BiFeO₃

The ambient pressure solubility limit of Mn in BiFeO₃ is clearly temperature dependent, as evidenced from the different amounts of secondary phases revealed by XRD in Figure 7.13 (a). Since all the reflections from secondary phases could be indexed as Bi₂Fe_{4-y}Mn_yO_{9+δ} (mullite) and Bi₂₅Fe_{1-z}Mn_zO_{39+δ} (sillenite), adding Mn beyond the solubility limit shifts the reaction



towards the left-hand side. As explained in chapter 5.3, increasing temperature above 800 °C drives reaction (7.2) towards the right-hand side. As the Gibbs energy of reaction (2) is close to zero, the influence of impurities is important for the phase formation. Attempts to increase the solubility of Mn in BiFeO₃ by firing samples with $x > 0.3$ in flowing O₂ atmosphere for 30 min at 850 °C were unsuccessful, yielding a larger fraction of sillenite and mullite than in the samples fired in air shown in Fig. 8 (a). Thus, Mn⁴⁺ is apparently more soluble in the mullite and sillenite phases than the perovskite phase, pointing to a higher tolerance of excess oxygen and cation vacancies in the former structures than the latter. This is supported by reports on Bi₂Mn₄O₁₀, possessing 50 % Mn⁴⁺.⁴⁴² The molar volume change of reaction (7.2) is large and negative, $\Delta_{r(7.2)}V_m < 0$, thus high pressure will favour formation of the perovskite phase. The small Gibbs energy of reaction (7.2), and the large, negative $\Delta_{r(7.2)}V_m$, are thermodynamic factors explaining why single-phase bulk BiFe_{1-x}Mn_xO_{3+δ} with $x > 0.3$ (e.g. BiMnO₃) are metastable and have to be prepared by high pressure synthesis. A theoretical study suggests that BiFe_{0.5}Mn_{0.5}O₃ has a positive enthalpy of formation relative to BiFeO₃ and BiMnO₃ at 0 K,⁴⁴³ implying that the enthalpy of solution is positive in the pseudo-binary system BiFeO₃-BiMnO₃. This is consistent with increasing solubility of Mn at higher temperatures as the entropy of solution is positive.

7.3.8 Conductivity and device applications

Leakage currents hamper the application of the ferroelectric polarisation in BiFeO₃, and is the probable origin of the low polarisation found experimentally¹⁰⁶ in BiFeO₃ until the recent measurements on high quality thin films, single crystals and ceramics.^{111-112, 171} Although some reports find that small amounts of Mn doping lowers the conductivity of BiFeO₃,⁴⁴⁴⁻⁴⁴⁵ other works point to an increasing conductivity with increasing Mn content,⁴⁴⁶⁻⁴⁴⁸ in line with the present results in Figure 7.8. In a mixed valence system like BiFe_{1-x}Mn_xO_{3+δ} polaron hopping is the commonly found mechanism of electrical conductivity at elevated temperatures. As BiFe_{0.7}Mn_{0.3}O_{3+δ} behaves like a *p*-type semiconductor, the conductivity will increase with increasing δ according to equation (7.1).³⁸⁸ A stoichiometric oxygen content will thus increase the resistivity of the material. The possibility of controlling the conductivity of BiFe_{1-x}Mn_xO_{3+δ} by varying x and δ may find technological applications, e.g. in photovoltaic diodes or photocatalysts.^{156, 299}

The influence of x and δ on the lattice parameters could be important with respect to strained, epitaxial interfaces in thin films. Strain gradients can be accommodated by compositional gradients, and opposite effects are anticipated for substrates yielding compressive and tensile epitaxial strain. The different ionic radii of Mn^{3+} and Mn^{4+} opens the possibility of “*chemical strain relaxation*” by compositional gradients at epitaxial interfaces or in the vicinity of ferroelectric or ferroelastic domain walls. The latter have been shown to possess different conductivity than the bulk of ferroelastic domains for pure BiFeO_3 .¹⁷² Vacancies, and compensating change of cation valence, have also recently been shown to be important for strain relaxation at epitaxial interfaces of SrTiO_3 and DyScO_3 substrates and pure BiFeO_3 thin films.¹⁴³⁻¹⁴⁴

Understanding of the influence of x and δ on the structural and electrical properties of bulk $\text{BiFe}_{1-x}\text{Mn}_x\text{O}_{3+\delta}$ is important for both optimising the performance ferroelectric or multiferroic memories, and to predict new technological applications of this material system.

7.4 Conclusions

The crystal structure of $\text{BiFe}_{1-x}\text{Mn}_x\text{O}_{3+\delta}$ shows systematic variations with x ($0.0 \leq x \leq 0.3$) and excess oxygen δ ($0.00 \leq \delta \leq 0.06$). Excess oxygen measured by thermogravimetry is compensated by cation vacancies and oxidation of Mn^{3+} to Mn^{4+} . Oxidation of Mn^{3+} to Mn^{4+} creates charge-carrying holes h^\bullet , and electrical conductivity measurements in air, N_2 and O_2 atmosphere all show that the paraelectric $Pbnm$ polymorph and the cubic $Pm\bar{3}m$ polymorph behave as p -type semiconductors.

The unit cell volume and rhombohedral distortion decrease with increasing x and δ . This correlates with the decreasing ferroelectric Curie temperature T_C and the temperature of transition to the cubic state, T_{cub} , which both decrease with increasing x and δ . X-ray diffraction patterns and lattice strain from Rietveld refinement suggest that structural disorder caused by Mn substitution and excess oxygen is responsible for the decay of ferroelectricity with x and δ . The Néel temperature T_N decreases rapidly with x and δ , and is proposed to scale with the number of e_g electrons responsible for antiferromagnetic superexchange interactions.

The proposed phase diagram displays the stability regions of phases with three, two, one and zero simultaneous ferroic orders. The solubility limit of Mn in $\text{BiFe}_{1-x}\text{Mn}_x\text{O}_{3+\delta}$ at ambient pressure is shown to be closely above $x = 0.3$, and to increase with increasing temperature. A thermodynamic explanation for the ambient pressure solid solubility limit is given, which also accounts for the formation of single phase perovskite with $x > 0.3$ by high pressure synthesis.

The electrical conductivity increases with increasing Mn substitution, while the apparent activation energy of conduction decreases. The present systematic study of the influence of x and δ on the conductivity and crystal structure of bulk $\text{BiFe}_{1-x}\text{Mn}_x\text{O}_{3+\delta}$ provides important insight to the effect of oxygen stoichiometry for technological applications of Mn substituted BiFeO_3 .

8 La-substituted BiFeO₃: Bi_{1-x}La_xFeO₃

8.1 Introduction

Bi can be substituted with La and other rare earth metals. Previous studies indicate complete solid solubility between BiFeO₃ and LaFeO₃,⁴⁴⁹ but the sequence of space groups or structural evolution with composition is debated. Selected properties of the end members BiFeO₃ and LaFeO₃ are given in table 8.1.

Table 8.1. Selected properties of BiFeO₃ and LaFeO₃.

	BiFeO ₃	LaFeO ₃	Ref.
Space group	<i>R3c</i>	<i>Pbnm</i>	
$a_{\text{norm.}}$ (Å)	3.984	3.929	101, 450
$b_{\text{norm.}}$ (Å)	(3.984)	3.935	
$c_{\text{norm.}}$ (Å)	4.004	3.927	
Volume ^a (Å ³)	63.546	60.721	
T_{N} (°C)	370	470	102, 450-451

^aPrimitive unit cell volume corresponding to one perovskite formula unit.

The majority of the reports on La-substituted BiFeO₃ have focused on the influence of substitution on the multiferroic properties, while the structural evolution with composition has received comparatively less attention. In an early work⁴⁵² three structural transitions were reported, from the *R3c* structure of the parent compound BiFeO₃ to three different orthorhombic phases at $x_{\text{La}} = 0.2, 0.55$ and 0.75 . It was also found that T_{C} decreases linearly with x , while T_{N} shows a small increase with x . Recent works have confirmed the decreasing T_{C} and increasing T_{N} with increasing La content.^{420, 449} The central questions of this chapter are: how much La can the ferroelectric *R3c* structure tolerate, and which structure does the system adopt when this limit is exceeded? Current literature provides very different answers to these two questions, see Table 8.2. Substitution with Nd, Sm, Gd and Dy is also included since these are chemically similar to La, but with smaller ionic radii. The LnFeO₃ (Ln = La, Nd, Sm, Gd, Dy) perovskites crystallise in the *Pbnm* structure at ambient conditions. A recent study suggests that substitution with La and Gd induces a structural transition from *R3c* to *Pbnm* at 20-25 % La and 15 % Gd. The same study also found an intermediate structure similar to that of PbZrO₃ at 15-25 % Nd substitution and 10-15 % Sm substitution.⁴⁵³

Table 8.2. Literature reports on the structural evolution of $\text{Bi}_{1-x}\text{Ln}_x\text{FeO}_3$ with x , Ln = La, Nd, Sm, Gd and Dy. Values of x at phase transitions are given above the arrows, in the column “Synthesis” m and h denotes minutes and hours, respectively, and the temperature at the synthesis conditions is given in °C.

Ln	Composition and structure	Synthesis	Ref.
La	$R3c \xrightarrow{0.06} P1 \xrightarrow{0.24} C222 \xrightarrow{0.55} Pbn2_1$	Single xtl.	454
La	$R3c \xrightarrow{\leq 0.05} P1 \xrightarrow{\leq 0.2} P4mm \xrightarrow{\leq 0.25} P4/mmm$	20 m, 855	455
La	$R3c \xrightarrow{\leq 0.2} C222$	850	456
La	$R3c \xrightarrow{\leq 0.2} C222 \xrightarrow{\leq 0.3} P4mm$	1 h, 1000	457
Nd	$R3c \xrightarrow{\leq 0.15} Pbam$	3 h, 870	458
Nd	$R3c \xrightarrow{\leq 0.05} P1 \xrightarrow{\leq 0.175} P4mm \xrightarrow{\leq 0.2} P4/mmm$	20 m, 855	459-460
Sm	$R3c \xrightarrow{\leq 0.125} P1$	20 m, 855	461
Sm	$R3c \xrightarrow{\leq 0.14} P1$	PLD	289-290
Gd	$R3c \xrightarrow{\leq 0.1} Pbn2_1 \xrightarrow{\leq 0.2} Pbnm$	4 h, 850	462-464
Dy	$R3c + Pbnm$ phase for $x > 0.1$	20 m, 880	465

There is no consensus regarding neither the La tolerance of the $R3c$ structure nor the structure adopted when exceeding this solubility limit. Given that BiFeO_3 has a tolerance factor lower than unity, and tilted FeO_6 octahedra to compensate for the undersized A cation, substituting Bi^{3+} with smaller Ln^{3+} cations is not likely to result in untilted structures like $P4mm$ and $P4/mmm$. Assignments of untilted structures may result from difficulties with detecting low intensity superreflections from oxygen planes arising from octahedral tilting by laboratory XRD. Yuan and coworkers^{455, 459-460} have proposed a model where the structural transitions occur for lower levels of substitution with Nd than La, implying that the structure is controlled largely by the effective tolerance factor. A morphotropic phase boundary (MPB) between a ferroelectric and antiferroelectric phase has been reported for Sm-substituted thin films grown by pulsed laser deposition (PLD).²⁸⁹⁻²⁹⁰ Structure determination is difficult in the vicinity of MPBs, and there is yet no consensus regarding the exact nature of even the most studied MPB, at $x \sim 0.48$ in $\text{PbZr}_{1-x}\text{Ti}_x\text{O}_3$.⁴⁶⁶⁻⁴⁷⁴ If segregation and compositional inhomogeneity is favoured, differences between PLD grown thin films and bulk ceramics prepared by firing binary oxides should be anticipated, as metastable phases may be kinetically stabilised in the former case. The structure $Pbn2_1$ can be regarded as a polar version of the centrosymmetric $Pbnm$ structure, and two groups have found $Pbn2_1$ as an intermediate structure when substituting with La and Gd.^{449, 462, 464} Coexistence of $R3c$ and another structure within limited compositional ranges has been proposed.⁴⁴⁹ An understanding of the structure-property relationships in $\text{Bi}_{1-x}\text{Ln}_x\text{FeO}_3$ rely on an accurate description of the structural evolution with x , and this has been the motivation for the study presented in this chapter.

8.2 Results

8.2.1 Composition and structure

Six $\text{Bi}_{1-x}\text{La}_x\text{FeO}_3$ -samples with $x = 0.05, 0.1, 0.125, 0.15, 0.2$ and 0.25 were prepared and characterised. The samples with $x > 0.1$ were fired twice for 5 min at 900 and 950 °C with intermediate grinding, the samples with $x \leq 0.1$ were fired once for 5 min at 900 °C. XRD patterns of a series of $\text{Bi}_{1-x}\text{La}_x\text{FeO}_3$ samples with $0 \leq x \leq 0.25$ are displayed in Figure 8.1. Compared to $x = 0$, the only changes in the XRD patterns of $x = 0.05$ and 0.1 are broader Bragg reflections and less resolved $K\alpha_1$ and α_2 contributions (Figure 8.1 (a)). La substitution up to $x = 0.1$ does not change the space group of BiFeO_3 , but introduces structural disorder and lattice strain, in line with Mn substitution on the Fe site (chapter 7). The splitting of the $(104)/(202)_{\text{hex}}$ and the $(006)/(202)_{\text{hex}}$ reflections decreases, pointing to a less distorted crystal structure with increasing La content. When exceeding $x = 0.1$, new Bragg reflections emerge at the higher 2θ side of the reflections from the $R3c$ phase, and increase in intensity with increasing x . Simultaneously, low intensity reflections only visible on a log scale (labelled x in Figure 8.1 (b)) emerge and increase systematically in intensity with increasing La content. The low-intensity reflections labelled (O) in Figure 8.1 (b) arise from the presence of small amounts of the secondary phases $\text{Bi}_{25}\text{FeO}_{39}$ and $\text{Bi}_2\text{Fe}_4\text{O}_9$. The position and intensity of the low-intensity reflections in Figure 8.1 (b) can be indexed with the centrosymmetric orthorhombic $Pbnm$ structure, see e.g. Figure 6.10.

HTXRD was performed on two samples with $x = 0.1$ and 0.25 to investigate the influence of La substitution on the structural evolution and phase transitions with temperature. Diffractograms in Figure 8.2 recorded at selected temperatures show that $\text{Bi}_{0.9}\text{La}_{0.1}\text{FeO}_3$ behaves qualitatively similar to BiFeO_3 , but with a transition from the ferroelectric $R3c$ structure to the paraelectric $Pbnm$ structure at a lower temperature, between 700 and 750 °C. At 750 °C both the $R3c$ and the $Pbnm$ polymorphs are present in the XRD pattern. Low-intensity Bragg reflections from oxygen planes observed for the $Pbnm$ structure, but not for $R3c$ structure, are labelled “x”, while the superreflection common to $R3c$ and $Pbnm$ is labelled “*”.

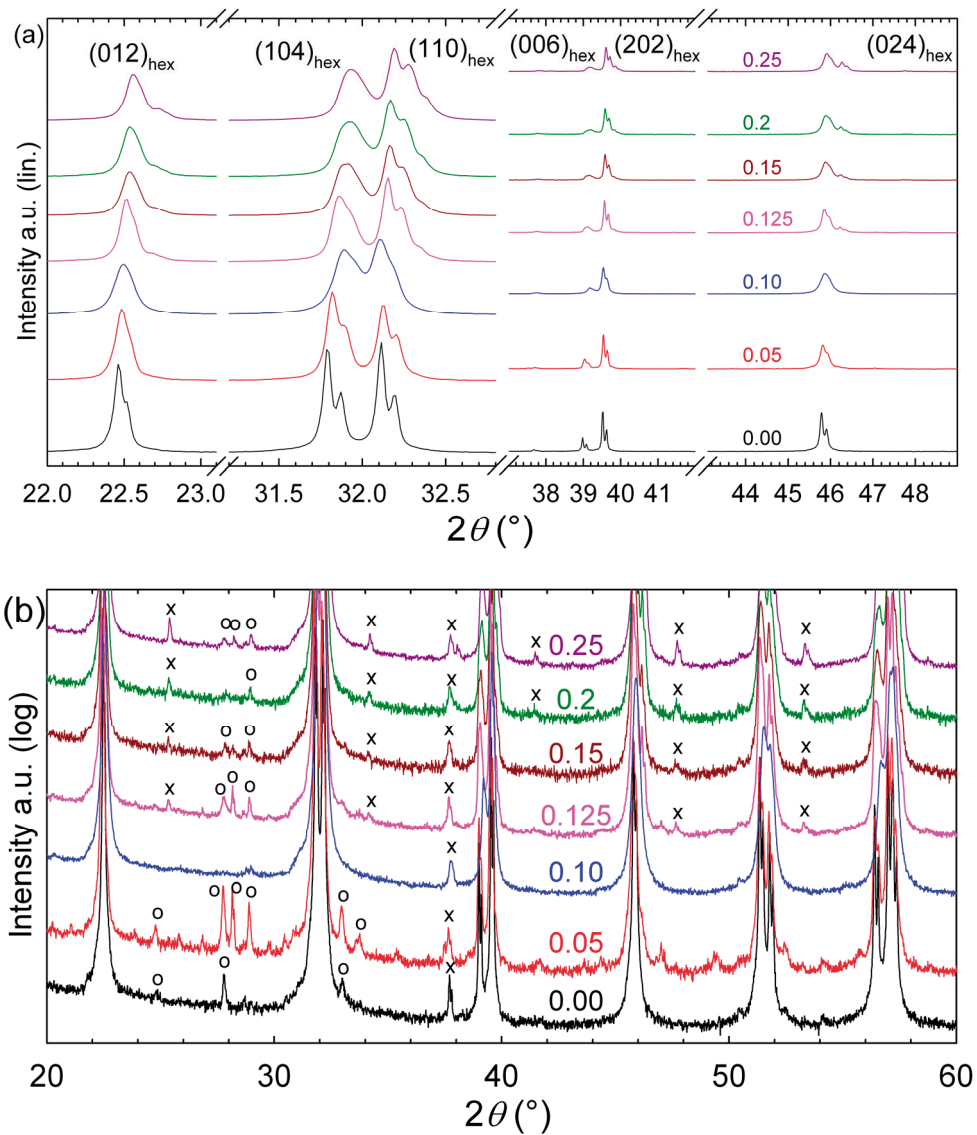


Figure 8.1. XRD patterns of La-substituted BiFeO_3 . Coloured labels refer to x in $\text{Bi}_{1-x}\text{La}_x\text{FeO}_3$. (a) Selected strong Bragg reflections are plotted on a linear scale to show the evolution of the peak shape and splitting. (b) Logarithmic scale to highlight the low-intensity reflections. Reflections marked “x” and “o” are due to the new phase emerging for $x > 0.1$ and trace amounts of $\text{Bi}_{25}\text{FeO}_{39}/\text{Bi}_2\text{Fe}_4\text{O}_9$, respectively.

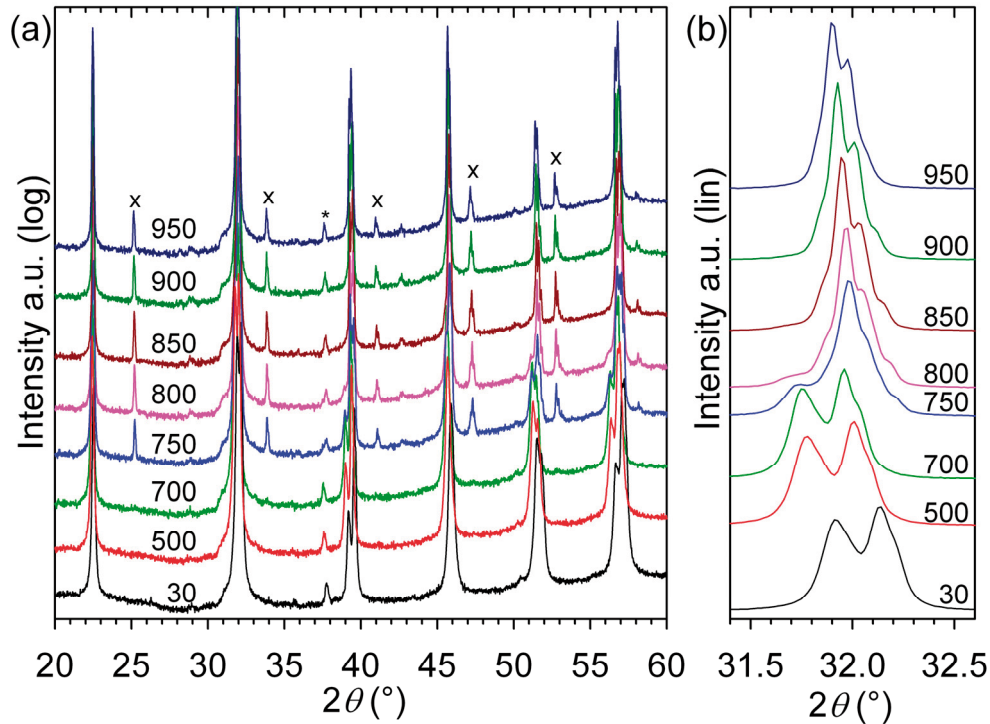


Figure 8.2. HTXRD patterns of $\text{Bi}_{0.9}\text{La}_{0.1}\text{FeO}_3$ at selected temperatures on a (a) common log-scale and (b) zoom-in on the $(110)_{\text{cb}}$ reflection on a linear scale. Reflections marked “x” are superreflections unique to the $Pbnm$ structure. The reflections marked “*” is common to the $R3c$ and $Pbnm$ structure.

HTXRD patterns of $\text{Bi}_{0.75}\text{La}_{0.25}\text{FeO}_3$ in Figure 8.3 change substantially between 600 and 700 °C. The temperature evolution of the $(110)_{\text{cub}}$ reflection in Figure 8.3 (b) shows that $R3c$ is the majority phase at 600 °C and below, and subtle triplet splitting is present at 800 °C and above. At 700 °C both the $R3c$ and $Pbnm$ polymorphs coexist. The superreflections highlighted in Figure 8.3 (a) increase abruptly in intensity from 600 to 700 °C with the expected shift towards lower 2θ values due to thermal expansion. This strongly suggests that the Bragg reflections which are observed to increase in intensity with increasing La content (Figure 8.1) are due to formation of a new phase with $Pbnm$ structure. Samples with $x > 0.1$ yields two phases, a Bi-rich ferroelectric $R3c$ phase, and a La-rich paraelectric $Pbnm$ phase at room temperature. The triplet splitting of the $(110)_{\text{cub}}$ reflections at 800 °C and above is more resolved for $\text{Bi}_{0.9}\text{La}_{0.1}\text{FeO}_3$ (Figure 8.2 (b)) than for $\text{Bi}_{0.75}\text{La}_{0.25}\text{FeO}_3$ (Figure 8.3 (b)). From the present data it is not possible to assess whether this is due to a strongly disordered single $Pbnm$ phase, or due to two $Pbnm$ phases with *different* chemical compositions, as e.g. proposed at room temperature for intermediate values of x in the system $\text{CaRu}_{1-x}\text{Mn}_x\text{O}_3$.⁴⁷⁵ The former alternative is tentatively assumed, but needs to be experimentally confirmed by electron microprobe analysis of a quenched sample.

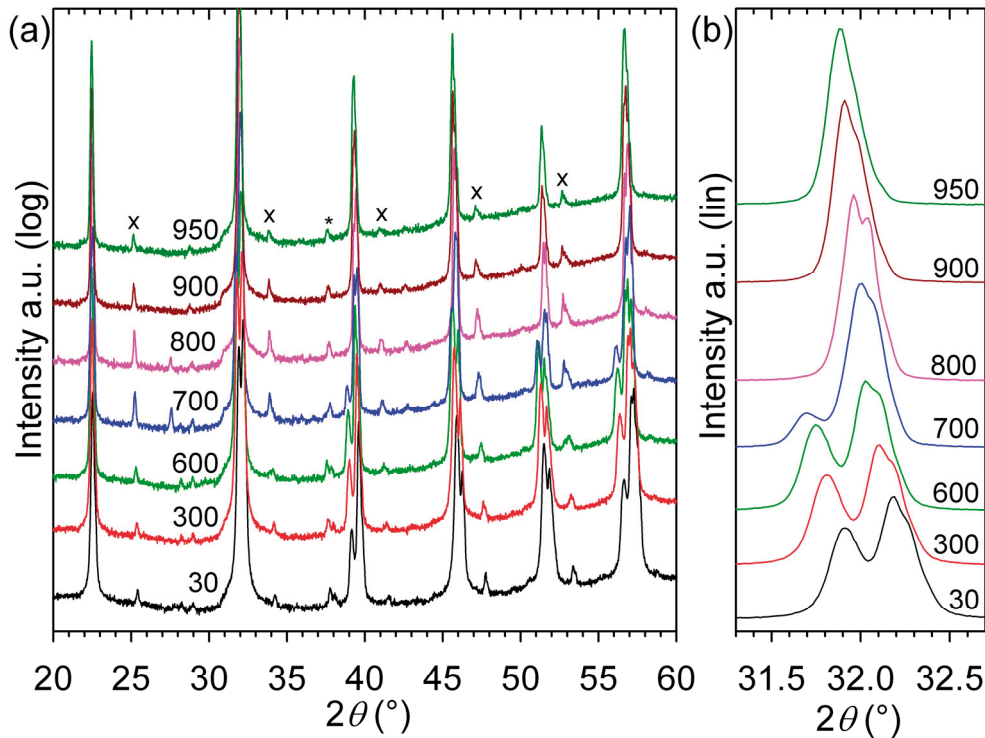


Figure 8.3. HTXRD patterns of $\text{Bi}_{0.75}\text{La}_{0.25}\text{FeO}_3$ at selected temperatures plotted on a (a) common log-scale and (b) zoom-in on the $(110)_{\text{cub}}$ reflection on a linear scale. Reflections marked “x” and “*” highlight superreflections unique to the $Pbnm$ phase and the only visible superreflection from the $R3c$ phase, respectively.

The temperature dependence of the intensity of the superreflections marked in Figures 8.2 and 8.3 is quantified by their intensity (taken as their net height in counts per second) in Figure 8.4. In $\text{Bi}_{0.9}\text{La}_{0.1}\text{FeO}_3$ (Figure 8.4 (a)) only the $(113)_{\text{hex}}$ reflection at $\sim 38^\circ 2\theta$ displays an intensity in the ferroelectric $R3c$ phase, and it prevails at 750°C and above where the $Pbnm$ phase becomes dominant. The maximum intensity of the superreflections from the $Pbnm$ phase occurs at $800\text{--}850^\circ\text{C}$, as the system is two-phase ($R3c$ and $Pbnm$) at 750°C . The intensity of the superreflections unique to the $Pbnm$ phase was also measured by the same method at $600\text{--}800^\circ\text{C}$, and the intensities included at these temperatures can be regarded as a measure of the uncertainty due to background noise. The intensity of the superreflections from $\text{Bi}_{0.75}\text{La}_{0.25}\text{FeO}_3$ in Figure 8.4 (b) supports the interpretation that for $x > 0.1$ the second phase has the same crystal structure as the paraelectric $Pbnm$ polymorph. At 700°C there is coexistence between $R3c$ and $Pbnm$, and at 800°C and above the material is $Pbnm$ single phase.

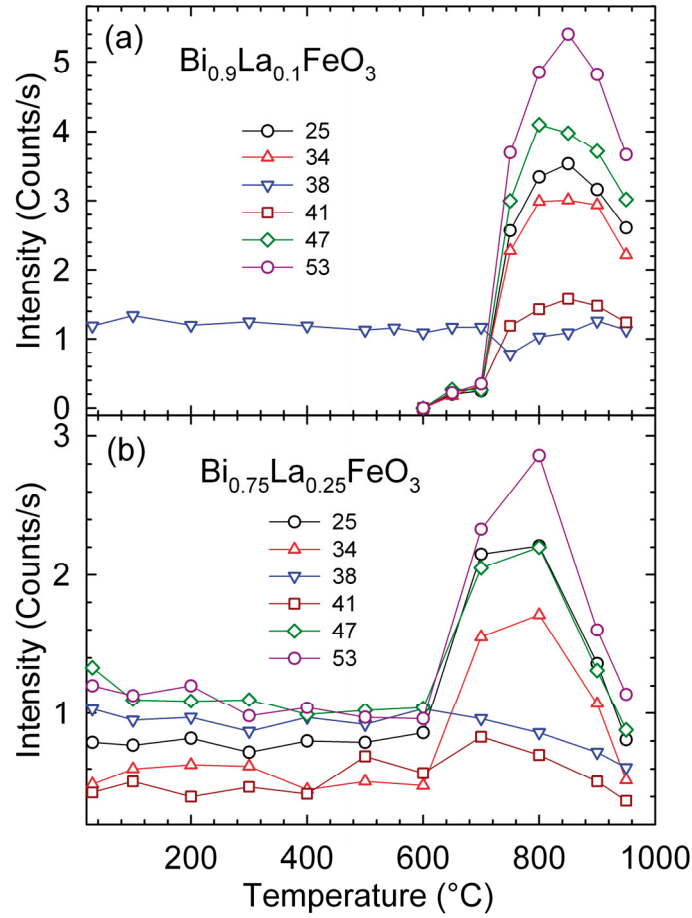


Figure 8.4. Net height of the low-intensity superreflections in Figure 8.2 (a) ($\text{Bi}_{0.9}\text{La}_{0.1}\text{FeO}_3$) and 8.4 (a) ($\text{Bi}_{0.75}\text{La}_{0.25}\text{FeO}_3$). Labels refer to their approximate 2θ position.

One precaution must be taken regarding the crystal structure of the second phase present for $x > 0.1$. The low phase fraction makes unambiguous structure determination from XRD impossible, as e.g. $Pbn2_1$, the polar version of $Pbnm$, is difficult to distinguish from the centrosymmetric parent structure $Pbnm$, see e.g. the determination of the space group of BiInO_3 by Belik and coworkers.¹⁸⁵

The structural sequence $R3c \xrightarrow{\leq 0.1} Pbn2_1 \xrightarrow{\leq 0.2} Pbnm$ for Gd-substituted BiFeO_3 reported by Khomchenko *et al.*⁴⁶⁴ was inferred from piezoelectric force microscopy measurements on ceramic samples, which indicated polar materials for $x_{\text{Gd}} = 0.2$ and non-polar for $x_{\text{Gd}} = 0.3$. Co-existing $R3c$ and $Pbn2_1$ for $x_{\text{Gd}} = 0.1$ was thus concluded by Khomchenko *et al.*⁴⁶⁴ Initial Rietveld refinements of XRD patterns from $\text{Bi}_{0.75}\text{La}_{0.25}\text{FeO}_3$ with $R3c + Pbnm$ and $R3c + Pbn2_1$ gave better fits for the latter combination of structures, but with a very small difference in R_{wp} values, 2.730 and 2.703, respectively. This small difference may be due to the lower symmetry of the $Pbn2_1$ structure, with more structural degrees of freedom in

terms of atomic positions, and should not necessarily be taken in favour of the latter combination of structures. Rietveld refinements of an XRD pattern from the $\text{Bi}_{0.75}\text{La}_{0.25}\text{FeO}_3$ sample with $R3c + Pbnm$ and $R3c + Pbn2_1$ are shown in Figure 8.5 (a) and (b), respectively. There is virtually no difference in the calculated profile for the second phase in the two different models. The combination of $R3c$ and $Pbnm$ was preferred for the remaining part of this chapter.

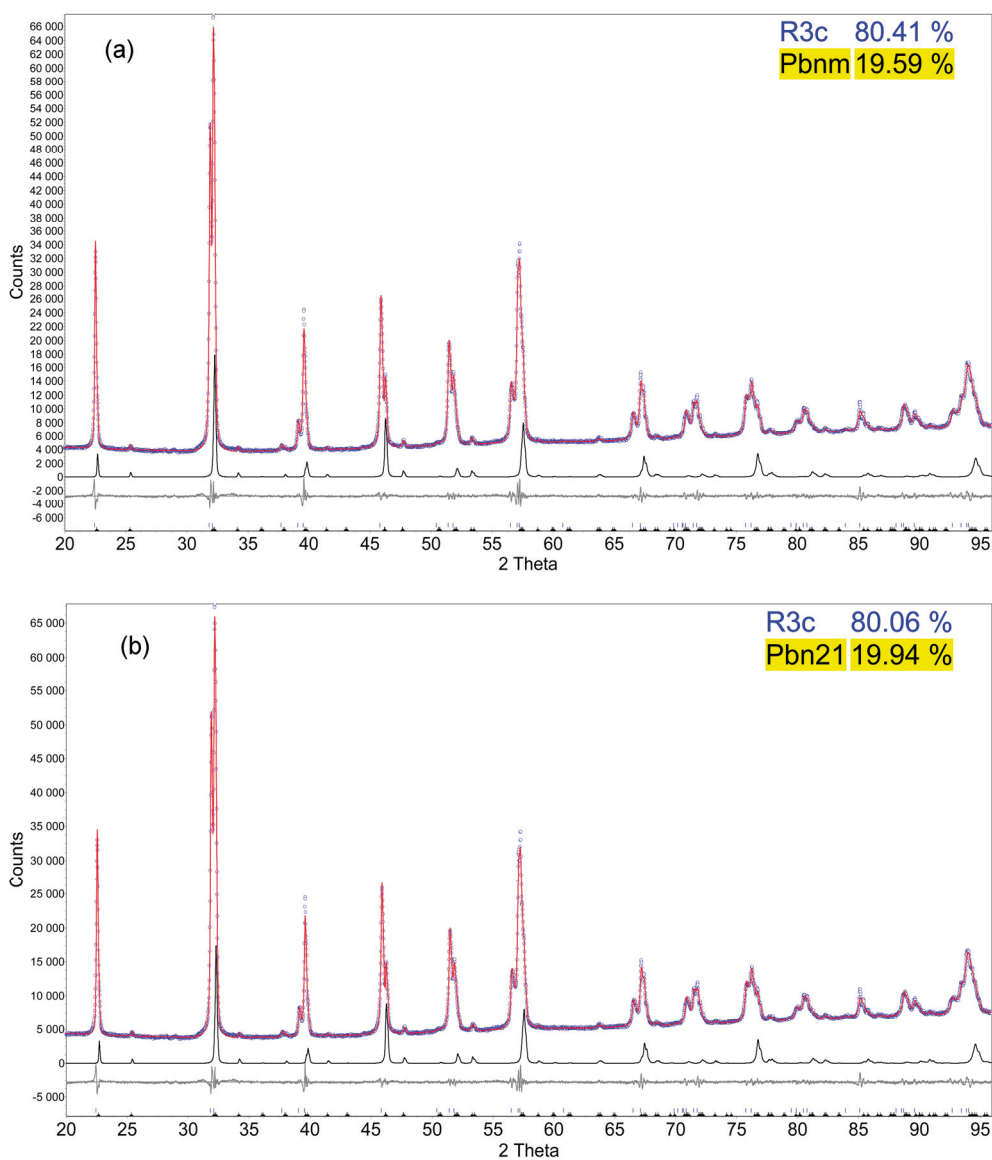


Figure 8.5. Rietveld refinements of the XRD pattern of the sample $\text{Bi}_{0.75}\text{La}_{0.25}\text{FeO}_3$ with (a) $R3c + Pbnm$ and (b) $R3c + Pbn2_1$. Observed and calculated data are represented by blue circles and a red line, respectively. The black line below the recorded pattern is the calculated pattern for the (a) $Pbnm$ and (b) $Pbn2_1$ phases.

The phase composition inferred from Rietveld refinements as a function of nominal composition is shown in Figure 8.6. The mole fraction of *Pbnm* increases with increasing nominal La content for $x > 0.1$. In the two-phase region with $x > 0.1$ the chemical composition of each phase is not necessarily equal to the nominal composition of the system. Specifically, mass balance for La requires that:

$$X_{R3c} \cdot x_{La}^{R3c} + (1 - X_{R3c}) \cdot x_{La}^{Pbnm} = x, \quad (8.1)$$

where x_{La}^{R3c} and x_{La}^{Pbnm} are the mole fractions of La in the *R3c* and the *Pbnm* phases, respectively. X_{R3c} is the mole fraction of the *R3c* phase, and x is the nominal mole fraction of La in the system. X_{Pbnm} is the mole fraction of the *Pbnm* phase, and $X_{R3c} + X_{Pbnm} = 1$. Bi ($Z = 83$) and La ($Z = 57$) are distinguishable by XRD, but the small mole fractions of the *Pbnm* phase yields substantial uncertainty in the refined chemical compositions of each phase. Table 8.3 summarises the refined chemical compositions the two phases for the samples with $x > 0.1$ and compares the refined composition $x^{ref.}$ of the sample with the nominal composition x .

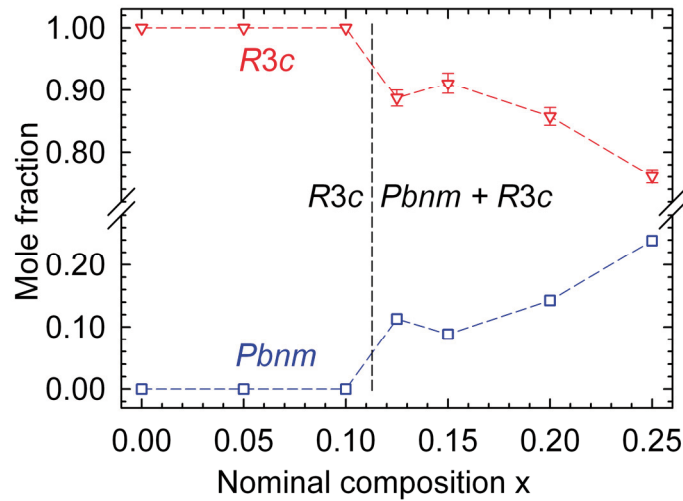


Figure 8.6. Refined phase composition as a function of nominal La content x at ambient temperature. Calculated uncertainties are smaller than the symbols.

Table 8.3. Refined chemical compositions x_{La}^{R3c} and x_{La}^{Pbnm} , phase fractions X_{R3c} and X_{Pbnm} , refined mole fraction of La in the system $x^{ref.}$ and % deviation of $x^{ref.}$ from the nominal mole fraction of La, x , for two-phase samples with $x > 0.1$.

x	X_{R3c}	x_{La}^{R3c}	X_{Pbnm}	x_{La}^{Pbnm}	$x^{ref.}$	% dev.
0.125	0.887	0.083 ± 0.045	0.113	0.680 ± 0.096	0.150	16.9
0.15	0.912	0.088 ± 0.042	0.088	0.816 ± 0.230	0.152	1.3
0.20	0.857	0.090 ± 0.043	0.143	0.815 ± 0.102	0.194	-3.3
0.25	0.761	0.081 ± 0.036	0.239	0.800 ± 0.048	0.253	1.0

The refined chemical compositions of the $R3c$ (x_{La}^{R3c}) and $Pbnm$ (x_{La}^{Pbnm}) phases give reasonable total La contents ($x^{ref.}$) with respect to the overall mass balance for La (and implicitly Bi). The ferroelectric $R3c$ phase clearly contains less La than the paraelectric $Pbnm$ phase, and the maximum La content of the $R3c$ phase is about $x_{La}^{R3c} = 0.1$. Extrapolation of the mole fractions of the $R3c$ phase and the $Pbnm$ phase as a function of the nominal composition of the system implies that the mole fractions are equal at about $x = 0.42$. Further extrapolation indicates that only the $Pbnm$ phase will be present in the system at $x = 0.75$, in reasonable agreement with the refined x_{La}^{Pbnm} . Based on the refinement, coexistence of La-substituted BiFeO_3 ($R3c$) and Bi-substituted LaFeO_3 ($Pbnm$) is found for $0.1 \leq x \leq 0.75$.

In figure 8.7 the uncertainty in refined chemical composition for the two-phase samples is taken into account when displaying the lattice parameters (a) and unit cell distortion (b) of the $R3c$ phase as a function of x . The lattice parameter c along the polar direction of the unit cell is the most sensitive to La substitution, and decreases rapidly with increasing x . The lattice parameter a normal to the polar direction is relatively insensitive to the La content, thus the associated trend in unit cell volume and unit cell distortion c/a (Figure 8.7 (b)) is primarily due to the changes in the lattice parameter c .

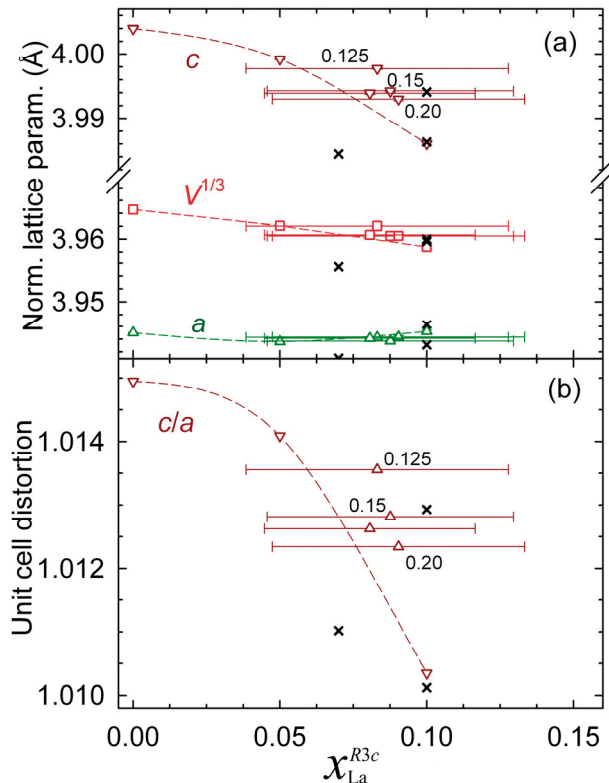


Figure 8.7. Normalised lattice parameters (a) and unit cell distortion c/a (b) for the $R3c$ phase. Single-phase samples are connected by a dashed line, two-phase $\text{Bi}_{1-x}\text{La}_x\text{FeO}_3$ samples are shown with the uncertainty in the refined chemical composition, labels refer to the nominal composition x . Literature values: x .^{420, 449}

8.2.2 High temperature behaviour

DTA traces of $\text{Bi}_{1-x}\text{La}_x\text{FeO}_3$ with $x = 0, 0.1$ and 0.25 are presented in Figure 8.8. For the single phase sample with $x = 0.1$, T_C is reduced from 830 to 675 ± 10 °C, in reasonable agreement with the T_C of $700\text{-}750$ °C from HTXRD. For $x = 0.1$ a distinct thermal event occurs at 983 ± 10 °C, which may be the transition to a cubic polymorph with space group $Pm\bar{3}m$, as the relative size of this peak corresponds to the relative sizes of the peaks at T_C and T_{cub} of pure BiFeO_3 . HTXRD patterns were not recorded at a high enough temperature to verify this conclusively, but for the following it is presumed that this thermal event corresponds to T_{cub} . Closely above T_{cub} the strongly endothermal signal points to peritectic decomposition, which takes place at substantially higher temperature (1000 ± 10 °C) compared to pure BiFeO_3 ($935\text{-}960$ °C). This is also reasonable taking into account the higher melting point of LaFeO_3 of 1890 ± 30 °C.⁴⁷⁶ The DTA trace from the two-phase sample with $x = 0.25$ is harder to interpret. Although the HTXRD patterns in Figure 8.3 indicate a phase transition at about 700 °C, there are no distinct thermal events in this temperature region.

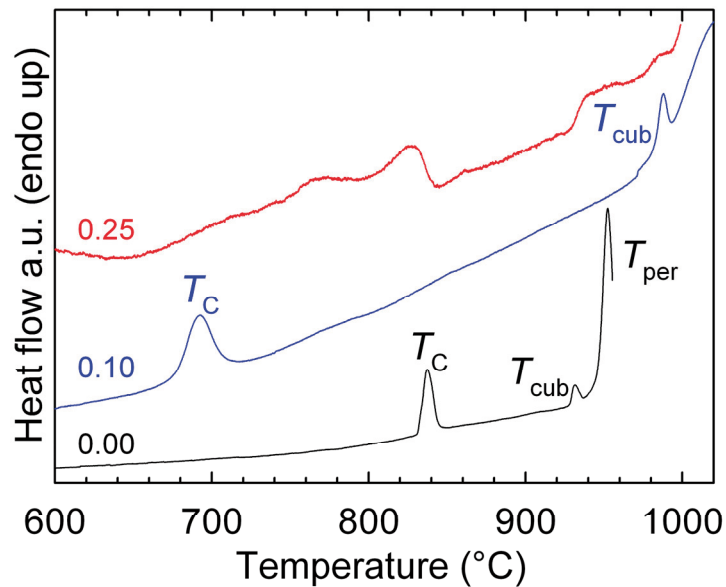


Figure 8.8. DTA traces of $\text{Bi}_{1-x}\text{La}_x\text{FeO}_3$ where the labels refer to x . T_C , T_{cub} and T_{per} denotes the ferroelectric Curie temperature, the transition to cubic structure and the peritectic decomposition temperature, respectively.

The DSC traces in Figure 8.9 suggest that T_N increases with increasing La content in line with the higher T_N of LaFeO_3 and available literature.^{449, 452} The T_N of the sample with $x = 0.25$ is similar to that of the single-phase sample with $x = 0.1$, pointing to a $x_{\text{La}}^{R3c} \sim 0.1$ in the main phase of this sample. A broad endothermal feature superimposed on the background can barely be seen between 441 and 478 °C, and may be the T_N of the secondary $Pbnm$ phase with $x_{\text{La}}^{Pbnm} \sim 0.9$, which would

be expected to have a T_N closer to that of LaFeO_3 than BiFeO_3 . The small and broad feature associated with T_N of the $Pbnm$ phase follows from $X_{Pbnm} \sim 0.2$ and possible disorder.

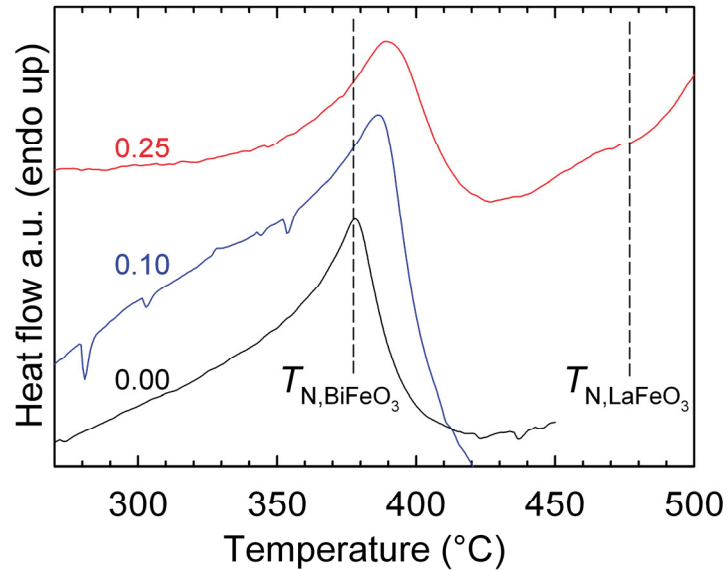


Figure 8.9. DSC traces for $\text{Bi}_{1-x}\text{La}_x\text{FeO}_3$ where the labels refer to x . The Néel temperatures of the parent compounds BiFeO_3 and LaFeO_3 are included for comparison.

Refined lattice parameters from HTXRD patterns (Figure 8.10 (a)) shows that $\text{Bi}_{0.9}\text{La}_{0.1}\text{FeO}_3$ behaves qualitatively similar to pure BiFeO_3 . The unit cell distortion of the $R3c$ phase, c/a , is smaller for $\text{Bi}_{0.9}\text{La}_{0.1}\text{FeO}_3$ than BiFeO_3 at all temperatures, and goes through a maximum at 400 °C, while for pure BiFeO_3 this occurs at ~450 °C. In the $Pbnm$ phase the unit cell distortion (Figure 8.10 (b)), c/a and b/a , decreases rapidly with increasing temperature towards a metrically cubic phase, which was not reached at the highest temperature investigated here (950 °C). Lattice parameters and unit cell distortions in the $Pbnm$ phase of $\text{Bi}_{0.9}\text{La}_{0.1}\text{FeO}_3$ are close to those of pure BiFeO_3 .

Refined atomic position parameters in the $R3c$ phase are qualitatively in line with those of pure BiFeO_3 , but with smaller polar displacements of both Bi/La (s) and Fe (t) (Figure 8.11 (a)) at low temperatures. The cooperative cation displacements $s - t$ in Figure 8.11 (b) decrease linearly with increasing temperature up to 700 °C, but retains a large finite value just below T_C , comparable to that of pure BiFeO_3 . The oxygen positions (Figure 8.11 (c)), the octahedral tilt angle ω and octahedral strain ζ in Figure 8.11 (d), inferred from the oxygen positions, change slowly with increasing temperature. Decreasing octahedral tilt angle and octahedral strain approaching unity imply a less distorted crystal structure with increasing temperature.

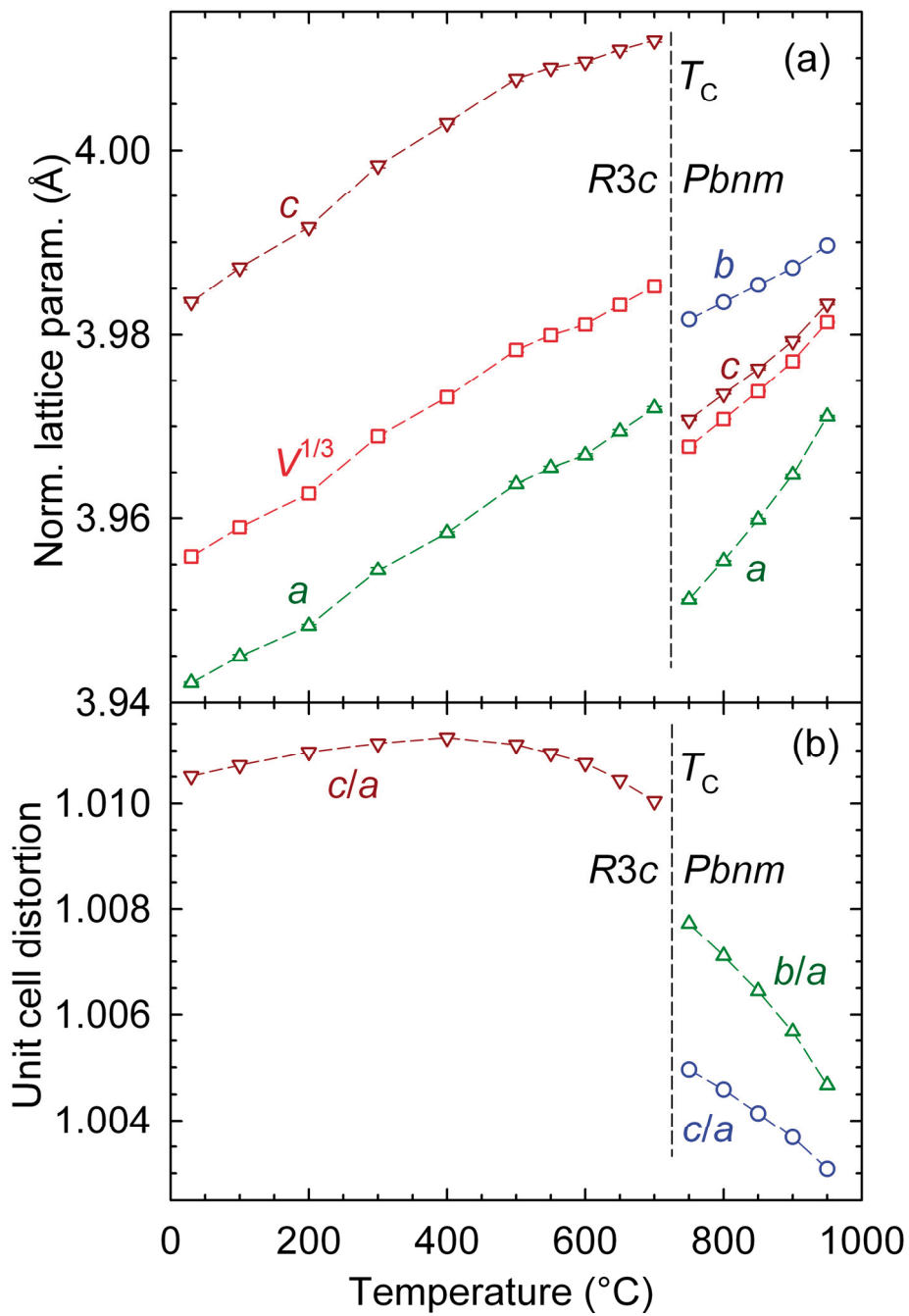


Figure 8.10. Refined normalised lattice parameters (a) and unit cell distortion (b) of $\text{Bi}_{0.9}\text{La}_{0.1}\text{FeO}_3$ as a function of temperature.

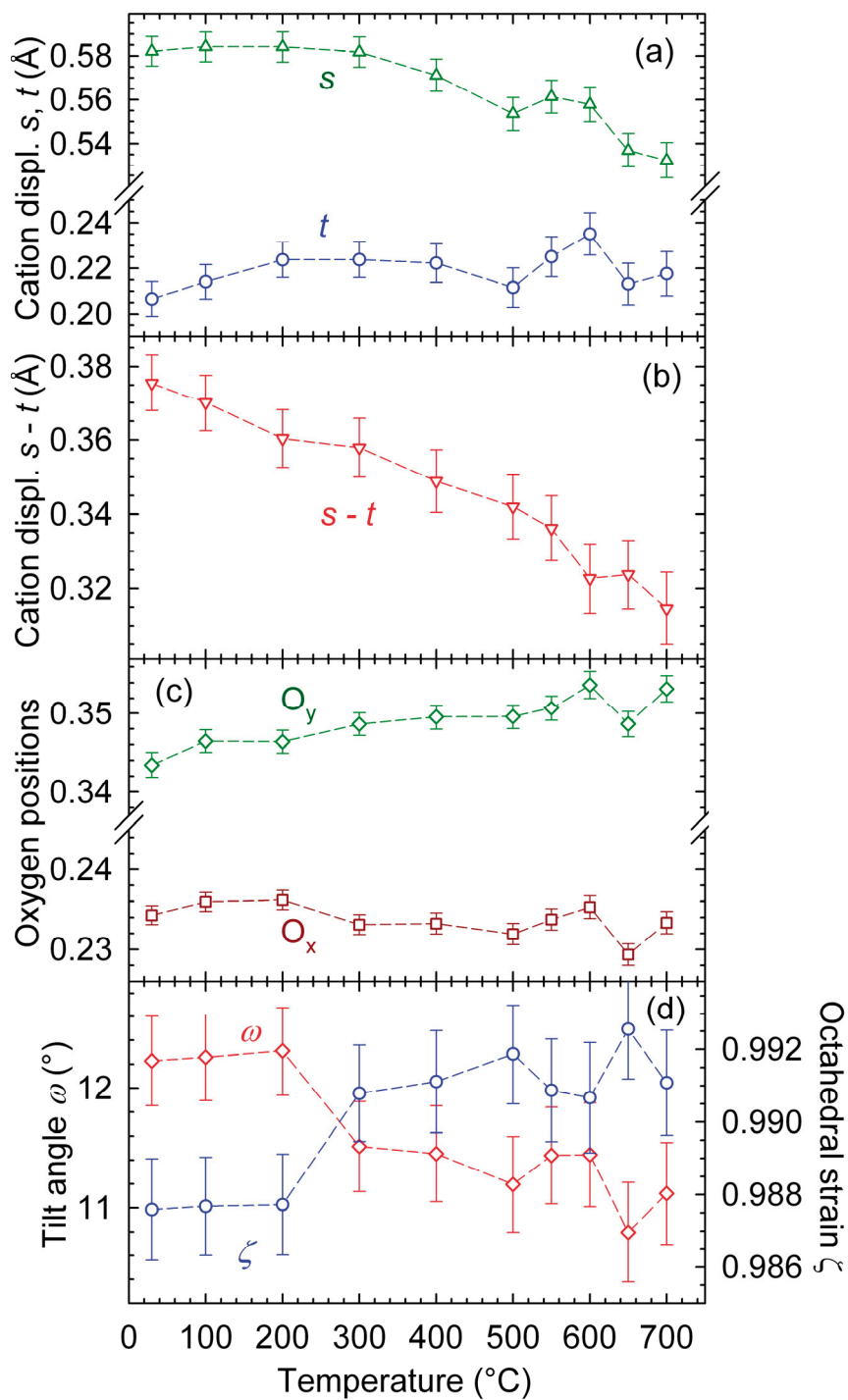


Figure 8.11. Refined atomic position parameters in $\text{Bi}_{0.9}\text{La}_{0.1}\text{FeO}_3$ as a function of temperature. (a) Polar cation displacements of Bi/La (s) and Fe (t). (b) Cooperative polar cation displacements $s - t$. (c) Oxygen position parameters and (d) octahedral tilt angle ω and octahedral strain ζ .

In $\text{Bi}_{0.75}\text{La}_{0.25}\text{FeO}_3$ two phases present below T_C , and the refined phase composition in terms of mole fractions X_{R3c} and X_{Pbnm} as a function of temperature is shown in Figure 8.12. Mass balance with respect to the distribution of La between the two phases below T_C is summarised in Table 8.4.

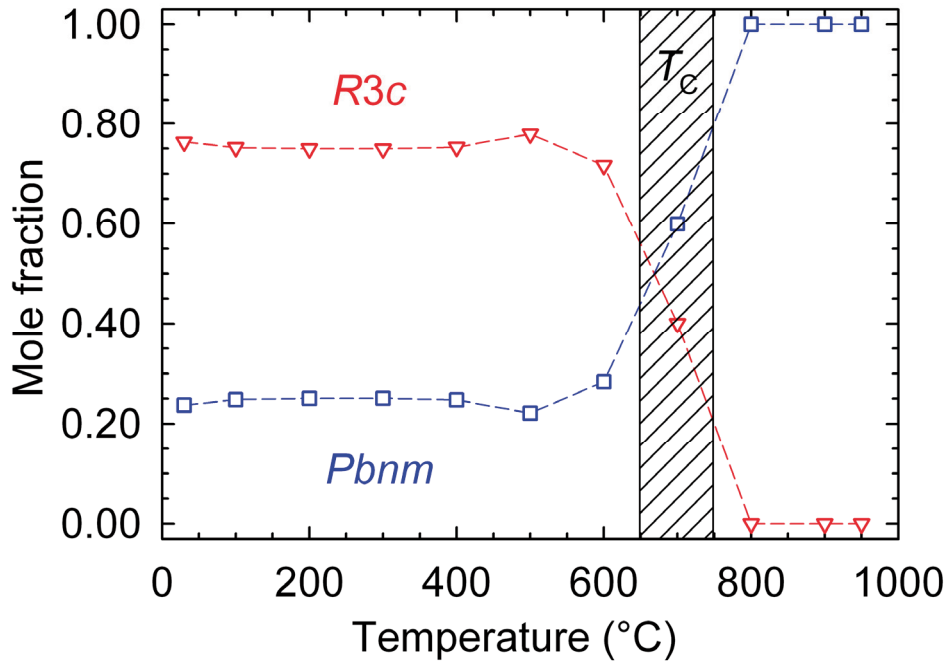


Figure 8.12. Refined phase composition as a function of temperature for the $\text{Bi}_{0.75}\text{La}_{0.25}\text{FeO}_3$ sample with nominal composition $x = 0.25$. Calculated uncertainties are smaller than the symbols.

Table 8.4. Refined chemical compositions x_{La}^{R3c} and x_{La}^{Pbnm} , phase fractions X_{R3c} and X_{Pbnm} , refined mole fraction of La in the system x^{ref} and % deviation of x^{ref} from the nominal mole fraction $x = 0.25$ below T_C in the $\text{Bi}_{0.75}\text{La}_{0.25}\text{FeO}_3$ sample.

T (°C)	X_{R3c}	x_{La}^{R3c}	X_{Pbnm}	x_{La}^{Pbnm}	x^{ref}	% dev.
30	0.763	0.084 ± 0.027	0.237	0.963 ± 0.051	0.292	14.5
100	0.752	0.084 ± 0.027	0.248	0.917 ± 0.054	0.291	14.1
200	0.750	0.086 ± 0.027	0.250	0.907 ± 0.052	0.292	14.3
300	0.749	0.084 ± 0.028	0.251	0.901 ± 0.053	0.289	13.5
400	0.752	0.089 ± 0.028	0.248	0.896 ± 0.050	0.289	13.4
500	0.779	0.082 ± 0.027	0.221	0.900 ± 0.046	0.263	5.0
600	0.716	0.088 ± 0.029	0.284	0.898 ± 0.039	0.318	21.3
700	0.401	0.085 ± 0.039	0.599	0.381 ± 0.039	0.263	4.8

At 700 °C the *Pbnm* phase becomes the dominating phase and at 800 °C only the *Pbnm* structure is present. The chemical composition of the *Pbnm* phase thus changes substantially across the transition region if the sample becomes single phase above T_C . Likewise, if two *Pbnm* phases are present above T_C , the different chemical compositions will give rise to small differences in lattice parameters, accounting for the broad reflections observed in Figure 8.3 (b). The strongly non-linear behaviour of the refined lattice parameters of the *Pbnm* phase across T_C in Figure 8.13 (a) can be rationalised both from the contingency of a single *Pbnm* phase with smaller $x_{\text{La}}^{\text{Pbnm}}$ than below T_C , or a new *Pbnm* phase emerging with $x_{\text{La}}^{\text{Pbnm}}$ equal to $x_{\text{La}}^{\text{R3c}}$ below T_C . In the *Pbnm* phase the A cation is effectively eight-coordinated, and Bi^{3+} (1.17 Å) is slightly larger than La^{3+} (1.16 Å) according to their tabulated Shannon radii.¹¹⁴ However, the volume occupied by Bi^{3+} depends on whether the $6s^2$ lone pair is stereochemically active or not. In the former situation Bi^{3+} occupies a larger volume than La^{3+} , and oppositely in compounds where the $6s^2$ lone pair is not stereochemically active. In general, the lone pair is only inactive when Bi^{3+} is situated in sites of high symmetry, which is not the case in neither the *R3c* nor the *Pbnm* structures.¹¹⁴ The ratio of the primitive unit cell volumes of BiFeO_3 and LaFeO_3 (Table 8.1) is 1.047, while the ratio of tabulated ionic radii 1.17/1.16 is 1.008. It appears that Bi^{3+} with a stereochemically active $6s^2$ lone pair occupies a substantially larger volume than La^{3+} in perovskite ferrites. This reasoning can account for the anomalous increase in the refined lattice parameters and unit cell volume (Figure 8.13 (b)) of the *Pbnm* phase as $x_{\text{La}}^{\text{Pbnm}}$ decreases across T_C . The structural consequence of the change in $x_{\text{La}}^{\text{Pbnm}}$ is particularly evident in the unit cell distortion of the *Pbnm* phase across T_C , Figure 8.13 (c). The paraelectric *Pbnm* phase of the $\text{Bi}_{0.75}\text{La}_{0.25}\text{FeO}_3$ sample is less distorted than the corresponding *Pbnm* phase of the $\text{Bi}_{0.9}\text{La}_{0.1}\text{FeO}_3$ sample at equal temperatures, reflecting the influence of the chemical composition on the structure of this polymorph. The less distorted *Pbnm* phase of the $\text{Bi}_{0.75}\text{La}_{0.25}\text{FeO}_3$ sample is closer to being metrically cubic, but no phase transition was observed at the highest temperature investigated here (950 °C).

The *R3c* phase of $\text{Bi}_{0.75}\text{La}_{0.25}\text{FeO}_3$ behaves qualitatively similar to BiFeO_3 and $\text{Bi}_{0.9}\text{La}_{0.1}\text{FeO}_3$, except at 700 °C, which is likely to be due to problems with the refinement when the fractions of the two phases are approximately equal. The maximum unit cell distortion occurs at 300 °C, a lower temperature than for pure BiFeO_3 . Compared to $\text{Bi}_{0.9}\text{La}_{0.1}\text{FeO}_3$, the *R3c* phase of the $\text{Bi}_{0.75}\text{La}_{0.25}\text{FeO}_3$ has a larger lattice parameter c , higher unit cell distortion c/a and larger unit cell volume, reflecting that $x_{\text{La}}^{\text{R3c}} < 0.1$.

The polar cation displacements of Bi/La (s) and Fe (t) of the *R3c* phase in $\text{Bi}_{0.75}\text{La}_{0.25}\text{FeO}_3$ (Figure 8.14 (a) and (b)) are larger than in the $\text{Bi}_{0.9}\text{La}_{0.1}\text{FeO}_3$ sample, implying that $x_{\text{La}}^{\text{R3c}} < 0.1$ in concordance with the lattice parameters, c/a and mass balance inferred from refinement of the chemical composition. Both s , t and $s - t$ are smaller than for pure BiFeO_3 . The octahedral tilt angle ω decreases and the octahedral strain ζ approaches unity with increasing temperature (Figure 8.14 (d)) and the structure becomes less distorted.

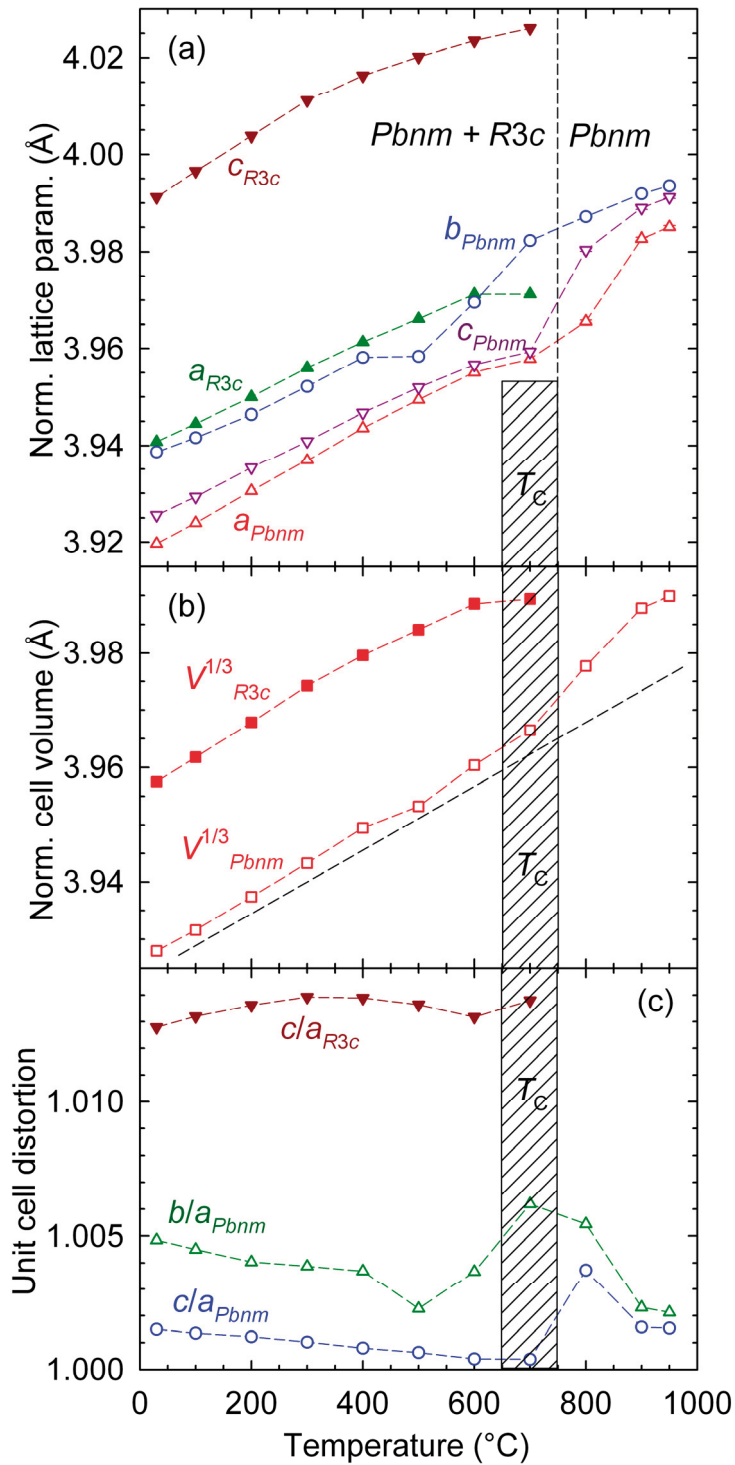


Figure 8.13. (a) Refined normalised lattice parameters, (b) normalised unit cell volume and (c) unit cell distortion of the phases in the $\text{Bi}_{0.75}\text{La}_{0.25}\text{FeO}_3$ sample with nominal composition $x = 0.25$ as a function of temperature.

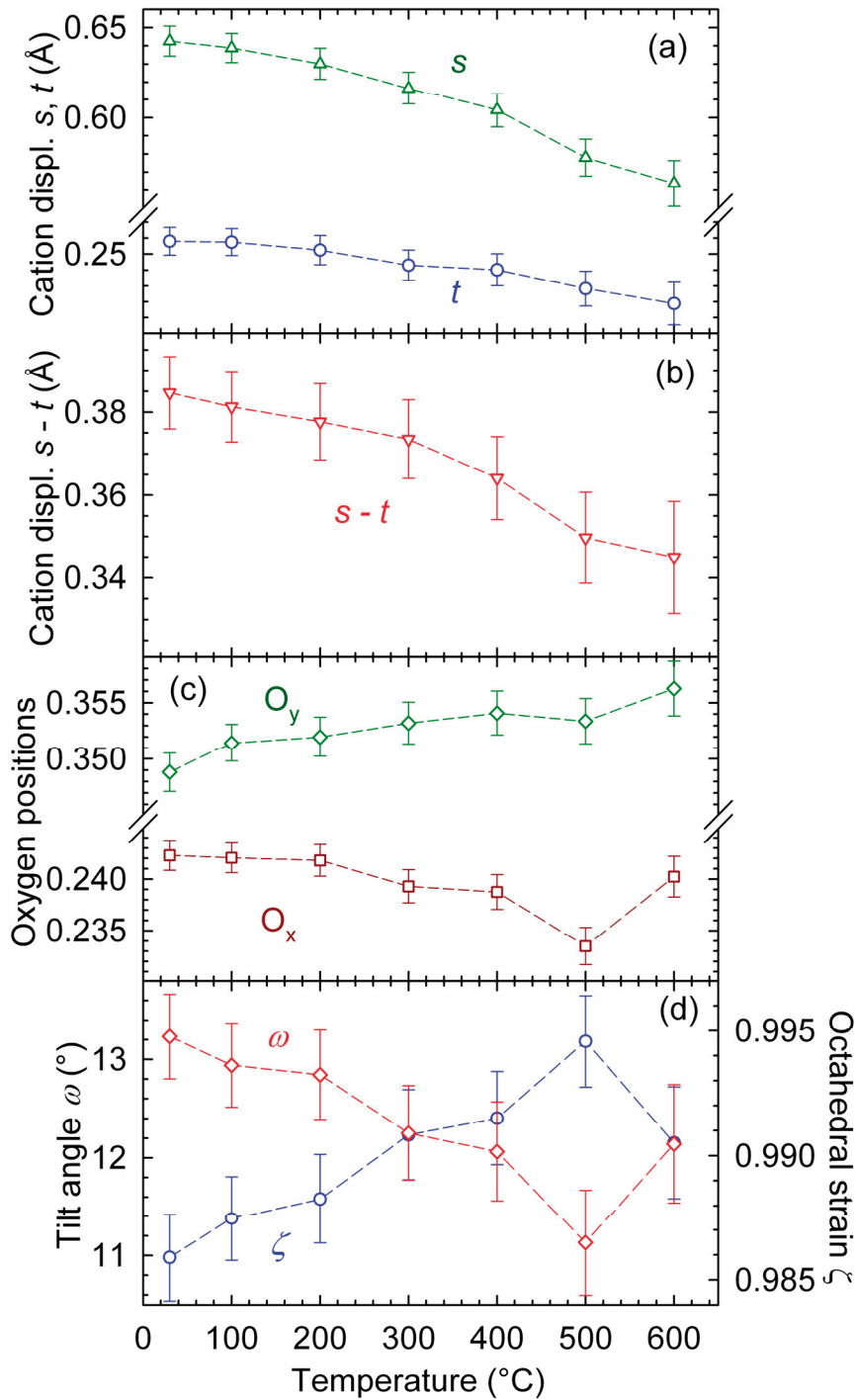


Figure 8.14. Refined atomic position parameters of the $\text{Bi}_{0.75}\text{La}_{0.25}\text{FeO}_3$ sample with nominal composition $x = 0.25$. (a) Polar cation displacements of Bi/La (s) and Fe (t). (b) Cooperative polar cation displacements $s - t$. (c) Oxygen position parameters and (d) octahedral tilt angle ω and octahedral strain ζ .

8.3 Discussion

8.3.1 Structure and solubility

With increasing La content the ferroelectric $R3c$ structure becomes less distorted along the polar c -axis, accompanied by a reduction in unit cell volume (Figure 8.7). The refined polar displacements of the A cation (Bi/La) and B cation (Fe) decrease with increasing La content. Unlike Bi^{3+} , La^{3+} does not possess a $6s^2$ lone pair, which is believed to be imperative for the stabilisation of the polar, ferroelectric $R3c$ structure. La^{3+} is also a more basic cation than Bi^{3+} and partial covalent bonding between O^{2-} and La^{3+} is not anticipated. Substitution with La is thus detrimental to the ferroelectric properties of BiFeO_3 . The lattice parameter a normal to the polarisation decreases only subtly with increasing La content.

La can be dissolved in the ferroelectric $R3c$ structure up to a concentration of $0.1 \leq x$ (x_{La}^{R3c}) < 0.125 ($\text{Bi}_{1-x}\text{La}_x\text{FeO}_3$) (Figure 8.1). The solid solubility of Bi in LaFeO_3 is suggested to be approximately $x_{\text{La}}^{Pbnm} = 0.75$ ($x = 0.25$ in $\text{La}_{1-x}\text{Bi}_x\text{FeO}_3$). Phase separation occurs when exceeding these solubility limits as a new phase appears. This unambiguous result is in contrast with the majority of reports on La-substituted BiFeO_3 , which conclude with a sequence of composition driven phase transitions, see Table 8.2. The structure of the new phase appearing at $x > 0.1$ is similar to that of the orthorhombic parent compound LaFeO_3 , and the most likely space groups are centrosymmetric $Pbnm$ and polar $Pbn2_1$, both with the Glazer tilt system $\bar{a}a^+b^+$. These structures are difficult to distinguish by XRD. The space group $Pbnm$ is tentatively assumed. A thorough structural characterisation of single-phase Bi-substituted LaFeO_3 is necessary to confirm this suggestion.

8.3.2 Chemical pressure and critical temperatures of the $R3c$ phase

The effect of La substitution on the critical temperatures of the $R3c$ phase can be understood from the associated changes in crystal structure and chemical bonding. Decreasing unit cell distortion with increasing La content combined with a smaller unit cell volume implies shorter Fe–O bond lengths and larger Fe–O–Fe angles, enhancing the overlap between Fe $3d e_g$ and $\text{O}^{2-} 2p$ orbitals, thus strengthening the antiferromagnetic superexchange and raising T_N (Figure 8.9). The structural consequences of La substitution resemble those of a small hydrostatic pressure, and as noted in chapter 3.1.2, $dT_N/dp > 0$ for antiferromagnets with localised d -electrons.⁷⁵

La destabilises the ferroelectric $R3c$ structure both in terms of unit cell distortion and thermal stability. With increasing La content T_C decreases as fewer A sites possess a $6s^2$ lone pair stabilising the ferroelectric $R3c$ polymorph. Assuming that the thermal event observed at 983 ± 10 °C for $x = 0.1$ in Figure 8.8 corresponds to a transition from $Pbnm$ to $Pm\bar{3}m$, La substitution stabilises the $Pbnm$ polymorph to both lower and higher temperatures compared to pure BiFeO_3 . Substituting Bi^{3+} with the smaller La^{3+} reduces the effective tolerance factor of the system, thereby raising T_{cub} , opposite of the effect of increasing δ in $\text{BiFe}_{1-x}\text{Mn}_x\text{O}_{3+\delta}$ in chapter 7 (Figure 7.15).

The interpretation of La-substitution as chemical pressure, being analogous to the effect of hydrostatic pressure, also holds for T_C and T_{cub} . As $\Delta_{trs}V_{T_C} < 0$, $\Delta_{trs}V_{T_{cub}} > 0$ and $|\Delta_{trs}V_{T_C}| \gg |\Delta_{trs}V_{T_{cub}}|$, hydrostatic pressure is expected to lower T_C and raise T_{cub} , the former being more sensitive to pressure than the latter. This is exactly the effect of increasing $x_{La,R3c}$ observed by DTA in Figure 8.8 and HTXRD in Figure 8.2. The melting point of $LaFeO_3$ is 1890 ± 30 °C⁴⁷⁶ accounting for the increasing peritectic decomposition temperature T_{per} with increasing La substitution.

8.3.3 Solution thermodynamics and phase diagram

The crystal structure of the $R3c$ polymorph in the two-phase samples with $x > 0.1$ is less distorted than for the single phase sample with $x = 0.1$, evidenced from both the splitting of the $(104)/(110)_{hex}$ Bragg reflection (Figure 8.1 (a)) and the refined lattice parameters (Figure 8.7). This shows that $x_{La,R3c} < 0.1$ in the two-phase samples. The distribution of La between the two phases is thus non-trivial, as excess La does not simply go into a pure $LaFeO_3$ $Pbnm$ phase when the La content of the system exceeds the solubility limit of the $R3c$ phase. Results from Rietveld refinements point to a Bi-rich $R3c$ phase with $x_{La,R3c} = \sim 0.07-0.09$ and a La-rich $Pbnm$ phase with $x_{La,Pbnm} = 0.75-0.8$. With increasing La content in the system, the mole fractions of the $R3c$ and $Pbnm$ phases change rather than the chemical compositions of the two phases.

One question insofar left unanswered is whether there is one or two $Pbnm$ phases present above T_C for $x > 0.1$. Either the $R3c$ phase transforms to a Bi-rich $Pbnm$ phase coexisting with the La-rich $Pbnm$ phase also present below T_C , or the $R3c$ phase “merges” with the original $Pbnm$ phase above T_C to form one $Pbnm$ phase with chemical composition equal to the nominal composition of the system. In the former case, immiscibility above T_C for $x > 0.1$ is implicitly assumed, and this scenario is explored further below.

Ignoring the small asymmetry of the system, the limited solubility of La in $BiFeO_3$ and Bi in $LaFeO_3$ can be described by a regular solution model with a positive interaction parameter, $\Omega_{BiLa} > 0$.⁴⁷⁷ Given the incomplete solid solubility, it is reasonable to suggest that the interaction parameter between the chemically different Bi^{3+} and La^{3+} is positive. In a regular solution model the enthalpy of mixing is positive and given by eq. (8.2):

$$\Delta_{mix}H_m = \Omega_{BiLa}x_{Bi}x_{La} \quad (8.2)$$

The observed compositions reflect the solubility limits at the firing temperature of 950 °C used for the two-phase samples. Complete solid solubility can be obtained above a critical temperature, T_{crit} , which can be estimated from the solubility limits at 950 °C (1223 K). The immiscibility gap of a regular solution, the binodal line, is given by:

$$\frac{\partial G_m}{\partial x_{La}} = RT(\ln x_{La} - \ln x_{Bi}) - \Omega_{BiLa}(1 - x_{La}) = 0, \quad (8.3)$$

and the the spinodal line, defining the metastable region of solubility, is given by eq. (8.4):

$$\frac{RT}{2\Omega_{BiLa}} = (1 - x_{La})x_{La} \quad (8.4)$$

The critical temperature for complete solid solubility, T_{crit} , is related to the interaction coefficient Ω_{BiLa} by eq. (8.5):

$$T_{crit} = \frac{\Omega_{BiLa}}{2R} = \frac{-T(\ln x_{La} - \ln x_{Bi})}{2(1 - x_{La})} \quad (8.5)$$

At 1223 K eq. (8.3) yields $\Omega_{BiLa} = 31.5, 27.6, 24.8$ and 22.6 kJ/mol for $x = 0.05, 0.075, 0.1$ and 0.125 , respectively, thus T_{crit} from eq. (8.5) becomes 1895, 1661, 1493 and 1360 K, respectively. The influence of the solubility quantified by x on T_{crit} from eq. (8.5), the binodal line from eq. (8.3) and spinodal line from eq. (8.4) is illustrated in Figure 8.15.

Solution (complete solubility) is stable at temperatures above the binodal line, and phase separation will not occur. Between the binodal and spinodal lines solution is metastable, and below the spinodal line solution is unstable. The solution is unstable towards compositional fluctuations below the spinodal line and phase separation occurs continuously without nucleation. In the metastable region phase separation of the homogenous solution requires nucleation of a new phase, and the solution is stable towards compositional fluctuations. Nucleation of a new phase is thermally activated, and can thus be kinetically hindered.

The apparent paradox that $x_{La}^{R3c} = 0.1$ in the single phase sample with nominal composition $x = 0.1$, and $x_{La}^{R3c} = \sim 0.07-0.09$ in the two-phase samples, is resolved by this interpretation of the thermodynamics of the system. A single $R3c$ phase with $x_{La}^{R3c} = 0.1$ is situated within the metastable region between the binodal and spinodal lines. When phase separation occurs, the chemical compositions of the $R3c$ and $Pbnm$ phases become equal to the compositions given by the binodal line, accounting for the associated decrease of x_{La}^{R3c} . The relative amounts of the two phases with different chemical compositions is governed by the mass balance through the lever rule, hence $X_{Pbnm} > x - 0.1$.

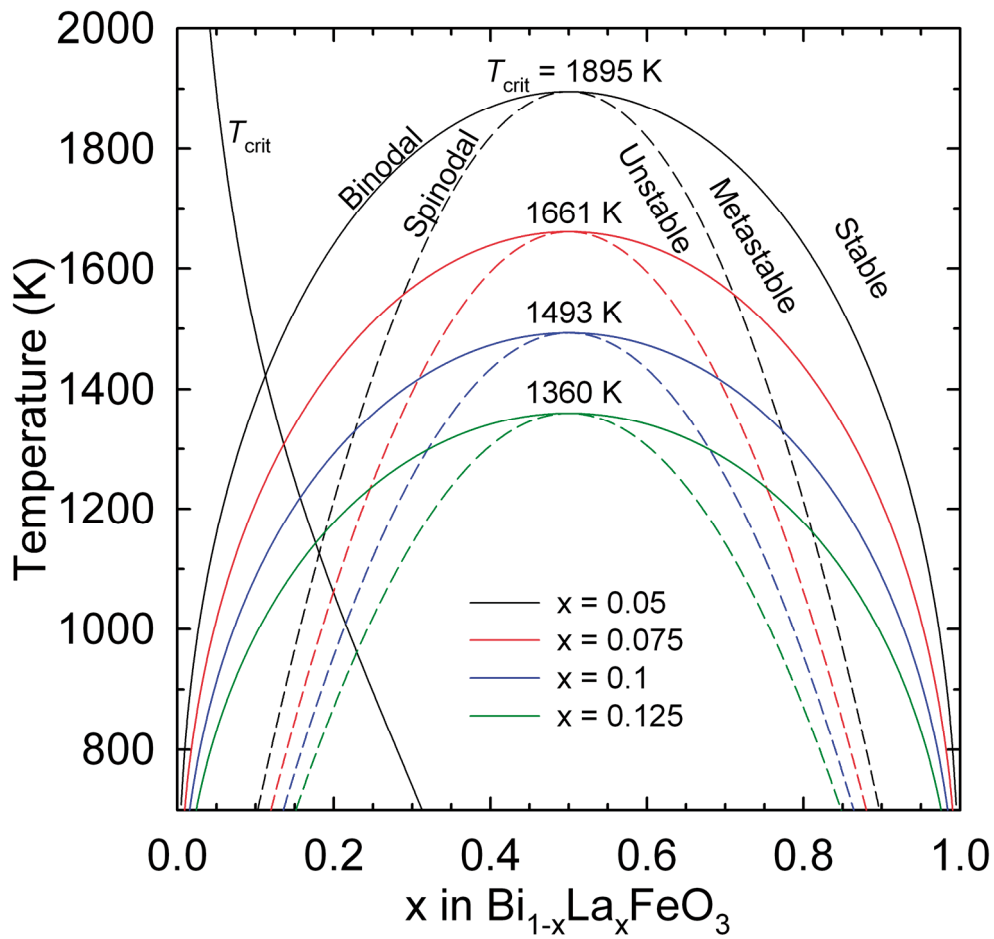


Figure 8.15. Critical temperature of solid solubility (T_{crit}), binodal (solid) and spinodal (dashed) lines in a regular solution model for the system $\text{Bi}_{1-x}\text{La}_x\text{FeO}_3$. Four different values of Ω_{BiLa} , 31.5, 27.6, 24.8 and 22.6 kJ/mol, for $x = 0.05$, 0.075, 0.1 and 0.125, respectively, yielding four different critical temperatures, are shown for illustration.

Pure LaFeO_3 undergoes a first order transition from $Pbnm$ to $R\bar{3}c$ at $980\text{--}987\text{ }^\circ\text{C}$ ⁴⁷⁸⁻⁴⁷⁹ and a second order transition from $R\bar{3}c$ to $Pm\bar{3}m$ at approximately $1250 \pm 100\text{ }^\circ\text{C}$ (extrapolated to $x = 0$ in $\text{La}_{1-x}\text{Sr}_x\text{FeO}_3$).³⁴⁵ The effect of Bi substitution on the phase transition temperatures of LaFeO_3 has not been thoroughly investigated. However, as Bi^{3+} is larger than La^{3+} , the structural phase transition temperatures of LaFeO_3 are anticipated to decrease with increasing Bi content, as the space groups $Pbnm$, $R\bar{3}c$ and $Pm\bar{3}m$ in perovskites are stable for increasing tolerance factors.¹²² Based on the results from HTXRD, DTA, DSC and the preceding discussion of the solution thermodynamics, a phase diagram of the pseudo-binary system $\text{BiFeO}_3\text{--LaFeO}_3$ is outlined in Figure 8.16. The solid and dashed red parabolas are the binodal and spinodal lines calculated from $x = 0.075$ and $\Omega_{\text{BiLa}} = 27.6\text{ kJ/mol}$. A

Redlich-Kister polynomial expression is tentatively suggested to account for the asymmetry of the solid solubility not accounted for by the regular solution model. As the compositional dependence of neither the liquidus nor the solidus curves are known, two possible liquidus curves are depicted, showing the influence of the interaction parameter in the liquid phase (where Fe can not be regarded simply as a “passive” sublattice, as implicitly presumed for the solid phases in the system). Additional experimental work remains before this phase diagram is fully mapped and understood.

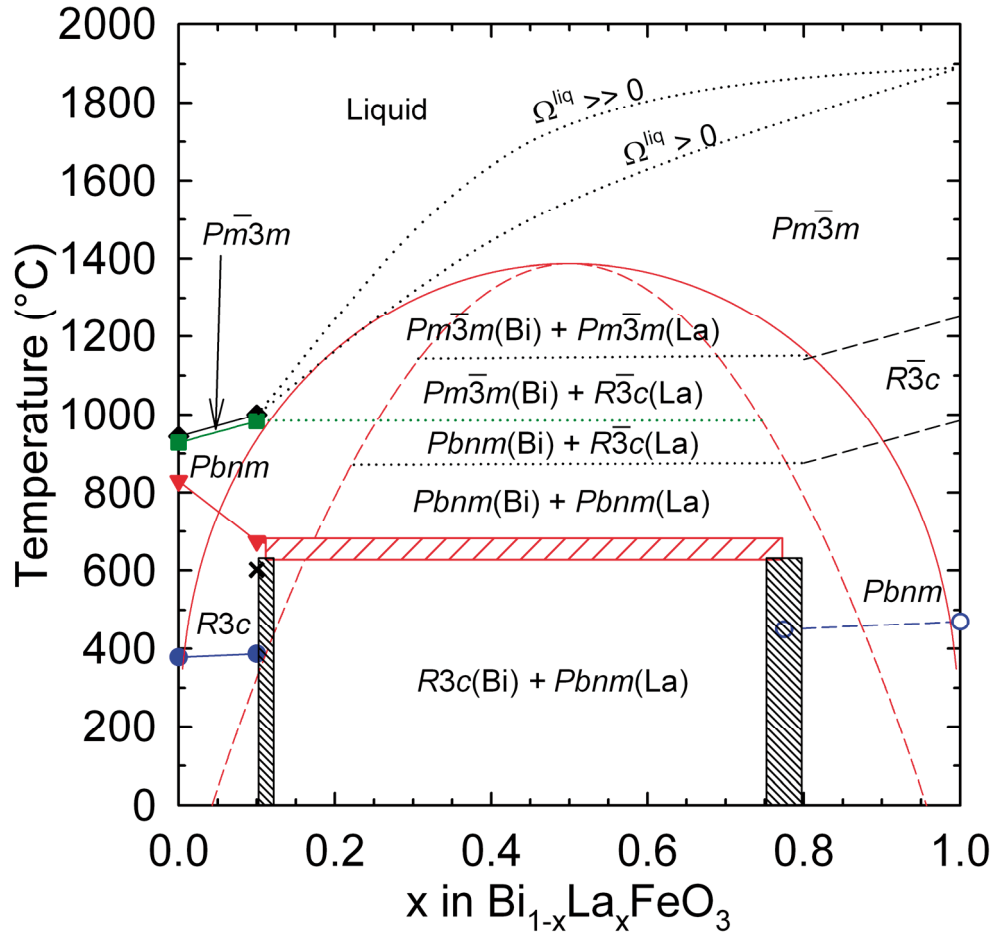


Figure 8.16. Outline of the phase diagram of the pseudobinary system BiFeO_3 - LaFeO_3 .

8.3.4 Metastable morphotropic phase boundaries

It should be stressed that the present discussion applies to bulk materials prepared at high temperatures where equilibrium can be reached. There is thus no contradiction between the interpretation of the present findings and reports of morphotropic phase boundaries (MPB) in thin films, e.g. for $\text{Bi}_{0.86}\text{Sm}_{0.14}\text{FeO}_3$, as

these films were grown layer by layer by PLD in a temperature region with low ionic mobility (600 °C).²⁸⁹⁻²⁹⁰ Materials crystallised from a chemically homogenous precursor (e.g. single crystal growth from a melt or crystallisation of an amorphous polymeric precursor) can be kinetically stabilised as homogenous single phase materials with $x_{\text{La},R3c}$ in the metastable region between the binodal and spinodal lines. Crystal structures different from those of the parent compounds BiFeO₃ and LaFeO₃ at room temperature can be obtained. An MPB in Bi_{1-x}La_xFeO₃ does not correspond to an equilibrium state of the system, but a kinetically stabilised state. Phase separation is anticipated upon heating of a single phase compound at a MPB in the Bi_{1-x}La_xFeO₃ system. Comparing the other Ln³⁺ to La³⁺ becomes gradually less straight-forward across the 4f period due to decreasing size and increasing acidity.

8.4 Conclusions

Substitution with La is detrimental to ferroelectricity as the unit cell distortion and ferroelectric Curie temperature T_C decreases with increasing La content. La stabilises the paraelectric *Pbnm* polymorph to both lower and higher temperatures compared to pure BiFeO₃. A lower effective tolerance factor with La substitution accounts for the stabilisation of the *Pbnm* polymorph over a larger temperature interval, and the elevation of the transition temperature to the cubic structure, T_{cub} . The Néel temperature T_N increases subtly with increasing La content. All the observed effects of La substitution on the crystal structure and phase transition temperatures resemble those expected from hydrostatic pressure, thus La substitution can be regarded to induce chemical pressure on the BiFeO₃ structure.

The system Bi_{1-x}La_xFeO₃ remains single phase *R3c* for nominal compositions $x \leq 0.1$, while for $x \geq 0.125$ phase separation occurs. Likewise, single phase *Pbnm* is expected for $x \geq 0.75-0.8$. The new phase appearing for $x \geq 0.125$ is similar to the structure of the parent compound LaFeO₃ with the orthorhombic space group *Pbnm*. This minority *Pbnm* phase was inferred to have a chemical composition of $x = 0.75-0.8$ (Bi_{1-x}La_xFeO₃) from Rietveld refinements and solution thermodynamics. In the two phase samples the chemical composition of the *R3c* phase was found to be $x = 0.07-0.09$ in Bi_{1-x}La_xFeO₃. This can be rationalised from a regular solution model. A tentative phase diagram of the system has been outlined, based on available experimental data and a simple thermodynamic model.

9 Size-dependent properties of BiFeO₃ nanocrystallites

9.1 Introduction

Ferroelectricity is a cooperative phenomenon and the size, geometry, mechanical and electrostatic boundary conditions affect the ferroelectric properties. Finite size effects⁴⁸⁰ in ferroelectric thin films have been studied extensively, both theoretically⁴⁸¹⁻⁴⁸⁴ and experimentally.⁴⁸⁵⁻⁴⁸⁶ In perovskite thin films ferroelectricity has been shown to prevail down to a thickness of 4 nm (10 unit cells) by electric force and piezoelectric microscopy,⁴⁸⁷ and down to only three unit cells thickness (~1.2 nm) by diffraction.⁴⁸⁸ Ferroelectricity in 2 nm thick BiFeO₃ thin films has been demonstrated.²⁸⁷

Ferroelectric nanoparticles have also received considerable attention, mostly towards the prototype ferroelectrics BaTiO₃⁴⁸⁹ and PbTiO₃.⁴⁹⁰ The general behaviour observed with decreasing particle size is that unit cell distortion along the direction of polarisation decreases, the ferroelectric Curie temperature T_C decreases, and the phase transition becomes more diffuse. Similar behaviour has also been reported for the prototype antiferroelectric material PbZrO₃.⁴⁹¹ Novel domain structures,⁴⁹² and ferrotoroidic ferroelectric domains⁴⁹³⁻⁴⁹⁴ are features unique to ferroelectric nanostructures⁴⁹⁵ compared to bulk ferroelectrics.

Another feature not unique to ferroelectric nanoparticles, but apparently common to all oxide nanoparticles, is unit cell expansion with decreasing particle size, e.g. as observed for TiO₂.⁴⁹⁶ Unit cell expansion has been attributed to surface layer relaxation,⁴⁹⁷ changes of the valence or ionicity of cations⁴⁹⁸⁻⁴⁹⁹ and truncation of the Madelung energy series at finite particle volumes.⁵⁰⁰ The ratio of surface to volume scales with the inverse particle size. From a thermodynamic point of view, the surface energy thus becomes increasingly important with decreasing particle size, and in e.g. TiO₂, Al₂O₃ and Fe₂O₃ the stable crystal structure changes below a critical size, with the transition from rutile to anatase in TiO₂ being perhaps the most classical example.⁵⁰¹⁻⁵⁰²

Finite size effects of nanoparticles of YMnO₃,^{233, 503} HoMnO₃,⁵⁰⁴ TbMnO₃,⁵⁰⁵ and YMn₂O_{5±δ}⁵⁰⁶ have been studied, but BiFeO₃ has attracted most of the attention towards multiferroic nanoparticles. Most studies on BiFeO₃ nanoparticles have focused on the magnetic and optical properties rather than the structural. The Néel temperature decreases and the transition becomes more diffuse with decreasing particle size.⁵⁰⁷⁻⁵⁰⁸ Increasing magnetisation with decreasing particle size has been found, and attributed to frustrated surface spins or release of the weak ferromagnetic moment in particles smaller than the periodicity of 62 nm of the spin spiral modulation.⁵⁰⁹ Oxygen vacancies compensated by Fe²⁺ have been proposed as the origin of the larger magnetisation of nanoparticles.⁵¹⁰ A recent report argues that Fe₃O₄ impurities can account for the higher magnetic moment of nanoparticles than bulk,⁵¹¹ in analogy with complementary studies of the effect of γ -Fe₂O₃ traces on the magnetic moment of BiFeO₃ thin films.⁵¹² Ferromagnetism at surfaces has been proposed as a universal feature of inorganic nanoparticles,⁵¹³ also for non-magnetic materials like BaTiO₃.⁵¹⁴

Several studies of the optical and photocatalytic properties of BiFeO₃ nanostructures have been conducted.^{294-297, 299, 515} The only size-dependence reported in these studies is an increasing bandgap with decreasing size down to 5 nm, which was attributed to quantum-size effects.²⁹⁹ Size-dependent lattice parameters were found in an early work by Shetty *et al.*,⁵⁰⁷ but the unit cell volume decreased with decreasing particle size, opposite of the general behaviour of oxide nanoparticles. An XAFS study did not find significant differences in the local structure of Fe³⁺ between bulk and 20 nm BiFeO₃ nanoparticles, thus implying that the lower T_N of nanoparticles is due to the smaller volume of the particles rather than changes in the local structure.⁵¹⁶ This chapter describes the effect of reduced size on the crystal structure and antiferromagnetic transition in BiFeO₃ nanoparticles.

9.2 Results

XRD patterns of selected batches of BiFeO₃ nanoparticles with different sizes, and bulk material as a reference, are shown on a log-scale in Figure 9.1. All patterns could be indexed as rhombohedral BiFeO₃ with space group $R3c$ (JCPDS no. 86-1518). Labels refer to the mean particle size in nm (estimated uncertainty). Reflection splittings from the rhombohedral distortion of the unit cell disappear in XRD patterns of crystallites smaller than 20 nm due to the combined effect of peak broadening and increasing unit cell symmetry. The XRD pattern of the smallest crystallites of 11 nm shows that this material contains mostly amorphous phase, thus the crystallites can be regarded as nuclei growing out of an amorphous precursor.

The mean crystallite sizes of powders, determined by the Scherrer equation, and the annealing temperature applied, is summarised in Table 9.1. The calculated particle size from surface area measurements (BET) are in reasonable agreement with the crystallite sizes obtained by the Scherrer equation (chapter 5.2). Additional support for the crystallite sizes obtained by the Scherrer equation was obtained by TEM characterisation, and typical morphology of particle agglomerates and an individual nanocrystallite was shown in Figure 5.7.

The possible oxygen nonstoichiometry of the nanocrystalline powders was studied by thermogravimetry. Unfortunately, the volatile suboxide BiO(g)⁵¹⁷ hinders direct determination of the absolute oxygen stoichiometry by *in situ* reduction, but relative change in the oxygen content during coarsening of the nanocrystalline powders could be determined by thermogravimetry. Only negligible weight change of the powders was observed during coarsening (preheated at 400 °C) at 600 °C for 8 h with initial size of 13.3 ± 1 and 20.4 ± 2 nm (Figure 9.2). The final crystallite size of the powders after the annealing process was 100 ± 20 nm, and the relative weight change during the isothermal annealing corresponds to a change in oxygen stoichiometry of less than 0.01. There is thus no reason to suspect a finite size effect on the oxidation state of Fe in these powders. This is also reasonable because significant reduction in the partial pressure of oxygen (10^{-15} to 10^{-20} bar) is necessary to make Fe²⁺ stable in this temperature range.⁵¹⁸

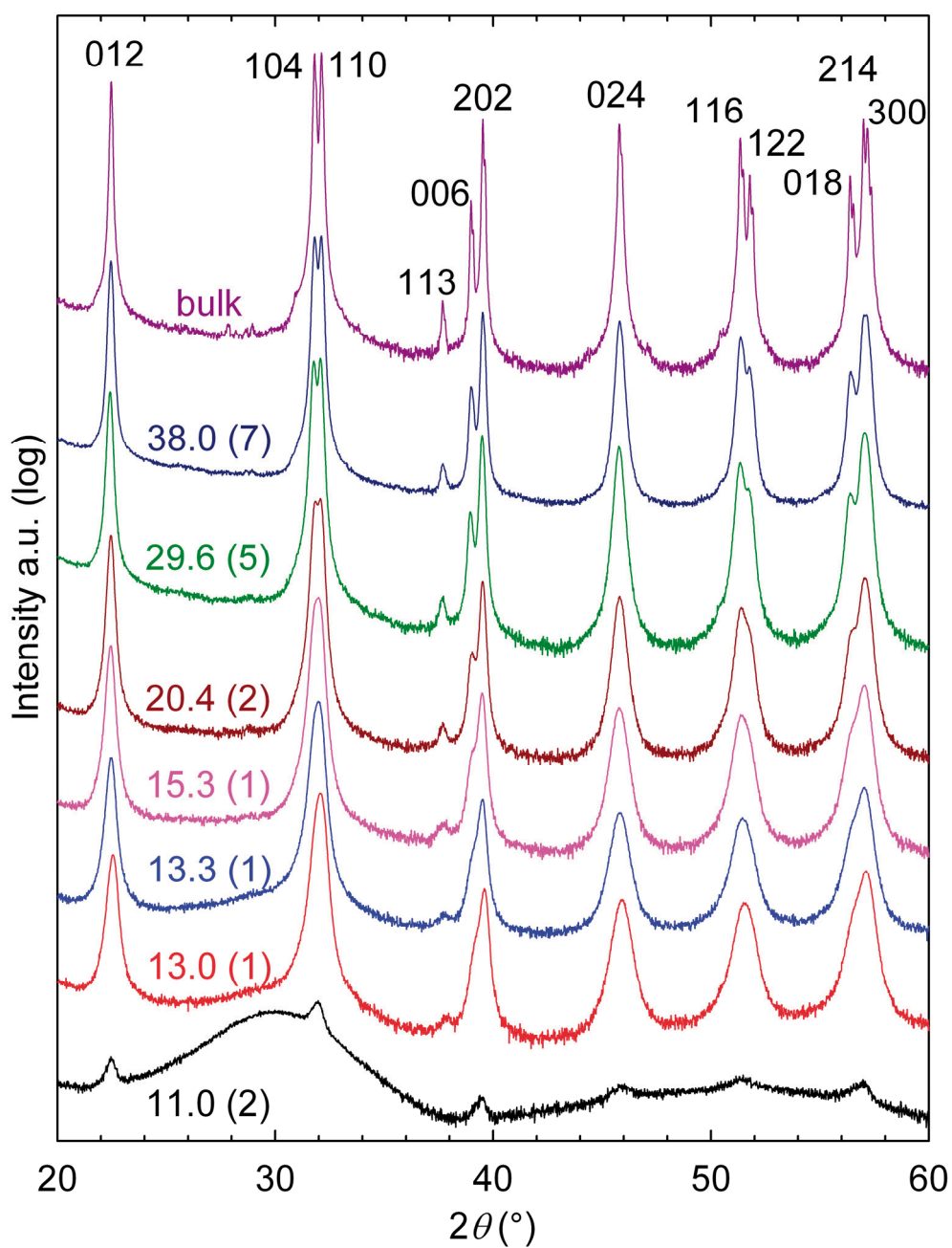


Figure 9.1. XRD patterns of BiFeO₃ nanoparticles and a bulk reference material on a log-scale. Labels refer to the mean particle size in nm (estimated uncertainty in paranthesis) determined by the Scherrer equation.

Lattice parameters obtained by Rietveld refinements are included in Table 9.1. The normalised lattice parameters $a = a_{\text{hex}}/\sqrt{2}$ and $c = c_{\text{hex}}/\sqrt{12}$ are shown as a function of crystallite size, along with the pseudotetragonality c/a in Figure 9.3. Crystallites larger than 30 nm display bulk lattice parameters. Below 30 nm the lattice parameters deviate from bulk, approaching a cubic perovskite structure with decreasing particle size, corresponding to the normalised lattice parameters becoming equal. Decreasing rhombohedral distortion of the unit cell with decreasing crystallite size is reflected in the reduction in c/a , which becomes equal to unity when the rhombohedral angle becomes 60° , corresponding to an ideal, cubic perovskite. The primitive unit cell volume versus the crystallite size is shown in the inset in Figure 9.3. The unit cell volume does not deviate from the bulk value for crystallites larger than 30 nm and increases with reduction in the crystallite size below 30 nm. The increase in unit cell volume observed is typical for partly covalent oxides.⁵¹⁹ Finite size effects on the lattice parameters of BiFeO₃ become pronounced at significantly smaller crystallite size (below 30 nm) than for the prototype ferroelectrics PbTiO₃ (below 50-150 nm)⁵²⁰⁻⁵²³ and BaTiO₃ (below 0.15-1 μm).^{489, 524-525} These two materials, which display a Curie temperature considerably lower than for BiFeO₃, are tetragonal perovskites and become cubic in the paraelectric state. For PbTiO₃ and BaTiO₃ the tetragonal distortion from ideality, $c/a - 1$, is a crystallographic order parameter for the ferroelectric phase transition, and the critical size for the existence of ferroelectricity in nanoparticles of these two materials have been reported at 7-15 nm^{490, 520-523, 526} and 70-120 nm,^{489, 499, 524-525, 527} respectively.

Table 9.1 Calcination temperature, size and lattice parameters of BiFeO₃ nanoparticles^a

<i>T</i> (°C)	Size (<i>d</i> , nm)	Lattice parameters	
		<i>a</i> _{hex} (Å)	<i>c</i> _{hex} (Å)
400	11.0 ± 2	5.59(36)	13.8(19)
410	13.0 ± 1	5.585(55)	13.83(88)
425	13.3 ± 1	5.587(87)	13.84(17)
450	15.3 ± 1	5.585(66)	13.84(60)
500	20.4 ± 2	5.580(67)	13.852(42)
500 ^b	29.6 ± 5	5.578(53)	13.860(10)
550	34.4 ± 6	5.578(26)	13.859(46)
575	38.0 ± 7	5.577(99)	13.860(20)
600 ^c	50.7 ± 10	5.577(29)	13.864(02)
587 ^b	52.1 ± 11	5.576(92)	13.864(40)
600 ^d	61.5 ± 14	5.577(49)	13.865(53)
600	72.1 ± 18	5.5775(23)	13.863(14)
650 ^b	86.4 ± 23	5.5770(8)	13.864(87)
Bulk	-	5.5772(04)	13.865(75)

^aUnmarked syntheses (Calc. temperatures) correspond to synthesis route 4 b) in Table 5.1.

^bSynthesis route 2 a) in Table 5.1.

^cSynthesis route 1 a) in Table 5.1.

^dSynthesis route 2 b) in Table 5.1.

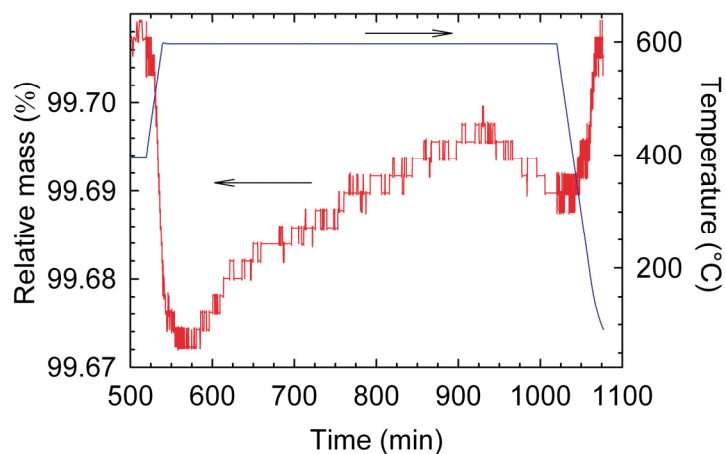


Figure 9.2. Thermogravimetry of a nanoparticles during *in situ* coarsening from 13 to 100 nm for 8 h at 600 °C. (Red line: mass %, blue line: temperature.)

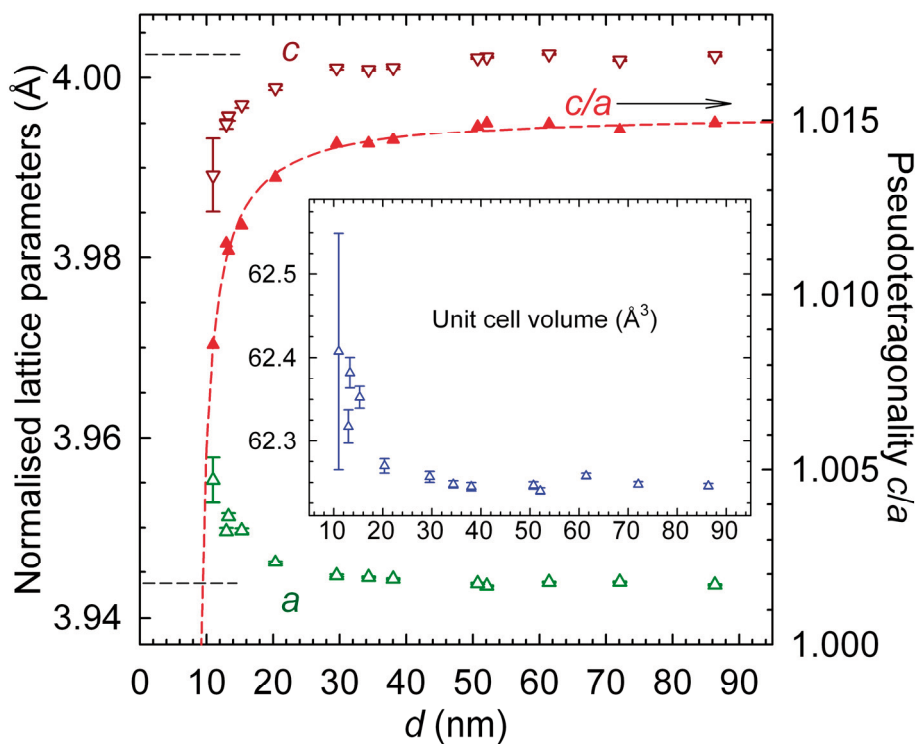


Figure 9.3. Normalised lattice parameters a and c and pseudotetragonality c/a of nanocrystalline BiFeO_3 as a function of crystallite size d . Dashed lines denote bulk values for comparison. The red dashed line is a fit to equation (9.1) for c/a , extrapolation indicates a critical size of 9 ± 1 nm. Inset: primitive unit cell volume versus crystallite size.

The ferroelectric phase of BiFeO₃ is observed for smaller crystallites than for BaTiO₃ and for most estimates for PbTiO₃. Ishikawa *et al.*⁵²² have fitted the size-dependent tetragonality of PbTiO₃ to the empirical model

$$\left(\frac{c}{a}\right)_d = \left(\frac{c}{a}\right)_\infty - \frac{A}{d - d_c} \quad (9.1)$$

where $(c/a)_d$ is the size-dependent tetragonality, $(c/a)_\infty$ the bulk tetragonality, A a fitting parameter and d_c a fitting parameter close to the critical size for ferroelectricity. Fitting our normalised lattice parameters to equation (9.1) yields $d_c = 9 \pm 1$ nm (Figure 9.3). When comparing BiFeO₃ to the prototype ferroelectrics PbTiO₃ and BaTiO₃, a high ferroelectric T_C is accompanied by a small critical size of ferroelectricity and bulk lattice parameters prevailing to smaller crystallite sizes.

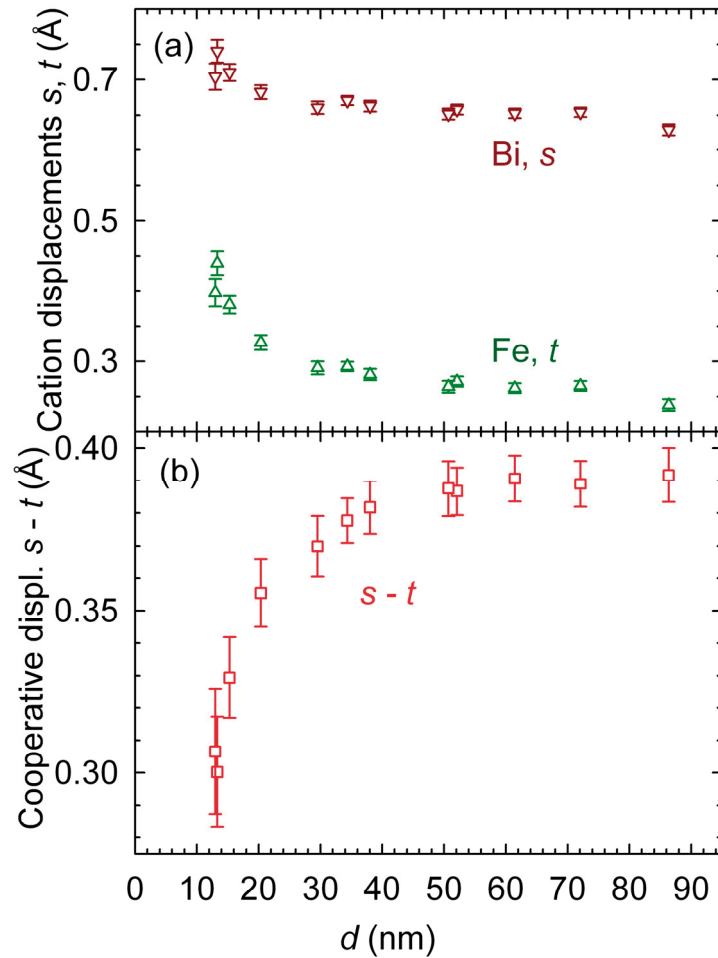


Figure 9.4. (a) Refined polar displacements s and t of Bi³⁺ and Fe³⁺ in BiFeO₃, respectively, as a function of size. (b) Cooperative cation displacements $s - t$, see text for explanation.

Polar displacement of Bi^{3+} and Fe^{3+} are shown as a function of the crystallite size in Figure 9.4 (a). The bulk value of s is approx. 2.8 times larger than t , while for the smallest crystallites the ratio s/t is less than 2. When t approaches s the cation sublattices become more regular, as $s = t$ would correspond to an equally spaced array of cations.¹²⁷ Note that the displacements of Bi^{3+} and Fe^{3+} do not approach the non-polar positions. The refined displacements from the centrosymmetric reference positions increase with decreasing crystallite size, in apparent contradiction with the decreasing unit cell distortion c/a in the same size range in Figure 9.3. The relative displacement of the cations, $s - t$, is equal to Δz_{hex} of Fe^{3+} with Bi^{3+} fixed at $z = 0$. The relative displacements of the two cations demonstrate a clear size dependence, and $s - t$ reduces with $\sim 25\%$ from bulk to 13 nm crystallites, Figure 9.4 (b).

Refined oxygen positions in Figure 9.5 (a) show a clear trend below 40-50 nm. Scattered values are due to difficult combination of oxygen being insensitive to X-rays, and small crystallites with relatively fewer diffracting Bragg planes relative to bulk material. Due to this scatter, no evident trend in the octahedral tilt angle can be distinguished. From the decreasing unit cell distortion with decreasing size (Figure 9.3) one would expect the FeO_6 tilt angle to decrease, but the refined oxygen positions do not support this.

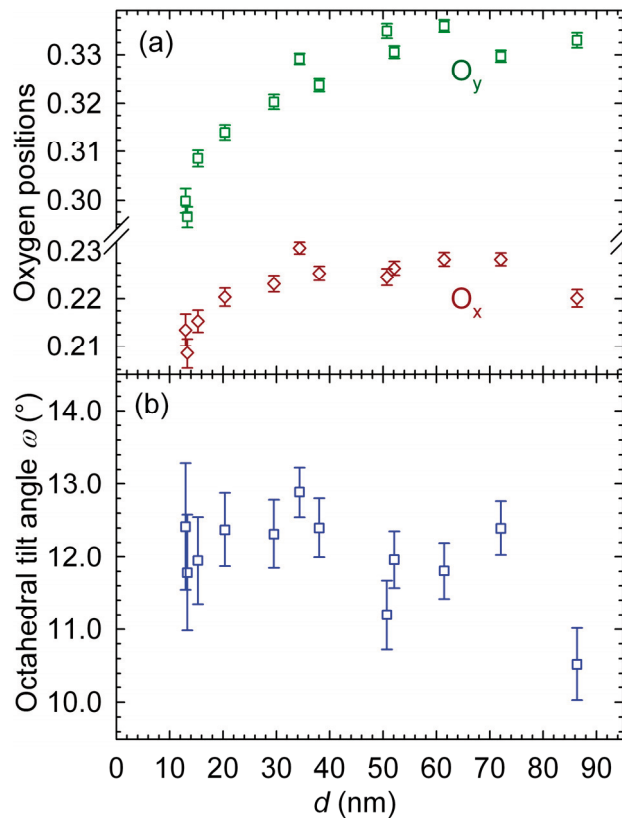


Figure 9.5. (a) Refined oxygen positions O_x and O_y in BiFeO_3 . (b) The calculated antiferrodistortive tilting angle ω of the FeO_6 octahedra.

The combined effects of finite size effects on lattice parameters and atomic positions are represented by the size dependence of the atomic bond lengths and angles. As the displacements of Fe^{3+} is more sensitive to size than the displacement of Bi^{3+} , we focus on the Fe-O bond lengths and Fe-O-Fe angle. These are displayed in Figure 9.6, where an illustration of two corner-sharing FeO_6 octahedra is included in the panel (a). With decreasing size the short Fe-O bond length decreases and the long Fe-O bond length increases (Figure 9.6 (b)), as a consequence of the increasing polar displacement of Fe^{3+} . The local structure of Fe^{3+} is thus sensitive to the crystallite size, in disagreement with the findings from a previous XAFS study. Although some scatter is present, the overall trend shows that the Fe-O-Fe angle decreases with decreasing crystallite size (Figure 9.6 (c)), in accordance with the influence of the parameter t on the Fe-O-Fe angle from equation (3.8).

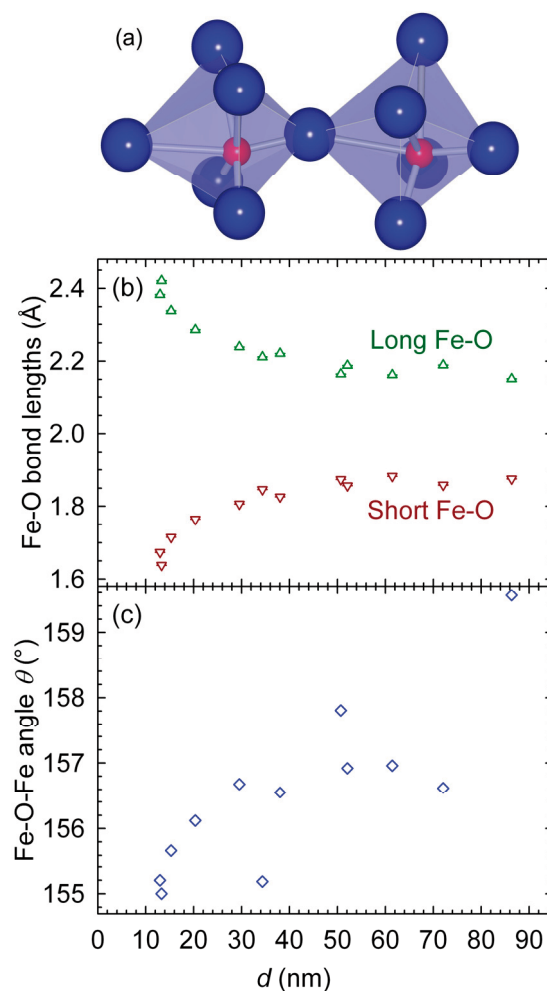


Figure 9.6. (a) Two FeO_6 -octahedra showing the two different Fe-O bond lengths caused by the polar displacement of Fe^{3+} with respect to the centre of the octahedron, and the Fe-O-Fe angle $< 180^\circ$. (b) The size dependence of the short and long Fe-O bonds. (c) The Fe-O-Fe angle as a function of crystallite size d .

The antiferromagnetic to paramagnetic transition of BiFeO₃ nanocrystallites was measured by DSC (Figure 9.7 (a)). T_N vs crystallite size is shown in Figure 9.7 (b). T_N was defined as the peak position of the DSC curves by numerical differentiation. The systematic shift towards higher temperatures than literature values originates from the high heating rate of 40 °C/min, which was necessary to detect a signal for the smallest crystallites. Additional measurements with a heating rate of 5-10 °C/min on bulk material confirmed this systematic shift towards higher temperatures (not shown). Below ~50 nm T_N decreases significantly below the bulk value. The calorimetric peaks become increasingly diffuse with decreasing crystallite size (Figure 9.7 (a)). The size-dependent ferroelectric Curie temperature T_C is not accessible by measurements on agglomerated nanocrystalline powders as rapid particle coarsening will occur upon heating before T_C is reached (not shown).

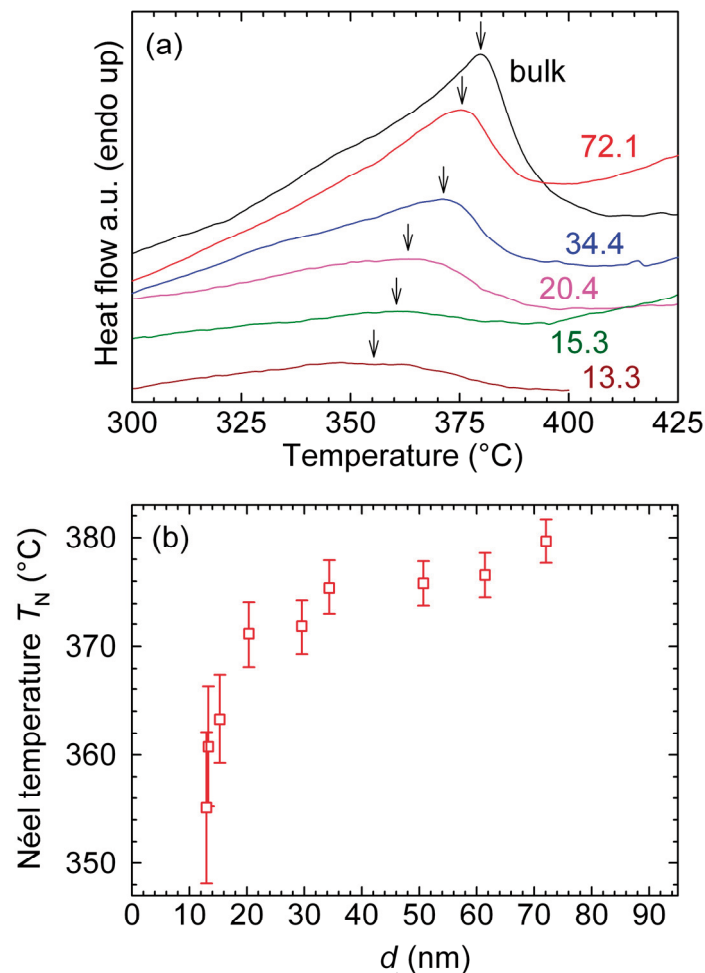


Figure 9.7. (a) DSC traces of bulk and nanocrystalline BiFeO₃ powders measured in air with a heating rate of 40 °C/min. Arrows depict the estimated T_N . (b) T_N as a function of crystallite size.

9.3 Discussion

9.3.1 Phenomenological interpretation of finite size effects

A finite size dependent magnetic ordering temperature of a ferro-, ferri- or antiferromagnetic material can be described by the phenomenological scaling relation⁵²⁸⁻⁵²⁹

$$\frac{T_N(d) - T_N(\infty)}{T_N(\infty)} = \pm \left(\frac{d}{d_0} \right)^{-1/\nu} \quad (9.2)$$

where $T_N(\infty)$ is the bulk T_N , $T_N(d)$ the size dependent T_N , d the crystallite size, d_0 the characteristic microscopic length of the system and ν the correlation length exponent. A least squares fit yields the values of $\nu = 0.6 \pm 0.1$ and $d_0 = 1.7 \pm 0.5$ nm, Figure 9.8 (a). A correlation length exponent of 0.5 would correspond to the theoretical critical exponent for a mean field behavior, while 0.7 would correspond to a 3D Heisenberg model.⁵²⁹⁻⁵³⁰

The magnetic transition temperature T_N scales linearly with the inverse volume V^{-1} in the size region where T_N decreases, Figure 9.8 (b). Ignoring possible magnetoelectric influence of polarisation on the magnetic ordering, the inverse volume dependence of T_N indicates that the ordering temperature is proportional to the number of antiferromagnetic exchange interactions in a certain size region larger than the magnetic correlation volume. Below this critical volume the ordering completely disappears, while bulk T_N prevails for particles larger than approx. 50 nm.

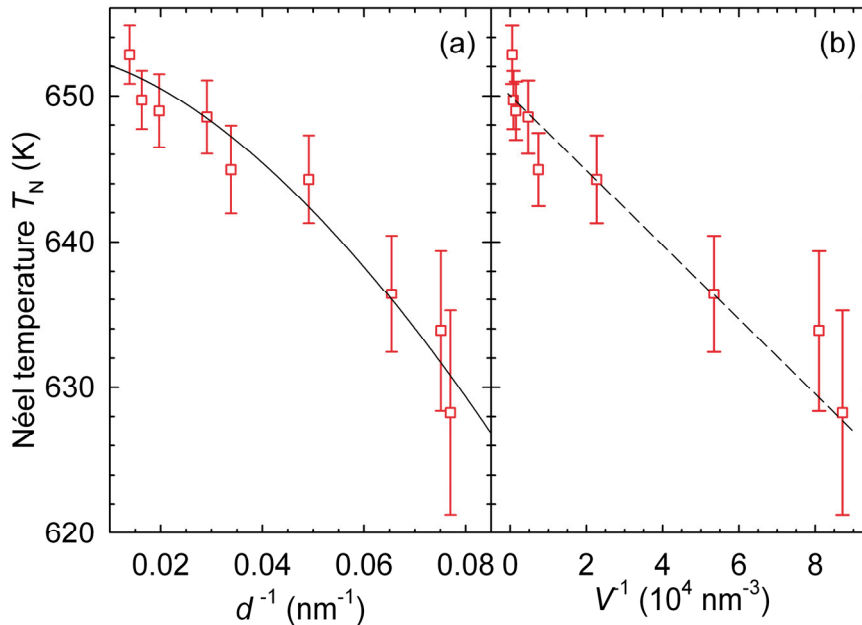


Figure 9.8. (a) T_N of BiFeO₃ nanocrystallites fitted to equation (9.2). (b) T_N vs inverse particle volume.

The depolarisation energy E_d of a ferroelectric nanoparticle scales with squared polarisation P^2 and inverse size,⁵³¹

$$E_d \propto \frac{P^2}{d}. \quad (9.3)$$

P^2 , represented by $(s - t)^2$, scales linearly with d^{-1} (Figure 9.9). Hence, the increase in deviation of $s - t$ from bulk value with decreasing crystallite size is likely to be caused by an increase in depolarisation field. The finite size effects on pseudotetragonality and polar displacements of cations show a different behaviour. We note that the parameter $s - t$ deviates from bulk value in crystallites larger than 30 nm, where lattice parameters are equal to bulk. This indicates an onset of a reduced polarisation before the pseudotetragonality is affected. It is not clear whether $(s - t)^2$ follow one linear trend with d^{-1} (dashed red line) or two trends (dashed blue lines) with a crossover between $d^{-1} = 0.0338 \text{ nm}^{-1}$ (29.6 nm) and $d^{-1} = 0.0654 \text{ nm}^{-1}$ (15.3 nm). The latter two trends may correspond to a crossover region between monodomain (below) and multidomain particles (above). Detailed TEM work would be necessary to assess this hypothesis. Even at 13 nm, $s - t$ has a significant finite value, approx. 75 % of bulk, which is a promising result regarding the possibility of making small nanostructures with sufficient polarisation for technological applications.

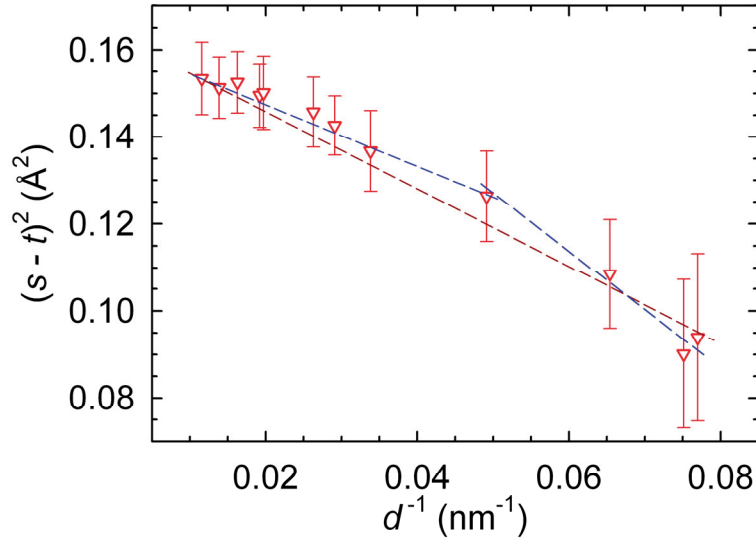


Figure 9.9. Correlation between squared polarisation, represented by $(s - t)^2$ and inverse particle size d^{-1} . Dashed lines are guides to the eye, see text for explanation.

Given the coupling between ferroelectric and magnetic order in BiFeO_3 in bulk and thin films, a correlation is also anticipated in nanoparticles. The linear decrease in $(s - t)^2$ with inverse crystallite size (Figure 9.9) and the linear decrease in T_N with inverse crystallite volume (Figure 9.8 (b)) has already been pointed out. Within the temperature interval in question for T_N , 300 to 400 °C, $s - t$ is close to room

temperature values (Figure 6.11 (b)), compared to the substantial influence of finite size on $s - t$ (Figure 9.4 (b)). T_N scales linearly with the decrease in $s - t$, as shown in Figure 9.10. The decrease in T_N observed could be associated with the decrease in spontaneous polarisation quantified by $s - t$, in addition to the decrease in number of antiferromagnetic interactions with decreasing particle volume.

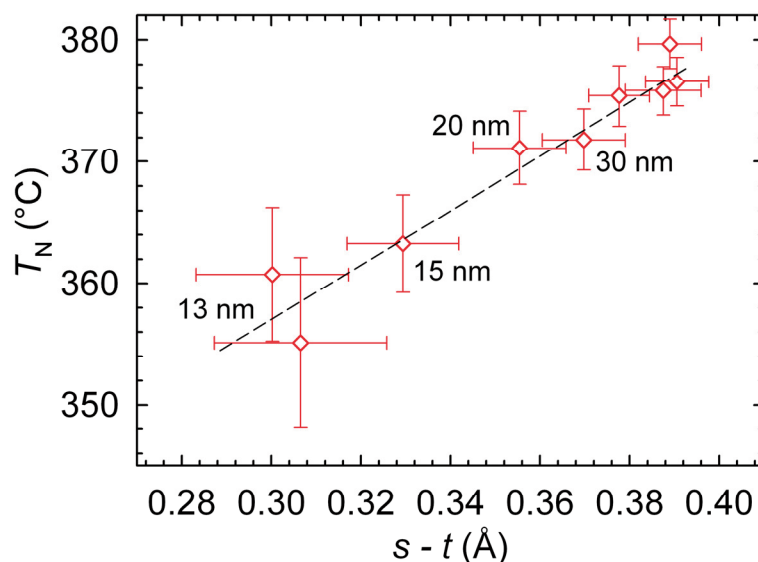


Figure 9.10. Correlation between T_N and $(s - t)$ for the same crystallite sizes of BiFeO_3 . The dashed line is a guide to the eye.

9.3.2 Local structure and structural coherence

The phenomenological interpretation of the observed finite size effects in the preceding chapter (9.3.1) implicitly presumes a mean-field behaviour; it presumes that the structural changes occurring are homogenous throughout the material. In analogy with the distinction between displacive and order-disorder structural transitions, the phenomenological interpretation of finite size effects corresponds to the displacive limit. The combination of decreasing unit cell distortion (Figure 9.3) and increasing cation displacements (Figure 9.4) is not consistent with a displacive picture of finite size effects in BiFeO_3 nanoparticles. Unlike ferroelectric thin films, which are clamped in two dimensions by the mechanical boundary conditions imposed by the substrate, ferroelectric nanoparticles are free to relax in three dimensions. Given that ferroelectrics in general are sensitive to strain, it is not surprising that the effect of reduced size is significantly different in nanoparticles than thin films, even in BiFeO_3 , which has been shown to be insensitive to strain compared to prototype ferroelectric PbTiO_3 and BaTiO_3 .¹³¹⁻¹³³ In addition to the previously mentioned higher T_C and P_S of BiFeO_3 , the insensitivity to strain may also be a part of the explanation of why BiFeO_3 is more structurally resilient towards finite size effects than the prototype ferroelectric perovskites. It should also be noted that BiFeO_3 is a III-III perovskite opposed to the II-IV perovskites

BaTiO₃ and PbTiO₃, which may be important if truncation of the Madelung energy is a part of the explanation of the lattice expansion observed for small oxide nanoparticles.

Unlike XAFS, which is only sensitive to the local structure of the first coordination sphere, pair distribution functions (PDF) are sensitive to the local structure of atoms up to several tens of Ångström, depending on the energy of the radiation used. See chapter 4.2.4 for details. PDFs of bulk and nanocrystalline BiFeO₃ obtained from SXRD at Argonne National Laboratory, IL, USA, are shown in Figure 9.10. Labels refer to mean crystallite size estimates by applying the Scherrer equation to conventional laboratory XRD patterns. The bulk materials can be regarded as a well-crystallised reference standard indicating the limitations of the experimental setup. The samples labelled 5 nm and 10 nm were calcined for 30 min at 350-400 °C, and were amorphous to conventional XRD, possibly with trace amounts of organic residuals. A size-dependent coherence length of the crystal structure is evident; smaller crystallites become more disordered on a 50 Å length scale as the PDF signal flattens at lower lengths. Loss of structural coherence occurs in the same size range as the strongest deviation in lattice parameters and bond lengths from the bulk values. Local polarisation or dipoles prevail to the smallest particle sizes studied in this work, but the average crystal structure becomes less distorted from cubic. This may lead to an overestimate of the nanocrystallite sizes using the Scherrer equation, as disorder will contribute to reflection broadening in addition to the size-induced broadening and the instrumental broadening which was subtracted. TEM investigation confirmed that the Scherrer equation estimates are reasonable.

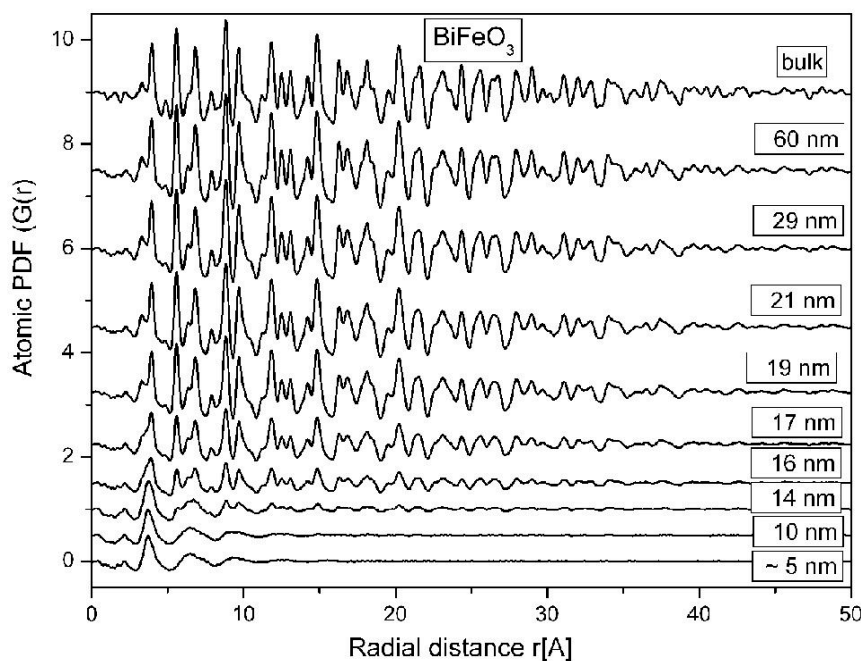


Figure 9.11. Pair distribution functions (PDF) obtained for bulk and nanocrystalline BiFeO₃.

Decreasing unit cell distortion and increasing polar cation displacements in BaTiO₃ inferred from spallation neutron PDFs⁵³² were reported few months after the present author's paper on finite size effects.⁵³³ A gradual decay of ferroelectricity in BaTiO₃ and Ba_{1-x}Sr_xTiO₃ nanoparticles was also inferred from SXRDFs by Petkov and coworkers.⁵³⁴⁻⁵³⁵ Recent HRTEM studies of PbZr_{0.2}Ti_{0.8}O₃ thin films have revealed that polar cation displacements do not necessarily scale with the unit cell tetragonality, even in epitaxially confined thin films.⁵³⁶ The finite size effects observed in this work is thus not unique to BiFeO₃ nanoparticles, but appears to be a general feature of ferroelectric nanoparticles. At the nanoscale, ferroelectricity hence decays gradually with decreasing size through a disordering process, rather than a displacive, in analogy with displacive and order-disorder structural phase transitions. Structural refinements of the PDF patterns are in progress, and have not been included in this thesis.

9.3.3 Structure-property relationships in BiFeO₃ nanoparticles

Ferroelectricity arises from a delicate competition between long range and short range electrostatic forces. Short range Coulombic forces favour a paraelectric state, while long-range forces are responsible for the alignment of dipoles within domains, yielding a spontaneous polarisation. Long-range forces will obviously decay with decreasing particle size, but the dipoles prevail on a local scale. The disordering process which leads to the decay of ferroelectricity at the nano-scale may thus be interpreted as decoupling of the dipole moments due to the weakening of long-range electrostatic forces aligning the dipoles. The persistence of local dipoles suggests that the partial covalent bonding between e.g. Ti⁴⁺ and O²⁻ in BaTiO₃ and Bi³⁺ and O²⁻ in BiFeO₃ (and possibly also between Fe³⁺ and O²⁻) does not disappear with decreasing size. Dipoles prevailing to the smallest particle sizes are not consistent with the suggestion that loss of covalent bonding is responsible for the lattice expansion of oxide nanoparticles.⁴⁹⁸⁻⁴⁹⁹ The displacement of Fe³⁺ increases more with decreasing size than then displacement of Bi³⁺, which may also be attributed to the loss of long range electrostatic forces. Parallel displacement of Bi³⁺ and Fe³⁺ is strongly favoured in terms of electrostatic repulsion between these trivalent cations,¹⁰³ and disordering of the dipole directions will change the electrostatic force fields within the nanoparticles. This may also be the origin of the observed scaling of the cooperative displacements ($s - t$) with inverse particle size, which could be attributed to depolarisation fields in a displacive picture. As lattice expansion is also found in non-ferroelectric oxide nanoparticles, it is likely that the lattice expansion allows larger displacement of the cations relative to the oxygen sublattice, rather than the increasing cation displacements driving the lattice expansion. Comparing the size regions where the unit cell distortion deviates from bulk values in BaTiO₃, PbTiO₃ and BiFeO₃, it appears that strong partial covalent bonding rather stabilises ferroelectric nanoparticles towards lattice expansion, and concomitant dipole disordering, than drives it. Disordering of dipoles would however explain the decreasing unit cell distortion and unit cell volume expansion in the region where finite size effects become pronounced. The presence of dipoles in an on average cubic lattice deserves a comment. It is not clear whether the crystal lattice is cubic on a local

scale or only appears to be cubic from XRD from a large number of Bragg planes. Modelling of PDFs of ferroelectric nanoparticles points to the former situation; a polar point group resides within a cubic lattice. There is no contradiction between a cubic unit cell and a polar tetragonal or rhombohedral point group (or space group) in disordered ferroelectric nanoparticles, while a cubic space group in a tetragonal or rhombohedral lattice is not possible.

The scaling of T_N with inverse particle size did not yield a result compatible with neither mean field behaviour nor a 3D Heisenberg model. Decreasing T_N with decreasing particle size arises naturally from the structural changes at the nanoscale, which a phenomenological scaling model does not take into account. Increasing long Fe-O bond lengths and decreasing Fe-O-Fe angles (Figure 9.6) weaken the Fe-O-Fe superexchange mechanism by reducing the Fe $3d - O 2p$ orbital overlap. It is thus proposed that structural changes are primarily responsible for the decreasing T_N , although frustrated spin ordering at surfaces must also be anticipated.

Increasing band gap with decreasing particle size, reported by Li *et al.*,²⁹⁹ arises naturally from the same reasoning as the decreasing T_N . Increasing long Fe-O bond lengths and decreasing Fe-O-Fe angles reduces the band-width in a band structure picture, thus accounting for the higher optical bandgap observed in nanoparticles.

The decreasing Fe-O-Fe angle may contribute to the higher magnetic moment measured for BiFeO₃ nanoparticles relative to bulk and thin film materials. As pointed out by Park *et al.*,⁵⁰⁹ in crystallites smaller than the periodicity (62 nm) of the incommensurate spiral modulation of the spin structure in bulk BiFeO₃, weak ferromagnetism may be “released”. The weak ferromagnetic moment from each Fe atom itself may however increase in small nanoparticles due to the decreasing Fe-O-Fe angle. When this angle decreases, Fe-O-Fe overlap decreases, weakening the 180 ° Fe-O-Fe superexchange favouring collinear G-type antiferromagnetic order. This may enhance the weak ferromagnetic moment from spin canting due to the Dzyaloshinskii-Moriya interaction. Frustrated surface spins will of course also be increasingly important as the surface to volume ratio increases with the inverse particle size.

Finally, the influence of reduced particle size on the structural properties also deserves a comparison with the response to hydrostatic pressure of bulk BiFeO₃. Decreasing Fe-O-Fe angle and decreasing T_N with decreasing particle size is the opposite of what is observed in perovskite (III)ferrites, where T_N and the Fe-O-Fe bond angles increase with hydrostatic pressure. Structural disorder and unit cell expansion is also directly opposite of the general response of an ordered material to hydrostatic pressure. The effect of finite size confinement on the structural properties and T_N resembles the response anticipated with the application of a *negative* hydrostatic pressure. As negative hydrostatic pressure is difficult to realise experimentally, theoretical calculations are needed to assess whether there is a general relationship between size confinement and negative hydrostatic pressure in ferroelectric nanoparticles.

9.4 Conclusions

BiFeO₃ nanoparticles retain bulk crystallographic properties down to smaller particle sizes than the prototype tetragonal ferroelectric perovskites BaTiO₃ and PbTiO₃, and can be regarded as more resilient towards finite size effects in line with the higher T_C and P_S of BiFeO₃. For crystallites smaller than 30 nm the average crystal structure gradually becomes more symmetric, approaching the ideal, cubic perovskite structure, with increasing unit cell volume. Extrapolation suggests a critical size of 9 ± 1 nm for the ferroelectric phase. Polar displacements of the cations Bi³⁺ and Fe³⁺ increase with decreasing size below 50 nm, in contrast with the average structure becoming more symmetrical. This is interpreted as the decay of ferroelectricity at the nanoscale through disordering rather than a displacive process, homogeneously taking place throughout the crystallites. Polar dipoles prevail to the smallest crystallite sizes, but the alignment of the dipoles decrease, evidenced by a gradually more cubic average structure. Truncation of long-range electrostatic forces stabilising the dipole alignment is proposed as the microscopic origin of the disordering.

The antiferromagnetic ordering temperature T_N decreases with decreasing particle size below 50 nm, and can be rationalised from the local structure changes around the Fe³⁺ cations in this size range. Reports of increasing optical bandgap in BiFeO₃ nanoparticles can also be attributed to the size-dependence of the Fe-O-Fe angle and Fe-O bond lengths.

10 Outlook

The purpose of this chapter is to propose further work in order to enhance the understanding of the topics investigated in the present thesis.

10.1 Stability and compatibility

Bulk BiFeO_3 has been shown to be metastable towards decomposition to $\text{Bi}_{25}\text{FeO}_{39}$ and $\text{Bi}_2\text{Fe}_4\text{O}_9$ at intermediate temperatures between 740 and 1040 K. This is of great importance for the preparation and processing of bulk ceramics to obtain phase pure material. Solution calorimetric data of high accuracy is required to quantify more accurately the temperature region of metastability and the important influence of impurities. Impurities in this respect are species more soluble in $\text{Bi}_{25}\text{FeO}_{39}$ and/or $\text{Bi}_2\text{Fe}_4\text{O}_9$ than BiFeO_3 , which thus will favour the formation of the secondary ternary phases. Species more soluble in BiFeO_3 than $\text{Bi}_{25}\text{FeO}_{39}$ and $\text{Bi}_2\text{Fe}_4\text{O}_9$, will on the other hand stabilise BiFeO_3 relative to the secondary ternary phases, like e.g. La_2O_3 . In thin films subjected to epitaxial compressive strain this effect is not anticipated due to the larger molar volumes of $\text{Bi}_{25}\text{FeO}_{39}$ and $\text{Bi}_2\text{Fe}_4\text{O}_9$ than BiFeO_3 .

BiFeO_3 is not chemically compatible with materials which were regarded as impurities in the preceding paragraph. Decomposition is thus anticipated at interfaces towards materials like Al_2O_3 and SiO_2 . For high temperature characterisation, the choice of supporting materials in direct contact with the BiFeO_3 sample is important, and challenging as the materials must be stable in high partial pressures of oxygen ($p\text{O}_2$), as a low $p\text{O}_2$ destabilises BiFeO_3 towards peritectic decomposition. Gold and platinum are stable at high $p\text{O}_2$, but form intermetallic compounds with bismuth. Silver and copper have less affinity towards bismuth, but oxidise in high $p\text{O}_2$. Since La_2O_3 is more soluble in BiFeO_3 than the secondary ternary phases, it will stabilise the perovskite phase towards decomposition, and LaFeO_3 may be a better choice of refractory material for supporting BiFeO_3 during high temperature characterisation than Al_2O_3 or SiO_2 . Both for further detailed studies of BiFeO_3 at high temperatures and for successful integration of BiFeO_3 into electronic circuitry, the chemical compatibility towards adjacent materials must be addressed.

10.2 Crystal structure and chemical bonding

Isovalent substitution on either the A or B site can give information about the importance of Bi^{3+} and Fe^{3+} for the structure and properties of BiFeO_3 . Substitution with La^{3+} reduces the unit cell distortion and polar cation displacements in the ferroelectric $R3c$ structure. The effect of Mn^{3+} substitution is similar to that of La^{3+} substitution, but less pronounced as 10 % La^{3+} reduces the unit cell distortion more than 30 % Mn^{3+} . La^{3+} does not possess a $6s^2$ lone pair like Bi^{3+} , explaining the detrimental effect of La^{3+} on the distortions of the crystal structure responsible for ferroelectricity. The origin of the detrimental effect of Mn^{3+} is less obvious, and deserves further detailed studies. Mn^{3+} and Fe^{3+} are approximately the same size, but with one and two e_g electrons, respectively. The energy and number of e_g

electrons may be important, thus implying that significant partial covalent bonding is present between Fe^{3+} and O^{2-} , not only between Bi^{3+} and O^{2-} . Mn^{3+} is Jahn-Teller active, and may cause local non-cooperative distortions of the oxygen octahedra. The displacements of Bi^{3+} and Fe^{3+} are strongly correlated, and any distortions of the Fe^{3+} positions is expected to affect the Bi^{3+} positions through electrostatic repulsion.

Oxidation of Mn^{3+} to Mn^{4+} , with concomitant cation vacancies, further decreases the crystal structure distortions associated with ferroelectricity. Mn^{4+} has zero e_g electrons and is smaller than Mn^{3+} and Fe^{3+} . In the prototype ferroelectric titanate perovskites the absence of d electrons is important for stabilising ferroelectric distortions, while in $\text{BiFe}_{1-x}\text{Mn}_x\text{O}_{3+\delta}$ the decreasing number of d electrons with increasing x and δ is accompanied by decreasing stability of the ferroelectric distortions. Further experimental and theoretical studies are required to fully understand the nature and influence of chemical bonding on the crystal structure of BiFeO_3 . Pair distribution functions and valence electron density analyses from high precision diffraction experiments combined with detailed spectroscopic studies would contribute to the understanding of the chemical bonding in BiFeO_3 .

10.3 Phase transitions

Detailed characterisation of the atomic positions across T_N may shed light on the microscopic nature of the magnetoelectric coupling in BiFeO_3 . Does loss of magnetic ordering increase or decrease the polar (cation displacements) and antiferrodistortive (octahedral tilting) distortions of the crystal structure? Similar detailed studies across the T_N of paraelectric LaFeO_3 would provide valuable data for assessing the influence of polarisation on the lattice dilation observed across T_N . Is this purely a magnetic effect or does polarisation either enhance or depress the lattice dilation and possible small changes in atomic positions?

Both La and Mn substitution reduces the ferroelectric Curie temperature and dT_C/dx (composition x) is more negative for La^{3+} than Mn^{3+} . Weakening of the partial covalent bonding stabilising the ferroelectric distortions also results in a lower thermal stability of the ferroelectric polymorph. The mechanism proposed in this work is that thermal destabilisation of the cation displacements drives the ferroelectric transition causing a change of Glazer tilt system as due to decreasing V_A/V_B ratio. More experimental and theoretical work is needed to fully understand the mechanism of the ferroelectric transition in BiFeO_3 .

The chemical incompatibility of BiFeO_3 towards commonly used sample supporting refractory materials, and the sensitivity to atmosphere of the peritectic decomposition reaction, makes characterisation of high temperature polymorphs and properties especially challenging, and some questions remain open.

The temperature of the transition from the paraelectric, ferroelastic $Pbnm$ polymorph to the paraelastic, cubic $Pm\bar{3}m$ polymorph (T_{cub}) increases with La^{3+} substitution and decreases with the $\text{Mn}^{3+}/\text{Mn}^{4+}$ content. This indicates that while changes in chemical bonding is responsible for the depression of T_C with La^{3+} or $\text{Mn}^{3+}/\text{Mn}^{4+}$ substitution, T_{cub} is largely governed by the effective tolerance factor t

of the system. As La^{3+} is smaller than Bi^{3+} , t decreases, and higher temperatures are necessary to reach the cubic polymorph. Concomitantly, T_{cub} decreases with increasing δ and Mn^{4+} content in $\text{BiFe}_{1-x}\text{Mn}_x\text{O}_{3+\delta}$ as t increases and lower temperatures are required to reach the cubic phase. It is not clear why the transition from $Pbnm$ to $Pm\bar{3}m$ occurs without an intermediate polymorph, or if an intermediate polymorph is found in the presence of impurities or under certain atmospheres. Furthermore, the positive Clapeyron slope of the transition at T_{cub} implies that hydrostatic pressure is anticipated to stabilise the $Pbnm$ polymorph rather than the $Pm\bar{3}m$, although a pressure-induced high spin to low spin transition for Fe^{3+} may increase t sufficiently to obtain a cubic phase also by high pressure. BiFeO_3 displays semiconducting behaviour for all temperatures and chemical substitutions investigated at ambient pressure. This will not necessarily hold for heterovalent substitution with e.g. Sr^{2+} or Ca^{2+} for Bi^{3+} , or under hydrostatic pressure. The temperature-pressure phase diagram of BiFeO_3 is far from fully understood, and caution must be taken to separate extrinsic from intrinsic effects during experimental studies.

10.4 The BiFeO_3 - LaFeO_3 and BiFeO_3 - BiMnO_3 phase diagrams

The Bi-rich side of the BiFeO_3 - LaFeO_3 phase diagram has been investigated, but some questions regarding the La-rich side remain open and require further experimental work. A binodal line at about $x = 0.075$ in $\text{Bi}_{1-x}\text{La}_x\text{FeO}_3$ was inferred, but more work is needed to determine the accurate position and temperature dependence of this binodal line. The influence of the annealing temperature and cooling rate should also be explored. The La-rich side of the phase diagram deserves more attention, and single phase Bi-substituted LaFeO_3 should be investigated systematically to assess whether there is a change of symmetry from $Pbnm$ to $Pbn2_1$ with increasing Bi content. The predicted lowering of the phase transition temperatures of LaFeO_3 with Bi substitution needs experimental verification. The higher solid solubility of Bi in LaFeO_3 than La in BiFeO_3 makes the system asymmetric with respect to solid solubility, and the regular solution model must be modified to accurately account for this asymmetry. Finally, the proposed metastability of a morphotropic phase boundary for $x > 0.1$ in single phase $\text{Bi}_{1-x}\text{La}_x\text{FeO}_3$ must be verified by heat treatment of a sample crystallised from a homogenous gas, liquid or polymeric precursor at temperatures where the ionic mobility is low.

In terms of thermodynamics, La^{3+} stabilises the perovskite phase, while Mn^{3+} can be regarded as a impurity, which destabilises BiFeO_3 mildly with respect to $\text{Bi}_{25}\text{FeO}_{39}$ and $\text{Bi}_2\text{Fe}_4\text{O}_9$. This is the thermodynamic origin of the limited solubility of Mn^{3+} in BiFeO_3 at ambient pressure, which was shown to be close to $x = 0.3$ in $\text{BiFe}_{1-x}\text{Mn}_x\text{O}_3$. Hydrostatic pressure or compressive epitaxial strain in thin films is anticipated to stabilise $x > 0.3$, but the magnitude of the pressure or strain necessary to stabilise $\text{BiFe}_{1-x}\text{Mn}_x\text{O}_3$ is not known. Correspondingly, substitution of Bi^{3+} with La^{3+} is expected to increase the ambient pressure solubility of Mn^{3+} in BiFeO_3 . Two interesting points arise from this prediction. Firstly, to enhance the understanding of the thermodynamic stability of BiFeO_3 , a systematic investigation

of how strongly La^{3+} stabilises the perovskite phase compared to how strongly Mn^{3+} destabilises it would be beneficial. Secondly, the tolerance of the ferroelectric $R3c$ structure to the combined detrimental effects of La^{3+} and Mn^{3+} is not known, and a systematic study may shed light on the chemical bonding stabilising the polar $R3c$ structure. Exceeding the tolerance of the $R3c$ structure to La^{3+} and Mn^{3+} may result in a two-phase system where the other phase is expected to be isostructural to LaMnO_3 with space group $Pbnm$.

10.5 Origins of finite size effects

The structural response to decreasing crystallite size has been well characterised, but the effects responsible for the observed effects are not obvious. Lattice expansion is a general feature observed for small oxide nanoparticles, but the origins are not fully understood. As lattice expansion is not unique to ferroelectric nanoparticles, the increasing polar displacements of cations should be regarded as a consequence of the lattice expansion rather than the driving force. Prevailing dipoles indicate that partial covalent bonding is not lost with reduced size, but the coherence of the dipoles decay with decreasing size.

The influence of depolarisation field in multiferroic nanoparticles has not been thoroughly investigated. Two possibilities to elucidate the influence of intrinsic finite size effects from the effect of surfaces and depolarisation fields is to modify the electrostatic boundary conditions by spark plasma sintering dense nanocrystalline ceramics, or to disperse nanoparticles in an ionic or metallic liquid, where a high density of charge carriers screening the depolarisation field, can be adsorbed at the surfaces.

11 References

1. G. E. Moore, "Cramming more components onto integrated circuits" *Electronics*, **38**, April 19th, (1965).
2. G. E. Moore. "Progress in digital integrated electronics" in *Electronic Devices Meeting, 1975 International*, **21**, 11-13 (1975)
3. R. Ramesh, S. Aggarwal and O. Auciello, "Science and technology of ferroelectric films and heterostructures for non-volatile ferroelectric memories" *Mate. Sci. Eng.*, **32**, 191-236 (2001).
4. J. F. Scott and C. A. P. de Araujo, "Ferroelectric Memories" *Science*, **246**, 1400-1405 (1989).
5. J. F. Scott, "Applications of modern ferroelectrics" *Science*, **315**, 954-959 (2007).
6. N. Setter, D. Damjanovic, L. Eng, G. Fox, S. Gevorgian, S. Hong, A. Kingon, H. Kohlstedt, N. Y. Park, G. B. Stephenson, I. Stolitchnov, A. K. Taganstev, D. V. Taylor, T. Yamada and S. Streiffer, "Ferroelectric thin films: Review of materials, properties, and applications" *J. Appl. Phys.*, **100**, 051606 (2006).
7. M. Dawber, K. M. Rabe and J. F. Scott, "Physics of thin-film ferroelectric oxides" *Rev. Mod. Phys.*, **77**, 1083-1130 (2005).
8. G. I. Meijer, "Materials science - Who wins the nonvolatile memory race?" *Science*, **319**, 1625-1626 (2008).
9. A. Beck, J. G. Bednorz, C. Gerber, C. Rossel and D. Widmer, "Reproducible switching effect in thin oxide films for memory applications" *Appl. Phys. Lett.*, **77**, 139-141 (2000).
10. M. Janousch, G. I. Meijer, U. Staub, B. Delley, S. F. Karg and B. P. Andreasson, "Role of oxygen vacancies in Cr-doped SrTiO₃ for resistance-change memory" *Adv. Mater.*, **19**, 2232-2235 (2007).
11. M. N. Kozicki, M. Park and M. Mitkova, "Nanoscale memory elements based on solid-state electrolytes" *IEEE Trans. Nanotech.*, **4**, 331-338 (2005).
12. R. Waser and M. Aono, "Nanoionics-based resistive switching memories" *Nat. Mater.*, **6**, 833-840 (2007).
13. S. Q. Liu, N. J. Wu and A. Ignatiev, "Electric-pulse-induced reversible resistance change effect in magnetoresistive films" *Appl. Phys. Lett.*, **76**, 2749-2751 (2000).
14. K. Terabe, T. Hasegawa, T. Nakayama and M. Aono, "Quantized conductance atomic switch" *Nature*, **433**, 47-50 (2005).
15. M. Wuttig and N. Yamada, "Phase-change materials for rewriteable data storage" *Nat. Mater.*, **6**, 824-832 (2007).
16. G. Binasch, P. Grünberg, F. Saurenbach and W. Zinn, "Enhanced Magnetoresistance in Layered Magnetic-Structures with Antiferromagnetic Interlayer Exchange" *Phys. Rev. B*, **39**, 4828-4830 (1989).
17. M. N. Baibich, J. M. Broto, A. Fert, F. N. Vandau, F. Petroff, P. Eitenne, G. Creuzet, A. Friederich and J. Chazelas, "Giant Magnetoresistance of (001)Fe/(001)Cr Magnetic Superlattices" *Phys. Rev. Lett.*, **61**, 2472-2475 (1988).

18. S. S. P. Parkin, M. Hayashi and L. Thomas, "Magnetic domain-wall racetrack memory" *Science*, **320**, 190-194 (2008).
19. M. Hayashi, L. Thomas, R. Moriya, C. Rettner and S. S. P. Parkin, "Current-controlled magnetic domain-wall nanowire shift register" *Science*, **320**, 209-211 (2008).
20. A. Barthelemy, A. Fert, J. P. Contour, M. Bowen, V. Cros, J. M. De Teresa, A. Hamzic, J. C. Faini, J. M. George, J. Grollier, F. Montaigne, F. Pailloux, F. Petroff and C. Vouille, "Magnetoresistance and spin electronics" *J. Magn. Mater.*, **242**, 68-76 (2002).
21. C. Chappert, A. Fert and F. N. Van Dau, "The emergence of spin electronics in data storage" *Nat. Mater.*, **6**, 813-823 (2007).
22. G. A. Smolenskii and I. E. Chupis, "Segnetomagnetism (English translation: Ferroelectromagnets, **25**, 475-493 (1982))" *Usp. Fiz. Nauk*, **137**, 415-448 (1982).
23. M. Gajek, M. Bibes, S. Fusil, K. Bouzehouane, J. Fontcuberta, A. E. Barthelemy and A. Fert, "Tunnel junctions with multiferroic barriers" *Nat. Mater.*, **6**, 296-302 (2007).
24. J. F. Scott, "Data storage - Multiferroic memories" *Nat. Mater.*, **6**, 256-257 (2007).
25. M. Fiebig, "Revival of the magnetoelectric effect" *J. Phys. D: Appl. Phys.*, **38**, R123-R152 (2005).
26. M. Bibes and A. Barthelemy, "Multiferroics: Towards a magnetoelectric memory" *Nat. Mater.*, **7**, 425-426 (2008).
27. Y. H. Chu, L. W. Martin, M. B. Holcomb, M. Gajek, S. J. Han, Q. He, N. Balke, C. H. Yang, D. Lee, W. Hu, Q. Zhan, P. L. Yang, A. Fraile-Rodriguez, A. Scholl, S. X. Wang and R. Ramesh, "Electric-field control of local ferromagnetism using a magnetoelectric multiferroic" *Nat. Mater.*, **7**, 478-482 (2008).
28. V. Garcia, S. Fusil, K. Bouzehouane, S. Enouz-Vedrenne, N. D. Mathur, A. Barthelemy and M. Bibes, "Giant tunnel electroresistance for non-destructive readout of ferroelectric states" *Nature*, **460**, 81-84 (2009).
29. P. Maksymovych, S. Jesse, P. Yu, R. Ramesh, A. P. Baddorf and S. V. Kalinin, "Polarization Control of Electron Tunneling into Ferroelectric Surfaces" *Science*, **324**, 1421-1425 (2009).
30. E. Y. Tsymbal and H. Kohlstedt, "Applied physics - Tunneling across a ferroelectric" *Science*, **313**, 181-183 (2006).
31. K. F. Wang, J. M. Liu and Z. F. Ren, "Multiferroicity: the coupling between magnetic and polarization orders" *Adv. Phys.*, **58**, 321-448 (2009).
32. H. Bea, M. Gajek, M. Bibes and A. Barthelemy, "Spintronics with multiferroics" *J. Phys.: Condens. Matter*, **20**, 434231 (2008).
33. L. Martin, S. P. Crane, Y. H. Chu, M. B. Holcomb, M. Gajek, M. Huijben, C. H. Yang, N. Balke and R. Ramesh, "Multiferroics and magnetoelectrics: thin films and nanostructures" *J. Phys.: Condens. Matter*, **20**, 434220 (2008).
34. H. Schmid, "Some symmetry aspects of ferroics and single phase multiferroics" *J. Phys.: Condens. Matter*, **20**, 434201 (2008).
35. S. W. Cheong and M. Mostovoy, "Multiferroics: a magnetic twist for ferroelectricity" *Nat. Mater.*, **6**, 13-20 (2007).

36. R. Ramesh and N. A. Spaldin, "Multiferroics: progress and prospects in thin films" *Nat. Mater.*, **6**, 21-29 (2007).
37. W. Eerenstein, N. D. Mathur and J. F. Scott, "Multiferroic and magnetoelectric materials" *Nature*, **442**, 759-765 (2006).
38. D. Khomskii, "Classifying multiferroics: Mechanisms and effects" *Physics*, **2**, 20 (2009).
39. J. G. Bednorz and K. A. Muller, "Possible High- T_C Superconductivity in the Ba-La-Cu-O System" *Zeitschr. Physik B - Condens. Matter*, **64**, 189-193 (1986).
40. G. Catalan and J. F. Scott, "Physics and Applications of Bismuth Ferrite" *Adv. Mater.*, **21**, 2463-2485 (2009).
41. C. H. Ahn, J. M. Triscone and J. Mannhart, "Electric field effect in correlated oxide systems" *Nature*, **424**, 1015-1018 (2003).
42. Y. Tokura and H. Y. Hwang, "Condensed-matter physics - Complex oxides on fire" *Nat. Mater.*, **7**, 694-695 (2008).
43. E. Dagotto, "Complexity in strongly correlated electronic systems" *Science*, **309**, 257-262 (2005).
44. J. G. Bednorz and K. A. Muller, "Perovskite-Type Oxides - the New Approach to High- T_C Superconductivity" *Rev. Mod. Phys.*, **60**, 585-600 (1988).
45. J. Zhao, Q. Huang, C. de la Cruz, S. L. Li, J. W. Lynn, Y. Chen, M. A. Green, G. F. Chen, G. Li, Z. Li, J. L. Luo, N. L. Wang and P. C. Dai, "Structural and magnetic phase diagram of $\text{CeFeAsO}_{1-x}\text{F}_x$ and its relation to high-temperature superconductivity" *Nat. Mater.*, **7**, 953-959 (2008).
46. A. V. Balatsky and D. Parker, "Not all iron superconductors are the same" *Physics*, **2**, 59 (2009).
47. Z. Tesanovic, "Are iron pnictides the new cuprates?" *Physics*, **2**, 60 (2009).
48. M. Imada, A. Fujimori and Y. Tokura, "Metal-insulator transitions" *Rev. Mod. Phys.*, **70**, 1039-1263 (1998).
49. A. D. Caviglia, S. Gariglio, N. Reyren, D. Jaccard, T. Schneider, M. Gabay, S. Thiel, G. Hammerl, J. Mannhart and J. M. Triscone, "Electric field control of the $\text{LaAlO}_3/\text{SrTiO}_3$ interface ground state" *Nature*, **456**, 624-627 (2008).
50. M. Huijben, G. Rijnders, D. H. A. Blank, S. Bals, S. Van Aert, J. Verbeeck, G. Van Tendeloo, A. Brinkman and H. Hilgenkamp, "Electronically coupled complementary interfaces between perovskite band insulators" *Nat. Mater.*, **5**, 556-560 (2006).
51. S. Thiel, G. Hammerl, A. Schmehl, C. W. Schneider and J. Mannhart, "Tunable quasi-two-dimensional electron gases in oxide heterostructures" *Science*, **313**, 1942-1945 (2006).
52. C. Cen, S. Thiel, G. Hammerl, C. W. Schneider, K. E. Andersen, C. S. Hellberg, J. Mannhart and J. Levy, "Nanoscale control of an interfacial metal-insulator transition at room temperature" *Nat. Mater.*, **7**, 298-302 (2008).
53. P. W. Anderson, "Twenty years of talking past each other: The theory of high T_C " *Physica C*, **460**, 3-6 (2007).
54. P. W. Anderson, "Is there glue in cuprate superconductors?" *Science*, **316**, 1705-1707 (2007).

55. P. W. Anderson, "Hidden Fermi liquid: The secret of high- T_C cuprates" *Phys. Rev. B*, **78**, 174505 (2008).
56. D. G. Schlom and J. H. Haeni, "A thermodynamic approach to selecting alternative gate dielectrics" *MRS Bull.*, **27**, 198-204 (2002).
57. K. J. Hubbard and D. G. Schlom, "Thermodynamic stability of binary oxides in contact with silicon" *J. Mater. Res.*, **11**, 2757-2776 (1996).
58. M. E. Lines and A. M. Glass, "*Principles and Applications of Ferroelectrics and Related Materials*". 2004, Oxford, UK Oxford University Press.
59. K. A. Rabe, M. Dawber, C. Lichtensteiger, C. H. Ahn and J. M. Triscone, "Modern physics of ferroelectrics: Essential background" *Top. Appl. Phys. - Physics of Ferroelectrics: A Modern Perspective*, **105**, 1-30 (2007).
60. J. van den Brink and D. I. Khomskii, "Multiferroicity due to charge ordering" *J. Phys.: Condens. Matter*, **20**, 434217 (2008).
61. N. Ikeda, "Ferroelectric properties of triangular charge-frustrated LuFe_2O_4 " *J. Phys.: Condens. Matter*, **20**, 434218 (2008).
62. N. Ikeda, H. Ohsumi, K. Ohwada, K. Ishii, T. Inami, K. Kakurai, Y. Murakami, K. Yoshii, S. Mori, Y. Horibe and H. Kito, "Ferroelectricity from iron valence ordering in the charge-frustrated system LuFe_2O_4 " *Nature*, **436**, 1136-1138 (2005).
63. B. Keimer, "Transition metal oxides - Ferroelectricity driven by orbital order" *Nat. Mater.*, **5**, 933-934 (2006).
64. D. V. Efremov, J. van den Brink and D. I. Khomskii, "Bond-versus site-centred ordering and possible ferroelectricity in manganites" *Nat. Mater.*, **3**, 853-856 (2004).
65. Y. Tokunaga, T. Lottermoser, Y. Lee, R. Kumai, M. Uchida, T. Arima and Y. Tokura, "Rotation of orbital stripes and the consequent charge-polarized state in bilayer manganites" *Nat. Mater.*, **5**, 937-941 (2006).
66. B. B. van Aken, T. T. M. Palstra, A. Filippetti and N. A. Spaldin, "The origin of ferroelectricity in magnetoelectric YMnO_3 " *Nat. Mater.*, **3**, 164-170 (2004).
67. H. N. Lee, H. M. Christen, M. F. Chisholm, C. M. Rouleau and D. H. Lowndes, "Strong polarization enhancement in asymmetric three-component ferroelectric superlattices" *Nature*, **433**, 395-399 (2005).
68. R. E. Cohen, "Origin of Ferroelectricity in Perovskite Oxides" *Nature*, **358**, 136-138 (1992).
69. Y. Kuroiwa, S. Aoyagi, A. Sawada, J. Harada, E. Nishibori, M. Takata and M. Sakata, "Evidence for Pb-O covalency in tetragonal PbTiO_3 " *Phys. Rev. Lett.*, **87**, 217601 (2001).
70. E. Mamontov, T. Egami, W. Dmowski, T. Gog and C. Venkataraman, "Anisotropic covalent bonds in KNbO_3 , observed by resonant X-ray scattering" *Phys. Rev. B*, **66**, 224105 (2002).
71. J. B. Goodenough, "Electronic and ionic transport properties and other physical aspects of perovskites" *Rep. Prog. Phys.*, **67**, 1915-1993 (2004).
72. J. B. Goodenough and J.-S. Zhou, "Localized to Itinerant Electronic Transition in Perovskite Oxides" *Structure Bonding*, **98**, 17-113 (2001).
73. S. Elliot, "*The Physics and Chemistry of Solids*". 1998, West Sussex John Wiley & Sons.

74. O. Chmaissem, B. Dabrowski, S. Kolesnik, J. Mais, D. E. Brown, R. Kruk, P. Prior, B. Pyles and J. D. Jorgensen, "Relationship between structural parameters and the Néel temperature in $\text{Sr}_{1-x}\text{Ca}_x\text{MnO}_3$ ($0 \leq x \leq 1$) and $\text{Sr}_{1-y}\text{Ba}_y\text{MnO}_3$ ($y \leq 0.2$)" *Phys. Rev. B*, **64**, 134412 (2001).
75. J. B. Goodenough, "Localized Versus Collective d Electrons and Neel Temperatures in Perovskite and Perovskite-Related Structures" *Phys. Rev.*, **164**, 785-789 (1967).
76. E. K. H. Salje, "*Phase transitions in ferroelastic and co-elastic crystals*". 1990, Cambridge, UK Cambridge University Press.
77. P. E. Vullum, "*Ferroelastic LaCoO₃-based Polycrystalline Ceramics: A Transmission Electron Microscopy and X-ray Diffraction Study*", Dr. Ing. Thesis, Norwegian University of Science and Technology (NTNU), (2005).
78. P. E. Vullum, J. Mastin, J. Wright, M.-A. Einarsrud, R. Holmestad and T. Grande, "In situ synchrotron X-ray diffraction of ferroelastic $\text{La}_{0.8}\text{Ca}_{0.2}\text{CoO}_3$ ceramics during uniaxial compression" *Acta Mater.*, **54**, 2615-2624 (2006).
79. P. E. Vullum, R. Holmestad, H. L. Lein, J. Mastin, M.-A. Einarsrud and T. Grande, "Monoclinic ferroelastic domains in LaCoO_3 -based perovskites" *Adv. Mater.*, **19**, 4399 (2007).
80. T. Mokkelbost, H. L. Lein, P. E. Vullum, R. Holmestad, T. Grande and M.-A. Einarsrud, "Thermal and mechanical properties of LaNbO_4 -based ceramics" *Ceram. Int.*, **35**, 2877-2883 (2009).
81. S. Faaland, T. Grande, M.-A. Einarsrud, P. E. Vullum and R. Holmestad, "Stress-strain behavior during compression of polycrystalline $\text{La}_{1-x}\text{Ca}_x\text{CoO}_3$ ceramics" *J. Am. Ceram. Soc.*, **88**, 726-730 (2005).
82. M. Karlsen, M.-A. Einarsrud, H. L. Lein, T. Grande, J. Hjelen and P. E. Vullum, "Backscatter Electron Imaging and Electron Backscatter Diffraction Characterization of LaCoO_3 During In Situ Compression" *J. Am. Ceram. Soc.*, **92**, 732-737 (2009).
83. P. E. Vullum, A. T. J. van Helvoort, R. Holmestad, J. Mastin, O. E. Andersen, M.-A. Einarsrud and T. Grande, "Grain boundary analysis and secondary phases in LaCoO_3 -based perovskites" *J. Mater. Sci.*, **42**, 6267-6273 (2007).
84. H. L. Lein, O. S. Andersen, P. E. Vullum, E. Lara-Curzio, R. Holmestad, M.-A. Einarsrud and T. Grande, "Mechanical properties of mixed conducting $\text{La}_{0.5}\text{Sr}_{0.5}\text{Fe}_{1-x}\text{Co}_x\text{O}_{3-\delta}$ ($0 \leq x \leq 1$) materials" *J. Solid State Electrochem.*, **10**, 635-642 (2006).
85. J. Mastin, "*Structure, ferroelastic properties and mechanical behaviour of LaCoO₃-based materials*", PhD Thesis, Norwegian University of Science and Technology (NTNU), (2005).
86. K. Kleveland, N. Orlovskaya, T. Grande, A. M. M. Moe, M.-A. Einarsrud, K. Breder and G. Gogotsi, "Ferroelastic behavior of LaCoO_3 -based ceramics" *J. Am. Ceram. Soc.*, **84**, 2029-2033 (2001).
87. A. Fossdal, "*Phase relations, thermal and mechanical properties of LaFeO₃-based ceramics*", Dr. Ing. Thesis, Norwegian University of Science and Technology (NTNU), (2003).
88. A. Fossdal, M.-A. Einarsrud and T. Grande, "Mechanical properties of LaFeO_3 ceramics" *J. Eur. Ceram. Soc.*, **25**, 927-933 (2005).

89. H. L. Lein, "*Mechanical properties and phase stability of oxygen permeable membranes $La_{0.5}Sr_{0.5}Fe_{1-x}Co_xO_{3-\delta}$* ", Dr. Ing. Thesis, Norwegian University of Science and Technology (NTNU), (2005).
90. T. Mokkelbost, "*Synthesis and characterization of ionic conducting CeO_2 - and $LaNbO_4$ -based materials*", PhD Thesis, Norwegian University of Science and Technology (NTNU), (2005).
91. K. M. Rabe, "Solid-state physics - Response with a twist" *Nature*, **449**, 674-675 (2007).
92. N. A. Spaldin, M. Fiebig and M. Mostovoy, "The toroidal moment in condensed-matter physics and its relation to the magnetoelectric effect" *J. Phys.: Condens. Matter*, **20**, 434203 (2008).
93. B. B. van Aken, J. P. Rivera, H. Schmid and M. Fiebig, "Observation of ferrotoroidic domains" *Nature*, **449**, 702-705 (2007).
94. N. A. Spaldin and M. Fiebig, "The renaissance of magnetoelectric multiferroics" *Science*, **309**, 391-392 (2005).
95. C. N. R. Rao and J. Gopalakrishnan, "*New Directions in Solid State Chemistry, 2nd ed.*". 1997, Cambridge, UK Cambridge University Press.
96. N. A. Hill, "Why are there so few magnetic ferroelectrics?" *J. Phys. Chem. B*, **104**, 6694-6709 (2000).
97. N. A. Hill and A. Filippetti, "Why are there any magnetic ferroelectrics?" *J. Magn. Magn. Mater.*, **242**, 976-979 (2002).
98. N. A. Hill and K. M. Rabe, "First-principles investigation of ferromagnetism and ferroelectricity in bismuth manganite" *Phys. Rev. B*, **59**, 8759-8769 (1999).
99. R. Seshadri and N. A. Hill, "Visualizing the role of Bi 6s "Lone pairs" in the off-center distortion in ferromagnetic $BiMnO_3$ " *Chem. Mater.*, **13**, 2892-2899 (2001).
100. C. Michel, J. M. Moreau, G. Achenbach, R. Gerson and W. J. James, "Atomic Structure of $BiFeO_3$ " *Solid State Commun.*, **7**, 701 (1969).
101. F. Kubel and H. Schmid, "Structure of a Ferroelectric and Ferroelastic Monodomain Crystal of the Perovskite $BiFeO_3$ " *Acta Crystallogr.*, **B46**, 698-702 (1990).
102. J. M. Moreau, C. Michel, R. Gerson and W. J. James, "Ferroelectric $BiFeO_3$ X-Ray and Neutron Diffraction Study" *J. Phys. Chem. Solids*, **32**, 1315 (1971).
103. N. W. Thomas and A. Beitollahi, "Interrelationship of Octahedral Geometry, Polyhedral Volume Ratio and Ferroelectric Properties in Rhombohedral Perovskites" *Acta Crystallogr.*, **B50**, 549-560 (1994).
104. J. D. Bucci, J. Robertson and W. J. James, "Precision Determination of Lattice Parameters and Coefficients of Thermal Expansion of $BiFeO_3$ " *J. Appl. Crystallogr.*, **5**, 187 (1972).
105. I. G. Ismailzade, "X-Ray Diffraction Study of Phase Transitions in Bismuth Ferrite" *Dokl. Akad. Nauk SSSR*, **170**, 85-87 (1966).
106. J. R. Teague, R. Gerson and W. J. James, "Dielectric Hysteresis in Single Crystal $BiFeO_3$ " *Solid State Commun.*, **8**, 1073 (1970).

107. M. M. Kumar, V. R. Palkar, K. Srinivas and S. V. Suryanarayana, "Ferroelectricity in a pure BiFeO₃ ceramic" *Appl. Phys. Lett.*, **76**, 2764-2766 (2000).
108. D. Lebeugle, D. Colson, A. Forget, M. Viret, P. Bonville, J. F. Marucco and S. Fusil, "Room-temperature coexistence of large electric polarization and magnetic order in BiFeO₃ single crystals" *Phys. Rev. B*, **76**, 024116 (2007).
109. J. B. Neaton, C. Ederer, U. V. Waghmare, N. A. Spaldin and K. M. Rabe, "First-principles study of spontaneous polarization in multiferroic BiFeO₃" *Phys. Rev. B*, **71**, 014113 (2005).
110. P. Ravindran, R. Vidya, A. Kjekshus, H. Fjellvåg and O. Eriksson, "Theoretical investigation of magnetoelectric behavior in BiFeO₃" *Phys. Rev. B*, **74**, 224412 (2006).
111. V. V. Shvartsman, W. Kleemann, R. Haumont and J. Kreisel, "Large bulk polarization and regular domain structure in ceramic BiFeO₃" *Appl. Phys. Lett.*, **90**, 172115 (2007).
112. J. Wang, J. B. Neaton, H. Zheng, V. Nagarajan, S. B. Ogale, B. Liu, D. Viehland, V. Vaithyanathan, D. G. Schlom, U. V. Waghmare, N. A. Spaldin, K. M. Rabe, M. Wuttig and R. Ramesh, "Epitaxial BiFeO₃ multiferroic thin film heterostructures" *Science*, **299**, 1719-1722 (2003).
113. S. Kamba, D. Nuzhnyy, M. Savinov, J. Sebek, J. Petzelt, J. Prokleska, R. Haumont and J. Kreisel, "Infrared and terahertz studies of polar phonons and magnetodielectric effect in multiferroic BiFeO₃ ceramics" *Phys. Rev. B*, **75**, 024403 (2007).
114. R. D. Shannon, "Revised Effective Ionic-Radii and Systematic Studies of Interatomic Distances in Halides and Chalcogenides" *Acta Crystallogr.*, **A32**, 751-767 (1976).
115. C. Li, K. C. K. Soh and P. Wu, "Formability of ABO₃ perovskites" *J. Alloys Compd.*, **372**, 40-48 (2004).
116. P. Wu and C. H. Li, "Stability and formability of complex oxides in M₂O₃-M'₂O₃-O₃ systems" *Calphad*, **27**, 201-211 (2003).
117. H. Yokokawa, T. Kawada and M. Dokiya, "Thermodynamic Regularities in Perovskite and K₂NiF₄ Compounds" *J. Am. Ceram. Soc.*, **72**, 152-153 (1989).
118. V. M. Goldschmidt, *Naturwissenschaften*, **14**, 477 (1926).
119. S. C. Abrahams, "Ferroelectricity and structure in the YMnO₃ family" *Acta Crystallogr.*, **B57**, 485-490 (2001).
120. B. B. van Aken, A. Meetsma and T. T. M. Palstra, "Hexagonal YMnO₃" *Acta Crystallogr.*, **C57**, 230-232 (2001).
121. N. W. Thomas, "Application of a Quantitative Polyhedral Analysis to the Design of Ceramic Oxides" *J. Mater. Chem.*, **2**, 663-669 (1992).
122. N. W. Thomas, "The compositional dependence of octahedral tilting in orthorhombic and tetragonal perovskites" *Acta Crystallogr.*, **B52**, 16-31 (1996).
123. N. W. Thomas, "A re-examination of the relationship between lattice strain, octahedral tilt angle and octahedral strain in rhombohedral perovskites" *Acta Crystallogr.*, **B52**, 954-960 (1996).
124. M. Avdeev, E. N. Caspi and S. Yakovlev, "On the polyhedral volume ratios V_A/V_B in perovskites ABX₃" *Acta Crystallogr.*, **B63**, 363-372 (2007).

125. A. M. Glazer, "Classification of Tilted Octahedra in Perovskites" *Acta Crystallogr.*, **B28**, 3384 (1972).
126. C. Ederer and C. J. Fennie, "Electric-field switchable magnetization via the Dzyaloshinskii-Moriya interaction: FeTiO_3 versus BiFeO_3 " *J. Phys.: Condens. Matter*, **20**, 434219 (2008).
127. H. D. Megaw and C. N. W. Darlington, "Geometrical and Structural Relations in Rhombohedral Perovskites" *Acta Crystallogr.*, **A31**, 161-173 (1975).
128. S. C. Abrahams, S. K. Kurtz and P. B. Jamieson, "Atomic Displacement Relationship to Curie Temperature and Spontaneous Polarization in Displacive Ferroelectrics" *Phys. Rev.*, **172**, 551 (1968).
129. J. F. Li, J. L. Wang, M. Wuttig, R. Ramesh, N. Wang, B. Ruetter, A. P. Pyatakov, A. K. Zvezdin and D. Viehland, "Dramatically enhanced polarization in (001), (101), and (111) BiFeO_3 thin films due to epitaxial-induced transitions" *Appl. Phys. Lett.*, **84**, 5261-5263 (2004).
130. W. Jaffe, R. Cook and H. Jaffe, "*Piezoelectric Ceramics*". 1971, New York, USA Academic Press.
131. D. H. Kim, H. N. Lee, M. D. Biegalski and H. M. Christen, "Effect of epitaxial strain on ferroelectric polarization in multiferroic BiFeO_3 films" *Appl. Phys. Lett.*, **92**, 012911 (2008).
132. C. Ederer and N. A. Spaldin, "Influence of strain and oxygen vacancies on the magnetoelectric properties of multiferroic bismuth ferrite" *Phys. Rev. B*, **71**, 224103 (2005).
133. C. Ederer and N. A. Spaldin, "Effect of epitaxial strain on the spontaneous polarization of thin film ferroelectrics" *Phys. Rev. Lett.*, **95**, 257601 (2005).
134. K. J. Choi, M. Biegalski, Y. L. Li, A. Sharan, J. Schubert, R. Uecker, P. Reiche, Y. B. Chen, X. Q. Pan, V. Gopalan, L. Q. Chen, D. G. Schlom and C. B. Eom, "Enhancement of ferroelectricity in strained BaTiO_3 thin films" *Science*, **306**, 1005-1009 (2004).
135. F. M. Bai, H. M. Zheng, H. Cao, L. E. Cross, R. Ramesh, J. F. Li and D. Viehland, "Epitaxially induced high temperature (> 900 K) cubic-tetragonal structural phase transition in BaTiO_3 thin films" *Appl. Phys. Lett.*, **85**, 4109-4111 (2004).
136. J. H. Haeni, P. Irvin, W. Chang, R. Uecker, P. Reiche, Y. L. Li, S. Choudhury, W. Tian, M. E. Hawley, B. Craigo, A. K. Tagantsev, X. Q. Pan, S. K. Streiffer, L. Q. Chen, S. W. Kirchoefer, J. Levy and D. G. Schlom, "Room-temperature ferroelectricity in strained SrTiO_3 " *Nature*, **430**, 758-761 (2004).
137. C. J. Eklund, C. J. Fennie and K. M. Rabe, "Strain-induced ferroelectricity in orthorhombic CaTiO_3 from first principles" *Phys. Rev. B*, **79**, 220101(R) (2009).
138. H. W. Jang, S. H. Baek, D. Ortiz, C. M. Folkman, R. R. Das, Y. H. Chu, P. Shafer, J. X. Zhang, S. Choudhury, V. Vaithyanathan, Y. B. Chen, D. A. Felker, M. D. Biegalski, M. S. Rzchowski, X. Q. Pan, D. G. Schlom, L. Q. Chen, R. Ramesh and C. B. Eom, "Strain-induced polarization rotation in epitaxial (001) BiFeO_3 thin films" *Phys. Rev. Lett.*, **101**, 107602 (2008).

139. G. Y. Xu, H. Hiraka, G. Shirane, J. F. Li, J. L. Wang and D. Viehland, "Low symmetry phase in (001) BiFeO₃ epitaxial constrained thin films" *Appl. Phys. Lett.*, **86**, 182905 (2005).
140. G. Y. Xu, J. F. Li and D. Viehland, "Ground state monoclinic (M_6) phase in (110)_c BiFeO₃ epitaxial thin films" *Appl. Phys. Lett.*, **89**, 222901 (2006).
141. H. Bea, B. Dupe, S. Fusil, R. Mattana, E. Jacquet, B. Warot-Fonrose, F. Wilhelm, A. Rogalev, S. Petit, V. Cros, A. Anane, F. Petroff, K. Bouzehouane, G. Geneste, B. Dkhil, S. Lisenkov, I. Ponomareva, L. Bellaiche, M. Bibes and A. Barthelemy, "Evidence for Room-Temperature Multiferroicity in a Compound with a Giant Axial Ratio" *Phys. Rev. Lett.*, **102**, 217603 (2009).
142. K. Y. Yun, D. Ricinschi, T. Kanashima, M. Noda and M. Okuyama, "Giant ferroelectric polarization beyond 150 $\mu\text{C}/\text{cm}^2$ in BiFeO₃ thin film" *Jpn. J. Appl. Phys.*, **43**, L647-L648 (2004).
143. G. L. Yuan, L. W. Martin, R. Ramesh and A. Uedono, "The dependence of oxygen vacancy distributions in BiFeO₃ films on oxygen pressure and substrate" *Appl. Phys. Lett.*, **95**, 012904 (2009).
144. G. L. Yuan and A. Uedono, "Behavior of oxygen vacancies in BiFeO₃/SrRuO₃/SrTiO₃(100) and DyScO₃(100) heterostructures" *Appl. Phys. Lett.*, **94**, 132905 (2009).
145. Y. H. Chu, Q. Zhan, L. W. Martin, M. P. Cruz, P. L. Yang, G. W. Pabst, F. Zavaliche, S. Y. Yang, J. X. Zhang, L. Q. Chen, D. G. Schlom, I. N. Lin, T. B. Wu and R. Ramesh, "Nanoscale domain control in multiferroic BiFeO₃ thin films" *Adv. Mater.*, **18**, 2307-2311 (2006).
146. M. P. Cruz, Y. H. Chu, J. X. Zhang, P. L. Yang, F. Zavaliche, Q. He, P. Shafer, L. Q. Chen and R. Ramesh, "Strain control of domain-wall stability in epitaxial BiFeO₃ (110) films" *Phys. Rev. Lett.*, **99**, 217601 (2007).
147. F. Zavaliche, R. R. Das, D. M. Kim, C. B. Eom, S. Y. Yang, P. Shafer and R. Ramesh, "Ferroelectric domain structure in epitaxial BiFeO₃ films" *Appl. Phys. Lett.*, **87**, 182912 (2005).
148. F. Zavaliche, S. Y. Yang, T. Zhao, Y. H. Chu, M. P. Cruz, C. B. Eom and R. Ramesh, "Multiferroic BiFeO₃ films: domain structure and polarization dynamics" *Phase Trans.*, **79**, 991-1017 (2006).
149. Y. H. Chu, M. P. Cruz, C. H. Yang, L. W. Martin, P. L. Yang, J. X. Zhang, K. Lee, P. Yu, L. Q. Chen and R. Ramesh, "Domain control in multiferroic BiFeO₃ through substrate vicinality" *Adv. Mater.*, **19**, 2662-2666 (2007).
150. G. Catalan, H. Bea, S. Fusil, M. Bibes, P. Paruch, A. Barthelemy and J. F. Scott, "Fractal dimension and size scaling of domains in thin films of multiferroic BiFeO₃" *Phys. Rev. Lett.*, **100**, 027602 (2008).
151. C. M. Folkman, S. H. Baek, H. W. Jang, C. B. Eom, C. T. Nelson, X. Q. Pan, Y. L. Li, L. Q. Chen, A. Kumar, V. Gopalan and S. K. Streiffer, "Stripe domain structure in epitaxial (001) BiFeO₃ thin films on orthorhombic TbScO₃ substrate" *Appl. Phys. Lett.*, **94**, 251911 (2009).
152. R. V. Pisarev, A. S. Moskvina, A. M. Kalashnikova and T. Rasing, "Charge transfer transitions in multiferroic BiFeO₃ and related ferrite insulators" *Phys. Rev. B*, **79**, 235128 (2009).

153. J. Zaanen, G. A. Sawatzky and J. W. Allen, "Band-Gaps and Electronic Structure of Transition-Metal Compounds" *Phys. Rev. Lett.*, **55**, 418-421 (1985).
154. V. Fruth, M. Popa, J. M. Calderon-Moreno, E. M. Anghel, D. Berger, M. Gartner, M. Anastasescu, P. Osiceanu and M. Zaharescu, "Chemical solution deposition and characterization of BiFeO₃ thin films" *J. Eur. Ceram. Soc.*, **27**, 4417-4420 (2007).
155. S. R. Basu, L. W. Martin, Y. H. Chu, M. Gajek, R. Ramesh, R. C. Rai, X. Xu and J. L. Musfeldt, "Photoconductivity in BiFeO₃ thin films" *Appl. Phys. Lett.*, **92**, 091905 (2008).
156. T. Choi, S. Lee, Y. J. Choi, V. Kiryukhin and S. W. Cheong, "Switchable Ferroelectric Diode and Photovoltaic Effect in BiFeO₃" *Science*, **324**, 63-66 (2009).
157. J. F. Ihlefeld, N. J. Podraza, Z. K. Liu, R. C. Rai, X. Xu, T. Heeg, Y. B. Chen, J. Li, R. W. Collins, J. L. Musfeldt, X. Q. Pan, J. Schubert, R. Ramesh and D. G. Schlom, "Optical band gap of BiFeO₃ grown by molecular-beam epitaxy" *Appl. Phys. Lett.*, **92**, 142908 (2008).
158. S. J. Clark and J. Robertson, "Band gap and Schottky barrier heights of multiferroic BiFeO₃" *Appl. Phys. Lett.*, **90**, 132903 (2007).
159. R. Palai, R. S. Katiyar, H. Schmid, P. Tissot, S. J. Clark, J. Robertson, S. A. T. Redfern, G. Catalan and J. F. Scott, " β -phase and β - γ metal-insulator transition in multiferroic BiFeO₃" *Phys. Rev. B*, **77**, 014110 (2008).
160. A. G. Gavriliuk, V. V. Struzhkin, I. S. Lyubutin, S. G. Ovchinnikov, M. Y. Hu and P. Chow, "Another mechanism for the insulator-metal transition observed in Mott insulators" *Phys. Rev. B*, **77**, 155112 (2008).
161. J. B. Goodenough, "Theory of the Role of Covalency in the Perovskite-Type Manganites [La,M(II)]MnO₃" *Phys. Rev.*, **100**, 564-573 (1955).
162. T. Zhao, A. Scholl, F. Zavaliche, K. Lee, M. Barry, A. Doran, M. P. Cruz, Y. H. Chu, C. Ederer, N. A. Spaldin, R. R. Das, D. M. Kim, S. H. Baek, C. B. Eom and R. Ramesh, "Electrical control of antiferromagnetic domains in multiferroic BiFeO₃ films at room temperature" *Nat. Mater.*, **5**, 823-829 (2006).
163. I. E. Dzyaloshinskii, *Sov. Phys. JETP*, **5**, 1259 (1957).
164. T. Moriya, *Phys. Rev.*, **120**, 91 (1960).
165. Y. F. Popov, A. K. Zvezdin, G. P. Vorobev, A. M. Kadomtseva, V. A. Murashev and D. N. Rakov, "Linear Magnetoelectric Effect and Phase-Transitions in Bismuth Ferrite, BiFeO₃" *JETP Lett.*, **57**, 69-73 (1993).
166. A. M. Kadomtseva, A. K. Zvezdin, Y. F. Popov, A. P. Pyatakov and G. P. Vorob'ev, "Space-time parity violation and magnetoelectric interactions in antiferromagnets" *JETP Lett.*, **79**, 571-581 (2004).
167. I. Sosnowska, T. Peterlin-Neumaier and E. Steichele, "Spiral Magnetic Ordering in Bismuth Ferrite" *J. Phys. C: Solid State Phys.*, **15**, 4835-4846 (1982).
168. D. Lebeugle, D. Colson, A. Forget, M. Viret, A. M. Bataille and A. Gukasov, "Electric-field-induced spin flop in BiFeO₃ single crystals at room temperature" *Phys. Rev. Lett.*, **100**, 227602 (2008).

169. H. Naganuma and S. Okamura, "Structural, magnetic, and ferroelectric properties of multiferroic BiFeO₃ film fabricated by chemical solution deposition" *J. Appl. Phys.*, **101**, 09103 (2007).
170. S. T. Zhang, M. H. Lu, D. Wu, Y. F. Chen and N. B. Ming, "Larger polarization and weak ferromagnetism in quenched BiFeO₃ ceramics with a distorted rhombohedral crystal structure" *Appl. Phys. Lett.*, **87**, 262907 (2005).
171. D. Lebeugle, D. Colson, A. Forget and M. Viret, "Very large spontaneous electric polarization in BiFeO₃ single crystals at room temperature and its evolution under cycling fields" *Appl. Phys. Lett.*, **91**, 022907 (2007).
172. J. Seidel, L. W. Martin, Q. He, Q. Zhan, Y. H. Chu, A. Rother, M. E. Hawkrigde, P. Maksymovych, P. Yu, M. Gajek, N. Balke, S. V. Kalinin, S. Gemming, F. Wang, G. Catalan, J. F. Scott, N. A. Spaldin, J. Orenstein and R. Ramesh, "Conduction at domain walls in oxide multiferroics" *Nat. Mater.*, **8**, 229-234 (2009).
173. F. Zavaliche, P. Shafer, R. Ramesh, M. P. Cruz, R. R. Das, D. M. Kim and C. B. Eom, "Polarization switching in epitaxial BiFeO₃ films" *Appl. Phys. Lett.*, **87**, 252902 (2005).
174. T. Kimura, T. Goto, H. Shintani, K. Ishizaka, T. Arima and Y. Tokura, "Magnetic control of ferroelectric polarization" *Nature*, **426**, 55-58 (2003).
175. C. Ederer and N. A. Spaldin, "Weak ferromagnetism and magnetoelectric coupling in bismuth ferrite" *Phys. Rev. B*, **71**, 060401(R) (2005).
176. S. Lee, W. Ratcliff, S. W. Cheong and V. Kiryukhin, "Electric field control of the magnetic state in BiFeO₃ single crystals" *Appl. Phys. Lett.*, **92**, 192906 (2008).
177. N. Mathur, "Materials science - A desirable wind up" *Nature*, **454**, 591-592 (2008).
178. P. Rovillain, M. Cazayous, Y. Gallais, A. Sacuto, R. P. S. M. Lobo, D. Lebeugle and D. Colson, "Polar phonons and spin excitations coupling in multiferroic BiFeO₃ crystals" *Phys. Rev. B*, **79**, 180411(R) (2009).
179. A. F. M. dos Santos, A. K. Cheetham, W. Tian, X. Q. Pan, Y. F. Jia, N. J. Murphy, J. Lettieri and D. G. Schlom, "Epitaxial growth and properties of metastable BiMnO₃ thin films" *Appl. Phys. Lett.*, **84**, 91-93 (2004).
180. S. Trolier-McKinstry, M. D. Biegalski, J. L. Wang, A. A. Belik, E. Takayama-Muromachi and I. Levin, "Growth, crystal structure, and properties of epitaxial BiScO₃ thin films" *J. Appl. Phys.*, **104**, 044102 (2008).
181. V. Samuel, S. C. Navale, A. D. Jadhav, A. B. Gaikwad and V. Ravi, "Synthesis of ultrafine BiMnO₃ particles at 100 degrees C" *Mater. Lett.*, **61**, 1050-1051 (2007).
182. B. Mazumder, I. Uddin, S. Khan, V. Ravi, K. Selvraj, P. Poddar and A. Ahmad, "Bio-milling technique for the size reduction of chemically synthesized BiMnO₃ nanoplates" *J. Mater. Chem.*, **17**, 3910-3914 (2007).
183. J. Zylberberg, A. A. Belik, E. Takayama-Muromachi and Z. G. Ye, "Bismuth aluminate: A new high-*T_C* lead-free piezo-/ferroelectric" *Chem. Mater.*, **19**, 6385-6390 (2007).
184. A. A. Belik, T. Wuernisha, T. Kamiyama, K. Mori, M. Maie, T. Nagai, Y. Matsui and E. Takayama-Muromachi, "High-pressure synthesis, crystal

- structures, and properties of perovskite-like BiAlO_3 and pyroxene-like BiGaO_3 " *Chem. Mater.*, **18**, 133-139 (2006).
185. A. A. Belik, S. Y. Stefanovich, B. I. Lazoryak and E. Takayama-Muromachi, "BiInO₃: A polar oxide with GdFeO₃-type perovskite structure" *Chem. Mater.*, **18**, 1964-1968 (2006).
 186. A. A. Belik, S. Iikubo, K. Kodama, N. Igawa, S. Shamoto, M. Maie, T. Nagai, Y. Matsui, S. Y. Stefanovich, B. I. Lazoryak and E. Takayama-Muromachi, "BiSCO₃: Centrosymmetric BiMnO₃-type oxide" *J. Am. Chem. Soc.*, **128**, 706-707 (2006).
 187. A. A. Belik, S. Iikubo, K. Kodama, N. Igawa, S. Shamoto and E. Takayama-Muromachi, "Neutron powder diffraction study on the crystal and magnetic structures of BiCrO₃" *Chem. Mater.*, **20**, 3765-3769 (2008).
 188. H. Faqir, H. Chiba, M. Kikuchi, Y. Syono, M. Mansori, P. Satre and A. Sebaoun, "High-temperature XRD and DTA studies of BiMnO₃ perovskite" *J. Solid State Chem.*, **142**, 113-119 (1999).
 189. T. Atou, H. Chiba, K. Ohoyama, Y. Yamaguchi and Y. Syono, "Structure determination of ferromagnetic perovskite BiMnO₃" *J. Solid State Chem.*, **145**, 639-642 (1999).
 190. A. M. dos Santos, S. Parashar, A. R. Raju, Y. S. Zhao, A. K. Cheetham and C. N. R. Rao, "Evidence for the likely occurrence of magnetoferroelectricity in the simple perovskite, BiMnO₃" *Solid State Commun.*, **122**, 49-52 (2002).
 191. T. Kimura, S. Kawamoto, I. Yamada, M. Azuma, M. Takano and Y. Tokura, "Magnetocapacitance effect in multiferroic BiMnO₃" *Phys. Rev. B*, **67**, 180401(R) (2003).
 192. E. Montanari, G. Calestani, A. Migliori, M. Dapiaggi, F. Bolzoni, R. Cabassi and E. Gilioli, "High-temperature polymorphism in metastable BiMnO₃" *Chem. Mater.*, **17**, 6457-6467 (2005).
 193. E. Montanari, G. Calestani, L. Righi, E. Gilioli, F. Bolzoni, K. S. Knight and P. G. Radaelli, "Structural anomalies at the magnetic transition in centrosymmetric BiMnO₃" *Phys. Rev. B*, **75**, 220101(R) (2007).
 194. E. Montanari, L. Righi, G. Calestani, A. Migliori, E. Gilioli and F. Bolzoni, "Room temperature polymorphism in metastable BiMnO₃ prepared by high-pressure synthesis" *Chem. Mater.*, **17**, 1765-1773 (2005).
 195. A. A. Belik, S. Iikubo, T. Yokosawa, K. Kodama, N. Igawa, S. Shamoto, M. Azuma, M. Takano, K. Kimoto, Y. Matsui and E. Takayama-Muromachi, "Origin of the monoclinic-to-monoclinic phase transition and evidence for the centrosymmetric crystal structure of BiMnO₃" *J. Am. Chem. Soc.*, **129**, 971-977 (2007).
 196. A. A. Belik and E. Takayama-Muromachi, "Magnetic properties of BiMnO₃ studied with DC and AC magnetization and specific heat" *Inorg. Chem.*, **45**, 10224-10229 (2006).
 197. P. Baettig, R. Seshadri and N. A. Spaldin, "Anti-polarity in ideal BiMnO₃" *J. Am. Chem. Soc.*, **129**, 9854 (2007).
 198. K. Kodama, S. Iikubo, S. I. Shamoto, A. A. Belik and E. Takayama-Muromachi, "Local crystal structure of multiferroic system BiMnO₃ by atomic pair distribution function analysis" *J. Phys. Soc. Japan*, **76**, 124605 (2007).

199. T. Yokosawa, A. A. Belik, T. Asaka, K. Kimoto, E. Takayama-Muromachi and Y. Matsui, "Crystal symmetry of BiMnO₃: Electron diffraction study" *Phys. Rev. B*, **77**, 024111 (2008).
200. Y. Uratani, T. Shishidou, F. Ishii and T. Oguchi, "First-principles predictions of giant electric polarization" *Jpn. J. Appl. Phys.*, **44**, 7130-7133 (2005).
201. P. Ravindran, R. Vidya, O. Eriksson and H. Fjellvåg, "Magnetic-instability-induced giant magnetoelectric coupling" *Adv. Mater.*, **20**, 1353-1356 (2008).
202. A. A. Belik, S. Iikubo, K. Kodama, N. Igawa, S. Shamoto, S. Niitaka, M. Azuma, Y. Shimakawa, M. Takano, F. Izumi and E. Takayama-Muromachi, "Neutron powder diffraction study on the crystal and magnetic structures of BiCoO₃" *Chem. Mater.*, **18**, 798-803 (2006).
203. M. Azuma, S. Carlsson, J. Rodgers, M. G. Tucker, M. Tsujimoto, S. Ishiwata, S. Isoda, Y. Shimakawa, M. Takano and J. P. Attfield, "Pressure-induced intermetallic valence transition in BiNiO₃" *J. Am. Chem. Soc.*, **129**, 14433-14436 (2007).
204. S. Ishiwata, M. Azuma, M. Takano, E. Nishibori, M. Takata, M. Sakata and K. Kato, "High pressure synthesis, crystal structure and physical properties of a new Ni(II) perovskite BiNiO₃" *J. Mater. Chem.*, **12**, 3733-3737 (2002).
205. M. R. Suchomel, C. I. Thomas, M. Allix, M. J. Rosseinsky, A. M. Fogg and M. F. Thomas, "High pressure bulk synthesis and characterization of the predicted multiferroic Bi(Fe_{1/2}Cr_{1/2})O₃" *Appl. Phys. Lett.*, **90**, 112909 (2007).
206. M. Azuma, K. Takata, T. Saito, S. Ishiwata, Y. Shimakawa and M. Takano, "Designed ferromagnetic, ferroelectric Bi₂NiMnO₆" *J. Am. Chem. Soc.*, **127**, 8889-8892 (2005).
207. H. Hughes, M. M. B. Allix, C. A. Bridges, J. B. Claridge, X. J. Kuang, H. J. Niu, S. Taylor, W. H. Song and M. J. Rosseinsky, "A polar oxide with a large magnetization synthesized at ambient pressure" *J. Am. Chem. Soc.*, **127**, 13790-13791 (2005).
208. C. A. Bridges, M. Allix, M. R. Suchomel, X. J. Kuang, I. Sterianou, D. C. Sinclair and M. J. Rosseinsky, "A pure bismuth a site polar perovskite synthesized at ambient pressure" *Angew. Chem. Int. Ed.*, **46**, 8785-8789 (2007).
209. Y. Tokunaga, S. Iguchi, T. Arima and Y. Tokura, "Magnetic-field-induced ferroelectric state in DyFeO₃" *Phys. Rev. Lett.*, **101**, 097205 (2008).
210. Y. Tokunaga, N. Furukawa, H. Sakai, Y. Taguchi, T. H. Arima and Y. Tokura, "Composite domain walls in a multiferroic perovskite ferrite" *Nat. Mater.*, **8**, 558-562 (2009).
211. S. A. Fedulov, P. B. Ladyzhinskii, I. L. Pyatigorskaya and Y. N. Venevtsev, "Complete Phase Diagram of the PbTiO₃-BiFeO₃ System" *Sov. Phys. Solid State*, **6**, 375-378 (1964).
212. T. Kanai, S. Ohkoshi, A. Nakajima, T. Watanabe and K. Hashimoto, "A ferroelectric ferromagnet composed of (PLZT)_x(BiFeO₃)_{1-x} solid solution" *Adv. Mater.*, **13**, 487-490 (2001).
213. K. Ueda, H. Tabata and T. Kawai, "Coexistence of ferroelectricity and ferromagnetism in BiFeO₃-BaTiO₃ thin films at room temperature" *Appl. Phys. Lett.*, **75**, 555-557 (1999).

214. R. A. M. Gotardo, I. A. Santos, L. F. Cotica, E. R. Botero, D. Garcia and J. A. Eiras, "Improved ferroelectric and magnetic properties of monoclinic structured $0.8\text{BiFeO}_3\text{-}0.2\text{BaTiO}_3$ magnetoelectric ceramics" *Scripta Mater.*, **61**, 508-511 (2009).
215. D. I. Woodward, I. M. Reaney, R. E. Eitel and C. A. Randall, "Crystal and domain structure of the $\text{BiFeO}_3\text{-PbTiO}_3$ solid solution" *J. Appl. Phys.*, **94**, 3313-3318 (2003).
216. T. P. Comyn, S. P. McBride and A. J. Bell, "Processing and electrical properties of $\text{BiFeO}_3\text{-PbTiO}_3$ ceramics" *Mater. Lett.*, **58**, 3844-3846 (2004).
217. N. G. Wang, J. Cheng, A. Pyatakov, A. K. Zvezdin, J. F. Li, L. E. Cross and D. Viehland, "Multiferroic properties of modified $\text{BiFeO}_3\text{-PbTiO}_3$ -based ceramics: Random-field induced release of latent magnetization and polarization" *Phys. Rev. B*, **72**, 104434 (2005).
218. S. Bhattacharjee, S. Tripathi and D. Pandey, "Morphotropic phase boundary in $(1-x)\text{BiFeO}_3\text{-}x\text{PbTiO}_3$: phase coexistence region and unusually large tetragonality" *Appl. Phys. Lett.*, **91**, 042903 (2007).
219. W. M. Zhu, H. Y. Guo and Z. G. Ye, "Structural and magnetic characterization of multiferroic $(\text{BiFeO}_3)_{1-x}(\text{PbTiO}_3)_x$ solid solutions" *Phys. Rev. B*, **78**, 014401 (2008).
220. P. Curie, *J. Physique*, **3**, 393 (1894).
221. D. N. Astrov, "The Magnetoelectric Effect in Antiferromagnetics" *Sov. Phys. JETP USSR*, **11**, 708-709 (1960).
222. T. Lottermoser, T. Lonkai, U. Amann, D. Hohlwein, J. Ihringer and M. Fiebig, "Magnetic phase control by an electric field" *Nature*, **430**, 541-544 (2004).
223. M. Fiebig, T. Lottermoser, D. Frohlich, A. V. Goltsev and R. V. Pisarev, "Observation of coupled magnetic and electric domains" *Nature*, **419**, 818-820 (2002).
224. Z. J. Huang, Y. Cao, Y. Y. Sun, Y. Y. Xue and C. W. Chu, "Coupling between the ferroelectric and antiferromagnetic orders in YMnO_3 " *Phys. Rev. B*, **56**, 2623-2626 (1997).
225. N. Fujimura, T. Ishida, T. Yoshimura and T. Ito, "Epitaxially grown YMnO_3 film: New candidate for nonvolatile memory devices" *Appl. Phys. Lett.*, **69**, 1011-1013 (1996).
226. M. Fiebig, D. Frohlich, K. Kohn, S. Leute, T. Lottermoser, V. V. Pavlov and R. V. Pisarev, "Determination of the magnetic symmetry of hexagonal manganites by second harmonic generation" *Phys. Rev. Lett.*, **84**, 5620-5623 (2000).
227. T. Katsufuji, S. Mori, M. Masaki, Y. Moritomo, N. Yamamoto and H. Takagi, "Dielectric and magnetic anomalies and spin frustration in hexagonal RMnO_3 (R = Y, Yb, and Lu)" *Phys. Rev. B*, **6410**, 104419 (2001).
228. D. Y. Cho, J. Y. Kim, B. G. Park, K. J. Rho, J. H. Park, H. J. Noh, B. J. Kim, S. J. Oh, H. M. Park, J. S. Ahn, H. Ishibashi, S. W. Cheong, J. H. Lee, P. Murugavel, T. W. Noh, A. Tanaka and T. Jo, "Ferroelectricity driven by Y d^0 -ness with rehybridization in YMnO_3 " *Phys. Rev. Lett.*, **98**, 217601 (2007).
229. H. Lueken, "A Magnetoelectric Effect in YMnO_3 and HoMnO_3 " *Angew. Chem. Int. Ed.*, **47**, 8562-8564 (2008).

230. J. S. Zhou, J. B. Goodenough, J. M. Gallardo-Amores, E. Moran, M. A. Alario-Franco and R. Caudillo, "Hexagonal versus perovskite phase of manganite RMnO_3 (R=Y, Ho, Er, Tm, Yb, Lu)" *Phys. Rev. B*, **74**, 014422 (2006).
231. Y. H. Huang, H. Fjellvåg, M. Karppinen, B. C. Hauback, H. Yamauchi and J. B. Goodenough, "Crystal and magnetic structure of the orthorhombic perovskite YbMnO_3 " *Chem. Mater.*, **18**, 2130-2134 (2006).
232. H. W. Brinks, H. Fjellvåg and A. Kjekshus, "Synthesis of metastable perovskite-type YMnO_3 and HoMnO_3 " *J. Solid State Chem.*, **129**, 334-340 (1997).
233. K. Bergum, "*Wet Chemical Preparation and Characterisation of Nanocrystalline and Bulk Yttrium Manganite*", Master's thesis, Norwegian University of Science and Technology (NTNU), (2009).
234. J. H. Lee, P. Murugavel, H. Ryu, D. Lee, J. Y. Jo, J. W. Kim, H. J. Kim, K. H. Kim, Y. Jo, M. H. Jung, Y. H. Oh, Y. W. Kim, J. G. Yoon, J. S. Chung and T. W. Noh, "Epitaxial stabilization of a new multiferroic hexagonal phase of TbMnO_3 thin films" *Adv. Mater.*, **18**, 3125 (2006).
235. T. Goto, T. Kimura, G. Lawes, A. P. Ramirez and Y. Tokura, "Ferroelectricity and giant magnetocapacitance in perovskite rare-earth manganites" *Phys. Rev. Lett.*, **92**, 257201 (2004).
236. M. Kenzelmann, A. B. Harris, S. Jonas, C. Broholm, J. Schefer, S. B. Kim, C. L. Zhang, S. W. Cheong, O. P. Vajk and J. W. Lynn, "Magnetic inversion symmetry breaking and ferroelectricity in TbMnO_3 " *Phys. Rev. Lett.*, **95**, 087206 (2005).
237. T. Kimura, G. Lawes, T. Goto, Y. Tokura and A. P. Ramirez, "Magnetoelectric phase diagrams of orthorhombic RMnO_3 (R=Gd, Tb, and Dy)" *Phys. Rev. B*, **71**, 224425 (2005).
238. N. Aliouane, O. Prokhnenko, R. Feyerherm, M. Mostovoy, J. Stempfer, K. Habicht, K. C. Rule, E. Dudzik, A. U. B. Wolter, A. Maljuk and D. N. Argyriou, "Magnetic order and ferroelectricity in RMnO_3 multiferroic manganites: coupling between R- and Mn-spins" *J. Phys.: Condens. Matter*, **20**, 434215 (2008).
239. I. A. Sergienko, C. Sen and E. Dagotto, "Ferroelectricity in the magnetic *E*-phase of orthorhombic perovskites" *Phys. Rev. Lett.*, **97**, 227204 (2006).
240. T. Kimura and Y. Tokura, "Magnetoelectric phase control in a magnetic system showing cycloidal/conical spin order" *J. Phys.: Condens. Matter*, **20**, 434204 (2008).
241. M. Mostovoy, "Ferroelectricity in spiral magnets" *Phys. Rev. Lett.*, **96**, 067601 (2006).
242. L. Yan, J. F. Li and D. Viehland, "Deposition conditions and electrical properties of relaxor ferroelectric $\text{Pb}(\text{Fe}_{1/2}\text{Nb}_{1/2})\text{O}_3$ thin films prepared by pulsed laser deposition" *J. Appl. Phys.*, **101**, 104107 (2007).
243. M. Alexe, M. Ziese, D. Hesse, P. Esquinazi, H. Yamauchi, T. Fukushima, S. Picozzi and U. Gösele, "Ferroelectric Switching in Multiferroic Magnetite (Fe_3O_4) Thin Films" *Adv. Mater.*, DOI: 10.1002/adma.200901381 (2009).

244. N. Hur, S. Park, P. A. Sharma, J. S. Ahn, S. Guha and S. W. Cheong, "Electric polarization reversal and memory in a multiferroic material induced by magnetic fields" *Nature*, **429**, 392-395 (2004).
245. G. R. Blake, L. C. Chapon, P. G. Radaelli, S. Park, N. Hur, S. W. Cheong and J. Rodriguez-Carvajal, "Spin structure and magnetic frustration in multiferroic RMn_2O_5 (R=Tb, Ho, Dy)" *Phys. Rev. B*, **71**, 214402 (2005).
246. J. Koo, C. Song, S. Ji, J. S. Lee, J. Park, T. H. Jang, C. H. Yang, J. H. Park, Y. H. Jeong, K. B. Lee, T. Y. Koo, Y. J. Park, J. Y. Kim, D. Wermeille, A. I. Goldman, G. Srajer, S. Park and S. W. Cheong, "Non-resonant and resonant x-ray scattering studies on multiferroic TbMn_2O_5 " *Phys. Rev. Lett.*, **99**, 197601 (2007).
247. P. G. Radaelli, L. C. Chapon, A. Daoud-Aladine, C. Vecchini, P. J. Brown, T. Chatterji, S. Park and S. W. Cheong, "Electric field switching of antiferromagnetic domains in YMn_2O_5 : A probe of the multiferroic mechanism" *Phys. Rev. Lett.*, **101**, 067205 (2008).
248. Y. Noda, H. Kimura, M. Fukunaga, S. Kobayashi, I. Kagomiya and K. Kohn, "Magnetic and ferroelectric properties of multiferroic RMn_2O_5 " *J. Phys.: Condens. Matter*, **20**, 434206 (2008).
249. P. G. Radaelli and L. C. Chapon, "A neutron diffraction study of RMn_2O_5 multiferroics" *J. Phys.: Condens. Matter*, **20**, 434213 (2008).
250. C. Ederer and N. A. Spaldin, "Magnetoelectrics - A new route to magnetic ferroelectrics" *Nat. Mater.*, **3**, 849-851 (2004).
251. G. Lawes, A. B. Harris, T. Kimura, N. Rogado, R. J. Cava, A. Aharony, O. Entin-Wohlman, T. Yildirim, M. Kenzelmann, C. Broholm and A. P. Ramirez, "Magnetically driven ferroelectric order in $\text{Ni}_3\text{V}_2\text{O}_8$ " *Phys. Rev. Lett.*, **95**, 087205 (2005).
252. G. Lawes, M. Kenzelmann and C. Broholm, "Magnetically induced ferroelectricity in the buckled Kagome antiferromagnet $\text{Ni}_3\text{V}_2\text{O}_8$ " *J. Phys.: Condens. Matter*, **20**, 434205 (2008).
253. T. Yildirim, L. I. Vergara, J. Iniguez, J. L. Musfeldt, A. B. Harris, N. Rogado, R. J. Cava, F. Yen, R. P. Chaudhury and B. Lorenz, "Phonons and magnetoelectric interactions in $\text{Ni}_3\text{V}_2\text{O}_8$ " *J. Phys.: Condens. Matter*, **20**, 434214 (2008).
254. S. Seki, Y. Onose and Y. Tokura, "Spin-driven ferroelectricity in triangular lattice antiferromagnets ACrO_2 (A=Cu, Ag, Li, or Na)" *Phys. Rev. Lett.*, **101**, 067204 (2008).
255. K. Kimura, H. Nakamura, K. Ohgushi and T. Kimura, "Magnetoelectric control of spin-chiral ferroelectric domains in a triangular lattice antiferromagnet" *Phys. Rev. B*, **78**, 140401(R) (2008).
256. T. Kimura, J. C. Lashley and A. P. Ramirez, "Inversion-symmetry breaking in the noncollinear magnetic phase of the triangular-lattice antiferromagnet CuFeO_2 " *Phys. Rev. B*, **73**, 220401(R) (2006).
257. Y. J. Choi, H. T. Yi, S. Lee, Q. Huang, V. Kiryukhin and S. W. Cheong, "Ferroelectricity in an Ising chain magnet" *Phys. Rev. Lett.*, **100**, 047601 (2008).

258. H. Wu, T. Burnus, Z. Hu, C. Martin, A. Maignan, J. C. Cezar, A. Tanaka, N. B. Brookes, D. I. Khomskii and L. H. Tjeng, "Ising Magnetism and Ferroelectricity in $\text{Ca}_3\text{CoMnO}_6$ " *Phys. Rev. Lett.*, **102**, 026404 (2009).
259. E. Ascher, H. Rieder, H. Schmid and H. Stossel, "Some Properties of Ferromagnetoelectric Nickel-Iodine Boracite $\text{Ni}_3\text{B}_7\text{O}_{13}\text{I}$ " *J. Appl. Phys.*, **37**, 1404-1405 (1966).
260. S. Ishiwata, Y. Taguchi, H. Murakawa, Y. Onose and Y. Tokura, "Low-magnetic-field control of electric polarization vector in a helimagnet" *Science*, **319**, 1643-1646 (2008).
261. M. Mostovoy, "Transition metal oxides - Multiferroics go high- T_C " *Nat. Mater.*, **7**, 269-270 (2008).
262. T. Kimura, Y. Sekio, H. Nakamura, T. Siegrist and A. P. Ramirez, "Cupric oxide as an induced-multiferroic with high- T_C " *Nat. Mater.*, **7**, 291-294 (2008).
263. Y. Yamasaki, S. Miyasaka, Y. Kaneko, J. P. He, T. Arima and Y. Tokura, "Magnetic reversal of the ferroelectric polarization in a multiferroic spinel oxide" *Phys. Rev. Lett.*, **96**, 207204 (2006).
264. J. Hemberger, P. Lunkenheimer, R. Fichtl, H. A. K. von Nidda, V. Tsurkan and A. Loidl, "Relaxor ferroelectricity and colossal magnetocapacitive coupling in ferromagnetic CdCr_2S_4 " *Nature*, **434**, 364-367 (2005).
265. G. Nenert and T. T. M. Palstra, "Prediction for new magnetoelectric fluorides" *J. Phys.: Condens. Matter*, **19**, 406213 (2007).
266. I. Kornev, M. Bichurin, J. P. Rivera, S. Gentil, H. Schmid, A. G. M. Jansen and P. Wyder, "Magnetoelectric properties of LiCoPO_4 and LiNiPO_4 " *Phys. Rev. B*, **62**, 12247-12253 (2000).
267. J. L. MacManus-Driscoll, P. Zerrer, H. Y. Wang, H. Yang, J. Yoon, A. Fouchet, R. Yu, M. G. Blamire and Q. X. Jia, "Strain control and spontaneous phase ordering in vertical nanocomposite heteroepitaxial thin films" *Nat. Mater.*, **7**, 314-320 (2008).
268. H. Zheng, J. Wang, S. E. Lofland, Z. Ma, L. Mohaddes-Ardabili, T. Zhao, L. Salamanca-Riba, S. R. Shinde, S. B. Ogale, F. Bai, D. Viehland, Y. Jia, D. G. Schlom, M. Wuttig, A. Roytburd and R. Ramesh, "Multiferroic BaTiO_3 - CoFe_2O_4 nanostructures" *Science*, **303**, 661-663 (2004).
269. R. P. Mahajan, K. K. Patankar, M. B. Kothale and S. A. Patil, "Conductivity, dielectric behaviour and magnetoelectric effect in copper ferrite-barium titanate composites" *Bull. Mater. Sci.*, **23**, 273-279 (2000).
270. K. K. Patankar, S. A. Patil, K. V. Sivakumar, R. P. Mahajan, Y. D. Kolekar and M. B. Kothale, "AC conductivity and magnetoelectric effect in $\text{CuFe}_{1.6}\text{Cr}_{0.4}\text{O}_4$ - BaTiO_3 composite ceramics" *Mater. Chem. Phys.*, **65**, 97-102 (2000).
271. G. Srinivasan, E. T. Rasmussen, B. J. Levin and R. Hayes, "Magnetoelectric effects in bilayers and multilayers of magnetostrictive and piezoelectric perovskite oxides" *Phys. Rev. B*, **65**, 134402 (2002).
272. F. Zavaliche, H. Zheng, L. Mohaddes-Ardabili, S. Y. Yang, Q. Zhan, P. Shafer, E. Reilly, R. Chopdekar, Y. Jia, P. Wright, D. G. Schlom, Y. Suzuki and R. Ramesh, "Electric field-induced magnetization switching in epitaxial columnar nanostructures" *Nano Lett.*, **5**, 1793-1796 (2005).

273. H. M. Zheng, F. Straub, Q. Zhan, P. L. Yang, W. K. Hsieh, F. Zavaliche, Y. H. Chu, U. Dahmen and R. Ramesh, "Self-assembled growth of BiFeO₃-CoFe₂O₄ nanostructures" *Adv. Mater.*, **18**, 2747-2752 (2006).
274. F. Zavaliche, T. Zhao, H. Zheng, F. Straub, M. P. Cruz, P. L. Yang, D. Hao and R. Ramesh, "Electrically assisted magnetic recording in multiferroic nanostructures" *Nano Lett.*, **7**, 1586-1590 (2007).
275. B. J. Rodriguez, S. Jesse, A. P. Baddorf, T. Zhao, Y. H. Chu, R. Ramesh, E. A. Eliseev, A. N. Morozovska and S. V. Kalinin, "Spatially resolved mapping of ferroelectric switching behavior in self-assembled multiferroic nanostructures: strain, size, and interface effects" *Nanotechnol.*, **18**, 405701 (2007).
276. N. Dix, R. Muralidharan, B. Warot-Fonrose, M. Varela, F. Sanchez and J. Fontcuberta, "Critical Limitations in the Fabrication of Biferroic BiFeO₃-CoFe₂O₄ Columnar Nanocomposites Due to Bismuth Loss" *Chem. Mater.*, **21**, 1375-1380 (2009).
277. C. H. Yang, F. Yildiz, S. H. Lee, Y. H. Jeong, U. Chon and T. Y. Koo, "Synthesis of nanoscale composites of exchange biased MnFe₂O₄ and Mn-doped BiFeO₃" *Appl. Phys. Lett.*, **90**, 163116 (2007).
278. M. Kumar and K. L. Yadav, "Synthesis of nanocrystalline xCuFe₂O₄-(1-x)BiFeO₃ magnetoelectric composite by chemical method" *Mater. Lett.*, **61**, 2089-2092 (2007).
279. M. Kumar and K. L. Yadav, "Magnetoelectric characterization of xNi_{0.75}Co_{0.25}Fe₂O₄-(1-x)BiFeO₃ nanocomposites" *J. Phys. Chem. Solids*, **68**, 1791-1795 (2007).
280. Q. Zhan, R. Yu, S. P. Crane, H. Zheng, C. Kisielowski and R. Ramesh, "Structure and interface chemistry of perovskite-spinel nanocomposite thin films" *Appl. Phys. Lett.*, **89**, 172902 (2006).
281. L. Silvestroni, H.-J. Kleebe, H. Kungl, S. Lauterbach, M. Müller and M. J. Hoffmann, "Lead Zirconate Titanate-Magnetoplumbite Composites: A First Step Toward Multiferroic Ceramics" *J. Am. Ceram. Soc.*, DOI: 10.1111/j.1551-2916.2009.03192.x (2009).
282. H. Yang, H. Wang, J. Yoon, J. Wang, M. Jain, D. M. Feldmann, P. C. Dowden, J. MacManus-Driscoll and Q. Jia, "Vertical Interface Effect on the Physical Properties of Self-Assembled Nanocomposite Epitaxial Films" *Adv. Mater.*, DOI: 10.1002/adma.200900781 (2009).
283. J. Nogues and I. K. Schuller, "Exchange bias" *J. Magn. Magn. Mater.*, **192**, 203-232 (1999).
284. H. Bea, M. Bibes, S. Cherifi, F. Nolting, B. Warot-Fonrose, S. Fusil, G. Herranz, C. Deranlot, E. Jacquet, K. Bouzehouane and A. Barthelemy, "Tunnel magnetoresistance and robust room temperature exchange bias with multiferroic BiFeO₃ epitaxial thin films" *Appl. Phys. Lett.*, **89**, 242114 (2006).
285. H. Bea, M. Bibes, F. Ott, B. Dupe, X. H. Zhu, S. Petit, S. Fusil, C. Deranlot, K. Bouzehouane and A. Barthelemy, "Mechanisms of exchange bias with multiferroic BiFeO₃ epitaxial thin films" *Phys. Rev. Lett.*, **100**, 017204 (2008).

286. H. Naganuma, T. Okubo, S. Sekiguchi, Y. Ando and S. Okamura, "Structural, magnetic, and ferroelectric properties of multiferroic BiFeO₃-based composite films with exchange bias" *J. Appl. Phys.*, **105**, 07D903 (2009).
287. H. Bea, S. Fusil, K. Bouzehouane, M. Bibes, M. Sirena, G. Herranz, E. Jacquet, J. P. Contour and A. Barthelemy, "Ferroelectricity down to at least 2 nm in multiferroic BiFeO₃ epitaxial thin films" *Jpn. J. Appl. Phys.*, **45**, L187-L189 (2006).
288. A. Gruverman, D. Wu, H. Lu, Y. Wang, H. W. Jang, C. M. Folkman, M. Y. Zhuravlev, D. Felker, M. Rzchowski, C. B. Eom and E. Y. Tsymbal, "Tunneling Electroresistance Effect in Ferroelectric Tunnel Junctions at the Nanoscale" *Nano Lett.*, DOI: 10.1021/nl901754t (2009).
289. C. J. Cheng, D. Kan, S. H. Lim, W. R. McKenzie, P. R. Munroe, L. G. Salamanca-Riba, R. L. Withers, I. Takeuchi and V. Nagarajan, "Structural transitions and complex domain structures across a ferroelectric-to-antiferroelectric phase boundary in epitaxial Sm-doped BiFeO₃ thin films" *Phys. Rev. B*, **80**, 014109 (2009).
290. S. Fujino, M. Murakami, V. Anbusathaiah, S. H. Lim, V. Nagarajan, C. J. Fennie, M. Wuttig, L. Salamanca-Riba and I. Takeuchi, "Combinatorial discovery of a lead-free morphotropic phase boundary in a thin-film piezoelectric perovskite" *Appl. Phys. Lett.*, **92**, 202904 (2008).
291. K. Takahashi, N. Kida and M. Tonouchi, "Terahertz radiation by an ultrafast spontaneous polarization modulation of multiferroic BiFeO₃ thin films" *Phys. Rev. Lett.*, **96**, 117402 (2006).
292. D. S. Rana, I. Kawayama, K. Mavani, K. Takahashi, H. Murakami and M. Tonouchi, "Understanding the Nature of Ultrafast Polarization Dynamics of Ferroelectric Memory in the Multiferroic BiFeO₃" *Adv. Mater.*, **21**, 2881 (2009).
293. J. H. Luo and P. A. Maggard, "Hydrothermal synthesis and photocatalytic activities of SrTiO₃-coated Fe₂O₃ and BiFeO₃" *Adv. Mater.*, **18**, 514 (2006).
294. F. Gao, Y. Yuan, K. F. Wang, X. Y. Chen, F. Chen and J. M. Liu, "Preparation and photoabsorption characterization of BiFeO₃ nanowires" *Appl. Phys. Lett.*, **89**, 102506 (2006).
295. X. M. Lu, J. M. Xie, Y. Z. Song and J. M. Lin, "Surfactant-assisted hydrothermal preparation of submicrometer-sized two-dimensional BiFeO₃ plates and their photocatalytic activity" *J. Mater. Sci.*, **42**, 6824-6827 (2007).
296. F. Gao, X. Y. Chen, K. B. Yin, S. Dong, Z. F. Ren, F. Yuan, T. Yu, Z. Zou and J. M. Liu, "Visible-light photocatalytic properties of weak magnetic BiFeO₃ nanoparticles" *Adv. Mater.*, **19**, 2889-2892 (2007).
297. U. A. Joshi, J. S. Jang, P. H. Borse and J. S. Lee, "Microwave synthesis of single-crystalline perovskite BiFeO₃ nanocubes for photoelectrode and photocatalytic applications" *Appl. Phys. Lett.*, **92**, 242106 (2008).
298. C. M. Cho, J. H. Noh, I. S. Cho, J. S. An, K. S. Hong and J. Y. Kim, "Low-Temperature Hydrothermal Synthesis of Pure BiFeO₃ Nanopowders Using Triethanolamine and Their Applications as Visible-Light Photocatalysts" *J. Am. Ceram. Soc.*, **91**, 3753-3755 (2008).

299. S. Li, Y. H. Lin, B. P. Zhang, C. W. Nan and Y. Wang, "Photocatalytic and magnetic behaviors observed in nanostructured BiFeO₃ particles" *J. Appl. Phys.*, **105**, 056105 (2009).
300. S. Li, Y. H. Lin, B. P. Zhang, J. F. Li and C. W. Nan, "BiFeO₃/TiO₂ core-shell structured nanocomposites as visible-active photocatalysts and their optical response mechanism" *J. Appl. Phys.*, **105**, 054310 (2009).
301. R. Haumont, I. A. Kornev, S. Lisenkov, L. Bellaiche, J. Kreisel and B. Dkhil, "Phase stability and structural temperature dependence in powdered multiferroic BiFeO₃" *Phys. Rev. B*, **78**, 134108 (2008).
302. A. Maitre, M. Francois and J. C. Gachon, "Experimental study of the Bi₂O₃-Fe₂O₃ pseudo-binary system" *J. Phase Equilib. and Diff.*, **25**, 59-67 (2004).
303. H. M. Rietveld, "A Profile Refinement Method for Nuclear and Magnetic Structures" *J. Appl. Crystallogr.*, **2**, 65 (1969).
304. B. AXS, "DIFFRACplus TOPAS/TOPAS R/TOPAS P Version 2.1 Technical Reference" (2003).
305. V. Petkov, "Nanostructure by high-energy X-ray diffraction" *Mater. Today*, **11**, 28-38 (2008).
306. A. L. Patterson, "The Scherrer Formula for X-ray Particle Size Determination" *Phys. Rev.*, **56**, 978-982 (1939).
307. S. Brunauer, P. H. Emmet and E. Teller, "Adsorption of Gases in Multimolecular Layers" *J. Am. Chem. Soc.*, **60**, 309 (1938).
308. I. Wærnhus, "*Defect chemistry, conductivity and mass transport properties of La_{1-x}Sr_xFeO_{3-δ} (x = 0 and 0.1)*", PhD Thesis, Norwegian University of Science and Technology (NTNU), (2003).
309. M. I. Morozov, N. A. Lomanova and V. V. Gusarov, "Specific features of BiFeO₃ formation in a mixture of bismuth(III) and iron(III) oxides" *Russ. J. Gen. Chem.*, **73**, 1676-1680 (2003).
310. S. A. Fedulov, "Determination of Curie Temperature for BiFeO₃ Ferroelectric" *Dokl. Akad. Nauk SSSR*, **139**, 1345 (1961).
311. D. C. Arnold, K. S. Knight, F. D. Morrison and P. Lightfoot, "Ferroelectric-Paraelectric Transition in BiFeO₃: Crystal Structure of the Orthorhombic beta Phase" *Phys. Rev. Lett.*, **102**, 027602 (2009).
312. G. Achenbach, W. J. James and R. Gerson, "Preparation of Single-Phase Polycrystalline BiFeO₃" *J. Am. Ceram. Soc.*, **50**, 437 (1967).
313. Y. P. Wang, L. Zhou, M. F. Zhang, X. Y. Chen, J. M. Liu and Z. G. Liu, "Room-temperature saturated ferroelectric polarization in BiFeO₃ ceramics synthesized by rapid liquid phase sintering" *Appl. Phys. Lett.*, **84**, 1731-1733 (2004).
314. M. Valant, A. K. Axelsson and N. Alford, "Peculiarities of a solid-state synthesis of multiferroic polycrystalline BiFeO₃" *Chem. Mater.*, **19**, 5431-5436 (2007).
315. F. Tyholdt, S. Jørgensen, H. Fjellvåg and A. E. Gunnaes, "Synthesis of oriented BiFeO₃ thin films by chemical solution deposition: Phase, texture, and microstructural development" *J. Mater. Res.*, **20**, 2127-2139 (2005).
316. S. Komarneni, V. C. Menon, Q. H. Li, R. Roy and E. Ainger, "Microwave-hydrothermal processing of BiFeO₃ and CsAl₂PO₆" *J. Am. Ceram. Soc.*, **79**, 1409-1412 (1996).

317. C. Chen, J. R. Cheng, S. W. Yu, L. J. Che and Z. Y. Meng, "Hydrothermal synthesis of perovskite bismuth ferrite crystallites" *J. Cryst. Growth*, **291**, 135-139 (2006).
318. J. T. Han, Y. H. Huang, X. J. Wu, C. L. Wu, W. Wei, B. Peng, W. Huang and J. B. Goodenough, "Tunable synthesis of bismuth ferrites with various morphologies" *Adv. Mater.*, **18**, 2145 (2006).
319. Y. G. Wang, G. Xu, L. L. Yang, Z. H. Ren, X. Wei, W. J. Weng, P. Y. Du, G. Shen and G. R. Han, "Hydrothermal synthesis of single-crystal bismuth ferrite nanoflakes assisted by potassium nitrate" *Ceram. Int.*, **35**, 1285-1287 (2009).
320. Y. G. Wang, G. Xu, Z. H. Ren, X. Wei, W. J. Weng, P. Du, G. Shen and G. R. Han, "Mineralizer-assisted hydrothermal synthesis and characterization of BiFeO₃ nanoparticles" *J. Am. Ceram. Soc.*, **90**, 2615-2617 (2007).
321. Y. G. Wang, G. Xu, L. L. Yang, Z. H. Ren, X. Wei, W. J. Weng, P. Du, G. Shen and G. R. Han, "Alkali metal ions-assisted controllable synthesis of bismuth ferrites by a hydrothermal method" *J. Am. Ceram. Soc.*, **90**, 3673-3675 (2007).
322. J. Prado-Gonjal, M. E. Villafuerte-Castrejon, L. Fuentes and E. Moran, "Microwave-hydrothermal synthesis of the multiferroic BiFeO₃" *Mater. Res. Bull.*, **44**, 1734-1737 (2009).
323. J. Chen, X. R. Xing, A. Watson, W. Wang, R. B. Yu, J. X. Deng, L. Yan, C. Sun and X. B. Chen, "Rapid synthesis of multiferroic BiFeO₃ single-crystalline nanostructures" *Chem. Mater.*, **19**, 3598-3600 (2007).
324. M. Popa, D. Crespo, J. M. Calderon-Moreno, S. Preda and V. Fruth, "Synthesis and structural characterization of single-phase BiFeO₃ powders from a polymeric precursor" *J. Am. Ceram. Soc.*, **90**, 2723-2727 (2007).
325. V. Fruth, D. Berger, C. Matei, A. Ianculescu, M. Popa, E. Tenea and M. Zaharescu, "Preparation and characterization of BiFeO₃ nanopowders" *J. Phys. IV*, **128**, 7-11 (2005).
326. M. P. Pechini, "Method of Preparing Lead and Alkaline Earth Titanates and Niobates and Coating Method Using the Same to Form a Capacitor"; US Patent 3330697, July 11 (1967).
327. S. Ghosh, S. Dasgupta, A. Sen and H. S. Maiti, "Low-temperature synthesis of nanosized bismuth ferrite by soft chemical route" *J. Am. Ceram. Soc.*, **88**, 1349-1352 (2005).
328. S. Ghosh, S. Dasgupta, A. Sen and H. S. Maiti, "Low temperature synthesis of bismuth ferrite nanoparticles by a ferrioxalate precursor method" *Mater. Res. Bull.*, **40**, 2073-2079 (2005).
329. J. K. Kim, S. S. Kim and W. J. Kim, "Sol-gel synthesis and properties of multiferroic BiFeO₃" *Mater. Lett.*, **59**, 4006-4009 (2005).
330. A. Hardy, S. Gielis, H. van der Ruel, J. D'Haen, M. K. van Bael and J. Mullens, "Effects of precursor chemistry and thermal treatment conditions on obtaining phase pure bismuth ferrite from aqueous gel precursors" *J. Eur. Ceram. Soc.*, **29**, 3007-3013 (2009).
331. J.-H. Xu, H. Ke, D.-C. Jia, W. Wang and Y. Zhou, "Low-temperature synthesis of BiFeO₃ nanopowders via a sol-gel method" *J. Alloys Compd.*, **472**, 473-477 (2009).

332. R. Haumont, R. Saint-Martin and C. Byl, "Centimeter-size BiFeO₃ single crystals grown by flux method" *Phase Trans.*, **81**, 881-888 (2008).
333. F. Kubel and H. Schmid, "Growth, Twinning and Etch Figures of Ferroelectric Ferroelastic Dendritic BiFeO₃ Single Domain Crystals" *J. Cryst. Growth*, **129**, 515-524 (1993).
334. S. Y. Yang, F. Zavaliche, L. Mohaddes-Ardabili, V. Vaithyanathan, D. G. Schlom, Y. J. Lee, Y. H. Chu, M. P. Cruz, Q. Zhan, T. Zhao and R. Ramesh, "Metalorganic chemical vapor deposition of lead-free ferroelectric BiFeO₃ films for memory applications" *Appl. Phys. Lett.*, **87**, 102903 (2005).
335. J. Kabelac, S. Ghosh, P. Dobal and R. Katiyar, "rf oxygen plasma assisted molecular beam epitaxy growth of BiFeO₃ thin films on SrTiO₃ (001)" *J. Vac. Sci. Tech. B*, **25**, 1049-1052 (2007).
336. J. F. Ihlefeld, W. Tian, Z. K. Liu, W. A. Doolittle, M. Bernhagen, P. Reiche, R. Uecker, R. Ramesh and D. G. Schlom, "Adsorption-Controlled Growth of BiFeO₃ by MBE and Integration with Wide Band Gap Semiconductors" *IEEE Trans. Ultrason, Ferroelectr. Freq. Control*, **56**, 1528-1533 (2009).
337. R. R. Das, D. M. Kim, S. H. Baek, C. B. Eom, F. Zavaliche, S. Y. Yang, R. Ramesh, Y. B. Chen, X. Q. Pan, X. Ke, M. S. Rzchowski and S. K. Streiffer, "Synthesis and ferroelectric properties of epitaxial BiFeO₃ thin films grown by sputtering" *Appl. Phys. Lett.*, **88**, 242904 (2006).
338. F. Tyholdt, H. Fjellvåg, A. E. Gunnaes and A. Olsen, "Synthesis of epitaxial BiFeO₃ films by chemical solution deposition on Pt(100)" *J. Appl. Phys.*, **102**, 074108 (2007).
339. X. D. Qi, J. H. Dho, M. Blamire, Q. X. Jia, J. S. Lee, S. Foltyn and J. L. MacManus-Driscoll, "Epitaxial growth of BiFeO₃ thin films by LPE and sol-gel methods" *J. Magn. Magn. Mater.*, **283**, 415-421 (2004).
340. S. Fujino, M. Murakami, S. H. Lim, M. Wuttig, L. G. Salamanca-Riba and I. Takeuchi, "Ferroelectric properties of multiphase Bi-Fe-O thin films" *Solid State Ionics*, **178**, 1257-1261 (2007).
341. S. H. Lim, M. Murakami, W. L. Sarney, S. Q. Ren, A. Varatharajan, V. Nagarajan, S. Fujino, M. Wuttig, I. Takeuchi and L. G. Salamanca-Riba, "The effects of multiphase formation on strain relaxation and magnetization in multiferroic BiFeO₃ thin films" *Adv. Funct. Mater.*, **17**, 2594-2599 (2007).
342. W. A. Herrmann, E. Herdtweck, W. Scherer, P. Kiprof and L. Pajdla, "Metal-Complexes in Biology and Medicine 5: New Bismuth Hydroxycarboxylate Complexes - Synthesis and Structure of Bismuth(III) Malate Monohydrate and Bismuth(III) Tartrate Trihydrate" *Chem. Ber.*, **126**, 51-56 (1993).
343. G. L. Yuan, S. W. Or, Y. P. Wang, Z. G. Liu and J. M. Liu, "Preparation and multi-properties of insulated single-phase BiFeO₃ ceramics" *Solid State Commun.*, **138**, 76-81 (2006).
344. S. Phapale, R. Mishra and D. Das, "Standard enthalpy of formation and heat capacity of compounds in the pseudo-binary Bi₂O₃-Fe₂O₃ system" *J. Nucl. Mater.*, **373**, 137-141 (2008).
345. A. Fossdal, M. Menon, I. Waernhus, K. Wiik, M.-A. Einarsrud and T. Grande, "Crystal structure and thermal expansion of La_{1-x}Sr_xFeO_{3-δ}" *J. Am. Ceram. Soc.*, **87**, 1952-1958 (2004).

346. H. Zhang, N. Li, K. Li and D. F. Xue, "Structural stability and formability of ABO_3 -type perovskite compounds" *Acta Crystallogr.*, **B63**, 812-818 (2007).
347. H. W. Xu, A. Navrotsky, Y. L. Su and M. L. Balmer, "Perovskite solid solutions along the $NaNbO_3$ - $SrTiO_3$ join: Phase transitions, formation enthalpies, and implications for general perovskite energetics" *Chem. Mater.*, **17**, 1880-1886 (2005).
348. J. R. Chena, W. L. Wang, J. B. Lia and G. H. Rao, "X-ray diffraction analysis and specific heat capacity of $(Bi_{1-x}La_x)FeO_3$ perovskites" *J. Alloys Compd.*, **459**, 66-70 (2008).
349. G. L. Yuan and S. W. Or, "Enhanced piezoelectric and pyroelectric effects in single-phase multiferroic $Bi_{1-x}Nd_xFeO_3$ ($x=0-0.15$) ceramics" *Appl. Phys. Lett.*, **88**, 062905 (2006).
350. Z. Yan, K. F. Wang, J. F. Qu, Y. Wang, Z. T. Song and S. L. Feng, "Processing and properties of Yb-doped $BiFeO_3$ ceramics" *Appl. Phys. Lett.*, **91**, 082906 (2007).
351. F. G. Chang, G. L. Song, K. Fang, P. Qin and Q. J. Zeng, "Effect of gadolinium substitution on dielectric properties of bismuth ferrite" *J. Rare Earths*, **24**, 273-276 (2006).
352. C. H. Yang, T. Y. Koo and Y. H. Jeong, "How to obtain magnetocapacitance effects at room temperature: The case of Mn-doped $BiFeO_3$ " *Solid State Commun.*, **134**, 299-301 (2005).
353. M. Azuma, H. Kanda, A. A. Belik, Y. Shimakawa and M. Takano, "Magnetic and structural properties of $BiFe_{1-x}Mn_xO_3$ " *J. Magn. Magn. Mater.*, **310**, 1177-1179 (2007).
354. L. R. Morss, "Thermochemical Regularities among Lanthanide and Actinide Oxides" *J. Less-Common Metals*, **93**, 301-321 (1983).
355. Y. Kanke and A. Navrotsky, "A calorimetric study of the lanthanide aluminum oxides and the lanthanide gallium oxides: Stability of the perovskites and the garnets" *J. Solid State Chem.*, **141**, 424-436 (1998).
356. C. Laberty, A. Navrotsky, C. N. R. Rao and P. Alphonse, "Energetics of rare earth manganese perovskites $A_{1-x}A'_xMnO_3$ ($A = La, Nd, Y$ and $A' = Sr, La$) systems" *J. Solid State Chem.*, **145**, 77-87 (1999).
357. L. Rormark, S. Stolen, K. Wiik and T. Grande, "Enthalpies of formation of $La_{1-x}A_xMnO_{3+\delta}$ ($A = Ca$ and Sr) measured by high-temperature solution calorimetry" *J. Solid State Chem.*, **163**, 186-193 (2002).
358. E. Takayamamuromachi and A. Navrotsky, "Energetics of Compounds ($A^{2+}B^{4+}O_3$) with the Perovskite Structure" *J. Solid State Chem.*, **72**, 244-256 (1988).
359. J. H. Cheng and A. Navrotsky, "Enthalpies of formation of $LaBO_3$ perovskites ($B = Al, Ga, Sc, \text{ and } In$)" *J. Mater. Res.*, **18**, 2501-2508 (2003).
360. T. T. Carvalho and P. B. Tavares, "Synthesis and thermodynamic stability of multiferroic $BiFeO_3$ " *Mater. Lett.*, **62**, 3984-3986 (2008).
361. K. J. D. MacKenzie, T. Dougherty and J. Barrel, "The electronic properties of complex oxides of bismuth with the mullite structure" *J. Eur. Ceram. Soc.*, **28**, 499-504 (2008).

362. D. C. Craig and N. C. Stephenson, "Structural Studies of Some Body-Centered Cubic Phases of Mixed Oxides Involving Bi_2O_3 - Structures of $\text{Bi}_{25}\text{FeO}_{40}$ and $\text{Bi}_{38}\text{ZnO}_{60}$ " *J. Solid State Chem.*, **15**, 1-8 (1975).
363. K. S. Nalwa, A. Garg and A. Upadhyaya, "Effect of samarium doping on the properties of solid-state synthesized multiferroic bismuth ferrite" *Mater. Lett.*, **62**, 878-881 (2008).
364. Y. P. Wang, G. L. Yuan, X. Y. Chen, J. M. Liu and Z. G. Liu, "Electrical and magnetic properties of single-phased and highly resistive ferroelectromagnet BiFeO_3 ceramic" *J. Phys. D: Appl. Phys.*, **39**, 2019-2023 (2006).
365. S. M. Selbach, M.-A. Einarsrud, T. Tybell and T. Grande, "Synthesis of BiFeO_3 by wet chemical methods" *J. Am. Ceram. Soc.*, **90**, 3430-3434 (2007).
366. S. M. Selbach, T. Tybell, M.-A. Einarsrud and T. Grande, "The Ferroic Phase Transitions of BiFeO_3 " *Adv. Mater.*, **20**, 3692-3696 (2008).
367. A. Palewicz, R. Przenioslo, I. Sosnowska and A. W. Hewat, "Atomic displacements in BiFeO_3 as a function of temperature: neutron diffraction study" *Acta Crystallogr.*, **B63**, 537-544 (2007).
368. M. C. Li and J. L. MacManus-Driscoll, "Phase stability, oxygen nonstoichiometry and magnetic properties of $\text{BiFeO}_{3-\delta}$ " *Appl. Phys. Lett.*, **87**, 252510 (2005).
369. C. Bale, P. Chartrand, S. A. Degterov, G. Eriksson, K. Hack, R. Ben Mahfoud, J. Melancon, A. D. Pelton and S. Petersen, "FactSage thermochemical software and databases" *Calphad*, **26**, 189-228 (2002).
370. H. Okamoto, "The Bi-Pt (Bismuth-Platinum) system" *J. Phase Equilib.*, **12**, 207-210 (1991).
371. S. Yakovlev, J. Zekonyte, C. H. Solterbeck and M. Es-Souni, "Interfacial effects on the electrical properties of multiferroic $\text{BiFeO}_3/\text{Pt}/\text{Si}$ thin film heterostructures" *Thin Solid Films*, **493**, 24-29 (2005).
372. H. Boysen and F. Altorfer, "A Neutron Powder Investigation of the High-Temperature Structure and Phase-Transition in LiNbO_3 " *Acta Crystallogr.*, **B50**, 405-414 (1994).
373. H. Lehnert, H. Boysen, F. Frey, A. Hewat and P. Radaelli, "A neutron powder investigation of the high-temperature structure and phase transition in stoichiometric LiNbO_3 " *Zeitschr. Kristallogr.*, **212**, 712-719 (1997).
374. P. Fischer, M. Polomska, I. Sosnowska and M. Szymanski, "Temperature-Dependence of the Crystal and Magnetic-Structures of BiFeO_3 " *J. Phys. C: Solid State Phys.*, **13**, 1931-1940 (1980).
375. C. Blaauw and Vanderwo.F, "Magnetic and Structural-Properties of BiFeO_3 " *J. Phys. C: Solid State Phys.*, **6**, 1422-1431 (1973).
376. R. Haumont, J. Kreisel, P. Bouvier and F. Hippert, "Phonon anomalies and the ferroelectric phase transition in multiferroic BiFeO_3 " *Phys. Rev. B*, **73**, 132101 (2006).
377. V. R. Palkar, J. John and R. Pinto, "Observation of saturated polarization and dielectric anomaly in magnetoelectric BiFeO_3 thin films" *Appl. Phys. Lett.*, **80**, 1628-1630 (2002).

378. R. Haumont, J. Kreisel and P. Bouvier, "Raman scattering of the model multiferroic oxide BiFeO₃: effect of temperature, pressure and stress" *Phase Trans.*, **79**, 1043-1064 (2006).
379. H. Fukumura, H. Harima, K. Kisoda, M. Tamada, Y. Noguchi and M. Miyayama, "Raman scattering study of multiferroic BiFeO₃ single crystal" *J. Magn. Magn. Mater.*, **310**, E367-E369 (2007).
380. H. Fukumura, S. Matsui, H. Harima, T. Takahashi, T. Itoh, K. Kisoda, M. Tamada, Y. Noguchi and M. Miyayama, "Observation of phonons in multiferroic BiFeO₃ single crystals by Raman scattering" *J. Phys.: Condens. Matter*, **19**, 365224 (2007).
381. M. O. Ramirez, M. Krishnamurthi, S. Denev, A. Kumar, S. Y. Yang, Y. H. Chu, E. Saiz, J. Seidel, A. P. Pyatakov, A. Bush, D. Viehland, J. Orenstein, R. Ramesh and V. Gopalan, "Two-phonon coupling to the antiferromagnetic phase transition in multiferroic BiFeO₃" *Appl. Phys. Lett.*, **92**, 022511 (2008).
382. M. O. Ramirez, A. Kumar, S. A. Denev, Y. H. Chu, J. Seidel, L. W. Martin, S. Y. Yang, R. C. Rai, X. S. Xue, J. F. Ihlefeld, N. J. Podraza, E. Saiz, S. Lee, J. Klug, S. W. Cheong, M. J. Bedzyk, O. Auciello, D. G. Schlom, J. Orenstein, R. Ramesh, J. L. Musfeldt, A. P. Litvinchuk and V. Gopalan, "Spin-charge-lattice coupling through resonant multimagnon excitations in multiferroic BiFeO₃" *Appl. Phys. Lett.*, **94**, 161905 (2009).
383. M. O. Ramirez, A. Kumar, S. A. Denev, N. J. Podraza, X. S. Xu, R. C. Rai, Y. H. Chu, J. Seidel, L. W. Martin, S. Y. Yang, E. Saiz, J. F. Ihlefeld, S. Lee, J. Klug, S. W. Cheong, M. J. Bedzyk, O. Auciello, D. G. Schlom, R. Ramesh, J. Orenstein, J. L. Musfeldt and V. Gopalan, "Magnon sidebands and spin-charge coupling in bismuth ferrite probed by nonlinear optical spectroscopy" *Phys. Rev. B*, **79**, 224106 (2009).
384. P. Hermet, M. Goffinet, J. Kreisel and P. Ghosez, "Raman and infrared spectra of multiferroic bismuth ferrite from first principles" *Phys. Rev. B*, **75**, 220102(R) (2007).
385. R. P. S. M. Lobo, R. L. Moreira, D. Lebeugle and D. Colson, "Infrared phonon dynamics of a multiferroic BiFeO₃ single crystal" *Phys. Rev. B*, **76**, 172105 (2007).
386. I. A. Kornev, S. Lisenkov, R. Haumont, B. Dkhil and L. Bellaiche, "Finite-temperature properties of multiferroic BiFeO₃" *Phys. Rev. Lett.*, **99**, 227602 (2007).
387. G. Shirane, R. Pepinsky and B. C. Frazer, "X-Ray and Neutron Diffraction Study of Ferroelectric PbTiO₃" *Phys. Rev.*, **97**, 1179-1180 (1955).
388. S. M. Selbach, T. Tybell, M. A. Einarsrud and T. Grande, "High-temperature semiconducting cubic phase of BiFe_{0.7}Mn_{0.3}O_{3+δ}" *Phys. Rev. B*, **79**, 214113 (2009).
389. S. M. Selbach, M.-A. Einarsrud and T. Grande, "On the Thermodynamic Stability of BiFeO₃" *Chem. Mater.*, **21**, 169-173 (2009).
390. C. dela Cruz, F. Yen, B. Lorenz, Y. Q. Wang, Y. Y. Sun, M. M. Gospodinov and C. W. Chu, "Strong spin-lattice coupling in multiferroic HoMnO₃: Thermal expansion anomalies and pressure effect" *Phys. Rev. B*, **71**, 060407(R) (2005).

391. A. C. Komarek, H. Roth, M. Cwik, W. D. Stein, J. Baier, M. Kriener, F. Bouree, T. Lorenz and M. Braden, "Magnetoelastic coupling in RTiO_3 (R=La,Nd,Sm,Gd,Y) investigated with diffraction techniques and thermal expansion measurements" *Phys. Rev. B*, **75**, 224402 (2007).
392. Q. H. Jiang, F. T. Liu, C. W. Nan, Y. H. Lin, M. J. Reece, H. X. Yan, H. P. Ning and Z. J. Shen, "High-temperature ferroelectric phase transition observed in multiferroic $\text{Bi}_{0.91}\text{La}_{0.05}\text{Tb}_{0.04}\text{FeO}_3$ " *Appl. Phys. Lett.*, **95**, 012909 (2009).
393. B. J. Kennedy, C. J. Howard and B. C. Chakoumakos, "Phase transitions in perovskite at elevated temperatures - a powder neutron diffraction study" *J. Phys.: Condens. Matter*, **11**, 1479-1488 (1999).
394. H. D. Megaw, "Crystal Structures and Thermal Expansion" *Mater. Res. Bull.*, **6**, 1007 (1971).
395. I. A. Kornev and L. Bellaiche, "Nature of the ferroelectric phase transition in multiferroic BiFeO_3 from first principles" *Phys. Rev. B*, **79**, 100105(R) (2009).
396. J. S. Zhou and J. B. Goodenough, "Universal octahedral-site distortion in orthorhombic perovskite oxides" *Phys. Rev. Lett.*, **94**, 065501 (2005).
397. J. S. Zhou, J. B. Goodenough and B. Dabrowski, "Structure anomaly and electronic transition in RNiO_3 (R=La,Pr,...,Gd)" *Phys. Rev. B*, **70**, 081102(R) (2004).
398. C. J. Howard and B. J. Kennedy, "The orthorhombic and rhombohedral phases of LaGaO_3 - a neutron powder diffraction study" *J. Phys.: Condens. Matter*, **11**, 3229-3236 (1999).
399. D. C. Arnold, K. S. Knight, G. Catalan, S. A. T. Redfern, J. F. Scott, P. Lightfoot and F. D. Morrison, "The β to γ (insulator-metal) transition in BiFeO_3 " *condmat arXiv.*, 0908.3613 (2009).
400. C. N. W. Darlington, "Normal-mode analysis of the structures of perovskites with tilted octahedra" *Acta Crystallogr.*, **A58**, 66-71 (2002).
401. C. J. Howard and H. T. Stokes, "Group-theoretical analysis of octahedral tilting in perovskites" *Acta Crystallogr.*, **B54**, 782-789 (1998).
402. C. J. Howard and H. T. Stokes, "Structures and phase transitions in perovskites - a group-theoretical approach" *Acta Crystallogr.*, **A61**, 93-111 (2005).
403. H. T. Stokes, E. H. Kisi, D. M. Hatch and C. J. Howard, "Group-theoretical analysis of octahedral tilting in ferroelectric perovskites" *Acta Crystallogr.*, **B58**, 934-938 (2002).
404. N. F. Mott, "Metal-Insulator Transition" *Rev. Mod. Phys.*, **40**, 677-683 (1968).
405. D. B. McWhan and J. P. Remeika, "Metal-insulator transition in $(\text{V}_{1-x}\text{Cr}_x)_2\text{O}_3$ " *Phys. Rev. B*, **2**, 3734-3750 (1970).
406. A. I. Frenkel, E. A. Stern and F. A. Chudnovsky, "Local structure changes in V_2O_3 below and above the metal-insulator transition" *Solid State Commun.*, **102**, 637-641 (1997).
407. O. E. Gonzalez-Vazquez and J. Iniguez, "Pressure-induced structural, electronic, and magnetic effects in BiFeO_3 " *Phys. Rev. B*, **79**, 064102 (2009).

408. J. B. Torrance, P. Lacorro, C. Asavaroengchai and R. M. Metzger, "Simple and Perovskite Oxides of Transition-Metals - Why Some Are Metallic, While Most Are Insulating" *J. Solid State Chem.*, **90**, 168-172 (1991).
409. Y. Takeda, S. Naka, M. Takano, T. Shinjo, T. Takada and M. Shimada, "Preparation and Characterization of Stoichiometric CaFeO_3 " *Mater. Res. Bull.*, **13**, 61-66 (1978).
410. C. H. Yang, J. Seidel, S. Y. Kim, P. B. Rossen, P. Yu, M. Gajek, Y. H. Chu, L. W. Martin, M. B. Holcomb, Q. He, P. Maksymovych, N. Balke, S. V. Kalinin, A. P. Baddorf, S. R. Basu, M. L. Scullin and R. Ramesh, "Electric modulation of conduction in multiferroic Ca-doped BiFeO_3 films" *Nat. Mater.*, **8**, 485-493 (2009).
411. J. Mizusaki, M. Okayasu, S. Yamauchi and K. Fueki, "Nonstoichiometry and Phase Relationship of the $\text{SrFeO}_{2.5}$ - SrFeO_3 System at High-Temperature" *J. Solid State Chem.*, **99**, 166-172 (1992).
412. R. Haumont, P. Bouvier, A. Pashkin, K. Rabia, S. Frank, B. Dkhil, W. A. Crichton, C. A. Kuntscher and J. Kreisel, "Effect of high pressure on multiferroic BiFeO_3 " *Phys. Rev. B*, **79**, 184110 (2009).
413. V. I. Zinenko and M. S. Pavlovskii, "Lattice dynamics of BiFeO_3 : The untypical behavior of the ferroelectric instability under hydrostatic pressure" *JETP Lett.*, **87**, 288-291 (2008).
414. V. I. Zinenko and M. S. Pavlovskii, "Lattice dynamics of BiFeO_3 under hydrostatic pressure" *Phys. Sol. State*, **51**, 1404-1408 (2009).
415. A. A. Belik, H. Yusa, N. Hirao, Y. Ohishi and E. Takayama-Muromachi, "Structural Properties of Multiferroic BiFeO_3 under Hydrostatic Pressure" *Chem. Mater.*, **21**, 3400-3405 (2009).
416. G. A. Samara, T. Sakudo and K. Yoshimitsu, "Important Generalization Concerning Role of Competing Forces in Displacive Phase-Transitions" *Phys. Rev. Lett.*, **35**, 1767-1769 (1975).
417. R. J. Angel, J. Zhao and N. L. Ross, "General rules for predicting phase transitions in perovskites due to octahedral tilting" *Phys. Rev. Lett.*, **95**, 025503 (2005).
418. T. Tohei, A. Kuwabara, T. Yamamoto, F. Oba and I. Tanaka, "General rule for displacive phase transitions in perovskite compounds revisited by first principles calculations" *Phys. Rev. Lett.*, **94**, 035502 (2005).
419. W. M. Xu, O. Naaman, G. H. Rozenberg, M. P. Pasternak and R. D. Taylor, "Pressure-induced breakdown of a correlated system: The progressive collapse of the Mott-Hubbard state in RFeO_3 " *Phys. Rev. B*, **6409**, 094411 (2001).
420. J. R. Sahu and C. N. R. Rao, "Beneficial modification of the properties of multiferroic BiFeO_3 by cation substitution" *Solid State Sci.*, **9**, 950-954 (2007).
421. M. Kumar and K. L. Yadav, "Rapid liquid phase sintered Mn doped BiFeO_3 ceramics with enhanced polarization and weak magnetization" *Appl. Phys. Lett.*, **91**, 242901 (2007).
422. A. A. Belik, T. Kolodiazhnyi, K. Kosuda and E. Takayama-Muromachi, "Synthesis and properties of oxygen non-stoichiometric BiMnO_3 " *J. Mater. Chem.*, **19**, 1593-1600 (2009).

423. A. Sundaresan, R. V. K. Mangalam, A. Iyo, Y. Tanaka and C. N. R. Rao, "Crucial role of oxygen stoichiometry in determining the structure and properties of BiMnO₃" *J. Mater. Chem.*, **18**, 2191-2193 (2008).
424. J. Töpfer and J. B. Goodenough, "LaMnO_{3+δ} revisited" *J. Solid State Chem.*, **130**, 117-128 (1997).
425. J. A. M. van Roosmalen and E. H. P. Cordfunke, "The Defect Chemistry of LaMnO₃+/-Delta .4. Defect Model for LaMnO₃+Delta" *J. Solid State Chem.*, **110**, 109-112 (1994).
426. J. A. M. van Roosmalen, P. van Vlaanderen, E. H. P. Cordfunke, W. L. Ijdo and D. J. W. Ijdo, "Phases in the Perovskite-Type LaMnO₃+Delta Solid Solution and the La₂O₃-Mn₂O₃ Phase-Diagram" *J. Solid State Chem.*, **114**, 516-523 (1995).
427. S. Fritsch and A. Navrotsky, "Thermodynamic properties of manganese oxides" *J. Am. Ceram. Soc.*, **79**, 1761-1768 (1996).
428. I. Sosnowska, W. Schaffer, W. Kockelmann, K. H. Andersen and I. O. Troyanchuk, "Crystal structure and spiral magnetic ordering of BiFeO₃ doped with manganese" *Appl. Phys. A Mater. Sci. Proc.*, **74**, S1040-S1042 (2002).
429. S. B. Adler, "Chemical expansivity of electrochemical ceramics" *J. Am. Ceram. Soc.*, **84**, 2117-2119 (2001).
430. G. A. Rossetti and A. Navrotsky, "Calorimetric investigation of tricritical behavior in tetragonal Pb(Zr_xTi_{1-x})O₃" *J. Solid State Chem.*, **144**, 188-194 (1999).
431. M. Palcut, K. Wiik and T. Grande, "Cation self-diffusion and nonstoichiometry of lanthanum manganite studied by diffusion couple measurements" *J. Phys. Chem. C*, **111**, 813-822 (2007).
432. D. Kothari, V. R. Reddy, A. Gupta, D. M. Phase, N. Lakshmi, S. K. Deshpande and A. M. Awasthi, "Study of the effect of Mn doping on the BiFeO₃ system" *J. Phys.: Condens. Matter*, **19**, 136202 (2007).
433. A. K. Kundu, R. Ranjith, B. Kundys, N. Nguyen, V. Caignaert, V. Pralong, W. Prellier and B. Raveau, "A multiferroic ceramic with perovskite structure: (La_{0.5}Bi_{0.5})(Mn_{0.5}Fe_{0.5})O_{3.09}" *Appl. Phys. Lett.*, **93**, 052906 (2008).
434. P. S. I. P. N. de Silva, F. M. Richards, L. F. Cohen, J. A. Alonso, M. J. Martinez-Lope, M. T. Casais, K. A. Thomas and J. L. MacManus-Driscoll, "Effects of high vacancy concentrations on the magnetic properties of La_{1-x}Mn_{1-y}O₃ (0.02 <= x, y <= 0.13)" *J. Appl. Phys.*, **83**, 394-399 (1998).
435. J. Töpfer and J. B. Goodenough, "Charge transport and magnetic properties in perovskites of the system La-Mn-O" *Solid State Ionics*, **101**, 1215-1220 (1997).
436. X. Y. Chen, J. S. Yu and S. B. Adler, "Thermal and chemical expansion of Sr-doped lanthanum cobalt oxide (La_{1-x}Sr_xCoO_{3-δ})" *Chem. Mater.*, **17**, 4537-4546 (2005).
437. X. D. Zhou, L. R. Pederson, Q. Cai, J. Yang, B. J. Scarfino, M. Kim, W. B. Yelon, W. J. James, H. U. Anderson and C. Wang, "Structural and magnetic properties of LaMn_{1-x}Fe_xO₃ (0 < x < 1.0)" *J. Appl. Phys.*, **99**, 08M918 (2006).
438. J. B. Goodenough, "*Magnetism and the Chemical Bond*". 1963 John Wiley and Sons.

439. K. De, R. Ray, R. N. Panda, S. Giri, H. Nakamura and T. Kohara, "The effect of Fe substitution on magnetic and transport properties of LaMnO_3 " *J. Magn. Magn. Mater.*, **288**, 339-346 (2005).
440. F. Prado, R. D. Sanchez, A. Caneiro, M. T. Causa and M. Tovar, "Discontinuous evolution of the highly distorted orthorhombic structure and the magnetic order in $\text{LaMnO}_{3+\delta}$ perovskite" *J. Solid State Chem.*, **146**, 418-427 (1999).
441. C. R. Sankar and P. A. Joy, "Superspin glass behavior of a nonstoichiometric lanthanum manganite $\text{LaMnO}_{3.13}$ " *Phys. Rev. B*, **72**, 132407 (2005).
442. N. Nguyen, M. Legrain, A. Ducouret and B. Raveau, "Distribution of Mn^{3+} and Mn^{4+} species between octahedral and square pyramidal sites in $\text{Bi}_2\text{Mn}_4\text{O}_{10}$ -type structure" *J. Mater. Chem.*, **9**, 731-734 (1999).
443. L. Bi, A. R. Taussig, H. S. Kim, L. Wang, G. F. Dionne, D. Bono, K. Persson, G. Ceder and C. A. Ross, "Structural, magnetic, and optical properties of BiFeO_3 and $\text{Bi}_2\text{FeMnO}_6$ epitaxial thin films: An experimental and first-principles study" *Phys. Rev. B*, **78**, 104106 (2008).
444. H. Naganuma, J. Miura and S. Okamura, "Ferroelectric, electrical and magnetic properties of Cr, Mn, Co, Ni, Cu added polycrystalline BiFeO_3 films" *Appl. Phys. Lett.*, **93**, 052901 (2008).
445. S. K. Singh, H. Ishiwara and K. Maruyama, "Room temperature ferroelectric properties of Mn-substituted BiFeO_3 thin films deposited on Pt electrodes using chemical solution deposition" *Appl. Phys. Lett.*, **88**, 262908 (2006).
446. C. F. Chung, J. P. Lin and J. M. Wu, "Influence of Mn and Nb dopants on electric properties of chemical-solution-deposited BiFeO_3 films" *Appl. Phys. Lett.*, **88**, 242909 (2006).
447. P. Kharel, S. Talebi, B. Ramachandran, A. Dixit, V. M. Naik, M. B. Sahana, C. Sudakar, R. Naik, M. S. R. Rao and G. Lawes, "Structural, magnetic, and electrical studies on polycrystalline transition-metal-doped BiFeO_3 thin films" *J. Phys.: Condens. Matter*, **21**, 036001 (2009).
448. Z. Wen, G. D. Hu, S. H. Fan, C. H. Yang, W. B. Wu, Y. Zhou, X. M. Chen and S. G. Cui, "Effects of annealing process and Mn substitution on structure and ferroelectric properties of BiFeO_3 films" *Thin Solid Films*, **517**, 4497-4501 (2009).
449. J. R. Chen, W. L. Wang, J. B. Lia and G. H. Rao, "X-ray diffraction analysis and specific heat capacity of $(\text{Bi}_{1-x}\text{La}_x)\text{FeO}_3$ perovskites" *J. Alloys Compd.*, **459**, 66-70 (2008).
450. W. C. Koehler, E. O. Wollan and M. K. Wilkinson, "Neutron Diffraction Study of the Magnetic Properties of Rare-Earth-Iron Perovskites" *Phys. Rev.*, **118**, 58-70 (1960).
451. S. V. Kiselev, G. S. Zhdanov and R. P. Ozerov, "Detection of Magnetic Arrangement in BiFeO_3 Ferroelectric by Means of Neutron Diffraction Study" *Dokl. Akad. Nauk SSSR*, **145**, 1255 (1962).
452. W. Kaczmarek, M. Polomska and Z. Pajak, "Phase-Diagram of $(\text{Bi}_{1-x}\text{La}_x)\text{FeO}_3$ Solid-Solution" *Phys. Lett. A*, **47**, 227-228 (1974).
453. S. Karimi, I. M. Reaney, Y. Han, J. Pokorny and I. Sterianou, "Crystal chemistry and domain structure of rare-earth doped BiFeO_3 ceramics" *J. Mater. Sci.*, **44**, 5102-5112 (2009).

454. Z. V. Gabbasova, M. D. Kuzmin, A. K. Zvezdin, I. S. Dubenko, V. A. Murashov, D. N. Rakov and I. B. Krynetsky, "Bi_{1-x}R_xFeO₃ (R = Rare-Earth) - a Family of Novel Magnetoelectrics" *Phys. Lett. A*, **158**, 491-498 (1991).
455. G. L. Yuan, S. W. Or and H. L. W. Chan, "Structural transformation and ferroelectric-paraelectric phase transition in Bi_{1-x}La_xFeO₃ (x=0-0.25) multiferroic ceramics" *J. Phys. D: Appl. Phys.*, **40**, 1196-1200 (2007).
456. J. Chen, R. B. Yu, L. H. Li, C. Sun, T. Zhang, H. W. Chen and X. R. Xing, "Structure and shape evolution of Bi_{1-x}La_xFeO₃ perovskite microcrystals by molten salt synthesis" *Eur. J. Inorg. Chem.*, 3655-3660 (2008).
457. Z. X. Cheng, A. H. Li, X. L. Wang, S. X. Dou, K. Ozawa, H. Kimura, S. J. Zhang and T. R. Shroud, "Structure, ferroelectric properties, and magnetic properties of the La-doped bismuth ferrite" *J. Appl. Phys.*, **103**, 07E507 (2008).
458. S. Karimi, I. M. Reaney, I. Levin and I. Sterianou, "Nd-doped BiFeO₃ ceramics with antipolar order" *Appl. Phys. Lett.*, **94**, 112903 (2009).
459. G. L. Yuan, S. W. Or and H. L. W. Chan, "Raman scattering spectra and ferroelectric properties of Bi_{1-x}Nd_xFeO₃ (x=0-0.2) multiferroic ceramics" *J. Appl. Phys.*, **101**, 064101 (2007).
460. G. L. Yuan, S. W. Or, J. M. Liu and Z. G. Liu, "Structural transformation and ferromagnetic behavior in single-phase Bi_{1-x}Nd_xFeO₃ multiferroic ceramics" *Appl. Phys. Lett.*, **89**, 052905 (2006).
461. G. L. Yuan and S. W. Or, "Multiferroicity in polarized single-phase Bi_{0.875}Sm_{0.125}FeO₃ ceramics" *J. Appl. Phys.*, **100**, 024109 (2006).
462. V. A. Khomchenko, D. A. Kiselev, I. K. Bdikin, V. V. Shvartsman, P. Borisov, W. Kleemann, J. M. Vieira and A. L. Kholkin, "Crystal structure and multiferroic properties of Gd-substituted BiFeO₃" *Appl. Phys. Lett.*, **93**, 262905 (2008).
463. V. A. Khomchenko, V. V. Shvartsman, P. Borisov, W. Kleemann, D. A. Kiselev, I. K. Bdikin, J. M. Vieira and A. L. Kholkin, "Crystal structure and magnetic properties of Bi_{0.8}(Gd_{1-x}Ba_x)_{0.2}FeO₃ (x= 0, 0.5, 1) multiferroics" *J. Phys. D: Appl. Phys.*, **42**, 045418 (2009).
464. V. A. Khomchenko, V. V. Shvartsman, P. Borisov, W. Kleemann, D. A. Kiselev, I. K. Bdikin, J. M. Viera and A. L. Kholkin, "Effect of Gd substitution on the crystal structure and multiferroic properties of BiFeO₃" *Acta Mater.*, DOI:10.1016/j.actamat.2009.07.013 (2009).
465. S. X. Zhang, W. J. Luo, D. L. Wang and Y. W. Ma, "Phase evolution and magnetic property of Bi_{1-x}Dy_xFeO₃ ceramics" *Mater. Lett.*, **63**, 1820-1822 (2009).
466. M. Ahart, M. Somayazulu, R. E. Cohen, P. Ganesh, P. Dera, H. K. Mao, R. J. Hemley, Y. Ren, P. Liermann and Z. G. Wu, "Origin of morphotropic phase boundaries in ferroelectrics" *Nature*, **451**, 545-U2 (2008).
467. J. Frantti, Y. Fujioka and R. M. Nieminen, "Evidence against the polarization rotation model of piezoelectric perovskites at the morphotropic phase boundary" *J. Phys.: Condens. Matter*, **20**, 472203 (2008).
468. J. Frantti, Y. Fujioka, J. Zhang, S. C. Vogel, Y. Wang, Y. Zhao and R. M. Nieminen, "The Factors Behind the Morphotropic Phase Boundary in Piezoelectric Perovskites" *J. Phys. Chem. B*, **113**, 7967-7972 (2009).

469. R. Guo, L. E. Cross, S. E. Park, B. Noheda, D. E. Cox and G. Shirane, "Origin of the high piezoelectric response in $\text{PbZr}_{1-x}\text{Ti}_x\text{O}_3$ " *Phys. Rev. Lett.*, **84**, 5423-5426 (2000).
470. B. Noheda, D. E. Cox, G. Shirane, J. A. Gonzalo, L. E. Cross and S. E. Park, "A monoclinic ferroelectric phase in the $\text{Pb}(\text{Zr}_{1-x}\text{Ti}_x)\text{O}_3$ solid solution" *Appl. Phys. Lett.*, **74**, 2059-2061 (1999).
471. K. A. Schonau, M. Knapp, H. Kungl, M. J. Hoffmann and H. Fuess, "In situ synchrotron diffraction investigation of morphotropic $\text{Pb}[\text{Zr}_{1-x}\text{Ti}_x]\text{O}_3$ under an applied electric field" *Phys. Rev. B*, **76**, 144112 (2007).
472. K. A. Schonau, M. Knapp, M. Maglione and H. Fuess, "In situ investigation of the stability field and relaxation behavior of nanodomain structures in morphotropic $\text{Pb}[\text{Zr}_{1-x}\text{Ti}_x]\text{O}_3$ under variations in electric field and temperature" *Appl. Phys. Lett.*, **94**, 122902 (2009).
473. K. A. Schonau, L. A. Schmitt, M. Knapp, H. Fuess, R. A. Eichel, H. Kungl and M. J. Hoffmann, "Nanodomain structure of $\text{Pb}[\text{Zr}_{1-x}\text{Ti}_x]\text{O}_3$ at its morphotropic phase boundary: Investigations from local to average structure" *Phys. Rev. B*, **75**, 184117 (2007).
474. Z. G. Wu and R. E. Cohen, "Pressure-induced anomalous phase transitions and colossal enhancement of piezoelectricity in PbTiO_3 " *Phys. Rev. Lett.*, **95**, 037601 (2005).
475. Q. Zhou, B. J. Kennedy, Z. Zhang, L.-Y. Jang and J. B. Aitken, "X-ray Absorption near Edge Structure and Crystallographic Studies of the Mixed Valence Oxides $\text{CaRu}_{1-x}\text{Mn}_x\text{O}_3$ " *Chem. Mater.*, DOI: 10.1021/cm9007238 (2009).
476. V. L. Moruzzi and M. W. Shafer, "Phase Equilibria in the System La_2O_3 -Iron Oxide in Air" *J. Am. Ceram. Soc.*, **43**, 367-372 (1960).
477. S. Stølen and T. Grande, "*Chemical Thermodynamics of Materials - Macroscopic and Microscopic Aspects*". 2004, West Sussex, England John Wiley & Sons Ltd.
478. S. Geller and P. M. Raccach, "Phase Transitions in Perovskitelike Compounds of Rare Earths" *Phys. Rev. B*, **2**, 1167-1172 (1970).
479. S. Geller and E. A. Wood, "Crystallographic Studies of Perovskite-Like Compounds .1. Rare Earth Orthoferrites and YFeO_3 , YCrO_3 , YAlO_3 " *Acta Crystallogr.*, **9**, 563-568 (1956).
480. N. A. Spaldin, "Fundamental size limits in ferroelectricity" *Science*, **304**, 1606-1607 (2004).
481. I. P. Batra, P. Wurfel and B. D. Silverman, "New Type of First-Order Phase-Transition in Ferroelectric Thin-Films" *Phys. Rev. Lett.*, **30**, 384-387 (1973).
482. I. P. Batra, P. Wurfel and B. D. Silverman, "Phase-Transition, Stability, and Depolarization Field in Ferroelectric Thin-Films" *Phys. Rev. B*, **8**, 3257-3265 (1973).
483. J. Junquera and P. Ghosez, "Critical thickness for ferroelectricity in perovskite ultrathin films" *Nature*, **422**, 506-509 (2003).
484. G. Gerra, A. K. Tagantsev, N. Setter and K. Parlinski, "Ionic polarizability of conductive metal oxides and critical thickness for ferroelectricity in BaTiO_3 " *Phys. Rev. Lett.*, **96**, 107603 (2006).

485. P. Wurfel, I. P. Batra and J. T. Jacobs, "Polarization Instability in Thin Ferroelectric Films" *Phys. Rev. Lett.*, **30**, 1218-1221 (1973).
486. S. K. Streiffer, J. A. Eastman, D. D. Fong, C. Thompson, A. Munkholm, M. V. R. Murty, O. Auciello, G. R. Bai and G. B. Stephenson, "Observation of nanoscale 180 degrees stripe domains in ferroelectric PbTiO₃ thin films" *Phys. Rev. Lett.*, **89**, 067601 (2002).
487. T. Tybell, C. H. Ahn and J. M. Triscone, "Ferroelectricity in thin perovskite films" *Appl. Phys. Lett.*, **75**, 856-858 (1999).
488. D. D. Fong, G. B. Stephenson, S. K. Streiffer, J. A. Eastman, O. Auciello, P. H. Fuoss and C. Thompson, "Ferroelectricity in ultrathin perovskite films" *Science*, **304**, 1650-1653 (2004).
489. K. Uchino, E. Sadanaga and T. Hirose, "Dependence of the Crystal-Structure on Particle-Size in Barium-Titanate" *J. Am. Ceram. Soc.*, **72**, 1555-1558 (1989).
490. K. Ishikawa, K. Yoshikawa and N. Okada, "Size Effect on the Ferroelectric Phase-Transition in PbTiO₃ Ultrafine Particles" *Phys. Rev. B*, **37**, 5852-5855 (1988).
491. S. Chattopadhyay, P. Ayyub, V. R. Palkar, A. V. Gurjar, R. M. Wankar and M. Multani, "Finite-size effects in antiferroelectric PbZrO₃ nanoparticles" *J. Phys.: Condens. Matter*, **9**, 8135-8145 (1997).
492. A. Schilling, D. Byrne, G. Catalan, K. G. Webber, Y. A. Genenko, G. S. Wu, J. F. Scott and J. M. Gregg, "Domains in Ferroelectric Nanodots" *Nano Lett.*, DOI: 10.1021/nl901661a (2009).
493. I. I. Naumov, L. Bellaiche and H. X. Fu, "Unusual phase transitions in ferroelectric nanodisks and nanorods" *Nature*, **432**, 737-740 (2004).
494. I. Naumov and H. X. Fu, "Vortex-to-polarization phase transformation path in ferroelectric Pb(ZrTi)O₃ nanoparticles" *Phys. Rev. Lett.*, **98**, 077603 (2007).
495. J. M. Gregg, "Ferroelectrics at the nanoscale" *Phys. Status Solidi A*, **206**, 577-587 (2009).
496. G. S. Li, J. Boerio-Goates, B. F. Woodfield and L. P. Li, "Evidence of linear lattice expansion and covalency enhancement in rutile TiO₂ nanocrystals" *Appl. Phys. Lett.*, **85**, 2059-2061 (2004).
497. K. Ishikawa and T. Uemori, "Surface relaxation in ferroelectric perovskites" *Phys. Rev. B*, **60**, 11841-11845 (1999).
498. S. Tsunekawa, K. Ishikawa, Z. Q. Li, Y. Kawazoe and A. Kasuya, "Origin of anomalous lattice expansion in oxide nanoparticles" *Phys. Rev. Lett.*, **85**, 3440-3443 (2000).
499. S. Tsunekawa, S. Ito, T. Mori, K. Ishikawa, Z. Q. Li and Y. Kawazoe, "Critical size and anomalous lattice expansion in nanocrystalline BaTiO₃ particles" *Phys. Rev. B*, **62**, 3065-3070 (2000).
500. V. Perebeinos, S. W. Chan and F. Zhang, "Madelung model prediction for dependence of lattice parameter on nanocrystal size" *Solid State Commun.*, **123**, 295-297 (2002).
501. A. Navrotsky, L. Mazeina and J. Majzlan, "Size-driven structural and thermodynamic complexity in iron oxides" *Science*, **319**, 1635-1638 (2008).

502. A. Navrotsky, "Energetics of nanoparticle oxides: interplay between surface energy and polymorphism" *Geochem. Trans.*, **4**, 34-37 (2003).
503. M. F. Zhang, J. M. Liu and Z. G. Liu, "Microstructural characterization of nanosized YMnO_3 powders: the size effect" *Appl. Phys. A: Mater. Sci. Proc.*, **79**, 1753-1756 (2004).
504. E. Galstyan, B. Lorenz, K. S. Martirosyan, F. Yen, Y. Y. Sun, M. M. Gospodinov and C. W. Chu, "Magnetic hysteretic phenomena in multiferroic HoMnO_3 single crystals and polycrystals with nano- and micrometer particle size" *J. Phys.: Condens. Matter*, **20**, 325241 (2008).
505. S. Kharrazi, D. C. Kundaliya, S. W. Gosavi, S. K. Kulkarni, T. Venkatesan, S. B. Ogale, J. Urban, S. Park and S. W. Cheong, "Multiferroic TbMnO_3 nanoparticles" *Solid State Commun.*, **138**, 395-398 (2006).
506. C. Ma, J. Q. Yan, K. W. Dennis, R. W. McCallum and X. Tan, "Size-dependent magnetic properties of high oxygen content YMn_2O_5 +/-delta multiferroic nanoparticles" *J. Appl. Phys.*, **105**, 033908 (2009).
507. S. Shetty, V. R. Palkar and R. Pinto, "Size effect study in magnetoelectric BiFeO_3 system" *Pramana J. Phys.*, **58**, 1027-1030 (2002).
508. R. Mazumder, S. Ghosh, P. Mondal, D. Bhattacharya, S. Dasgupta, N. Das, A. Sen, A. K. Tyagi, M. Sivakumar, T. Takami and H. Ikuta, "Particle size dependence of magnetization and phase transition near T_N in multiferroic BiFeO_3 " *J. Appl. Phys.*, **100**, 033908 (2006).
509. T. J. Park, G. C. Papaefthymiou, A. J. Viescas, A. R. Moodenbaugh and S. S. Wong, "Size-dependent magnetic properties of single-crystalline multiferroic BiFeO_3 nanoparticles" *Nano Lett.*, **7**, 766-772 (2007).
510. R. Mazumder, P. S. Devi, D. Bhattacharya, P. Choudhury, A. Sen and M. Raja, "Ferromagnetism in nanoscale BiFeO_3 " *Appl. Phys. Lett.*, **91**, 062510 (2007).
511. S. Vijayanand, H. S. Potdar and P. A. Joy, "Origin of high room temperature ferromagnetic moment of nanocrystalline multiferroic BiFeO_3 " *Appl. Phys. Lett.*, **94**, 182507 (2009).
512. H. Bea, M. Bibes, S. Fusil, K. Bouzehouane, E. Jacquet, K. Rode, P. Bencok and A. Barthelemy, "Investigation on the origin of the magnetic moment of BiFeO_3 thin films by advanced X-ray characterizations" *Phys. Rev. B*, **74**, 020101(R) (2006).
513. A. Sundaresan and C. N. R. Rao, "Ferromagnetism as a universal feature of inorganic nanoparticles" *Nano Today*, **4**, 96-106 (2009).
514. R. V. K. Mangalam, N. Ray, U. V. Waghmare, A. Sundaresan and C. N. R. Rao, "Multiferroic properties of nanocrystalline BaTiO_3 " *Solid State Commun.*, **149**, 1-5 (2009).
515. H. Wei, D. S. Xue and Y. Xu, "Photoabsorption characterization and magnetic property of multiferroic BiFeO_3 nanotubes synthesized by a facile sol-gel template process" *Scripta Mater.*, **58**, 45-48 (2008).
516. S. Chattopadhyay, S. D. Kelly, V. R. Palkar, L. Fan and C. U. Segre, "Investigation of size effects in magnetoelectric BiFeO_3 " *Phys Scripta*, **T115**, 709-713 (2005).
517. E. Oniyama and P. G. Wahlbeck, "Phase equilibria in the bismuth-oxygen system" *J. Phys. Chem. B*, **102**, 4418-4425 (1998).

518. L. S. Darken and R. W. Gurry, "The System Iron Oxygen .2. Equilibrium and Thermodynamics of Liquid Oxide and Other Phases" *J. Am. Chem. Soc.*, **68**, 798-816 (1946).
519. P. Ayyub, V. R. Palkar, S. Chattopadhyay and M. Multani, "Effect of Crystal Size-Reduction on Lattice Symmetry and Cooperative Properties" *Phys. Rev. B*, **51**, 6135-6138 (1995).
520. S. Chattopadhyay, P. Ayyub, V. R. Palkar and M. Multani, "Size-Induced Diffuse Phase-Transition in the Nanocrystalline Ferroelectric PbTiO_3 " *Phys. Rev. B*, **52**, 13177-13183 (1995).
521. W. L. Zhong, B. Jiang, P. L. Zhang, J. M. Ma, H. M. Cheng, Z. H. Yang and L. X. Li, "Phase-Transition in PbTiO_3 Ultrafine Particles of Different Sizes" *J. Phys.: Condens. Matter*, **5**, 2619-2624 (1993).
522. K. Ishikawa, T. Nomura, N. Okada and K. Takada, "Size effect on the phase transition in PbTiO_3 fine particles" *Jpn. J. Appl. Phys.*, **35**, 5196-5198 (1996).
523. E. K. Akdogan, C. J. Rawn, W. D. Porter, E. A. Payzant and A. Safari, "Size effects in PbTiO_3 nanocrystals: Effect of particle size on spontaneous polarization and strains" *J. Appl. Phys.*, **97**, 084305 (2005).
524. T. Yamamoto, K. Urabe and H. Banno, " BaTiO_3 Particle-Size Dependence of Ferroelectricity in BaTiO_3 Polymer Composites" *Jpn. J. Appl. Phys.*, **32**, 4272-4276 (1993).
525. T. Yan, Z. G. Shen, W. W. Zhang and J. F. Chen, "Size dependence on the ferroelectric transition of nanosized BaTiO_3 particles" *Mater. Chem. Phys.*, **98**, 450-455 (2006).
526. E. Erdem, H. C. Semmelhack, R. Bottcher, H. Rumpf, J. Banys, A. Matthes, H. J. Glasel, D. Hirsch and E. Hartmann, "Study of the tetragonal-to-cubic phase transition in PbTiO_3 nanopowders" *J. Phys.: Condens. Matter*, **18**, 3861-3874 (2006).
527. E. K. Akdogan and A. Safari, "Phenomenological theory of size effects on the cubic-tetragonal phase transition in BaTiO_3 nanocrystals" *Jpn. J. Appl. Phys.*, **41**, 7170-7175 (2002).
528. D. P. Landau, "Finite-Size Behavior of Simple-Cubic Ising Lattice" *Phys. Rev. B*, **14**, 255-262 (1976).
529. X. Batlle and A. Labarta, "Finite-size effects in fine particles: magnetic and transport properties" *J. Phys. D: Appl. Phys.*, **35**, R15-R42 (2002).
530. P. M. Chaiken and T. C. Lubensky, "*Principles of Condensed Matter Physics*". 1995, Cambridge, UK Cambridge University Press.
531. W. Y. Shih, W. H. Shih and I. A. Aksay, "Size Dependence of the Ferroelectric Transition of Small BaTiO_3 Particles - Effect of Depolarization" *Phys. Rev. B*, **50**, 15575-15585 (1994).
532. M. B. Smith, K. Page, T. Siegrist, P. L. Redmond, E. C. Walter, R. Seshadri, L. E. Brus and M. L. Steigerwald, "Crystal structure and the paraelectric-to-ferroelectric phase transition of nanoscale BaTiO_3 " *J. Am. Chem. Soc.*, **130**, 6955-6963 (2008).
533. S. M. Selbach, T. Tybell, M.-A. Einarsrud and T. Grande, "Size-dependent properties of multiferroic BiFeO_3 nanoparticles" *Chem. Mater.*, **19**, 6478-6484 (2007).

534. V. Petkov, V. Buscaglia, M. T. Buscaglia, Z. Zhao and Y. Ren, "Structural coherence and ferroelectricity decay in submicron- and nano-sized perovskites" *Phys. Rev. B*, **78**, 054107 (2008).
535. V. Petkov, M. Gateshki, M. Niederberger and Y. Ren, "Atomic-scale structure of nanocrystalline $\text{Ba}_x\text{Sr}_{1-x}\text{TiO}_3$ ($x=1, 0.5, 0$) by X-ray diffraction and the atomic pair distribution function technique" *Chem. Mater.*, **18**, 814-821 (2006).
536. C. L. Jia, V. Nagarajan, J. Q. He, L. Houben, T. Zhao, R. Ramesh, K. Urban and R. Waser, "Unit-cell scale mapping of ferroelectricity and tetragonality in epitaxial ultrathin ferroelectric films" *Nat. Mater.*, **6**, 64-69 (2007).